SOLID OXIDE FUEL CELL STACK SIMULATION AND OPTIMIZATION, INCLUDING EXPERIMENTAL VALIDATION AND TRANSIENT BEHAVIOR

THÈSE N^{O} 3275 (2005)

PRÉSENTÉE À LA FACULTÉ SCIENCES ET TECHNIQUES DE L'INGÉNIEUR

Institut des sciences de l'énergie

SECTION DE GÉNIE MÉCANIQUE

ÉCOLE POLYTECHNIQUE FÉDÉRALE DE LAUSANNE

POUR L'OBTENTION DU GRADE DE DOCTEUR ÈS SCIENCES

PAR

Diego LARRAIN

ingénieur mécanicien diplômé EPF
et de nationalité française

acceptée sur proposition du jury:

Prof. D. Favrat, Dr J. Van Herle, directeurs de thèse
Prof. J. Brouwer, rapporteur
Dr M. Roos, rapporteur
Prof. A.-Ch. Rufer, rapporteur

Lausanne, EPFL
2005

Abstract

This thesis presents the development of models for the simulation and optimization of the design of a planar solid oxide fuel cell (SOFC) stack. Fuel cells produce electric power directly from a fuel by electrochemical reactions. The high efficiencies demonstrated make them a promising technology for energy conversion. The main challenges lie with reliability and cost reduction. Some applications demand at the same time strong requirements on the compactness of the system and its ability to load following. The models have been developed to represent the novel stack proposed by HTceramix SA (Yverdon, Switzerland) which is tested and partly developed at the Laboratoire d'Energétique Industrielle (LENI).
The model has been created in a way which allows its use for design optimization: this requires detailed and validated outputs to gain insight in the behavior of a new stack design and computational efficiency to allow sensitivity studies and optimization. Electrochemistry, mass and heat transfer phenomena are combined with a 2D fluid motion description to obtain a generalized model which can be applied to a large range of geometries. An efficient stack modeling approach is proposed.
Validation of the model has been carried out with measurements and a 3D computational fluid dynamics model. A methodology based on parameter estimation has been used to identify kinetic parameters and other uncertain parameters. Local temperature measurements and a local current density measurement have been performed and also used for model validation. The 2D model has been successfully validated showing good agreement with both the experiments and the detailed 3D model.
Simulation of the novel stack geometry (counter-flow) has allowed to identify the main problems arising from this compact geometry where the non-homogeneous velocity field creates stagnant zones which limit the operation at high efficiency. The simulated temperatures are characterized by important gradients and excessive level values (>850°C) for an intermediate temperature SOFC (700-800°C). This motivated to work on an alternative geometry, which based on simulation results, solves most of the problems previously identified.
The thesis presents several examples of the influence of design on the system performance and reliability. Transient simulations have been performed and the design choice had only a small impact on the transient behavior which presents intrinsically an important thermal inertia. On the contrary, degradation behavior is dependent on the design. Stack degradation has been simulated by including the metal interconnect degradation into the stack model. The approach has allowed to identify a new criterion to express degradation consistently for different test conditions.
To assist stack design, new approaches are necessary. The geometry of a stack was initially determined by a number of decision variables (such as cell area, thickness of the channels and interconnects) on which extensive sensitivity analysis were conducted. This method is of limited use as each of the objectives on stack design led to different solutions. To overcome this limitation, multi-objective optimization has been applied to the stack design problem. Application of this method is new in this field and different optimization strategies are tested. The results from the optimization allow to identify a clear trade-off between the compactness of the stack and the temperature level (and therefore the degradation).

Résumé

Cette thèse présente le développement de modèles pour la simulation et l'optimisation de la conception d'un élément de répétition de pile à combustible à oxyde solide (SOFC). Les piles à combustible convertissent directement l'énergie d'un combustible en électricité, ce qui permet de hauts rendements et explique l'intérêt pour cette technologie. Les principaux défis à relever sont la fiabilité et la réduction des coûts. Certaines applications imposent des contraintes sévères sur la compacité du système et sa capacité à suivre les fluctuations de demande. Le modèle a été conçu pour représenter un concept d'empilement novateur proposé par HTceramix SA (Yverdon, Suisse) qui est testé et a été partiellement développé au Laboratoire d'Energétique Industrielle.

Le modèle a été orienté vers l'optimisation de la conception de l'élément de répétition. Un compromis a donc été fait entre le niveau de détail des résultats, qui sont utiles à la compréhension du comportement d'un empilement, et l'efficacité de calcul nécessaire pour mener à bien les études de sensibilité et l'optimisation. Les phénomènes électrochimiques, de transfert de chaleur et de masse sont couplés à une description en 2D de l'écoulement des fluides : ceci permet l'application de ce modèle à une large palette de géométries possibles. Un modèle permettant la simulation efficace de l'empilement a été réalisé.

Le modèle a été validé à l'aide de données experimentales et par la comparaison rigoureuse avec un modèle 3D plus détaillé, basé sur un outil de mécanique des fluides numérique. Une méthodologie utilisant un algorithme d'estimation paramétrique a été appliquée pour identifier les paramètres incertains (en particulier pour la cinétique). Des mesures locales de température et de densité de courant ont été réalisées et utilisées pour la validation. Le modèle a été validé avec succès et présente des résultats concordant aussi bien avec les mesures qu'avec le modèle détaillé.

La simulation du nouveau concept d'empilement a permis de déceler les problèmes majeurs causés par sa géométrie. L'écoulement des réactifs, qui est très inhomogène, présente des zones stagnantes qui limitent les performances de l'empilement pour une opération à rendement élevé. De plus, la simulation révèle des gradients de température conséquents et un niveau de température excessif (>850°C) pour une SOFC à température intermédiaire (700-800°C). Ces problèmes ont conduit à la proposition d'une nouvelle géométrie qui permet de résoudre une grande partie des défauts observés.

L'influence du design sur le comportement, la performance et la fiabilité de l'empilement est montrée dans de nombreux exemples. L'influence sur le comportement en transitoire est limitée, car les piles SOFC possèdent intrinsèquement une importante inertie thermique. En revanche, l'influence sur le comportement à long terme est montrée par l'insertion, dans le modèle d'empilement, de l'oxydation des interconnecteurs. La simulation du vieillissement de la pile a permis d'identifier un critère pour la dégradation, qui compare de manière cohérente des cas de figures simulés dans des conditions opératoires différentes.

Afin d'assister la conception de l'empilement, de nouvelles méthodes sont nécessaires. La géométrie de l'empilement est définie par des variables de décision comme par exemple la surface de la cellule, l'épaisseur des interconnecteurs ou des canaux d'écoulement. Des études de sensibilité ont été réalisées mais l'utilité de cette méthode est limitée puisque les différents objectifs de design conduisent à différentes solutions. Pour dépasser cette limitation, de nouvelles méthodes d'optimisation multi-objectifs ont été appliquées avec succès. Un compromis clair entre la compacité de l'empilement et le niveau de température, lui-même lié à la dégradation, est identifié.

Acknowledgment

My first thank goes to Prof. Favrat and Dr. Jan Van herle who offered me the possibility to join the newly formed fuel cell group at LENI. I really appreciated the freedom I had in my work, the working conditions, the atmosphere and the opportunity to join a project at its early stage. Jan is also to be acknowledged for his introduction to SOFCs and a number of discussions, even when he's very busy (and that's often the case) he found some time to answer a question or discuss a point. He also carefully reviewed the different papers and chapters of this thesis (even sometimes at an early stage). Thanks for all!
This thesis has been carefully studied by the examiners who had a large number of interesting questions. Thanks are due to all of them for the good discussion.

This work has been supported financially by the Swiss Commision for Technology and Innovation (project 5401.2 SUS) and the Swiss Federal Office of Energy (project 46795). Both organisations are gratefully thanked for having made this work possible.
These projects were in joined collaboration with HTceramix S.A. at Yverdon and which is thanked for providing cells and stacks for the experimental work.

Within LENI, first thank goes to the fuel cell group - Michele, Nordahl, Zacharie - for the many hours spent together in the lab preparing experiments or struggling with a model, the discussions, the working atmosphere (even in hard times) and finally a number of apéros. Nordahl and Zacharie have not only contributed to the CFD model, but also reviewed some of the chapters. Merci! Michele has greatly contributed to his work by his hand on the experimental side which gave me some time for the simulation work. Grazie! John Schild, who made a short stay at LENI, is thanked for the positive thinking he brought in the project at a critical stage and the interesting discussions.
Dr. François Maréchal is thanked for the interesting discussions on simulation and optimization topics as well as for the musical experience of the "Léniphémère" sessions which I enjoyed a lot and improved significantly my didgeridoo playing.
The optimization work has been partly done with the QMOO algorithm and a specially developed interface for which I'd like to thank Geoff Leyland.
Experimental work would be difficult without the hands of Marc and Roger, merci à vous pour tous ces coups de mains (même en urgence!).
Some of the visitors at the LENI have, at a given period, helped this work and are acknowledged here: Prof. Costamagna on the modeling side and Hugh Middleton for experimental topics. Thanks also to Björn Thorud who passed a week in Lausanne when my model was at a very preliminary stage, and for the week I spent in Norway a year latter.

During my stay at LENI, I shared my disordered office first with Michele Zehnder and then with Nordahl. I'd like to thank them for the good times spent in and outside the office (barbecues, Aareschwimmen, concerts...). The atmosphere at LENI has been great during this years (with LeniCiné, LeniApéros, LeniSki and all the variations) and everyone contributes to it. Merci à tous!!! and grazie a Francesca per il positivismo, to Jürg, Brigitte, Céline, Pierre-Alain, Irwin, Xavier and Geoff.

Then, I'd like to give a special and big, big thank to Bettina for all that we have shared and for always being by my side. Un million de gracias por todo!
Beside the thesis, I had other experiences and activities (can you really believe that?) shared

with friends from Lausanne and around. Thanks to Yariv, Mathieu, Séverine, Sylvain, Arnaud, Raj, Delphine, Nikolaus and Pierre-Yves for the evenings, brunches, week-ends, barbecues, concerts or waves we had together... and just for being there!!! Vielen Dank auch to Gertrud und Beat for the relaxing summer weeks in Camargue.
Finally, I would like to acknowledge my family, especially my parents and brothers for their support during my studies and then this thesis. Gracias y Un gran abrazo a todos!

Contents

List of Figures

List of Tables

Abbreviations and symbols

Abbreviations

APU	auxiliary power unit
AASR	apparent area specific resistance
ASE	anode supported electrolyte cell
ASR	area specific resistance
CFD	computational fluid dynamics
CHP	combined heat and power generation
DLR	Deutschen Zentrum für Luft- und Raumfahrt
EIS	electrochemical impedance spectroscopy
LENI	Laboratoire d'Energétique Industrielle
LSC	strontium doped lantanum cobaltite
LSF	strontium doped lantanum ferrite
LSM	strontium doped lantanum manganite
MIC	metallic interconnect
MOO	multi-objective optimization
NDS	non-dominated set
NLP	non-linear programming (optimization method)
OCV	open circuit voltage
PEMFC	polymer electrolyte fuel cell
POF	Pareto optimal front
SOFC	solid oxide fuel cell
YSZ	Yttria Stabilized Zirconia
3YSZ	3% molar Yttria Stabilized Zirconia
8YSZ	8% molar Yttria Stabilized Zirconia

Electrochemical model

U_{cell}	cell potential	V
U_{OCV}	cell potential at OCV	V

U_{Nernst}	Nernst potential	V
j	current density	A/cm^2
j_{ion}	ionic current density	A/cm^2
j_{loss}	short circuit current density	A/cm^2
j_{load}	current density external circuit	A/cm^2
η_C	cathode overpotential	V
η_A	anode overpotential	V
j_{oe}	electrode exchange current density	A/cm^2
k_{jo_e}	exchange current density constant	Ω^{-1}.m^{-2}
${E_a}^{j_o}$	activation energy for charge transfer	J/mol
R_{ionic}	electrolyte ionic specific resistance	Ω.cm^2
R_{ohm}	ohmic specific resistance	Ω.cm^2
${R_{ohm}}^{MIC}$	interconnect area specific resistance	Ω.cm^2
σ_{mic}	interconnect oxide layer conductivity	S/m
σ_{ion}	electrolyte ionic conductivity	S/m
ρ_e^i	electrolyte ionic resistivity	Ω.cm
ξ	interconnect oxide layer thickness	*cm*
l_e	electrolyte thickness	cm
R	gas constant	J/mol.K
ΔG_o	standard Gibbs free enthalpy	J/mol
F	Faraday constant	C/mol

Fluid motion and species conservation

$\overline{\overline{D}}$	permeability tensor	m^2
K	permeability	m^2
μ	dynamic viscosity	kg/(s^1.m^1)
L_{ch}	channel height	cm
P	pressure	Pa
$\overline{\overline{\tau}}$	stress tensor	
$\vec{v}$	velocity vector	m/s
$\mathcal{C}$	molar concentration	mol/cm^3
$\mathcal{C}_i$	molar concentration of i	mol$_\mathrm{i}$/cm^3

D	binary diffusion coefficient	cm^2/s
$\vec{F_i}$	molar flux vector	$mol_i/(cm^3.s)$
$\dot{r}_i$	rate of reaction species i	$mol/(cm^2.s^1)$
χ_i	molar fraction of i	mol_i/mol
ρ	fluid density	kg/m^3
Y_i	mass fraction of the mixture component i	kg_i/kg
$\dot{r}_i$	rate of reaction for i	$kg_i/(m^3.s)$

Energy equations

$\mathcal{C}_{gas}$	heat capacity	J/(mol.K)
$\dot{E}_{elec}$	surface specific electric power	W/m^2
E_j	mass specific energy	J/kg
d_{tube}	tube diameter	m
k_{eff}	thermal conductivity	W/(mK)
H_i	molar specific enthalpy	J/mol
h_{conv}	heat transfer coefficient	$W/(m^2.K)$
h_{tube}	heat transfer coefficient	$W/(m^2.K)$
L_s	height of the solid	m
L_z	height of the stack	m
$\lambda_{s_{x,y}}$	thermal conduction in x and y	W/(mK)
λ_{s_z}	thermal conduction in z	W/(mK)
N_{cells}	number of cells in stack	cells
$\dot{Q}$	volumetric heat source	W/m^3
$\dot{Q}_{loss}$	heat losses	W/m^3

Performance indicators

$V_{repeatelement}$	repeat element volume	cm^3
ϵ_{spe}	volumetric power density	W/cm^3
ΔT_{max}	maximum temperature difference	°C
$T_{maxsolid}$	maximum temperature	°C
$T_{minsolid}$	minimum temperature	°C

Chapter 1

Introduction

1.1 Introduction

This thesis considers the simulation and optimization of a planar solid oxide fuel cell (SOFC) stack. SOFCs are a promising energy conversion technology. The main challenges for fuel cells are associated with reliability and cost reduction. Solid oxide fuel cell stacks are developed and tested at the Laboratoire d'Energétique Industrielle (LENI) in collaboration with HTceramix SA (Yverdon, Switzerland).

Simulation of the repeat element and stack is necessary to understand their behavior. Electrochemistry, fluid mechanics, mass and heat transfer phenomena are combined in such systems, where simulation can provide valuable insight. The novel stack proposed by HTceramix has motivated the direction of this work on design optimization: defining a stack is a complex task, a number of options are possible. These different options lead to different performance, that can be defined by several criteria.

The thesis presents several examples of the influence of design on the system performance and reliability. Different cases have been evaluated by steady state simulation, and transient as well as long term behavior have been investigated. To assist the choice among design options, optimization procedures were applied and the interest of such methods demonstrated.

The main contribution of this work is the development of an efficient model allowing simulation not only of a specific configuration but also application to other planar stack configurations. The model is presented together with the main results obtained. To take design decisions with confidence on the basis of simulation results, model validation is essential. Different approaches to validation are presented.

1.2 Context and motivation

Concern on energy efficiency is growing under the influence of environmental, institutional and economical driving forces: Emission and pollution reductions in large urban areas are motivated by health consequences, the Kyoto protocol is now applied and greenhouse gas emissions will have to be significantly reduced in the next years by signatory countries, the recurrent announcement of the future oil crisis has lately been confirmed by a strong increase in oil prices. The development of efficient energy conversion technologies is therefore to be promoted.
Among the possible technologies, fuel cells are particularly promising: high efficiency is expected especially for small systems and they are furthermore anticipated to be both benign in emissions and silent, making them good candidates for distributed power generation. Applications are in residential and building combined heat and power (CHP), auxiliary power units, portable power and even in small power plants (up to the MW size). Fuel cells define a system of energy conversion where electricity is directly generated from a fuel by electrochemical reactions. There are different types of fuel cells, listed by electrolyte type and, simultaneously increasing operating temperature:

- Polymer electrolyte membrane fuel cells operate (PEMFC) at low temperature (between ambient and 100°C). Strong development efforts are made for this technology in transport and residential applications. PEMFCs operate with hydrogen and are very sensitive to its quality and operation with carbon fuel like natural gas is a challenge for the system, particularly for the reformer. Water management in the membrane is another key issue.

- Direct methanol fuel cells (DMFC) use similar materials as the PEMFC but operate with liquid methanol is a fuel. Applications are in portable electronic devices.

- Alkaline fuel cells (AFC) operate at around 100°C , the main problem is that air and fuel feed must be CO_2 free.

- Phosphoric acid fuel cell (PAFC) operate at around 220°C and several systems of ca. 200 kW CHP in use.

- Molten carbonate fuel cell (MCFC) operate at around 650°C and operation with carbon fuel is not a problem. Reliability problems are encountered owing to the corrosive electrolyte.

- Solid oxide fuel cells (SOFC) operate between 650°C and 1000°C , the electrolyte being a solid dense oxide. SOFCs are relatively fuel flexible: operation is possible with hydrogen, carbon monoxide and carbon fuels with or without a prior reforming step.

The present work concerns solid oxide fuel cells. Compared to other technologies, they have the potential to reach a competitive cost as no expensive catalyst is necessary (high temperature), for CHP high grade heat is available. The principle is introduced in the following.

1.3 The solid oxide fuel cell

1.3.1 Operating principle

A fuel cell converts directly the energy of a fuel into electricity by electrochemical reactions. These reactions occur on both sides of an electrolyte, which is a gas tight selective ionic conductor. Figure 1.1 illustrates the solid oxide fuel cell principle: oxygen is reduced to oxygen ions (O^{2-}) at the cathode which provides electrons, the oxygen ion crosses the electrolyte to oxidize a fuel at the anode (e.g. hydrogen is converted into water) which resorbs the excess electrons. The oxygen partial pressure gradient between the two sides of the electrolyte creates the electric potential. The two half reactions on the cathode (equation 1.1) and the anode (equation 1.2) are:

$$0.5O_2 + 2e^- \leftrightarrow O^{2-} \tag{1.1}$$

$$H_2 + O^{2-} \leftrightarrow H_2O + 2e^- \tag{1.2}$$

The electrolyte is gas tight to avoid mixing of the reactants which would decrease the

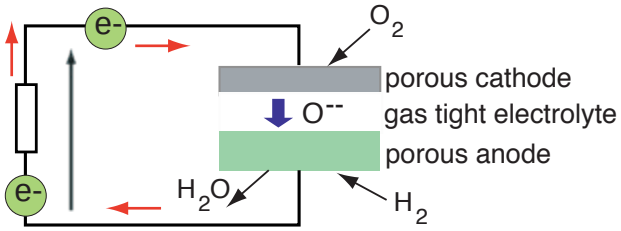

Figure 1.1: Principle of a SOFC cell

operating potential. Electrodes are porous to allow the diffusive transport of reactants from the channels to the reaction sites located at the electrode-electrolyte-gas interface. This interface is called the triple-phase boundary (TPB). Reaction rates are strongly dependent on the length of the triple phase boundary, the latter depending on the microstructure and the materials used for the electrodes. In the following, more details on the properties of each layer are given. Figure 1.2 presents a scanning electron microscope image of the 3 different layers.

1.3.1.1 Electrolyte

The SOFC electrolyte is a solid oxide material possessing ionic conductivity. The most common electrolyte is Yttria Stabilized Zirconia, the amount of yttrium doping ranging from 3% to 12% molar. The most commonly employed composition are 8 mol% Y_2O_3-92 mol% ZrO_2 (called 8YSZ hereinafter) for its high ionic conductivity or 3% mol YSZ (3YSZ) for its mechanical strength. The electrolyte thickness depends on the operating temperature: for a temperature above 850-900°C the electrolyte is generally between 80 and 120μm thick, in this case the electrodes are thin (ca. 30μm) and the electrolyte is the mechanical support for the cell (called electrolyte supported cells). At lower temperature, in the range of 700 to 850°C , the electrolyte thickness is decreased to 5 to 20μm for sufficient conduction. Ionic conductivity is a function of temperature and to avoid large ohmic loss in the electrolyte, the thickness is decreased. For such thin electrolytes, one of the electrodes is the mechanical support, in general the anode (called anode supported cells ASE). For still lower temperature, in the range between 550 to 600°C , alternative electrolytes based for example on ceria oxides are used for sufficient ionic conduction.

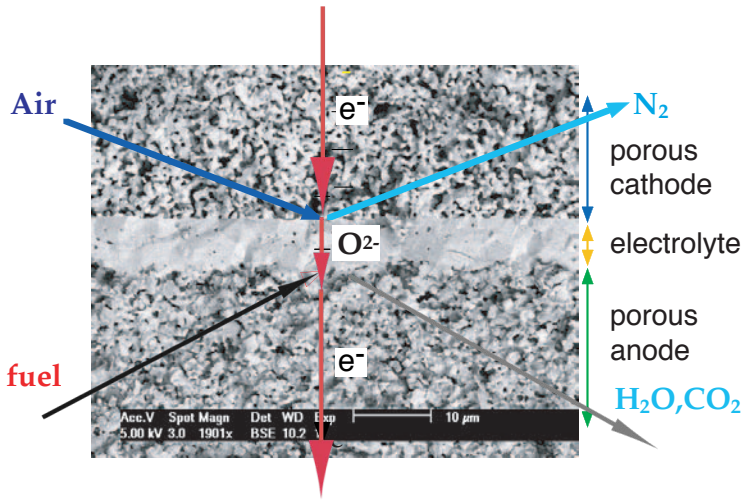

Figure 1.2: Scanning electron microscope image of the 3 layers of a cell

1.3.1.2 Anode

The fuel side electrode is generally made of a porous cermet (a fine mixture of ceramic and metal grains) of nickel and zirconia (YSZ) often designated as Ni/YSZ cermet. Nickel is chosen for its high catalytic activity, electronic conductivity and stability in reducing conditions. The ceramic YSZ has a structural role as it prevents the sintering of nickel. YSZ plays an electrochemical role as well: the triple phase boundary (TPB) length is extended

by the use of this composite material. The porosity ranges from 30% to 50% depending on the manufacturing process and composition. The anode thickness is in the range of 20 to 50μm for electrolyte supported cells. For anode supported cells, the thickness ranges from 200μm to 2mm depending on the manufacturer.

1.3.1.3 Cathode

The air side electrode is composed of a porous perovskite material. Perovskites are oxides with the property of relatively good electronic conduction at high temperature in oxidizing atmosphere. The most commonly used in SOFC are strontium doped lantanum manganite (LSM), strontium doped lantanum colbatite (LSC) and more recently strontium doped lantanum ferrite (LSF). The latter two are not only good electronic conductor but also good ionic conductors, with the effect of increasing the reaction zone at the cathode/electrolyte interface. The thickness is ca. 30μm and the porosity is on the order of 30-40%.

1.3.2 From cell to stack

The power output of a SOFC is generally in the range of 0.3 to 1W/cm^2 at a potential of 0.6 to 0.8V. To achieve useful power, the cell surface can be enlarged to increase the current or cells can be assembled in series to increase the operating potential. Two main configurations are developed: the tubular and the planar stack. The main advantage of the tubular configuration is easier sealing; however the manufacturing processes are not yet cost effective and performance is limited by the long current path. Planar configurations have the advantage of being compact, with a higher specific performance (per unit surface and per unit volume) than for the tubular approach; however, seals and reliability are key issues. The present work considers a planar design, described in detail in the following.

In a stack, cells are assembled in series and fed by reactants. An interconnect is placed between the 2 adjacent cells (figure 1.3), with the function of electrically connecting cells in series and of separating the gaseous reactants. The interconnects has to be gas tight and a good electronic conductor. They are usually shaped to ensure a space for the reactants to flow and to collect current from the cells. The interconnects are made of ceramics or refractory metals for high temperature SOFC, whereas alloys based on ferritic stainless steel can be used for intermediate temperature SOFC. The use of high iron containing metallic interconnects allows a reduction of the cost of the stack.

The assembly of one cell with interconnects is called a repeat element, and forms the base component for a stack.

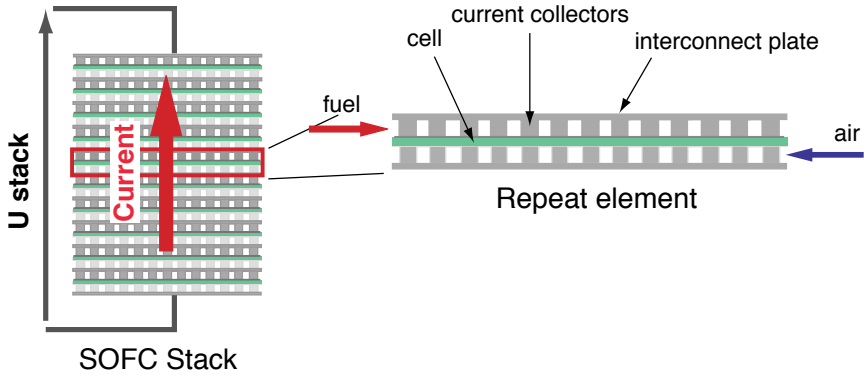

Figure 1.3: Principle of stacking: the repeat elements are assembled in series.

1.3.3 Status of SOFC technology

A number of research groups and companies are active in SOFC technology development. In intermediate temperature planar technology, stacks of several kW have been demonstrated (Steinberger-Wilckens et al. [2003], Steinberger-Wilckens et al. [2004] and Borglum et al. [2003]), operating either with hydrogen or directly with methane fuel (Steinberger-Wilckens et al. [2003]). While the electrochemical performance is still improving, the focus is now on reliability and long term degradation. Long term stack tests have been performed with stacks by several groups and degradation rates of 2 to 3% per 1000h operation have been achieved, the goal being to degrade less than 1% per 1000 hours. As larger stacks are now constructed, system integration is becoming an important field (Steinberger-Wilckens et al. [2004]).

For the planar high temperature stack, the situation is similar. Sulzer Hexis has realized a large pre-series system (Raak et al. [2002]) operated in realistic conditions (with load changes).

Cost reduction is a key issue: achieving a competitive price is necessary to enter the market and price level as low as 400 $/kW (for the system) are aimed for (Williams and Strakey [2003]). This cost is a driving force for the simplification of the manufacturing processes and for reduction of the system size (Raak et al. [2002]). Compactness of the system for auxiliary power units in mobile applications is essential.

With the tubular design, Siemens-Westinghouse has demonstrated long term operation over 7 years on 2 tubes (Williams [2001]). However, the demand for lower manufacturing costs could cause problems and new production processes can alter this excellent result. The size of such system is being reduced to increase the power density per unit volume (Stöver et al. [2001]) and achieve 388 kW/m^3.

1.3.4 Status at LENI laboratory

Fuel cell activities at LENI have begun late 2000 with a first stack realized with anode supported cells provided by HT-Ceramix SA (Molinelli [2001]). Since then a novel stack design has been developed, tested and demonstrated (Molinelli et al. [2003] and Molinelli et al. [2004]) in collaboration with HTceramix SA.
The main characteristic of this stack is to be assembled on flat interconnect metal sheets, with gas distribution and current collection ensured by a proprietary porous structure called SOFConnex$^{(TM)1}$. Gas manifolding for the stack is achieved by holes in the cells and in the interconnects. Appropriate seals are used to limit gas cross-over.
Figure 1.4 presents a scheme with the cell dimension, the gas inlets and the seals location. The general flow pattern is counter-flow, the gas outlet being on a side of the cell. The 3 other sides of the cells are sealed to limit reactant leakage which could cause hot-spots and may limit the achievable fuel utilization. At the fuel outlet, the remaining fuel is burnt with the air present in the environment.
This concept has been demonstrated in stacks up to 29 cells with a maximum power output achieved so far of 250W. The main advantage of the concept is compactness (power density of ca. $1kW/l$ has been achieved on short stacks) and its potentially low manufacturing cost. Long term operation has been tested with a repeat element for 5000 hours, the rate of degradation being in the order of 5% per 1000 h (Molinelli et al. [2004]).
LENI is active in system modeling and optimization and thus simple black-box models for fuel cells have been developed. However, the detailed modeling of the SOFC repeat element and stack has started in late 2000 with a first attempt (Molinelli [2001]) of a computational fluid dynamic (CFD) based model.

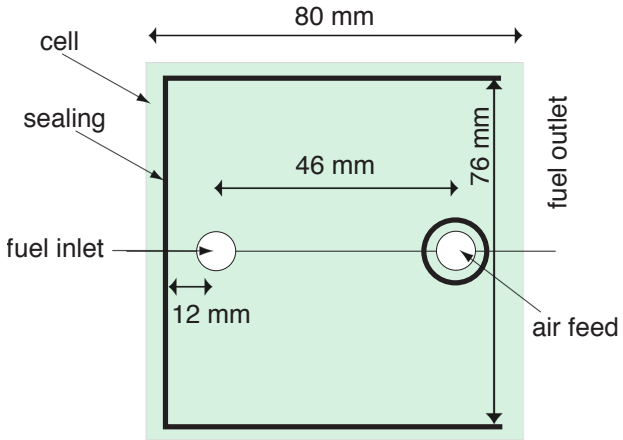

Figure 1.4: Scheme of the counter-flow repeat element configuration

[1]SOFConnex$^{(TM)}$is a registrated trade mark, property of HT Ceramix SA, which has provided cells and repeat element components for this research

1.4 Status on SOFC modeling

Modeling of fuel cells in general is an essential tool as fuel cell behavior is driven by several coupled phenomena: reactant flow, electrochemical reactions, electric and ionic conduction, heat transfer. Interest in SOFC modeling has increased significantly these last years and the range of published models goes from the basic phenomena at the interfaces between electrolyte and electrodes to stacks and systems models.
Detailed models describing the cell behavior intend to model the cell or electrode from basic parameters such as porosity of the microstructure and conductivity of the materials used (both electronic and ionic). Such models allow to perform sensitivity studies on the performance of the cell with respect to different compositions, thicknesses of the layers, porosity, etc. These models can be 1D (Chan et al. [2001]) or 2D (Costamagna et al. [1998]). Concern with diffusion limitation at the electrode increases and several studies are focusing on the diffusion modeling (Lehnert et al. [2000] and Ackmann et al. [2003]).
On the electrode level, another important field of modeling concerns the state-space approach of kinetic processes at the electrodes (Bieberle and Gaukler [2002], Bessler [2005]). A reaction path is assumed and modeled for the electrode, and model parameters are then identified from specific dynamic measurements (electrochemical impedance spectroscopy -EIS-) on well defined cells. This method allows to identify the rate determining steps in the reactions and therefore could be a support to electrode engineering.
With a change in scale from μm to cm , models becomes focused on the repeat element and stack. Since the early state model presented by Vayenas and Hegedus [1985], models have been presented for different configurations (planar and tubular) and with increasing complexity. The purpose of these models is to provide information and insight on the flow, concentration of species, temperatures and reaction rates on the cell surface to understand the interactions between these phenomena. Among the different published models, two main approaches are identified:

- Reducing the repeat element to a 2D (even to 1D when possible) problem by averaging the solid properties (for thermal conduction and electrical conduction) (Achenbach [1994], Costamagna [1997], Costamagna and Honegger [1998], Petruzzi et al. [2003], Roos et al. [2003] and Larrain et al. [2004]). Most of these models rely on the combination of parallel and series connexion to compute the conductivity properties (Karoliussen et al. [1998]), while others rely on more rigorous volume averaging methods (see Roos et al. [2003]). These models are used to perform a performance comparison between different configurations or even to perform transient behavior simulations of repeat element and stack.

- Developing full 3D models based on computational fluid dynamics. First, only a sin-

gle channel was modeled (Yakabe et al. [1999] and Yakabe et al. [2001]), then repeat elements and even stacks have been modeled (Khaleel et al. [2001], Recknagle et al. [2003], Gubner et al. [2003], Autissier et al. [2004]). These models allow a more accurate definition of the repeat element geometry. The results have been combined with internal stress computations (Yakabe et al. [1999]). However, the required CPU time for these models to perform a simulation is still important (from one hour to days of computing time for one operating point depending on the model complexity).

Most of these models have been developed for a specific configuration. For the planar stack, co-, counter- and cross-flow configurations are compared in several works (Achenbach [1994] and Recknagle et al. [2003]). In some cases, a few design parameters are changed and the consequences on the systems studied (for example Costamagna [1997] where the impact of an integrated heat-exchanger design on the temperature profile is considered).
Finally, system models focus on the balance of plant and on the evaluation of design options.

1.5 About this work

Driving forces in stack and system development are the increase of specific performance, reliability and lifetime. Compactness of the system, and therefore of the stack, receives increasing importance (see Raak et al. [2002] and Botti [2003]) for both stationary and mobile applications. The increased concern for degradation and reliability (see Tu and Stimming [2004]) leads to a limitation of the maximum temperature and gradient. Degradation phenomena are in general strongly activated by temperature (see Yang et al. [2003]), and ceramic cells are considered to be sensitive to gradients.
The previous work in SOFC stack modeling has in most of the cases focused on simulation of a given stack configuration. No systematic sensitivity study on the design decision variables was reported. This work will therefore provide a model capable of performing sensitivity analysis on the broadest possible range of decision variables. The model will have to be adaptable to not only one configuration (i.e. the configuration examined experimentally), but should allow to explore different configurations. As the number of decision variables is large, multi-objective optimization methods have been applied to define optimal configurations satisfying the different driving forces for the stack development.
Experimental validation of a model is often lacking in literature. From experiments performed in this work, validation and methods to define the electrochemical kinetics have been implemented. As the simulation of stack performances is not considered sufficient, validation with locally resolved measurements has been carried out.

1.5.1 Chapter Two: Models for a solid oxide fuel cell stacks

The model developed will be used to perform design optimization, a compromise between accuracy, complexity and simplicity has therefore to be found.
This chapter defines the main requirements for the developed model. This will have to provide detailed information on local fields (concentrations, reaction rates, temperature) as well as be efficient in computational time to be used in a optimization context. Two models, a benchmark CFD model and the 2D simplified model, are presented. The CFD model assumptions and equations for momentum, species conservation and energy are described. For the simplified model, the equation of motion and the molar balance equations, which introduce a 2D flow field description, are described with the detailed assumptions and simplifications decided.
An electrochemical reaction model will be given. It accounts for imperfect electrolyte behavior. As kinetic parameter identification is a recurrent problem, two different choices for the modeling of losses are presented.
Finally, a stack model is described together with its main assumptions.

1.5.2 Chapter Three: Modeling results

Simulation of the experimentally tested planar configuration has allowed to point out the problems and advantages of the design.
Simulation results for this counter-flow base configuration as well as for a co-flow alternative configuration are presented. Complete fields of concentration, current density and temperature are computed. Problems with the counter-flow configuration are identified by simulation and experiment will be discussed. The importance of the boundary conditions on the simulated temperature field is illustrated. Sensitivity studies on decision variables for the repeat element configuration are performed. Finally, the simulation of complete stacks and the sensitivity of temperature to the number of cells are shown.

1.5.3 Chapter Four: Electrochemical scheme choice and validation

Kinetic parameter identification is a necessary step to simulate a real system and compare the outputs with experimental results. This chapter presents the different set-ups and the experimental procedures for button cell and repeat element testing.
First the imperfect electrolyte behavior is discussed and elements of validation are presented. Then identification of kinetic parameters for a complete Butler-Volmer and a simplified scheme, from button cell and repeat element measurements, is presented.

The limits and problems identified in the procedures and the parameter validity are discussed.

1.5.4 Chapter Five: Model calibration by locally resolved measurements

Experiments with locally resolved current density and temperature measurements have been performed. The experiments are described and the main results outlined. The measurements have been used to validate the model and the results from this validation procedure are presented.
The model has proven its ability to simulate the behavior identified in the tests. However, some differences remain. Possible improvements for the model are discussed.

1.5.5 Chapter Six: Simplified model verification: comparison with a CFD model

The simplified model relies on strong assumptions for the simulation of the flow field and the strongly coupled species conservation equations. The verification of the chosen model is performed in this chapter.
Velocity, concentration, current density and temperature fields are compared with a CFD benchmark model for a given operating point. As the simplified model is used for sensitivity studies and optimization, the output of the two models have been compared for over hundred simulated points at different fuel and air flow rates, temperatures and repeat element areas. The range of use and suggestions for improvement of both the CFD and simplified models are given.

1.5.6 Chapter Seven: Transient behavior of SOFC stack

The simplified model allows to efficiently simulate transient behavior by the introduction of thermal inertia.
Transient simulation for load change is presented in detail for the base counter-flow configuration. Then the sensitivity of the transient response to the design choice is explored by the comparison of 3 different configurations for the base case counter-flow design. Simulation of the start-up of the stack has been performed, highlighting the problems caused by the substantial inertia and the possible strategies to decrease the start-up time.
Finally, conclusions on the influence of the design on transient behavior are drawn.

1.5.7 Chapter Eight: Simulation of the degradation behavior of stacks

This chapter presents results of simulations of repeat elements and stacks where a degradation behavior of the interconnect has been introduced in the model.
An overview on degradation phenomena is given. The well identified interconnect oxide layer formation is then modeled. Parameters for the degradation model are identified from measurements and literature.
Variations of operating parameters and design decision variables have been performed which allow to identify a clear trade-off between degradation and temperature.

1.5.8 Chapter Nine: Optimisation of the repeat element geometry

This chapter presents the optimization of the repeat element geometry. The conflicting objectives on the stack design require multi-objective optimization methods to provide valuable engineering outputs. The different methods for optimization are discussed. Results for the multi-objective optimization of the repeat element geometry are given for the two configurations.

Bibliography

E. Achenbach. Three-dimensional and time-dependent simulation of a planar solid oxide fuel cell stack. *J. of Power Sources*, 49:333–348, 1994.

T. Ackmann, L. G. J. de Haart, W. Lehnert, and D. Stolten. Modeling of mass and heat transport in planar substrate type SOFCs. *J. of the Electrochem. Soc.*, 6(150):A783–A789, 2003.

N. Autissier, D. Larrain, J. Van herle, and D. Favrat. CFD simulation tool for solid oxide fuel cells. *J. of Power Sources*, 1-2(131):313–319, may 2004 2004.

W. G. Bessler. A new computational approach for SOFC impedance from detailed electrochemical reaction diffusion models. *Solid State Ionics*, 176(11-12):997–1011, 2005.

A. Bieberle and L. Gaukler. State space modeling of the anodic SOFC system $H_2 - H_2O \| YSZ$. *Solid State Ionics*, (146):23–41, 2002.

B. Borglum, J.-J. Fan, and E. Neary. Following the critical path to ommercilizatin: an update on global thermoelectric's SOFC technology and product development. In S. C. Singhal and M. Dokiya, editors, *SOFC VIII, Proc. of the int. Symposium, Electrochemical Society*, pages 60–69, 2003.

J. J. Botti. The revolution through evolution: Delphi solid oxide fuel cell for APU and hydrogen reformation. In S. C. Singhal and M. Dokiya, editors, *SOFC VIII, Proc. of the int. Symposium, Electrochemical Society*, pages 16–30, 2003.

H. Chan, , K. Khor, and Z. Xia. A complete polarization model of a solid oxide fuel cell and its sensitivity to the change of cell component thickness. *J. of Power Sources*, 93:130–140, 2001.

P. Costamagna. The benefit of solid oxide fuel cells with integrated air pre-heater. *J. of Power Sources*, 69:1–9, 1997.

P. Costamagna, P. Costa, and V. Antonucci. Micro-modelling of solid oxide fuel cell electrodes. *Electrochemica Acta*, 43-3/4:375–394, 1998.

P. Costamagna and K. Honegger. Modeling of Solid oxide heat exchanger integrated stacks and simulation at high fuel utilization. *J. of the Electrochem. Soc.*, 145-11:3995–4007, 1998.

A. Gubner, D. Froning, B. de Haart, and D. Stolten. Complete modeling of kW-range SOFC stacks. *SOFC VIII, Proc. of the int. Symposium, Electrochemical Society*, pages 1436–1441, PV 2003-07 2003.

H. Karoliussen, K. Nisansioglu, and A. Solheim. Use of effective conductivities and unit cell-based supraelements in the numerical simulation of solid oxide fuel cell stacks. *Journal of applied electrochemistry*, (28):283–288, 1998.

M. Khaleel, K. Recknagle, J. Deibler, C. L.A., and J. Stevenson. Thermo-mechanical and electrochemistry modeling of planar SOFC stacks. In H. Yokokawa and S. Singhal, editors, *SOFC VII, Proc. of the int. Symposium, Electrochemical Society*, pages 1032–1041, 2001.

D. Larrain, J. Van herle, F. Maréchal, and D. Favrat. Generalized model of planar SOFC repeat element for design optimization. *J. of Power Sources*, 1-2(131):304–312, 2004.

W. Lehnert, J. Meusinger, and F. Thom. Modelling of gas transport phenomena in SOFC anodes. *J. of Power Sources*, (87):57–63, 2000.

M. Molinelli. Conception, modélisation et réalisation d'un empilement de cellules céramiques telles qu'utilisées dans le piles à combustibles SOFC. Master's thesis, Ecole Polytechnique Fédérale de Lausanne, 2001.

M. Molinelli, D. Larrain, N. Autissier, I. R., J. Sfeir, B. N., O. Bucheli, and J. Van herle. Compact 100W stacks using thin components of anode-supported cells and metal interconnects. In M. Mogensen, editor, *Proc. of the 6th European SOFC Forum*, pages 135–144, 2004.

M. Molinelli, D. Larrain, R. Ihringer, L. Constantin, N. Autissier, O. Bucheli, D. Favrat, and J. Van herle. Current collection and stacking of anode supported cells with metal interconnects to compact repeating units. *SOFC VIII, Proc. of the int. Symposium, Electrochemical Society*, PV 2003-07:203–212, 2003.

L. Petruzzi, S. Cocchi, and F. Fineschi. A global thermo-electrochemical model of SOFC systems design and engineering. *J. of Power Sources*, (118):96–107, 2003.

H. Raak, R. Diethelm, and S. Riggenbach. The Sulzer Hexis story: from demonstrator to commercial products. In M. Nurdin, editor, *Proc. of The Fuel Cell World*, pages 81–88, 1-5 July 2002.

K. Recknagle, R. Williford, L. Chick, D. Rector, and M. Khaleel. Three-dimensional thermo-fluid electrochemical modeling of planar sofc stacks. *J. of Power Sources*, (113):109–114, 2003.

M. Roos, E. Batawi, U. Harnisch, and T. Hocker. Efficient simulation of fuel cell stacks with the volume averaging method. *J. of Power Sources*, 118:86–95, 2003.

R. Steinberger-Wilckens, L. de Haart, I. Vinke, L. Blum, A. Cramer, J. Remmel, G. Blaß, F. Tietz, and W. Quaddakkers. Recent results of stack developement at Forschungzentrum Jülich. In S. C. Singhal and M. Dokiya, editors, *SOFC VIII, Proc. of the int. Symposium, Electrochemical Society*, pages 98–104, 2003.

R. Steinberger-Wilckens, I. Vinke, L. Blum, L. de Haart, J. Remmel, F. Tietz, and W. Quaddakkers. Progress in SOFC stack development at Forschungzentrum Jülich. In M. Mogensen, editor, *Proc. of the 6th European SOFC Forum*, pages 11–19, 2004.

D. Stöver, R. Henne, P. Otschik, and S. H. Recent developments o fSOFC technologies in Germany. In H. Yokokawa and S. Singhal, editors, *SOFC VII, Proc. of the int. Symposium, Electrochemical Society*, pages 38–49, 2001.

H. Tu and U. Stimming. Advances, aging mechanisms and lifetime in solid-oxide fuel cells. *J. of Power Sources*, 1-2(127):284–293, 2004.

C. Vayenas and L. Hegedus. *Ind. Eng. Chem. Fundam.*, (24):316–324, 1985.

M. C. Williams. Status and market applications for the solid oxide fuel cell in the US: a new direction. In H. Yokokawa and S. Singhal, editors, *SOFC VII, Proc. of the int. Symposium, Electrochemical Society*, pages 3–7, 2001.

M. C. Williams and J. P. Strakey. U.S. DOE office of fossil energy's solid oxide fuel cell program. In S. C. Singhal and M. Dokiya, editors, *SOFC VIII, Proc. of the int. Symposium, Electrochemical Society*, pages 3–8, 2003.

H. Yakabe, T. Ogiwara, M. Hishinuma, and I. Yasuda. 3-D model calculation for planar SOFC. *J. of Power Sources*, 102:144–154, 2001.

H. Yakabe, T. Ogiwara, I. Yasuda, and M. Hishinuma. Model calculation for planar SOFC focusing on internal stresses. *SOFC VI, Proc. of the int. Symposium, Electrochemical Society*, 99-19:1087–1098, 1999.

Z. Yang, K. S. Weil, D. M. Paxton, and J. W. Stevenson. Selection and evaluation of heat-resistant alloys for SOFC interconnect applications. *J. of the Electrochem. Soc.*, (150(9)): A1188–A1201, 2003.

Chapter 2

Models for a solid oxide fuel cell stack

2.1 Introduction

This chapter presents the different models developed in this study. The modeling work has been oriented to assist the design of repeat element and stack which require a compromise between computational efficiency and accurate outputs. Two modeling approaches have been used: a computational fluid dynamic 3D detailed model and 2D simplified model are presented.
The main focus is on the simplified model, which has been applied to several geometries and extended to complete stack simulation. The CFD model has been mainly used for benchmarking purposes.
In the following, the stack geometry that has been modeled is presented. Then the specifications for the models are presented. Finally, both models are presented in detail.

2.1.1 Repeat element geometry

The first repeat element considered is based on a planar anode supported cell with metallic interconnects and is designed to operate at around 800 °C . The general flow pattern is counter flow. One of the main characteristics of the configuration is internal manifolding: cells and interconnects have holes through which the reactants are fed; sealing is used to prevent gas mixing as shown on figure 2.1(a). The resulting design is compact; no additional pieces are necessary to realize a stack assembly. As a result from the manifolding configuration, the inlet of the gas is punctual, the outlet is on the opposite side of the feeding hole. The flow streamlines, which are clearly in 2D, are presented on figures 2.2(a) and 2.2(b) for the fuel and air flow. The unconverted fuel is burnt at the fuel outlet with the air

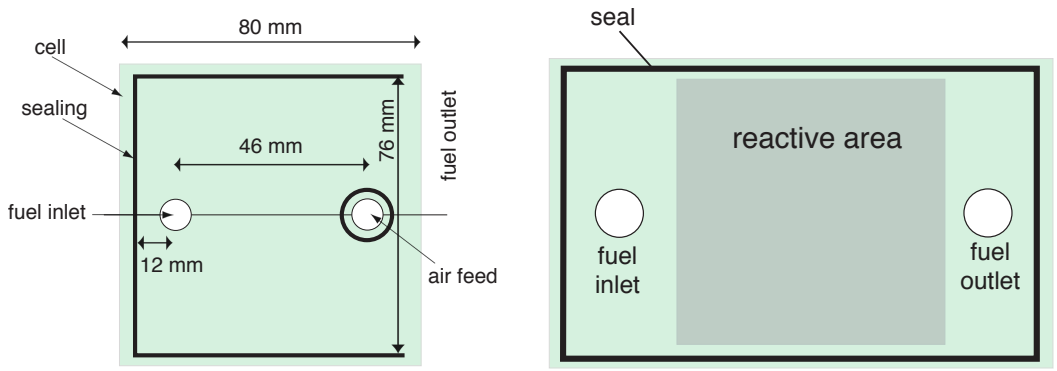

(a) Schematic of the counter-flow design (fuel side view)

(b) Schematic of the co-flow alternative design (fuel side view)

Figure 2.1: Repeat element configuration and dimensions

surrounding the stack. The cell dimension is of ca. 80 mm side; the cell active area, taking into account the area occupied by the sealing around the hole and on the border of the gas chamber is of ca. 51 cm^2 . The thicknesses for the different layers are reported in table 2.1. The main characteristic of this stack is the use of flat interconnect metal sheets, mounted

Table 2.1: Thickness of the different repeat element components

component	thickness	unit
anode	170-260	μm
electrolyte	5-15	μm
cathode	20-40	μm
interconnect	1	mm
anode gas channel	0.5	mm
cathode gas channel	0.9	mm

with a proprietary porous structure called SOFConnex$^{(TM)}$which ensures the current collection from the cell to the interconnect and the distribution of the reactants to the cell.
An alternative configuration, based on the same technology, has been proposed. The flow pattern is a coflow (figure 2.1(b)). The fuel is recovered at the outlet with a similar manifold as for the inlet and thus no post-combustion occurs at the edges of the stack.

2.1.2 Requirements for the models

The models developed are used to:

- provide the necessary insight and understanding on the behavior of novel stack geometries and therefore detailed outputs on the main fields such as fluid flow, concentration

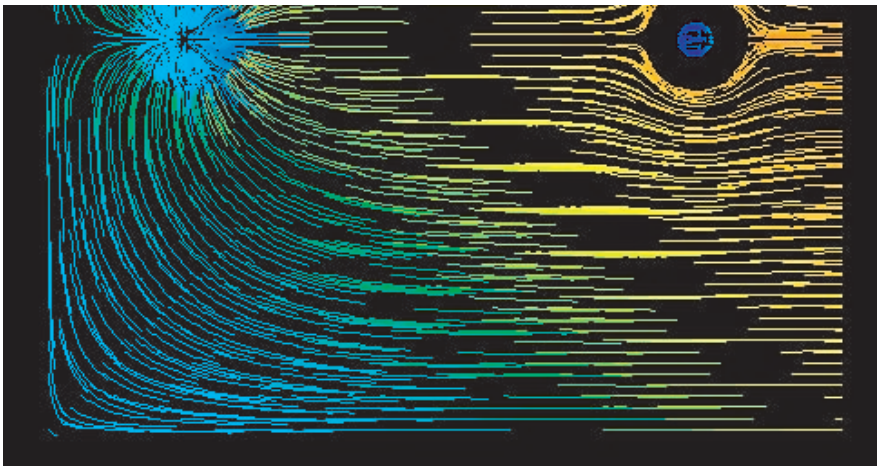

(a) Fuel flow stream lines

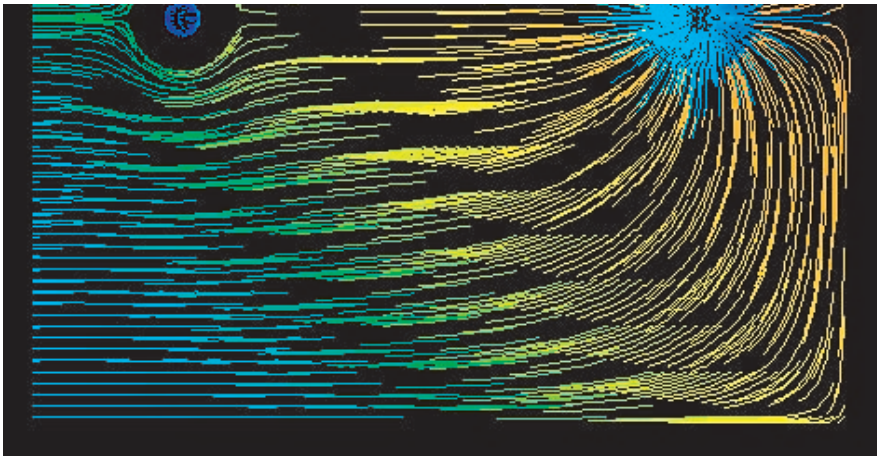

(b) Air flow stream lines

Figure 2.2: Flow stream lines for the counter-flow repeat element obtained with the CFD model

of reactants, reaction rates and temperature have to be provided.

- perform sensitivity analysis. This requires an efficient model to allow an extensive exploration of the different possible geometries and operating conditions.
- perform transient simulation on load changes and start-up phase.
- compare simulation outputs with experimental data. This usually requires the simulation of a large number of cases, uncertain parameters have to be estimated.
- perform design optimization with a multi-objective optimization algorithm.

From the different use of the models, it appears that computational efficiency is an important requirement. On the other hand, detailed outputs has to be provided. The choice of the

modeling level of detail has been based on the following criteria: for a simplified model, a 1D model is not sufficient as the geometry and the flow pattern presents a clear 2D characterisitic. A 1D model can be applied for co-flow and counter-flow configurations (see Aguiar et al. [2004]). However, the reduction to a 1D model has some limits even in the case of a unidirectional flow, as the 2D shape of the cell has an impact on the temperature field. Heat exchange occurs on the edges and therefore the width of the cell has its importance. The model must therefore be at least 2D.
In the following, the CFD model is first presented. Then, the simplified 2D model and the kinetic models for the electrochemical reactions are presented. Finally the adaptation of the 2D repeat element to the modeling of a stack is introduced.

2.2 CFD model for the repeat element

In recent years, modeling efforts towards complete 3D modeling of SOFC repeat elements or channels have significantly increased. The main motivation in this development is the geometrical definition that can be obtained with a CFD model, which can represent most of the details of the real geometry. A CFD model allows the modeling of a SOFC repeat element (on the fluid/energy part) from the defined geometry and the basic material and fluid properties.
Previous CFD based model studies have focused on the modeling of a repeat element or channel in order to perform thermal stress computation. Effect of the thickness of the electrodes has been included (Yakabe et al. [2000]). The case that is considered here addresses a geometry and a flow configuration more complex than the usual SOFC design where the fluid follows a quasi-unidimensional path. The present case has a clear 2D main flow pattern with a punctual inlet and distributed outlets. CFD is therefore required to provide an accurate flow description.
The assumptions on which the CFD model is based are summarized in the following. First, the electrical current path in the plane of the cell is not considered, and assumed to take place only on the direction normal to the cell plane. The cell is considered as an homogeneous solid, the thermal properties of which are computed from Kawashima and Hishinuma [1996]. As the Reynolds number of the flow are below 50, the flow is considered laminar and incompressible (Mach number is below 0.4)(Ryhming [1991]). The mixture of individual gases is represented by the ideal gas law. Therefore, the heat capacity and thermal conductivity are computed from weight-mixing laws (Todd and Young [2002]). Each of the individual gas properties is computed as a function of temperature (in our case, the system works at atmospheric pressure and pressure variation can be discarded from the thermal properties computation). The reactions are defined as volume reactions in the computational cell adjacent to the cell

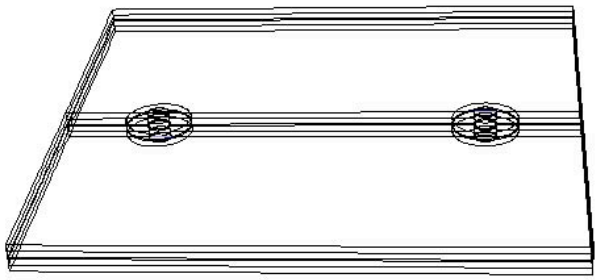

Figure 2.3: Geometry modeled in the CFD model

surface on both sides of the cell. The reaction rates for the anode and cathode are coupled. The model has been implemented in the CFD package Fluent by Fluent Inc., the mesh has been realized in Gambit and counts more than 100'000 computing cells. The fluid and energy equations are solved by the package, however the electrochemical reactions (and the associated mass and energy sources) have been implemented by user defined routines.
The momentum conservation equation is computed from the Navier-Stokes equation for a laminar flow. The medium between the cell and the interconnect is considered isotropic with 80% porosity. To account for this, source terms for the porous media are added to the momentum equation. Considering a steady-state case, equations can therefore be described as:

$$\rho(\vec{v}.\nabla)\vec{v} = -\nabla P + \nabla \cdot \overline{\overline{\tau}} + \vec{F} \tag{2.1}$$

where the left hand side term expresses the rate of change of the fluid momentum, ρ is the fluid density in kg/m^3 and $\vec{v}$ the velocity vector; on the right hand side P is the pressure, $\overline{\overline{\tau}}$ is the stress tensor and $\vec{F}$ accounts for additional source terms. As the flow is considered incompressible and a Newtonian fluid is assumed, the tensor $\overline{\overline{\tau}}$ is simply

$$\overline{\overline{\tau}} = \mu\nabla^2\vec{v} \tag{2.2}$$

where μ is the dynamic viscosity (in kg.s^{-1}.m^{-1}).
In the case presented here, the channel volume is represented by a porous medium and therefore $\vec{F}$ accounts for a Darcy source term. The porous medium is permeable in the principal directions and the permeability tensor is assumed diagonal:

$$\vec{F} = -\mu\overline{\overline{D}}\vec{v} \tag{2.3}$$

where $\overline{\overline{D}}$ is the permeability tensor (in m^{-2}). The permeability tensor is assumed to be diagonal and isotropic, the components are:

$$D_{11} = D_{22} = D_{33} = 1/K \tag{2.4}$$

where K is the permeability in m^2. The mass conservation equation accounts for the convective, diffusive transport and the reaction rates and gives for a specie i:

$$\nabla \cdot (\rho \vec{v} Y_i) = -\nabla \cdot \vec{J_i} + \dot{r} \tag{2.5}$$

where Y_i is the mass fraction of the mixture component i (in kg_i/kg), and $\dot{r}_i$ the volumetric reaction rate (in kg_i/m^3s). The term $\vec{J_i}$ (in $kg/m^2.s$) defines the diffusive transport following Fick's law:

$$\vec{J_i} = -\sum_{j=1}^{N-1} \rho D_{ij} \nabla Y_j \tag{2.6}$$

where D_{ij} is the binary diffusion matrix allowing the computation of multicomponent diffusion (in m^2/s). Stefan-Maxwell equations are used to define the diffusion coefficients.
The energy equation for the fluid part computes a composite energy equation where the solid part and fluid parts are considered, transport properties depend on the medium considered:

$$\nabla \cdot (\vec{v}(\rho_f E_j + P)) = \nabla \cdot \left[k_{eff} \nabla T - \left(\sum_i h_i J_i \right) + (\overline{\overline{\tau}} \cdot \vec{v}) \right] \tag{2.7}$$

where E_j is the total energy of the fluid (in J/kg) , $k_{eff} \nabla T$ the heat conduction term, $\sum_i h_i J_i$ the species source terms and $\overline{\overline{\tau}} \cdot \vec{v}$ the viscous dissipation. The effective conductivity for the porous structure is computed from the void fraction by a simple volume averaging of the conductivities.

2.3 The simplified 2D model

The 3D description of the fluid motion combined with the molar balance and energy balance equations has to be solved within a coarse mesh with the finite volume method. This method has the main drawback of requiring large computing time, furthermore for each new geometry definition, a new mesh must be realized and this operation is time consuming as well. To be used as a design tool, an efficient (i.e., fast and sufficiently accurate) model able to describe the repeat element main features is required. The model developed within this thesis is described in this section.

2.3.1 Fluid motion and molar balance equations

Several models using a simplified approach of volume averaging of the thermal transport properties have been developed. Some (Achenbach [1994], Petruzzi et al. [2003]) are focused on the typical cross/counter/co-flow geometry, which allows consideration of the fluid motion at constant velocity in one direction. Others consider the Sulzer-Hexis configuration where rotational symmetry is used (Costamagna and Honegger [1998], Roos et al. [2003]), ending in a simple 1D flow equation. These models were developed to represent configurations that did not require a 2D description of the fluid pattern although the models are in 2D. The case considered in this work has an obvious need for a 2D description as the inlet is punctual. The approach developed to describe efficiently the fluid pattern and the associated species and energy conservation equation is described here.

2.3.1.1 Molar balance equations

Conservation equations link the velocity field with the concentration fields and reaction rates. The local balance for the species i is expressed as:

$$\vec{\nabla} \cdot \vec{F_i} - D.\triangle \mathcal{C}_i = \dot{r}_i / L_{ch} \tag{2.8}$$

where $\vec{F_i}$ is the local molar flux vector (in $\mathrm{mol_i/cm^2.s}$) for the species i (with a component on x and a component on y), $\mathcal{C}_i$ is the molar concentration of i in $\mathrm{mol_i/cm^3}$, D the binary diffusion coefficient (in $\mathrm{cm^2/s}$), $\dot{r}_i$ the reaction rate of a given species i (in $\mathrm{mol/(cm^2.s^1)}$), and L_{ch} the height of the channel in cm. The molar flux vector can be expressed as

$$\vec{F_i} = \mathcal{C}_i \vec{v} = \mathcal{C} \chi_i \vec{v} \tag{2.9}$$

where $\mathcal{C}$ is the total molar concentration (in $\mathrm{mol/cm^3}$) and χ_i the molar fraction (in $\mathrm{mol_i/mol}$). From the local species balance for each of the components, the total conservation equation gives

$$\vec{\nabla}.\sum_i \vec{F_i} \;=\; \frac{1}{L_{ch}} \sum_i^{n_{species}} \dot{r}_i \tag{2.10}$$

The sum of the reaction rates gives the net molar balance of the reaction. In the case considered the reactions are 1) the electrochemical oxidation of hydrogen or carbon monoxide, 2) the steam reforming of methane, 3) the water gas shift reaction on the fuel side and 4) the reduction of oxygen into ions on the air side. On the fuel side, except for the steam

reforming, all reactions have a neutral molar balance. Therefore, if the steam reforming reaction is excluded from the reaction scheme, the total molar balance on the fuel side is simply:

$$\vec{\nabla}.\sum_i \vec{F_i} \;=\; 0 \tag{2.11}$$

This model may be applicable to the reforming case although it should be verified that the results are satisfactory. However, for a case with partly pre-reformed methane (50% pre-reformed) the total molar change is still be within a reasonable range. Extension to reforming is currently at an early-stage and is not presented in this thesis.
On the air side, the molar flow rate decreases with oxygen utilization, therefore, the equation 2.11 is not used on the air side. The air side model has no equation constraining the sum of the molar fraction to unity ($\sum_i^n \chi_i = 1$). On the fuel side, as the number of moles is assumed constant, this condition is fulfilled. On the air side, however, the oxygen is consumed: the $\mathcal{C}_i$ is a "pseudo" concentration and the sum of molar fractions is not equal to one. The error is nevertheless small: for a case at 70% fuel utilization, the oxygen utilization will be of 35% for an excess air of 2, leading to a decrease in the total molar flow rate of ca. 7% as the oxygen is diluted in nitrogen. In terms of molar flow rates, the equations 2.9 and 2.10 are consistent.
From equation 2.11 and equation 2.9 we obtain

$$\vec{\nabla}.(\sum_i \mathcal{C}\chi_i\vec{v}) = \vec{\nabla}.(\mathcal{C}\vec{v}) = 0 \tag{2.12}$$

The molar concentration $\mathcal{C}$, considering an ideal gas, is a function of pressure and temperature. Pressure drops are in the range of 10 mbar and therefore pressure dependence can be neglected. Temperature variations in the repeat element can reach 100 K, therefore the total molar concentration variation is not negligible. On hot spots the decrease in molar concentration leads to an increase in fluid velocity. The next section presents the equations used to compute the velocity field in the plane.

2.3.1.2 Fluid motion equations

The requirement for an efficient simulation has motivated the application of a number of simplifications from the complete Navier-Stokes equations reported in the section 2.2. The first simplification on the fluid description assumes that the velocities in the z direction are negligible. In fact, velocity in the height of the channel is expected to be very low as it could only be related to the transport of reactant and products between the reaction sites and the

channel. Reynolds (Re) numbers are generally low in fuel cells: for flow cases where Re $\ll 1$ the convective term in the momentum equation can be neglected (Ryhming [1991]). In our case the Reynolds numbers for the fuel flow is between 0.7 are the outlet and 0.2 at the inlet; for the air flow Re are between 6 and 25. The Re numbers are therefore in a range around 1 for the fuel and 10 to 30 for the air. The assumption of neglecting the convective terms could therefore be used for the fuel without inducing major errors. On the air side, the case is different but this assumption will be applied as well as an accurate flow pattern description is less critical on the air side (since the air is fed in excess to SOFCs stacks; moreover reaction rates -Nernst potential- are much more sensitive to fuel concentrations). With the presented assumption, for an isotropic porous medium, the Navier-Stokes equations simplify to:

$$0 = -\frac{\partial P}{\partial x} + \mu\Big\{\frac{\partial^2 v_x}{\partial x^2} + \frac{\partial^2 v_x}{\partial y^2} + \frac{\partial^2 v_x}{\partial z^2} - \frac{1}{K}v_x\Big\} \tag{2.13}$$

$$0 = -\frac{\partial P}{\partial y} + \mu\Big\{\frac{\partial^2 v_y}{\partial x^2} + \frac{\partial^2 v_y}{\partial y^2} + \frac{\partial^2 v_y}{\partial z^2} - \frac{1}{K}v_y\Big\} \tag{2.14}$$

In equation 2.13 and 2.14, second order derivative terms in the x and y direction can be neglected when compared to the z contribution. In the in-plane direction, strong velocity gradients exist at the inlet. Comparing these gradients to the gradients in the height of the channel, the former are around 5 orders of magnitude smaller. Thus out of plane velocity gradients are neglected. Table 2.2 gives the values for the gradients that are computed on a point of the fluid flow. The remaining terms are the viscous drag due the velocity profile in

Table 2.2: Values for the different components of equations 2.13 and 2.14

$\frac{\partial^2 v_x}{\partial x^2}$	$\frac{\partial^2 v_x}{\partial y^2}$	$\frac{\partial^2 v_y}{\partial x^2}$	$\frac{\partial^2 v_y}{\partial y^2}$
-1.6.10^3	2.4.10^3	2.8.10^3	-3.7.10^3
$\frac{\partial^2 v_x}{\partial z^2}$	$\frac{\partial^2 v_y}{\partial z^2}$	$\frac{v_x}{K}$	$\frac{v_y}{K}$
2.5.10^8	10^8	2.5.10^8	2.5.10^8

the height of the channel and the Darcy source term describing the momentum sink in the porous media. As these term have similar orders of magnitude, these two terms cannot be neglected and the momentum equation describing the fluid motion reduced to:

$$0 = -\frac{\partial P}{\partial x} + \mu\Big\{\frac{\partial^2 v_x}{\partial z^2} - \frac{1}{K}v_x\Big\} \tag{2.15}$$

$$0 = -\frac{\partial P}{\partial y} + \mu\Big\{\frac{\partial^2 v_y}{\partial z^2} - \frac{1}{K}v_y\Big\} \tag{2.16}$$

The flow motion equation can therefore be expressed as the superposition of 2 flows. Let us consider here the component in x :

$$\{\frac{\partial P}{\partial x}\}^{visco} = \mu\frac{\partial^2 v_x}{\partial z^2} \tag{2.17}$$

$$\{\frac{\partial P}{\partial x}\}^{porous} = -\mu\frac{v_x}{K} \tag{2.18}$$

$$\frac{\partial P}{\partial x} = \{\frac{\partial P}{\partial x}\}^{visco} + \{\frac{\partial P}{\partial x}\}^{porous} \tag{2.19}$$

The equation 2.17 is similar to a Poiseuille flow in the x direction. Applying a no-slip boundary condition ($v_x = 0$) at the walls, the velocity profile is defined (Ryhming [1991] and Munson et al. [1998]). Hence, a simple expression linking the pressure gradient to the mean velocity is derived:

$$\bar{v_x} = -\frac{L_{ch}^2}{3 \cdot 4\mu}\{\frac{\partial P}{\partial x}\}^{visco} \tag{2.20}$$

where L_{ch} is the height of the channel. The previous expression (2.20) can then be transformed to express the local pressure gradient as a function of the average velocity. Combining 2.19 with 2.20 and 2.18 we finally obtain the following expression for the pressure gradient in x as a function of the viscous drag and porous medium resistance:

$$-\frac{\partial P}{\partial x} = \bar{v_x}\mu\left[\frac{12}{L_{ch}^2} + \frac{1}{K}\right] \tag{2.21}$$

A similar expression can be found for the local mean velocity in y . Finally the mean velocity in the height of the profile can be expressed as a Darcy equation where the permeability term is modified to account for the porous media and the viscous drag.

$$\frac{1}{K_{eff}} = \frac{12}{L_{ch}^2} + \frac{1}{K} \tag{2.22}$$

$$-\nabla P = \frac{\mu}{K_{eff}}\vec{v} \tag{2.23}$$

The momentum equations are finally reduced to a simple expression linking the pressure field with the velocity. The viscosity of the mixture is not computed locally but kept constant over the domain.

From the species conservation equation we have the total conservation equation 2.12, by neglecting the variations of the molar concentration we can obtain the simple expression for the conservation:

$$\vec{\nabla}.\vec{v} = 0 \tag{2.24}$$

Combining equation 2.24 with 2.21, a simple Laplace equation is obtained which allows a straight forward computation of the pressure field.

$$\vec{\nabla}^2.P = 0 \tag{2.25}$$

This equation can be solved by applying appropriate boundary conditions:

- at punctual inlet or outlet, the pressure is set to a singular value P_{inlet} or P_{outlet} (figure 2.4)
- on the wall, the velocity is assumed to be zero in the direction normal to the wall and therefore

$$\frac{\partial P}{\partial n} = 0 \tag{2.26}$$

  where n is the direction normal to the wall
- for distributed outlets (like for the base case geometry) or inlet, the pressure is set to a reference value P_{outlet} or P_{inlet} (figure 2.4).

For the punctual inlet or outlet, the velocity field shows a mathematical singularity which leads velocity components to infinity (Ryhming [1991]) at the given point. To avoid problems

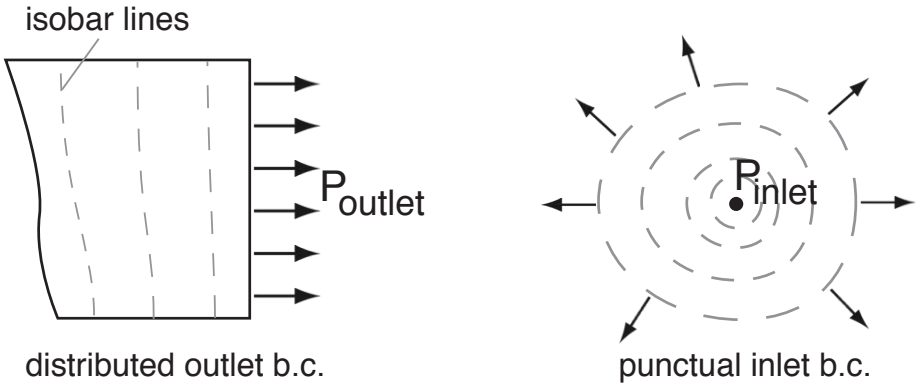

Figure 2.4: Boundary condition for the flow field, illustrated here for a distributed outlet and a punctual outlet. Also valid for distributed inlets and outlets.

with the solver the velocity components are therefore set to zero at the inlet or outlet point. The simplified model relies on a simplified description for the equation of motion where the velocity field is decoupled from the molar and energy balance equations by neglecting the variations of the molar concentration.
This decoupling allows an efficient simulation of the flow field, the counter-part result is that the velocity field obtained, although it describes the main characteristics of the flow path

has an accuracy in the range of 15%. The consistency of the species balance is nevertheless not affected.

2.3.2 Energy equations

Energy equations are solved for the solid and the two fluids separately but these equations are however strongly coupled through the heat transfer from solid to fluids. For the gas streams, the energy conservation equation is based on a local energy balance for the fluid, in which the source terms include the species exchange with the solid and the convective heat transfer with the solid. The reactions are assumed to take place in the solid. The solid energy equation is based on the 2D thermal conduction equation with heat source, the sources being the chemical reactions, the heat transfer with the fluids, and the heat transfer with the surrounding environment. Similarly to the model developed by Achenbach [1994], Costamagna and Honegger [1998], Costamagna [1997], Roos et al. [2003], the thermal transport properties are averaged over a unit volume. The method used for the volume averaging is based on series and parallel thermal conduction (Karoliussen et al. [1998] and Incropera and De Witt [1990]). The thermal conductivity of the anode supported cells is computed from the model by Kawashima and Hishinuma [1996]. Although the conductivity of the anode supported cells is relatively high (with value around 10W/(mK) , determined experimentally in agreement with Kawashima and Hishinuma [1996]) the in-plane thermal conductivity is dominated by the metallic interconnect (which conductivity is around 25 W/(mK)).
The energy conservation for the fluid can be detailed as:

$$\nabla \cdot (\vec{v}(\sum_{i}^{n} \mathcal{C}_i H_i) = \left[h_{conv}(T_{solid} - T_{gas}) + \sum_{i}^{n} \dot{r}_i H_i \right] / L_{ch} \tag{2.27}$$

where H_i is the total enthalpy of the species i (in J/mol$_\mathrm{i}$), h_{conv} is the heat transfer coefficient (in W/m^2.K), T_{solid} and T_{gas} are the solid and gas temperatures and L_{ch} the channel height (in m). The heat transfer coefficient is assumed a fully developed laminar flow between 2 plates, with a Nusselt number of ca. 8 (Incropera and De Witt [1990]).
The solid energy equation is:

$$\lambda_{s_{x,y}}(\frac{\partial^2 T_{solid}}{\partial x^2} + \frac{\partial^2 T_{solid}}{\partial y^2}) + \dot{Q} = 0 \tag{2.28}$$

where $\lambda_{s_{x,y}}$ is the average thermal conductivity (in W/(mK)), $\dot{Q}$ is the sum of the volumic sources in W/m^3 detailed as:

$$\dot{Q} = \left[h_{conv}^{air}(T_{air} - T_{solid}) + h_{conv}^{fuel}(T_{fuel} - T_{solid}) + \sum_{j}^{n_{fluid}} \sum_{i}^{n} \dot{r}_i H_i - \dot{E}_{elec} - \dot{Q}_{loss} \right] / L_s \quad (2.29)$$

where the different terms account for the heat transfer with the gases, the enthalpy of reactants and products and the useful electric power $\dot{E}_{elec}$ produced locally, with $\dot{Q}_{loss}$ the losses to the surrounding environment and L_s the total thickness of a repeat element.
The enthalpy of the mixture is evaluated by a molar mixing law, and the enthalpy of each component is computed from the enthalpy at a reference temperature and the heat capacity at this reference temperature. The heat transfer coefficient is computed from the Nusselt number for a forced convection between 2 parallel plates. The entry region is not considered and the Nusselt number is constant over the surface. The variations of the fluid heat conductivity with the mixture composition are not accounted in the heat transfer coefficient computation. This simplifying assumption has been verified to have little influence on the results as the heat transfer coefficient is high (owing to the small characteristic length).

2.3.3 Thermal boundary conditions

Considering a repeat element, different boundary conditions can be defined. Usually, studies consider the repeat element as being part of a stack. Heat losses (generally radiative exchange with the surrounding environment) are therefore accounted for on the edges of the repeat element and no losses are assumed in the z direction (stacking direction). Such a boundary condition is applied in previous works from Achenbach [1994], Costamagna and Honegger [1998] and Petruzzi et al. [2003]. This assumes that the repeat element considered is in a stack sufficiently high so that surrounding elements have the same temperature profile.
However, experiments performed in our laboratory concern in most cases either a single repeat element (assembled as a stack) or short stacks with 3 to 10 cells. In this case, the height of the stack is too small to assume adiabatic conditions in the z direction. Therefore the energy equation includes a heat loss term which can be activated when short stack or single repeat element cases are considered. Figure 2.5 shows the boundary conditions of a repeat element tested in a set-up. The radiative heat transfer with the surroundings is intense though the test flanges may limit it.
To simulate these experimental boundary conditions, the heat loss term of the solid energy equation is defined as

$$\dot{Q}_{loss} = 2\epsilon_{REz}\sigma({T_{solid}}^4 - {T_{env}}^4) \quad (2.30)$$

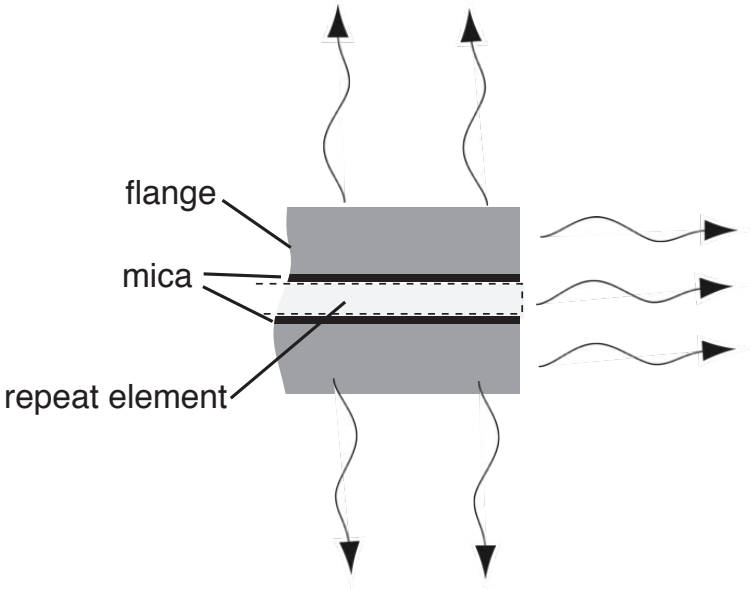

Figure 2.5: Boundary conditions for a repeat element in a set-up

where ϵ_{REz} is the emissivity assumed for the flange, T_{env} is the temperature of the test environment and σ the Stefan-Boltzman constant for radiation (in W.m^{-4}.K^{-1}). The heat exchange is assumed to take place on the bottom and top wall of the repeat element. The value of the emissivity is set to a lower value than these on the edges of the repeat element as the flanges moderate the effect. This parameter value is quite uncertain.
Nevertheless, with the definition of thermal boundary condition for a repeat element, the problem of simulating short stacks is not solved: a repeat element in the middle of a 10 cell stack is in an intermediate situation between the stack and repeat element conditions. A stack model has therefore been defined to address this specific problem. This model will be presented in a latter section (2.5). The next section will present the kinetic models developed and used in the repeat element model.

2.3.4 Implementation of the simplified 2D model

The model described in the previous section has been implemented in the gPROMS (Oh and Pantelides [1996]) software from Process System Enterprise Ltd. This tool is based on an equation solver and it allows the computation of distributed domains that were in this work generally in 2D. The partial derivative equations on the domain are discretized using a centered finite difference scheme (of 4^{th} order).
gPROMS includes a parameter estimation algorithm to identify parameters from experimental data and optimization algorithms allowing solution of the Non-Linear Programming (NLP) optimization problem. Both algorithms use sequential quadratic programming (SQP)

techniques.
The thermodynamic properties are provided by a database linked with the software.

2.4 Kinetic model

Fuel cells are by definition reactive systems. Reaction rate modeling and its validity is therefore essential to the model output quality. The reactions considered here are on one hand the electrochemical reactions with the oxidation of hydrogen and on the other hand the reactions related to the reforming of methane, ie. the methane steam-reforming and shift reaction. In the first part, the electrochemical reactions are described.

2.4.1 Electrochemical model

2.4.1.1 Reaction scheme

Modeling of electrochemical reactions aims to define the cell potential and the current associated with this potential depending on the operating conditions, i.e., temperature and concentrations. The reversible cell voltage U_{Nernst} is defined for an electrochemical cell as the potential that can be measured on the cell when it is discharged through an infinite resistance (Bard and Faulkner [1980]). This potential is computed from the Gibbs free enthalpy (ΔG in J/mol) of the reaction:

$$U_{Nernst} = \frac{-\Delta G}{n_e F} \tag{2.31}$$

where n_e is the charge number involved in the reaction and F the Faraday constant (in C/s). From basic thermodynamics this potential can be expressed as a function of reactants activities or partial pressure. For the electrochemical oxidation of hydrogen the two half reactions are:

$$0.5O_2 + 2e^- \leftrightarrow O^{2-} \tag{2.32}$$

$$H_2 + O^{2-} \leftrightarrow H_2O + 2e^- \tag{2.33}$$

giving the complete reaction

$$H_2 + 0.5O_2 \leftrightarrow H_2O \tag{2.34}$$

The reversible potential can be computed from the Nernst equation as:

$$U_{Nernst} = \frac{-\Delta G_o}{2F} + \frac{RT}{2F} \ln(\frac{(p_{o2})^{1/2} p_{H2}}{p_{H2O}}) \tag{2.35}$$

where ΔG_o is the standard Gibbs free enthalpy, R the gas constant (in J/mol.K) and p_{O2}, p_{H2}, p_{H2O} the respective partial pressure for oxygen, hydrogen and water (in atm). When the cell is discharged through a finite resistance, a current is observed in the circuit and the cell potential decreases due to irreversible processes. These losses have several sources:

- ohmic losses in the electron path, this includes losses due to the ionic resistance in the electrolyte, ohmic losses in the electrodes and ohmic losses due to current collection
- activation losses at the electrolyte-electrode interfaces, these losses are due to the charge transfer kinetics
- diffusion over-potential induced by the diffusion of species in the electrodes

The equation describing the losses will be detailed further on. The equation that defines the effective cell potential U_{cell} from the reversible cell potential and the local current density is simply:

$$U_{cell} = U_{Nernst} - \eta_C(j_{ion}) - \eta_A(j_{ion}) - j_{ion}.R_{ionic} - j.R_{ohm} \tag{2.36}$$

where j is the local value of the current density (in A/cm^2), η_C and η_A the total polarization overpotential at the cathode and anode (in V), R_{ionic} the ionic resistance of the electrolyte and R_{ohm} the sum of the ohmic losses including the current collection and interconnect interface (in Ω.cm^2).
Open circuit voltage (OCV) observed experimentally is usually significantly lower than expected: it ranges between 0.95 to 1.05V under hydrogen (97% mole fraction hydrogen and 3% water) and 750°C compared to the theoretical value of more than 1.1V. This large deviation could be explained by leakages from seals and diffusion of species from post-combustion area (in either repeat elements test or button cell tests, both carried out in a seal-less set-up). Although these phenomena contribute to lower the OCV, an imperfect behavior of the electrolyte could also contribute to explain this deviation. Other work performed on anode supported cells reports OCVs lower than theoretical values on button cell tests carried out in well-sealed experiments (Simner et al. [2003] and Ralph et al. [2003] with values in the range of 1.07 to 1.1V for 700°C - theoretical value 1.12 V -).
The thin film (5 to 12μm thick) electrolyte is co-sintered with the anode support. This sintering process takes place at a temperature around 1400°C and diffusion of nickel oxide from the anode to the electrolyte occurs. Linderoth et al. [2001] and Van herle and Vasquez

[2004] showed that a small amount of NiO in the electrolyte lowers its conductivity by about 50% when the electrolyte is in a reducing atmosphere. This lowering of conductivity is ir-

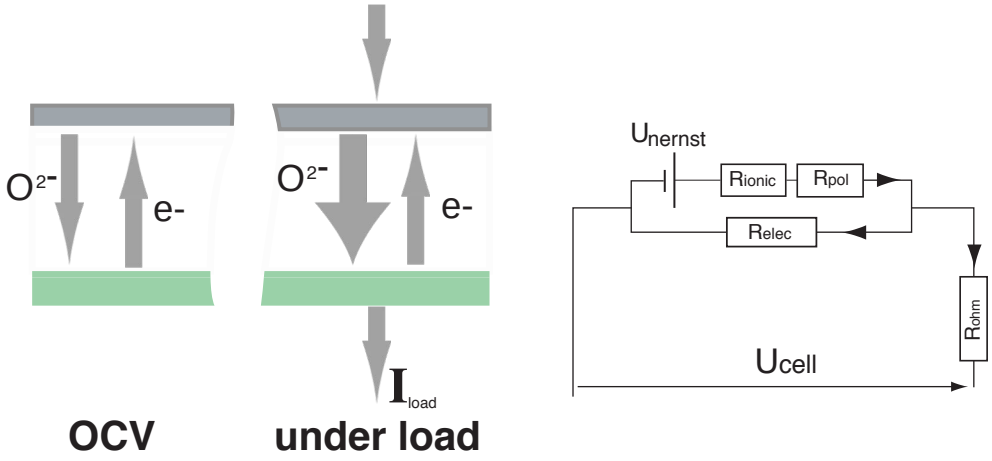

(a) Schematic of the behavior of an imperfect electrolyte at OCV and under load

(b) Equivalent circuit for the cell including the electronic losses at the electrolyte

Figure 2.6: Imperfect electrolyte and short circuit current

reversible. Other works report that a small amount of doping by titanium or manganese (a few %) affects significantly the conduction properties of the electrolyte (see Kobayachi et al. [1997], Kobayachi et al. [2000], Kawada et al. [1992]). Electronic conductivity of 8YSZ depends on the oxygen partial pressure. In reducing conditions the conductivity is dominated by electron mobility (in the range of p_{O_2} between 10^{-12} to 10^{-20}). In the high range of oxygen partial pressures the conductivity is explained by hole mobility (Park and Blumenthal [1989]). According to Kawada et al. [1992], Mn-doped-YSZ shows a similar electronic conductivity to pure 8YSZ at low p_{O_2} whereas the conductivity at high p_{O_2} is increased by one order of magnitude. Studies on the electronic conductivity of Ni doped 8YSZ have not been done, however, the effect on the ionic conductivity is important (Linderoth et al. [2001] and Van herle and Vasquez [2004]) and a significant effect due to the Ni doping on the electronic conductivity seems possible.

The electrochemical model has therefore been modified to account for the electronic conductivity of the electrolyte (Virkar [1991]). The OCV of the cell is thus dependent on the Nernst potential, the electronic and ionic resistance of the electrolyte and the polarization losses which are created by the small short circuiting current (figure 2.6(a)). The current scheme (see figure 2.6(b)) has been modified from the one published in Larrain et al. [2004]. Although the cell is at OCV, charge transfer at the electrodes occurs and therefore polarization losses apply (Matsui et al. [2004]). At OCV the equation describing the system is:

$$U_{cell} = U_{Nernst} - R_{ionic}.j_{ion} - \eta_C(j_{ion}) - \eta_A(j_{ion}) - j.R_{ohm} \tag{2.37}$$

where j_{loss} is the local short-circuit current density, j_{ion} is the local ionic current density and j the current density in the external circuit. The equations describing the relations between the different currents are

$$j_{ion} = j_{loss} + j \tag{2.38}$$

$$j_{loss} = \frac{U_{cell}+j.R_{ohm}}{R_{elec}} \tag{2.39}$$

where R_{elec} the electronic conductivity for the electrolyte.
At OCV the system is simplified as the current in the external circuit is zero, therefore:

$$j_{ion} = j_{loss} \tag{2.40}$$

The consequences of this short-circuit current are extremely important for the behavior of the repeat element and the fuel cell: at OCV the species consumption is not zero and part of the fuel is consumed without any useful energy conversion. Under polarization, the contribution of the short-circuit current tends to decrease (equation 2.39) but is still significant. This short-circuit limits the fuel cell's efficiency by decreasing the operating potential and limiting the achievable fuel utilization. The range of values estimated for the short circuit current depend on the experimental OCV and on the polarization losses on the cell. The order of magnitude is in the range of 0.02 to 0.10A/cm^2 at OCV (see section 4.4). The following section presents the detailed expressions for the different losses.

2.4.1.2 Expressions for the losses

Electrolyte contribution to the total losses can be defined from previous studies. Ionic conductivity of the 8YSZ electrolyte is well characterized by Park and Blumenthal [1989]. Yet the contribution of the electrolyte to the total resistance cannot be computed using the standard relation for anode supported electrolyte cells (Ihringer et al. [2001] and Zhao and Virkar [2004]). This contribution can only be applied when the dominating resistance is the bulk resistance. For electrolyte thickness in the range of 4 to 20μm , the electrode/electrolyte interfaces are expected to play a significant role in the resistance. The ohmic contribution of the electrolyte can be defined, at a constant temperature, by a linear dependence with the electrolyte thickness with non-zero intercept at zero thickness. This dependence has been reported by Ihringer et al. [2001] and Zhao and Virkar [2004]. The explanation for this non-zero electrolyte resistance at zero thickness is attributed to other sources than the electrolyte, according to Zhao and Virkar [2004], other possible reasons are current constrictions (Fleig and Maier [1997]) and impurities. Nevertheless, the dependence with the thickness is in agreement with electrolyte ionic conductivity.

The activation energy for the constant term could be estimated from the value at 700 and

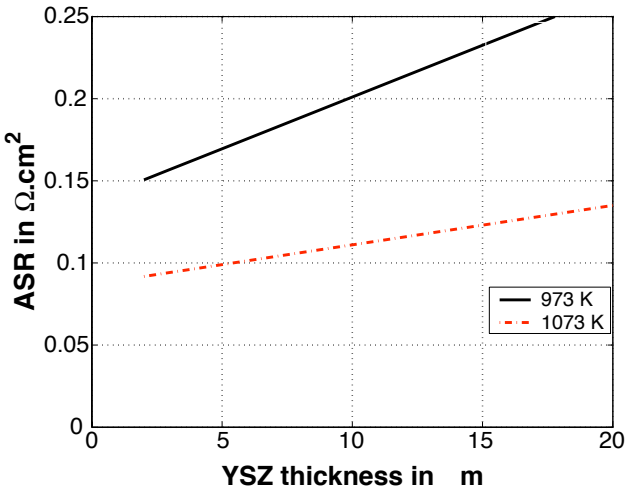

Figure 2.7: Dependence of the ohmic resistance as a function of the electrolyte thickness (Zhao and Virkar [2004])

800°C , an estimate giving ca. 48.7 kJ/mol. This estimate has to be taken with caution as it is based on a limited amount of data (figure 2.7).
From the previous statements, the electrolyte area specific resistance (ASR) contribution can then be simply expressed as

$$R_{ionic} = \rho_e^i . l_e + R_{cst}^e \tag{2.41}$$

where R_{ionic} is the ASR contribution from the electrolyte ionic conductivity, ρ_e^i is the electrolyte ionic resistivity (in Ω.cm), l_e the electrolyte thickness and R_{cst}^e the residual resistance. The dependence of the ionic conductivity with temperature can be expressed as (Park and Blumenthal [1989])

$$\sigma_{ion} = \sigma_{ion} . \exp(\frac{-E_a^{ion}}{kT}) \tag{2.42}$$

where the values for the constants σ_{ion} and E_a^{ion} are respectively 1.6310^2 in S/cm and 0.79 eV (76.2 kJ/mol). The resistivity is simply the inverse

$$\rho_e^i = 1/\sigma_{ion} \tag{2.43}$$

Polarization losses have been considered in the model for the anode and the cathode side. The expression uses a Butler-Volmer formulation. For each electrode, the local exchange current density is computed from the temperature (equation 2.44) and the overpotential is computed from the Butler-Volmer equation simplified by considering a transfer coefficient of 0.5 (Chan et al. [2001]). With this assumption the overpotential can be expressed as a function of the local current j and the local exchange current density j_{oe} (in A/cm^2) as

reported in equation 2.45.

$$j_{oe} = \frac{RT}{2F} k_{jo_e} \exp(\frac{-{E_a}^{j_o}}{RT}) \quad (2.44)$$

$$\eta_e = \frac{RT}{F} \text{asinh}(\frac{j}{2.j_{oe}}) \quad (2.45)$$

The main parameters determining the polarization losses are the activation energy ${E_a}^{j_o}$ and the rate constant k_{jo_e} (in $\Omega^{-1}.\text{m}^{-2}$). Values for these parameters are difficult to obtain from literature. Experimental work carried out on symmetrical cells allows the identification of parameters and reaction paths for one of the electrodes (as for example in Holtappels et al. [1999] and Divisek et al. [1994]). The information provided, however, is difficult to extend to materials used in our specific case as the microstructure and primary materials (powders) have a strong impact on the resulting losses and cell performance as reported by Brown et al. [2000] and Hansen et al. [2004]. Some complete modeling studies on the whole cell (Chan et al. [2001]) or one of the electrodes are found as well (Costamagna et al. [1998] and Xia et al. [2004], Chan et al. [2004]). Possible values for activation losses on anode supported cells can be found in Aguiar et al. [2004] and Van herle et al. [2003]. Values for the activation energy are of the same order of magnitude for both cases. The value for these parameters remains quite uncertain and efforts to determine the polarization losses of each electrode on a symmetrical cell would be valuable for modeling studies.

Diffusion limitation is considered in most of the modeling studies as well. Studies focusing on the diffusion in the cell and the interaction with current collector ribs are given by several authors (Ackmann et al. [2003], Jiang and Virkar [2003] and Lehnert et al. [2000]). It appears that the results from the diffusion models are extremely sensitive to parameters describing the microstructure of the electrode such as the mean pore size, porosity and tortuosity of the electrodes. Their effective reliability is therefore questionable (Ackmann et al. [2003]). Within this study, as the cells tested in our facilities, either as button cells or stacks, have not shown diffusion limitation, even for high current densities (up to 2 A/cm^2), this aspect is not accounted for. Subsequent work on that topic is currently on-going.

The next contribution that has to be computed is the ohmic resistance for interconnects and current collection. The main contribution to the resistance is the contact between the current collector and the interconnect where an oxide layer is formed under operating conditions. This is particularly significant on the cathode side, but studies report a non-negligible degradation also on the anode side (Piron Abellan et al. [2002]). The ohmic contribution of this oxide layer is evaluated from measurements which will be presented in chapter 8. The contribution of this oxide scale is computed with the following expression:

$$\sigma_{mic} = {\sigma_{mic}}^o / T \exp(\frac{{E_a}^{mic}}{RT}) \quad (2.46)$$

where σ_o is the constant, T the temperature, Ea the activation energy. The thickness of the oxide scale is assumed to be of 4 μm and constant in time for all the steady-state and transient simulations. Simulation accounting for the growth of this layer are found in chapter 8.
The effective resistance is finally computed from the oxide layer thickness ξ and the surface coverage A_{cc} of the current collectors on the interconnects:

$$R_{ohm}{}^{MIC} = \frac{\xi}{\sigma_{mic}.A_{cc}} \tag{2.47}$$

2.4.1.3 Simplified scheme

The reaction scheme presented in section 2.4.1.1 requires the computation of local values for the following variables: U_{Nernst}, R_{ionic}, $R_{totcell}$, η_C, η_A, j_{oe} for the 2 electrodes, j_{ion}, j_{loss} and j. This reaction scheme, though complete, has several drawbacks: the electrochemical reactions definition is complex and increases the model size and computing time, the kinetic model depends on a number of uncertain parameters for which orders of magnitude are known but accurate values for the cell used in our stack are not found. Therefore, a simplified model has been defined to allow a more efficient simulation of the repeat element and stack behavior. This simplified reaction scheme has to define the main characteristics of the stacks and cells used in this work: the cell performance is a function of the temperature, OCVs are significantly lower when compared to theoretical values. The simplified scheme will therefore account for the short circuit current at OCV and a local resistance including the losses at the electrodes.

$$U_{cell} = U_{Nernst} - R_{ionic}.j_{ion} - \eta_C(j_{loss}) - \eta_A(j_{loss}) - j.R_{totcell} \tag{2.48}$$

where the term $R_{totcell}$ is the term including the losses in the electrode and current collection. The short-circuit current j_{loss} is here computed as homogeneous on the surface as detailed simulations have shown that its distribution is quasi-homogeneous. The ionic resistance for the electrolyte is the same as defined in equation 2.41. The global resistance term is defined as:

$$R_{totcell} = C_r.T^{p_r} + R_{ohm}^{MIC} \tag{2.49}$$

where R_{ohm}^{MIC} is the contribution from the ohmic resistances in the current collection and C_r and p_r the parameters defining the dependence of this global loss to the local temperature. In chapter 4, the differences in the model output when using the 2 different models are discussed.

2.4.1.4 Input parameters for the models

The parameter values used in the modeling work are summarized in the table 2.3. The parameter K is adapted to fit with pressure drop measurements.

Table 2.3: Input parameters for the model

K	1.10^{-9}	m^{-2}
λ_{cell}	$\sim$10	W/(mK)
$\lambda_{interconnect}$	25.5	W/(mK)
$\lambda_{s_{x,y}}$	8...13	W/(mK)
λ_{s_z}	1...2	W/(mK)
ϵ_{REz}	0.26	-
σ_{ion}	$1.63.10^2$	S/cm
E_a^{ion}	76.2	kJ/mol
${\sigma_{mic}}^o$	$3.2.10^5$	S/cm
${E_a}^{mic}$	75.2	kJ/mol
C_r	0.36	Ω.cm^2 $/K^{p_r}$
p_r	-2.469	-
ξ	4	μm (except in chapter 8)
A_{cc}	0.42	-

2.5 Stack model

To have a more representative boundary condition for the repeat element model, a stack model has been developed. Its main purpose is to study the sensitivity of the temperature profile and performances to the number of cells in a stack. The problem of defining appropriate boundary conditions to simulate short stacks has been previously discussed (section 2.3.3).

Stack models for SOFCs usually require a large computing time. The "stacking" of repeat element models multiplies the size of the problem. Despite this limit, stack models have been developed by several authors (Gubner et al. [2003]).

The model developed aims at an efficient simulation of stacks. The basic idea of the stack model is that the state of a cell is sufficiently close to its adjacent cells to allow a model using less computing nodes in the z direction than the effective number of cells in the stack (e.g., a 30 cell-stack can be modeled with 15 computing nodes in the stacking direction). This main feature of the stack model has been implemented using the same equations as for the repeat element model; in the solid energy equation, the heat conduction in the z direction has been added. The energy equations are expressed in W/cm^3 .

The model is adapted from the repeat element model under the assumption that the flow distribution in the height of the stack is homogeneous; this allows computation of the equation for the flow field only once. The other variables: local Nernst potential, current density, species concentration, gas and solid temperatures are computed for each node on the height of the stack. The energy equation for the solid is simply:

$$\lambda_{s_z}\frac{\partial^2 T_{solid}}{\partial z^2}+\lambda_{s_{x,y}}(\frac{\partial^2 T_{solid}}{\partial x^2}+\frac{\partial^2 T_{solid}}{\partial y^2})+\dot{Q}=0 \tag{2.50}$$

where λ_{s_z} is the thermal conductivity in the z direction (obtained by volume averaging of thermal conduction properties -see section 2.3.2 -). The heat sources are the same as for the repeat element case. The cell potentials are treated in this model as a continuous variable on the z domain. The cell potential $U_{cell}(z_o)$ represents the average cell potential of the cell located at z_o and not the potential of a given cell number. The stack total voltage is computed by an integral of this distributed cell voltage:

$$U_{stack}=\frac{N_{cells}}{L_z}\int_0^{L_z}U_{cell}(z)dz \tag{2.51}$$

where N_{cells} is the number of cells in the stack and L_z the total height of the stack. The total current is conserved in the height of the stack.
In a stack the inlet gases enter at a given temperature (defined by the system), in the manifolds, the gases are heated which has been accounted for in the model. The model for the temperature of the fluid within the manifold of the stack is as follows: a simple conservation equation computes the flow rate in the manifolding tube along the height of the stack; then an energy equation for the gas in the manifold computes the temperature of the gases.
The conservation equation along the stack is described by 2.52 which assumes a uniform distribution of the gas stream along the stack height and therefore a linear decrease of the flow rate:

$$\mathcal{F}_{gas}(z)=\mathcal{F}_{gas}^{total}-\frac{z}{L_z}\mathcal{F}_{gas}^{cell} \tag{2.52}$$

where $\mathcal{F}_{gas}^{total}$ is the total gas stream to the stack, $\mathcal{F}_{gas}^{cell}$ the flux to a cell.
The energy equation for the gases implies a heat transfer from the stack to the gas and the stack temperature is considered as T_s the temperature of the solid at the inlet position. Thus

$$\frac{\partial T_{tube}}{\partial z}\mathcal{F}_{gas}\mathcal{C}_{gas}=h_{tube}(T_{tube}-T_s)d_{tube}\pi \tag{2.53}$$

where $\mathcal{F}_{gas}$ is the molar flux of the gas in mol/s, $\mathcal{C}_{gas}$ its heat capacity in J/mol.K, h_{tube} the heat transfer coefficient in W/m^2.K, and d_{tube} the tube diameter.

The parameter values used are an hydraulic diameter of 6mm and a Nusselt number for the tube of 10 (usually the value is 4 for a tube in laminar conditions, however here the tube surface is irregular and the heat transfer is probably increased). The boundary conditions used are that the inlet temperature of the fluid at the beginning of the stack height is specified (in most of the case, set to be equal to the oven temperature).
The solid energy equation is adapted at the inlet to account for this additional sink term. The approach has been validated by simulating without significant error a 15-cell stack with a 7 node, 11 node and 15 node mesh in the height of the stack. These verification results are found in the annex in section A.1.4.

2.6 Conclusion

A model for planar SOFC stack and repeat element is presented. The model equations allow representation of configurations with non unidimensional flow field, therefore the model can be applied to a wide range of possible designs. To be used as a design tool, the model has to be computationally effective: sensitivity studies and optimization have to be possible. However, spatially resolved outputs are provided. Simplifications and assumptions were necessary to fulfill these specifications.
The kinetic scheme accounts for phenomena that were identified in experiments, such as an imperfect behavior of the electrolyte leading to a short-circuit current. Validation of the kinetic scheme is performed and reported in chapter 4. To verify the model veracity and increase confidence in the results, comparison with a CFD model and validations with experiments measuring local temperatures and local currents have been carried out.
The stack model developed provides a tool to define the thermal boundary conditions adapted to short stacks where the commonly used adiabatic boundary condition cannot be applied.

Bibliography

E. Achenbach. Three-dimensional and time-dependent simulation of a planar solid oxide fuel cell stack. *J. of Power Sources*, 49:333–348, 1994.

T. Ackmann, L. G. J. de Haart, W. Lehnert, and D. Stolten. Modeling of mass and heat transport in planar substrate type SOFCs. *J. of the Electrochem. Soc.*, 6(150):A783–A789, 2003.

P. Aguiar, C. Adjiman, and N. Brandon. Anode-supported intermediate temperature direct internal reforming solid oxide fuel cell. I: model-based steady-state performance. *J. of Power Sources*, (138):120–136, 2004.

A. J. Bard and L. R. Faulkner. *Electrochemical methods. Fundamentals and applications.* Wiley, 1980.

M. Brown, S. Primdahl, and M. Mogensen. Structure/Performance Relations for Ni/Yttria-Stabilized Zirconia Anodes for Solid Oxide Fuel Cells. *J. of the Electrochem. Soc.*, 2(147): 475–485, 2000.

H. Chan, , K. Khor, and Z. Xia. A complete polarization model of a solid oxide fuel cell and its sensitivity to the change of cell component thickness. *J. of Power Sources*, 93:130–140, 2001.

S. Chan, X. J. Chen, and K. A. Khor. Cathode micromodel of solid oxide fuel cell. *J. of the Electrochem. Soc.*, 1(151):A164–A172, 2004.

P. Costamagna. The benefit of solid oxide fuel cells with integrated air pre-heater. *J. of Power Sources*, 69:1–9, 1997.

P. Costamagna, P. Costa, and V. Antonucci. Micro-modelling of solid oxide fuel cell electrodes. *Electrochemica Acta*, 43-3/4:375–394, 1998.

P. Costamagna and K. Honegger. Modeling of Solid oxide heat exchanger integrated stacks and simulation at high fuel utilization. *J. of the Electrochem. Soc.*, 145-11:3995–4007, 1998.

J. Divisek, L. G. J. de Haart, P. Holtappels, T. Lennartz, W. Malléner, U. Stimming, and K. Wippermann. The kinetics of electrochemical reactions on high temperature fuel cell electrodes. *J. of Power Sources*, (49):257–270, 1994.

J. Fleig and J. Maier. The influence of inhomogeneous potential distributions on the electrolyte resistance in solid oxide fuel cells. In *SOFC V, Proc. of the int. Symposium, Electrochemical Society*, pages 1374–1384, 1997.

A. Gubner, D. Froning, B. de Haart, and D. Stolten. Complete modeling of kW-range SOFC stacks. *SOFC VIII, Proc. of the int. Symposium, Electrochemical Society*, pages 1436–1441, PV 2003-07 2003.

K. V. Hansen, K. Norrman, and M. Mogensen. $H_2 - H_2O - Ni - YSZ$ electrode performance: Effect of segregation to the interface. *J. of the Electrochem. Soc.*, 9(151):A1436–A1444, 2004.

P. Holtappels, I. C. Vinke, L. G. J. de Haart, and U. Stimming. Reaction of hydrogen/water mixture on Nickel-Zirconia cermet electrodes 1.: DC Polarization characteristics. *J. of the Electrochem. Soc.*, 146-5:1620–1625, 1999.

R. Ihringer, S. Rambert, L. Constantin, and J. Van herle. Anode supported thin zirconia based cells for intermediate temperature SOFC. In S. C. Singhal, editor, *SOFC VII, Proc. of the int. Symposium, Electrochemical Society*, pages 1002–1011, 2001.

F. P. Incropera and D. De Witt. *Fundamentals of heat and mass transfer*. John Wiley and Sons, 1990.

Y. Jiang and A. V. Virkar. Fuel composition and diluent effect on gas transport and performances of anode-supported SOFCs. *J. of the Electrochem. Soc.*, 7(150(11)):A942–A951, 2003.

H. Karoliussen, K. Nisansioglu, and A. Solheim. Use of effective conductivities and unit cell-based supraelements in the numerical simulation of solid oxide fuel cell stacks. *Journal of applied electrochemistry*, (28):283–288, 1998.

T. Kawada, H. Sakai, H. Yokokawa, and M. Dokiya. Electrical properties of transition-metal-doped YSZ. *Solid State Ionics*, 53-56:418–425, 1992.

T. Kawashima and M. Hishinuma. Thermal Properties of Porous Ni/YSZ Particulate Composites at High Temperatures. *Materials Transactions JIM*, 37-9:1518–1524, 1996.

K. Kobayachi, S. Yamaguchi, T. Higuchi, S. Shin, and Y. Iguchi. Electronic transport properties and electronic structure of TiO_2-doped YSZ. *Solid State Ionics*, (135):643–651, 2000.

K. Kobayachi, K. Yukiharu, S. Yamaguchi, N. Fukatsu, K. Tsuyoshi, and Y. Iguchi. Electronic conductivity measurements of 5 mol% TiO_2-dopedYSZ by a d.c polarization technique. *Solid State Ionics*, (93):193–199, 1997.

D. Larrain, J. Van herle, F. Maréchal, and D. Favrat. Generalized model of planar SOFC repeat element for design optimization. *J. of Power Sources*, 1-2(131):304–312, 2004.

W. Lehnert, J. Meusinger, and F. Thom. Modelling of gas transport phenomena in SOFC anodes. *J. of Power Sources*, (87):57–63, 2000.

S. Linderoth, N. Bonanos, K. V. Jensen, and J. Bilde-Sorensen. Effect of NiO-to-Ni transformation on conductivity and structure of Yttria-Stabilized ZrO_2. *J. Am. Ceram. Soc.*, 11(84):2652–2656, 2001.

T. Matsui, T. Kosaka, M. Inaba, A. Mineshige, and Z. Ogumi. Effets of mixed conduction on the open-circuit voltate of intermediate-temperature SOFCs based on Sm-doped ceria electrolytes. *Solid State Ionics*, (in press), 2004.

B. R. Munson, D. F. Young, and T. H. Okiishi. *Fundamentals of fluid mechanics*. Wiley, 3rd edition edition, 1998.

M. Oh and C. Pantelides. A modelling and simulation language for combined lumped and distributed parameters systems. *Computer and Chemical Engineering*, 20-6/7:611–633, 1996.

J.-H. Park and R. N. Blumenthal. Electronic transport in 8 mole percent $Y_2O_3 - ZrO_2$. *J. of the Electrochem. Soc.*, 136(10):2867–2876, 1989.

L. Petruzzi, S. Cocchi, and F. Fineschi. A global thermo-electrochemical model of SOFC systems design and engineering. *J. of Power Sources*, (118):96–107, 2003.

J. Piron Abellan, F. Tietz, V. Shemet, A. Gil, T. Ladwein, L. Singheiser, and W. Quaddakers. Long term oxidation behavior and compatibility with contact materials of newly developed ferritic interconnector steel. In J. Huijsmans, editor, *Proc. of the 5th European SOFC Forum*, pages 248–253, 2002.

J. M. Ralph, C. Rossignol, and R. Kumar. Cathode Materials for Reduced-Temperature SOFCs. *J. of the Electrochem. Soc.*, (150(11)):1518–1522, 2003.

M. Roos, E. Batawi, U. Harnisch, and T. Hocker. Efficient simulation of fuel cell stacks with the volume averaging method. *J. of Power Sources*, 118:86–95, 2003.

I. L. Ryhming. *Dynamique des fluides*. Presses Polytechniques et Universitaires Romandes, 1991.

S. Simner, J. F. Bonnett, N. Canfield, K. Meinhardt, J. Shelton, V. Sprenkle, and J. Stevenson. Development of lanthanum ferrite SOFC cathodes. *J. of Power Sources*, (113):1–10, 2003.

B. Todd and J. Young. Thermodynamic and transport properties of gases for use in solid oxide fuel cell modelling. *J. of Power Sources*, 110:186–200, 2002.

J. Van herle, F. Maréchal, S. Leuenberger, and D. Favrat. Energy balance model of a SOFC cogenerator operated with biogas. *J. of Power Sources*, (118):375–383, 2003.

J. Van herle and R. Vasquez. Conductivity of Mn and Ni-doped stabilized zirconia electrolyte. *J. of the European Ceramic Society*, (24):1177–1180, 2004.

A. V. Virkar. Theoritical analysis of Solid Oxide Fuel Cells with two-layer, composite electrolytes: electrolyte stability. *J. of the Electrochem. Soc.*, 138(5), 1991.

Z. Xia, S. Chan, and K. Khor. An improved anode micro model of SOFC. *Electrochemical and solid state letters*, 3(7):63–65, 2004.

H. Yakabe, M. Hishinuma, M. Uratani, Y. Matsuzaki, and I. Yasuda. Evaluation and modeling of performance of anode-supported solid oxide fuel cell . *J. of Power Sources*, 86 (1-2):423–431, 2000.

F. Zhao and A. V. Virkar. Dependence of polarization in anode-supported solid oxide fuel cells on various parameters. *J. of Power Sources*, (141):79–95, 2004.

Chapter 3

Modeling results

3.1 Introduction

This chapter presents the main simulation results obtained with the model developed for two configurations: the counter-flow case and the co-flow alternative configuration. Modeling of different configurations and their comparison is found mainly for the cases of counter-flow, co-flow and cross-flow geometries with external manifolding (Achenbach [1994], Aguiar et al. [2004] and Recknagle et al. [2003]). Other models are specific to a configuration (Gubner et al. [2003] for the Jülich stack, and Costamagna and Honegger [1998] for the Sulzer Hexis stack). From this work, it appears that co-flow configuration is more appropriate to limit temperature differences in the cell.

The counter-flow configuration considered in our case is significantly different from studies previously published, as the fuel inlets are punctual. This chapter presents the results for the simulation of this new geometry. From the results, problems and weaknesses specific to the design have been identified (Larrain et al. [2004] and Autissier et al. [2004]). This has motivated the simulation of a new design based on the same concept, also presented here.

Sensitivity studies have been performed on decision variables. Supposing that the main design concept is fixed, the number of possible configurations is still large, because the thickness of the layers, the cell area, the cell geometry or the design point air flow rate have to be decided upon. Sensitivity studies performed on the counter-flow case allowed to evaluate the impact of decision variables on the stack behavior. Sensitivity studies have been published for some configurations (Costamagna [1997] and Iora and Campanari [2004]), changing the size of the channel and studying the impact on performance and temperature profile.

3.2 Repeat element simulation

3.2.1 Results for the counter flow case

Dimensions of the repeat element considered are: 50cm^2 area, 0.5mm and 0.9mm height for the fuel and air channel respectively, 1mm thickness for the interconnect. Operating conditions are 770°C environment temperature (corresponding to the most common testing conditions), 250 ml/min fuel flow rate and an air ratio of 3.
Figure 3.1(a) presents the hydrogen concentration at open circuit voltage (OCV). Owing to the shorting current, hydrogen consumption at OCV is not negligible as ca. 5% of the fuel is converted at OCV. The gradient in concentration explains the current density profile at OCV (figure 3.1(b)), where the hydrogen concentration is low, currents are negative and the cell behaves as an electrolyzer. The kinetics of the electrodes in electrolysis mode are assumed to be the same as in fuel cell mode, this may lead to an over-estimation of the negative current magnitude. On the contrary, at the fuel inlet, where concentration is high, current density is positive. The resulting current integral is zero at OCV.
Concentration at 30% and 80% fuel utilization is shown on figures 3.2(a) and 3.3(a). Current density at the same fuel utilization is shown on figures 3.2(b) and 3.3(b). The concentration profile exhibits regions with lean concentration and the outlet concentration (on coordinate $y = 1$) is not homogeneous. This is observed for 30% and even much more pronounced for 80% fuel utilization. These low concentration areas are explained by the flow configuration: velocities close to the edges are small and the residence time is longer, resulting in low concentrations. The minimum fuel concentration observed at 80% overall fuel utilization is as low as 5%. The current density profile, which is strongly coupled to the concentration profile, shows a strong maximum at the fuel inlet (at 30% fuel utilization the maximum current density is 0.5A/cm^2 for an average of 0.22A/cm^2 , at 80% fuel utilization the maximum is 1.5A/cm^2 for 0.6A/cm^2 average current density) with low values in regions close to the edges. The non-homogeneity of the current density and concentration fields limits the operation at high fuel utilization and efficiency. With the flow configuration chosen and the punctual inlet, this problem is intrinsic to the design as low velocities and resulting problems are difficult to avoid unless the active area is restricted to the area between the gas inlets.

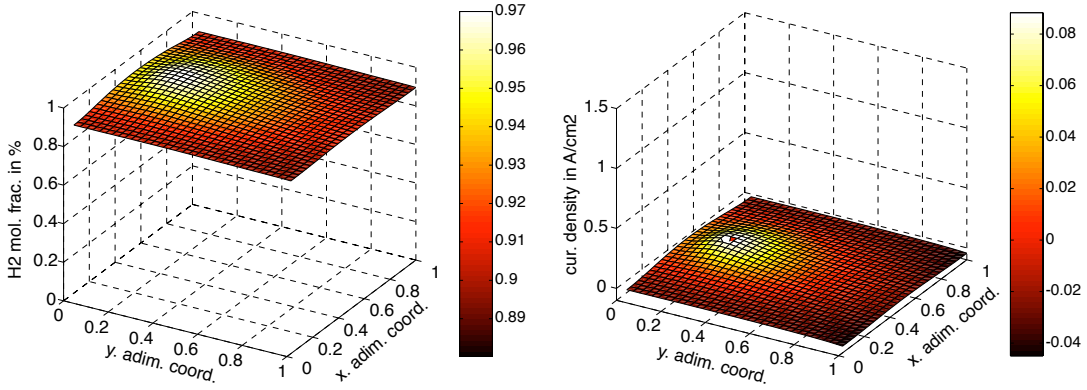

(a) Concentration in mol_{H_2}/mol (b) Current density in A/cm^2

Figure 3.1: Hydrogen concentration and current density at OCV for the counter-flow case

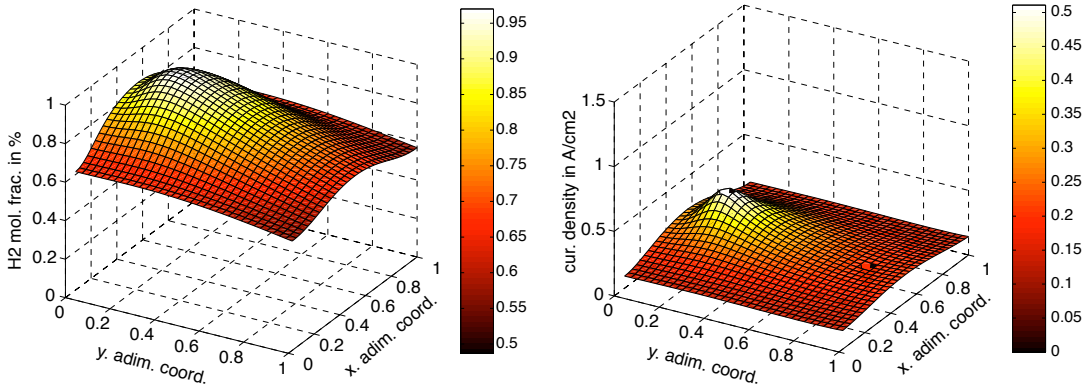

(a) Concentration in mol_{H_2}/mol (b) Current density in A/cm^2

Figure 3.2: Hydrogen concentration and current density at 30% fuel utilization for the counter-flow case

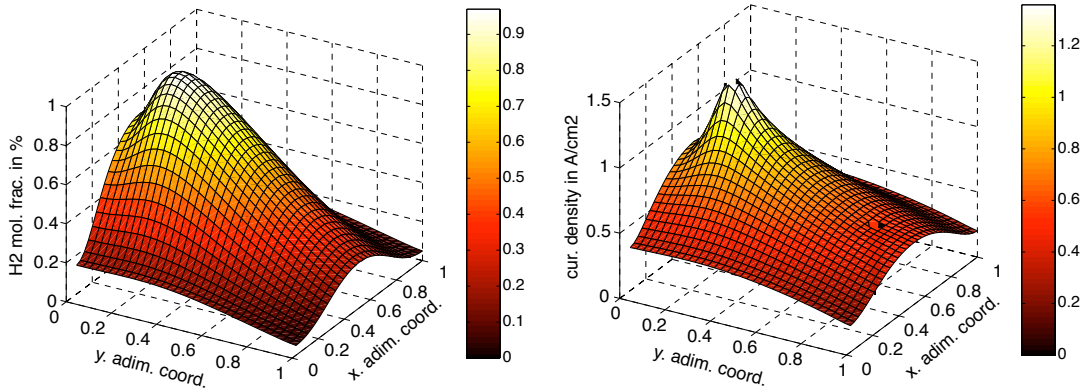

(a) Concentration in mol_{H_2}/mol (b) Current density in A/cm^2

Figure 3.3: Hydrogen concentration and current density at 80% fuel utilization for the counter-flow case

The temperature field is shown on figure 3.4(b) and 3.4(c) for 30% and 80% fuel utilization. At 30% fuel utilization, the maximum temperature is at the fuel outlet (y =1) where the post-combustion of the unconverted fuel occurs. The air inlet creates strong gradients although the minimum temperature is not at the same location for this operating point. At high fuel utilization, the maximum temperature is located near the fuel inlet, as the maximum current density is in this region. As the available fuel for post combustion is low, the fuel outlet is at low temperature and the minimum temperature is now at the air inlet. The post combustion makes the temperature field highly dependent upon the fuel utilization. This was already reported by Costamagna and Honegger [1998] based on an experimental and simulation study of the Sulzer-Hexis stack which is a circular coflow with post-combustion at the fuel outlet. Temperature levels simulated for the present simulation are excessively high (maximum temperature of 870°C) for an intermediate temperature SOFC using metallic interconnect.

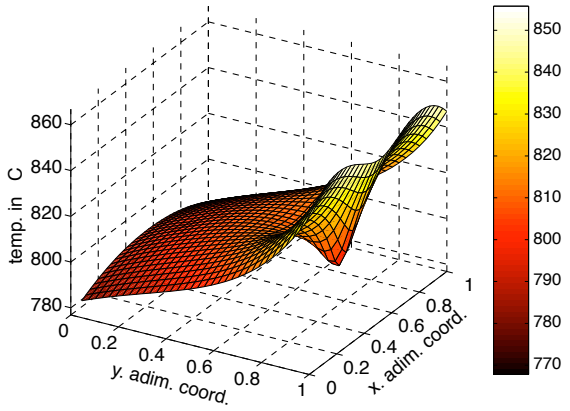

(a) OCV

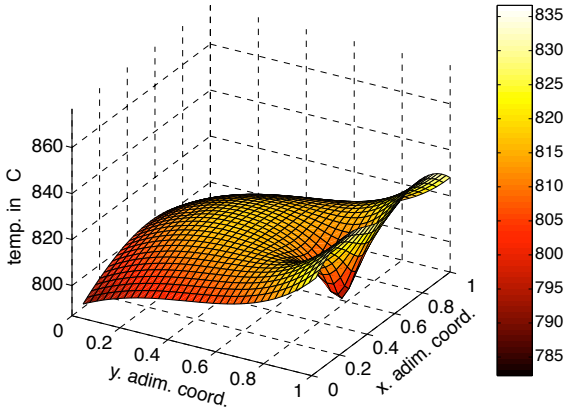

(b) 30% fuel utilization

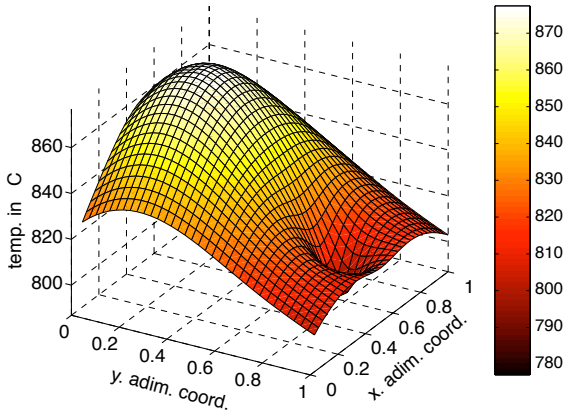

(c) 80% fuel utilization

Figure 3.4: Temperature adiabatic case for the counter-flow case

The counter-flow simulation has allowed identification of some disadvantages:

- the internal manifolding, which results in a compact stack, leads to highly non-homogeneous concentration and current density fields, which are prone to cause problems in operation at high efficiency (and fuel utilization $> 60\%$). This could be avoided by separating the reactive area from the inlets.

- the post combustion generates several problems: the stand-by mode at OCV has to be avoided as temperatures are high (especially in the fuel outlet region). Furthermore back-diffusion decreases slightly the OCV. Finally post-combustion creates temperature and concentration gradients with a redox front on the cell that may induce failures.

3.2.2 Sensitivity to boundary conditions

The previous results assume a repeat element in a large stack. However, a large number of tests have been performed for single repeat elements and adiabatic boundary condition assumptions on the cell surface are no longer valid to represent such a case. Simulations have therefore been carried out with non-adiabatic boundary conditions (defined in section 2.3.3) to point out the difference in behavior.
The temperature profiles at 30% and 80% fuel utilization are shown in figure 3.5. At low fuel utilization the dominating phenomena on the temperature is the post-combustion, the gradients at the fuel outlet is important with 20 to 25K temperature difference between the fuel outlet and the air inlet. The situation is even worse at OCV (see figure 3.5(a)). The temperature on the remaining part of the cell (from $y = 0$ to $y = 0.8$) is quite homogeneous. At high fuel utilization (80%) the maximum temperature is shifted to the area of the fuel inlet as the electrochemical reaction occurs mostly in that area.

Temperature variations are low as a variation of 20 to 25K is predicted by simulation in the area at the fuel inlet. The test conditions on a repeat element are significantly different from the conditions expected in a stack. Temperatures are significantly lower (ca. 805°C for the repeat element vs. 870°C for the adiabatic repeat element at 80% fuel utilization seen on figure 3.4(c)) and temperature variations smaller. Post-combustion dominates the temperature for most of the operating range as its effect is still visible at 80% fuel utilization (figure 3.5(c)). For a short stack (e.g. 5 cells), an intermediate situation between the adiabatic case and the single repeat element case is expected. Results from stack simulation will provide some insight on this issue.

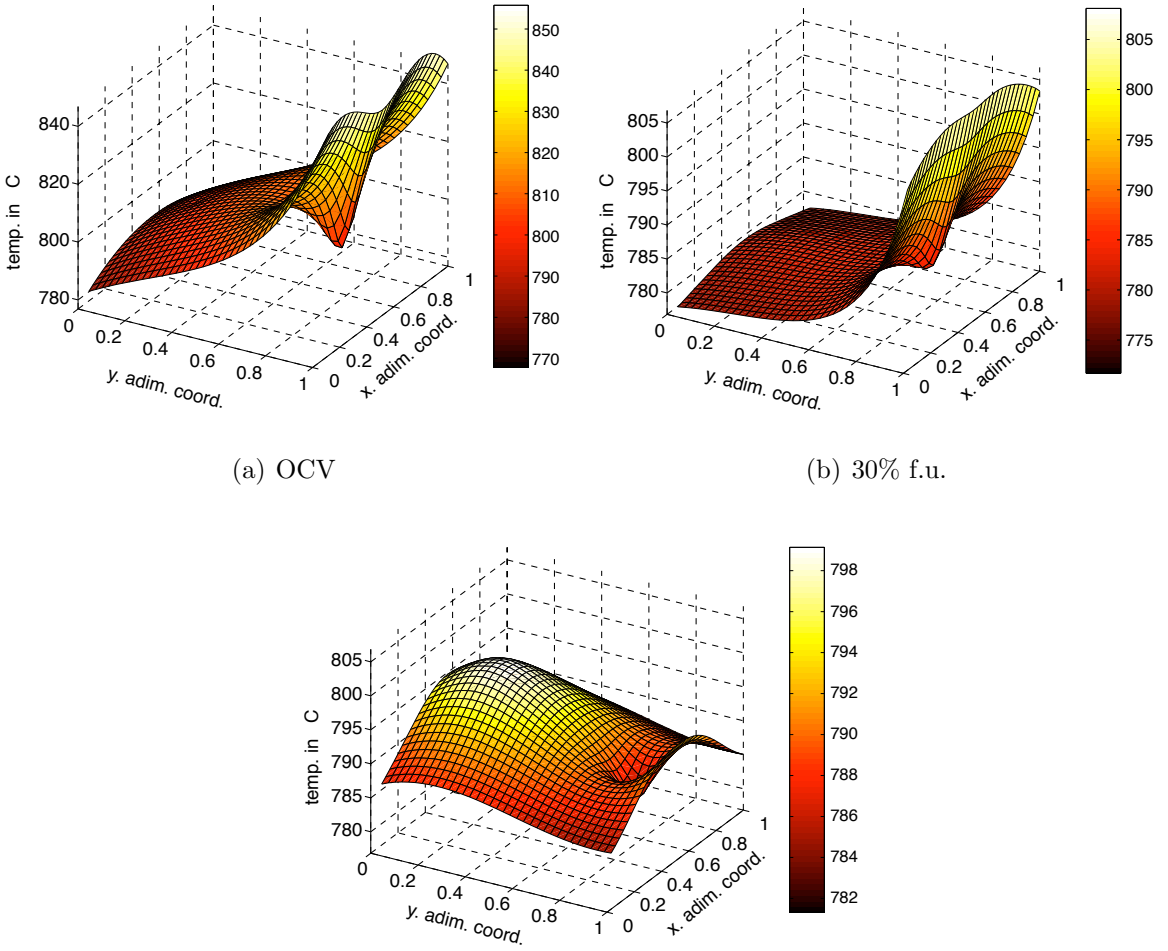

(a) OCV

(b) 30% f.u.

(c) 80% f.u.

Figure 3.5: Temperature non-adiabatic case for the counter-flow case

3.2.3 Results for the coflow case

The problems identified on the counter-flow (section 3.2.1) configuration have motivated an alternative design. The main differences with the previous design are:

- the gas inlet and the active area are separated in order to have homogeneous concentrations on the direction normal to the flow (as uni-dimensional as possible)
- post-combustion at the fuel outlet is avoided: the fuel is recovered (without air mixing) by a similar manifold as the fuel inlet

The uni-directional flow produces a more homogeneous concentration at the outlet of the reaction zone; this leads to a better distributed current density and should allow operation oof the stack at higher fuel utilization.

The new flow pattern is a co-flow, co-flow reactant configuration creating the smoothest temperature profiles (Achenbach [1994],Aguiar et al. [2004],Recknagle et al. [2003]). The results from the simulation of this alternative design are shown on figure 3.7(a) for the hydrogen concentration at 80% fuel utilization and on figure 3.7(b) for the current density. The fuel concentration shows a regular decrease from the inlet of the active area to the outlet, the concentration at the outlet being fairly homogeneous. The current density shows a maximum at the fuel inlet, and then a regular decrease. The maximum current density is here of 1.1A/cm^2 for 0.6A/cm^2 average.
The temperature profile is shown on figure 3.6(a) and 3.6(b) for 30% and 80% fuel utilization respectively. The temperature profile is in this case regular with a maximum temperature close to the cell center. Temperatures are higher towards the gas outlet, as a result of the air flow rate conductive transport and the maximum temperature is 830°C at 30 A.

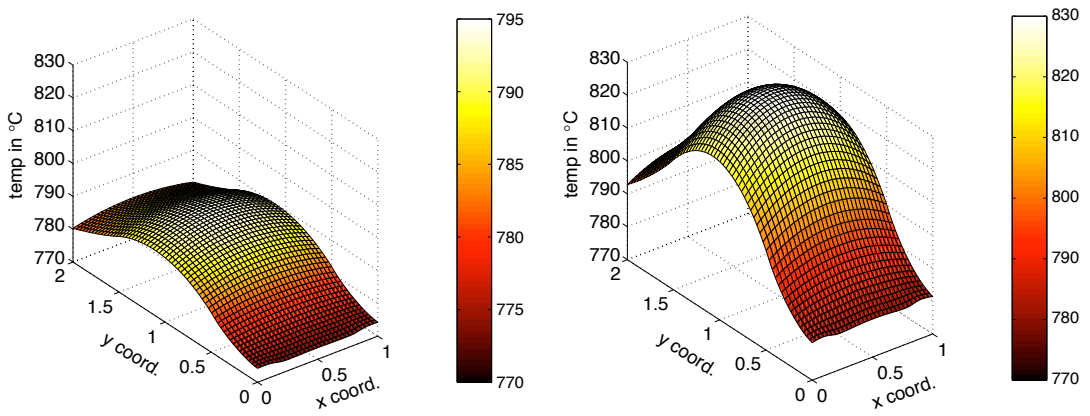

(a) 30% f.u. (b) 80% f.u.

Figure 3.6: Temperature Coflow case

3.2.4 Comparison of the 2 configurations

The two presented configurations exhibit a different behavior. The concentration and current density profiles differ strongly, the coflow design presents a quasi 1D current density and concentration distribution which is favorable for the reliability and the operation at high fuel utilization. The difference in the current-potential characteristic is seen in figure 3.8 where the performance of both configurations are compared for non adiabatic conditions. The iV curves are close below 60% fuel utilization, at high current density, however, the counter-flow characteristic shows a limitation (although no diffusion over-potentials are included in the model). This limitation is not observed for the coflow characteristic.

Temperatures are quite different for both cases: at the same current and environment tem-

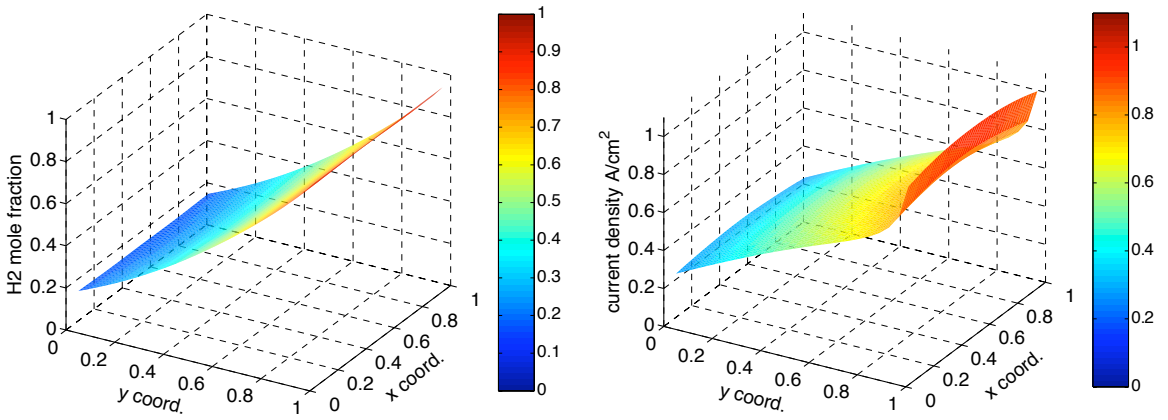

(a) hydrogen concentration profile at 80% f.u. in mol_{H_2}/mol

(b) current density profile at 80% f.u. in A/cm^2

Figure 3.7: Concentration and current density coflow case

perature the maximum temperature is 830°C for the coflow design (figure 3.6(b)) vs. 870°C for the counter-flow design (adiabatic case on figure 3.4(c)). This difference in temperature is explained by several factors:

- the current density maximum is extremely high for the counter-flow case
- the air flow, for the counter-flow case, moves the maximum temperature towards the fuel inlet where heat sources are at maximum. On the contrary, for a coflow the air removes the heat from the location where the heat generation is maximum.
- the additional surface (coflow design) for the inlet and outlet of the gases absorbs part of the heat
- the disadvantage is that the design is not as compact
- the counter-flow repeat element absorbs heat from the post-combustion, even at 80% fuel utilization, which is not the case for co-flow

The compactness of the internal manifold repeat element is a disadvantage in terms of temperature and operation at high efficiency. The effect of the design compactness will be studied in a further section where sensitivity studies are reported.

3.3 Stack results

A stack model has been implemented for the counter-flow base case. The main purpose of this model is to study the effect of stacking on the temperature profile. As seen in section

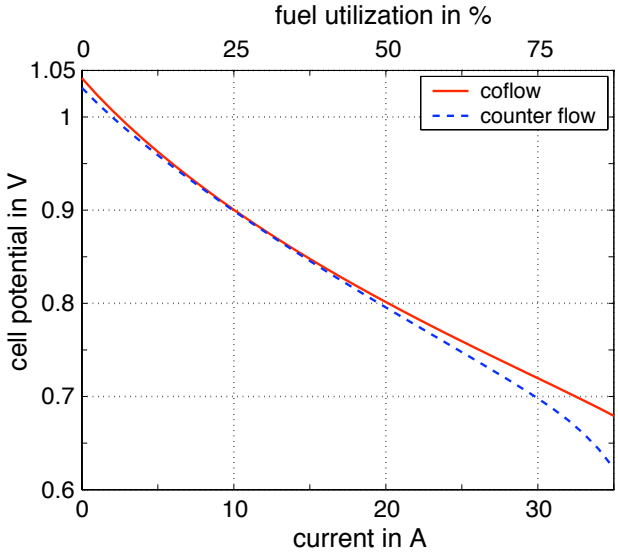

Figure 3.8: Current potential characteristic comparison for the coflow and counter flow case -simulation for 300 ml/min, air ratio of 3, environment 770°C and for a single repeat element with the complete reaction scheme -

3.2.2 the behavior of a single cell is different from that of a cell in a stack (as assumed by adiabatic boundary conditions). The stack model will therefore provide some key information on the behavior of short stacks and will allow definition of the range of validity of the adiabatic boundary condition.

The number of cells in a stack depends on the application and the electrical inverters used for the electric power conditioning. For a given power output, there is nevertheless a choice between the number of cells and the cell area. The developed stack model allows simulation of large stacks with a limited number of computational nodes in height direction (see 2.5). The present study has been performed on a mesh of 15 nodes on the height. In the following, the number of cells has been varied from 5 to 60 cells. The boundary conditions applied are those for a stack in a test oven, in this configuration heat losses are large at the bottom and top-end cells. Figure 3.9 shows the temperature profile along the height of the stack for different numbers of cells, the reported temperature is the maximum value at the coordinate z (stacking direction). This simulation has been performed with the base case configuration thicknesses.

The maximum temperature is not at the stack center but at $z = 0.6$. This is explained by preheating of air and fuel in the manifolds, which enter the stack at $z = 0$ and shift the maximum temperature. The maximum temperature increases with increasing number of cells. However, for a cell number above 30, the increase is small. For a 30 cell-stack, quasi adiabatic conditions (with little variation of the temperature in the stacking direction) are simulated between $z = 0.4$ to z =0.7. This result differs from that presented by Achenbach [1994], Larrain et al. [2003] and Gubner et al. [2003] where the gradient of temperature in the

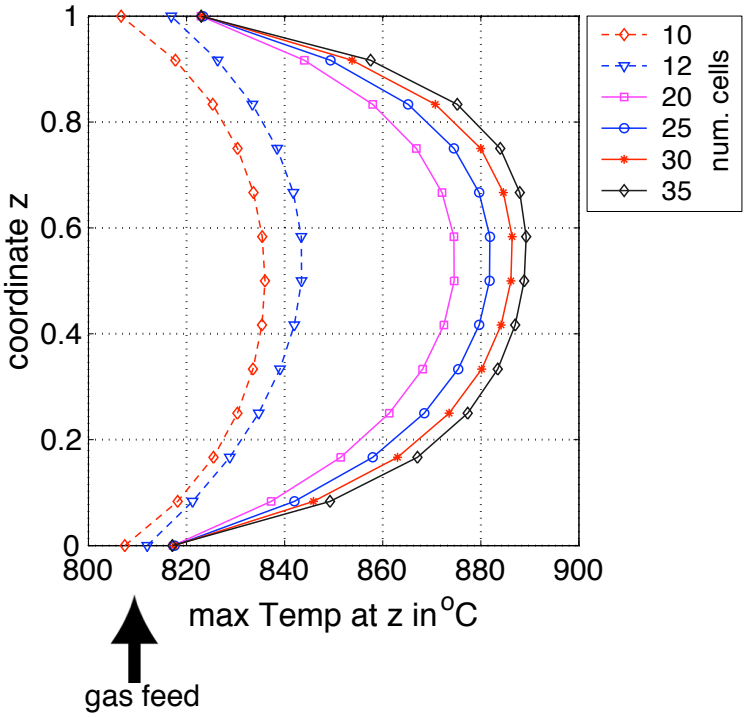

Figure 3.9: Maximum temperature along the stack height depending on the number of cells in the stack. Operating point at 20A, 50% fuel utilization and cell potential 0.78V. (counter-flow case)

stacking direction is important. The main reason for this difference is the low conductivity in z direction obtained with the SOFConnex$^{(TM)}$current collectors. The thermal conductivity in z direction is as low as 2W/(mK) for the simulated case (compared to ca. 10 W/(mK) for the in-plane directions).

For short stacks of 10 to 15 cells, the situation is different and temperature levels reach ca. 830 °C compared to more than 880 °C for stacks of 25 cells and more. This is explained by the shorter length in the stacking direction, heat transfer in this direction occurs and keeps the stack temperature at reasonable values. The stack was here simulated with the boundary conditions in a test oven. In the case of a system, the stack is often integrated with the system and is placed with one end on a insulating plate. For such a case, the situation is even worse as one of the sides can be considered as quasi adiabatic.

3.4 Sensitivity analysis on decision variables

Previous sections presented the detailed results for a given configuration. In the following, sensitivity analysis on operating and design decision variables is presented. For this kind

of study, the results are summarized by a set of performance indicators for the state of the stack. Some of these performance indicators are discussed.
Two main types of sensitivity results are presented:

- the performance maps, where the cell state is function of the fuel flow rate and of the cell potential for a given configuration with the geometry of the stack being kept constant for the whole simulation.
- The combined sensitivity maps where 2 design variables are changed and the performance indicators monitored.

For such a sensitivity study, the environment temperature, fuel flow rate and power output are kept constant. The air excess ratio is considered as a *design variable*: the pressure drop is set as at a constant target value, which is assumed to be the pressure drop at the design point. The air channel dimensions are therefore adapted to obtain a constant pressure drop for different air flow rates.

3.4.1 Choice of performance indicators

Sensitivity analysis is useful to understand the impact of a given operating parameter or design parameter on the system performance and behavior. In the following, performance maps and combined sensitivity for 2 design parameters are presented. Such analysis brings in general a large amount of information and the results are analyzed on selected performance indicators. The possible indicators are:

- energy conversion indicators: power output, fuel utilization, cell potential, power density (per unit volume), efficiency
- temperature field indicators: maximum temperature, minimum temperature, maximum temperature difference in the cell, mean temperature, air outlet temperature
- other indicators like the minimum hydrogen concentration

In the following, the indicators most often used will be the power density, and the maximum temperature and maximum temperature difference. Power density allows to compare different systems and configurations on the same basis. The definition is:

$$\epsilon_{spe} = \frac{\dot{E}_{elec}}{V_{repeatelement}} \quad \text{in} \quad \mathrm{W/cm^3} \tag{3.1}$$

where $V_{repeatelement}$ is the volume of the repeat element (in cm^3) and $\dot{E}_{elec}$ the electric power. The maximum temperature is an important indicator as materials (especially the interconnect) used in intermediate temperature SOFC are usually designed to be operated at a temperature of 800°C . The temperature has an strong impact on the degradation rate, discussed in chapter 8. Finally, ceramics are known to be sensitive to temperature gradients, therefore the temperature difference in the cell is monitored as well. It is defined as

$$\Delta T_{max} = T_{maxsolid} - T_{minsolid} \tag{3.2}$$

where $T_{maxsolid}$ and $T_{minsolid}$ are the maximum and minimum temperature on the cell. The temperature gradient itself is not considered in this work because for the counter-flow configuration, the maximum gradients are close to the inlet holes and the mesh resolution of the simplified model is too coarse to accurately predict gradients in this region.

3.4.2 Performance maps

For a given geometry, the fuel flow rate and cell potential can be varied to obtain a performance map. Results can be seen in figure 3.10(a) and 3.10(b). The difference between figure 3.10(a) and figure 3.10(b) is the electrochemical performance of the cell which has been decreased for the second performance map.
With increasing fuel flow the maximum power output increases but is obtained at lower cell potential and therefore lower efficiency. The maximum temperature in the repeat element decreases first with increasing current, and then increases this effect being due to the post combustion (section 3.2.1).
The change in electrochemical characteristics does not alter the intrinsic behavior of the repeat element. Obviously lower power outputs are obtained for the same cell potential, good efficiencies can still be obtained (>40%) at low fuel flow rate. With respect to the temperature difference, for the same power output, temperatures are higher with a less performing cell. This is explained by the efficiency decrease: the same power output may be achievable but will be achieved at an operating point at lower cell voltage.

3.4.3 Sensitivity on design variables

For a given stack design, several decision variables define the final geometry: the cell area, its shape, the air ratio or the interconnect thickness. Sensitivity analysis allows quantification and determination of the impact of a design decision variable on selected performance indicators. The results from two combined sensitivity analyses for the counter flow case

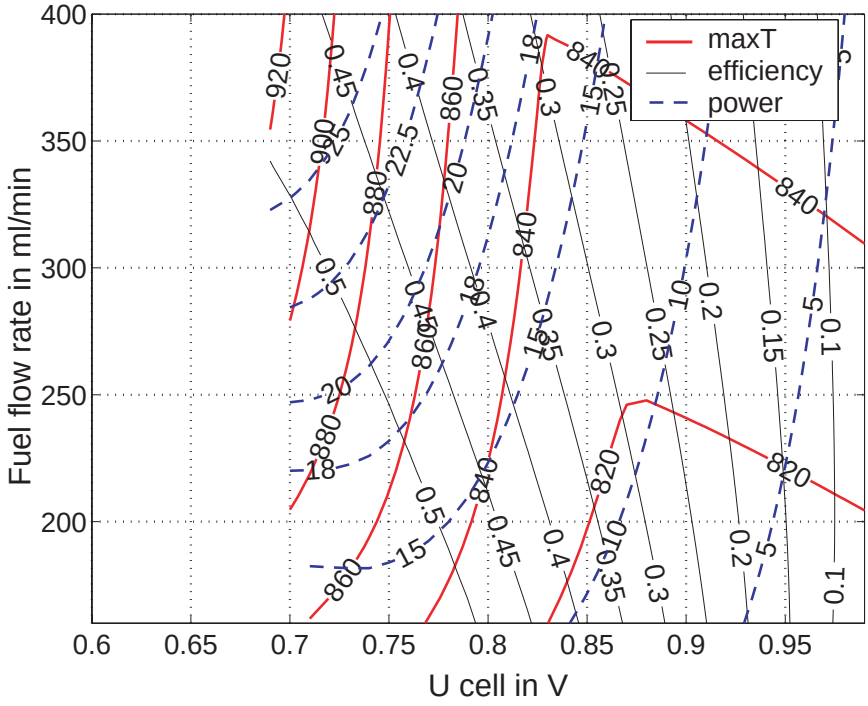

(a) Case standard electrochemical model

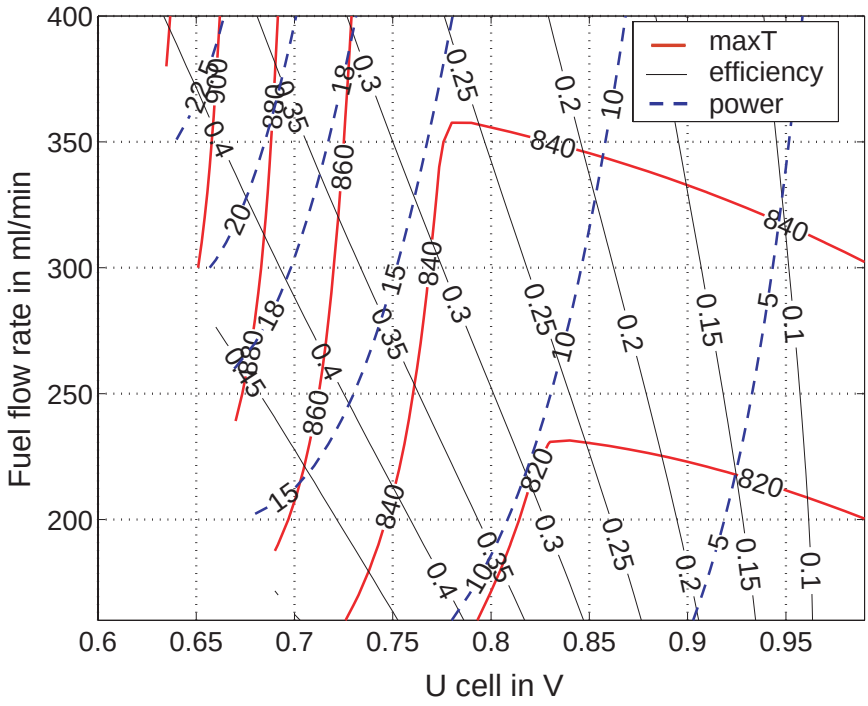

(b) Case worse kinetics

Figure 3.10: Performance map for a counter flow case with different electrochemical performances

are presented. In the reported maps, to keep the results readable, only two indicators are reported: the power density (in W/cm^3) and the maximum temperature (in °C).
Figure 3.11(a) presents the sensitivity on the cell active area and air ratio. The results indicate that the maximum temperature is not dependent on the cell area. For lower area the current density is high but the heat conduction path short. For a larger area, the longer heat conduction path is compensated by the lower current density. The power density obviously decreases with increasing area and increasing air flow rate.
Figure 3.11(b) present the results for the sensitivity on air excess ratio and interconnect thickness. Temperature and power density decrease with increasing air ratio and interconnect thickness. The dependence of the temperature on the interconnect thickness tends to decrease with high air flow rate values (both effects combine to decrease the temperature). Air ratio obviously impacts the temperature but in the presented results, 2 effects are combined: the channel height is changed which decreases the power density and temperature and the increase in air flow rate increases the amount of heat transported by the air. For the interconnect, the same applies as increasing thickness increases the in-plane thermal conductivity (as the metallic interconnect is the component having the higher thermal conductivity) and decreases the power density.
In terms of design, compactness is important for some applications and for cost reasons as well. For the cell reliability, temperature should be kept reasonably low as aging of the material is thermally sensitive. To increase compactness, the area, air ratio and interconnect thickness should be limited, but this results in high temperatures in the repeat element (close to 900°C). Minimization of the temperature level leads a less compact design. Power density and maximum temperature are conflicting objectives. Sensitivity study provides an understanding on the behavior of indicators with a given variable, however it does not indicate the best compromise solution. Multi-objective optimization methods will be applied later to solve this limitation of sensitivity studies (chapter 9).

3.5 Discussion and conclusion

Simulation of the counter-flow allows identification of the main problems for this design: the internal manifolding creates lean regions where the local concentrations of fuel are low resulting in problems at high fuel utilization, and excessively high temperature levels. This temperature is explained by the design of the configuration and its compactness.
Non adiabatic boundary conditions for a single repeat element leads to a different temperature profile with moderated temperature variation and a temperature profile dominated by the post-combustion up to a fuel utilization of about 70%. Stack simulations point out that the adiabatic boundary conditions are realistic for our design as quasi adiabatic cells

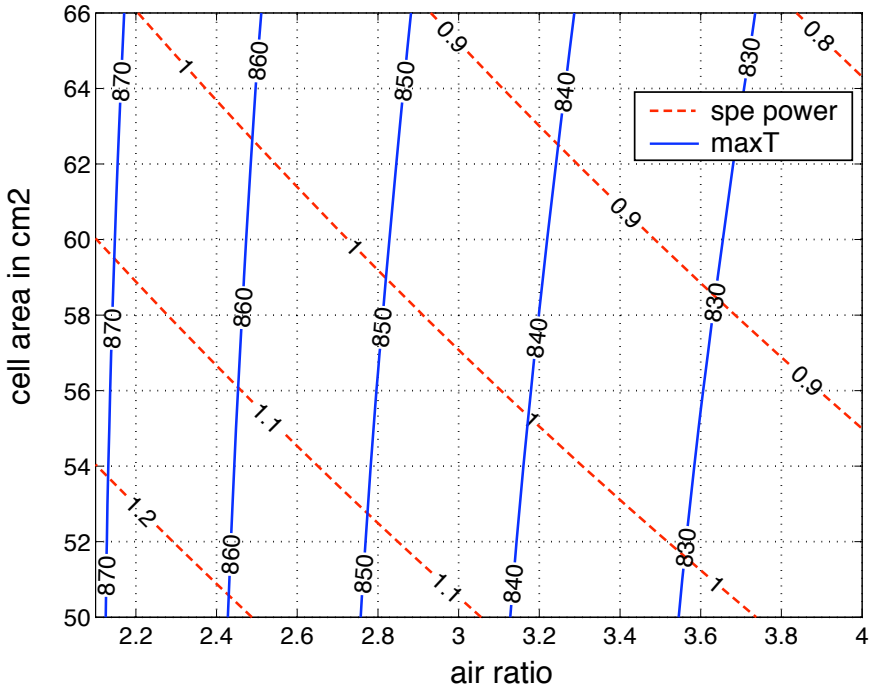

(a) Combined sensitivity to area and air excess ratio

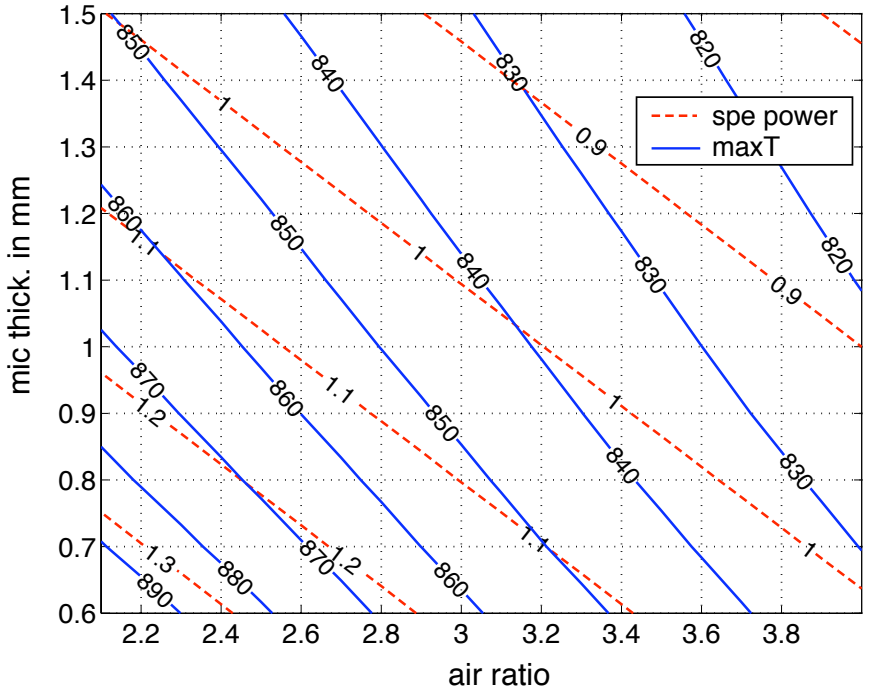

(b) Combined sensitivity to interconnect thickness and air excess ratio

Figure 3.11: Sensitivity maps on design decision variables for the counter-flow case

are observed for a 30 cell-stack with boundary conditions representative of a stack tested in an oven. These results differ from the results of Achenbach [1994] where no adiabatic

conditions were found in a large stack (60 cells) with metallic interconnects. This difference is explained by the low conductivity in z of the SOFConnex$^{(TM)}$current collector. Further investigation may be necessary on this aspect. The case of a stack in a fuel cell system is different and new boundary conditions would have to be defined. The stack model could be more intensively exploited in the future to identify realistic boundary conditions for the short stacks (of 5 to 15 elements) which are usually tested.

Sensitivity studies have been performed and their usefullness to identify the trend between a decision variable and the stack behavior has been established. However, when performing cross-sensitivity on 2 decision variables, the choice of the optimal combination of both variables is not obvious. For most of the cases, sensitivity results are conflictive. This limits the usefullness of sensitivity studies as a tool to assist design decision. To go further and allow an optimization of the repeat element design, multi-objective optimization methods are necessary.

The new design based on co-flow of fuel and oxidant and elimination of the post-combustion avoids most of the problems identified in the counter-flow design.

Bibliography

E. Achenbach. Three-dimensional and time-dependent simulation of a planar solid oxide fuel cell stack. *J. of Power Sources*, 49:333–348, 1994.

P. Aguiar, C. Adjiman, and N. Brandon. Anode-supported intermediate temperature direct internal reforming solid oxide fuel cell. I: model-based steady-state performance. *J. of Power Sources*, (138):120–136, 2004.

N. Autissier, D. Larrain, J. Van herle, and D. Favrat. CFD simulation tool for solid oxide fuel cells. *J. of Power Sources*, 1-2(131):313–319, may 2004 2004.

P. Costamagna. The benefit of solid oxide fuel cells with integrated air pre-heater. *J. of Power Sources*, 69:1–9, 1997.

P. Costamagna and K. Honegger. Modeling of Solid oxide heat exchanger integrated stacks and simulation at high fuel utilization. *J. of the Electrochem. Soc.*, 145-11:3995–4007, 1998.

A. Gubner, D. Froning, B. de Haart, and D. Stolten. Complete modeling of kW-range SOFC stacks. *SOFC VIII, Proc. of the int. Symposium, Electrochemical Society*, pages 1436–1441, PV 2003-07 2003.

P. Iora and S. Campanari. Parametric analysis of a planar SOFC model with geometric optimization. In M. Mogensen, editor, *Proc. of the 6th European SOFC Forum*, pages 656–670, 2004.

D. Larrain, J. Van herle, M. Graetzel, and D. Favrat. Modeling of cross-flow stack: sensitivity to thermal properties of the materials. *Proceeding of the 8th SOFC int. symposium, edited by the Electrochemical Society*, PV 2003-07:1478–1486, 2003.

D. Larrain, J. Van herle, F. Maréchal, and D. Favrat. Generalized model of planar SOFC repeat element for design optimization. *J. of Power Sources*, 1-2(131):304–312, 2004.

K. Recknagle, R. Williford, L. Chick, D. Rector, and M. Khaleel. Three-dimensional thermo-fluid electrochemical modeling of planar sofc stacks. *J. of Power Sources*, (113):109–114, 2003.

Chapter 4

Electrochemical scheme choice and validation

4.1 Introduction

The first step in model validation is the simulation of the current potential (iV) characteristic. The accurate simulation of a real system behavior requires calibrated kinetic parameters to describe the electrochemical performances of the cell tested and a model representing the system with sufficient accuracy. This chapter assumes that the simulation of the velocities and the resulting concentration and current density profiles are satisfactory. The focus is here on the identification of the kinetic parameters.

This chapter presents the methodology applied to identify kinetic parameters from button cell and repeat element tests. The method have been presented in Larrain et al. [2003]. From this early work electrochemical model (sections 2.4.1.1 and 2.4.1.3) and the button cell model have been modified and the method extended. The experiments are performed on complete cells and may not be appropriate to identify complete kinetic scheme parameters such as the parameters for the Butler-Volmer equation expressing activation losses. The validity and range of use of the two kinetic models is discussed as well as their suitability to identify parameters with the experimental data available.

First, the two kinetic models are briefly described. Then, experimental set-up, procedure and parameter identification methodology are presented. The model of electrolyte imperfect behavior model is partly validated. Results from parameter identification carried out with data from a repeat element and from a button cell are presented for the two possible kinetic models.

4.1.1 The possible kinetic schemes

The kinetic schemes are presented in sections 2.4.1.1 and 2.4.1.3. The expressions for the complete and simplified schemes are briefly given here. The equivalent circuit accounts for an imperfect behavior of the electrolyte (figure 4.1). The two different schemes differ

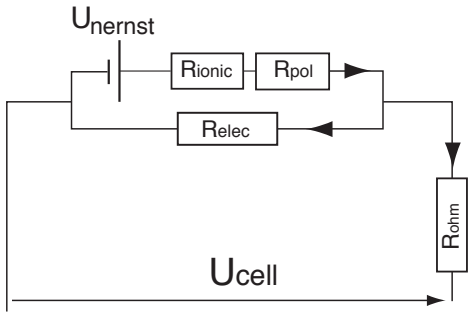

Figure 4.1: Equivalent circuit accounting for a non negligible electronic conductivity of the electrolyte.

essentially in the definition of the activation losses. The complete scheme uses a Butler-Volmer expression (function of temperature and current) for each electrode (equation 2.45). The simplified scheme uses a total resistance as function of temperature which accounts for the activation losses in the electrodes (equation 2.49). Activation losses are accounted with the shorting current only to allow the computation of a realistic OCV, and are aggregated in only one activation loss (for both electrodes).
The complete scheme gives:

$$U_{cell} = U_{Nernst} - \eta_C(j_{ion}) - \eta_A(j_{ion}) - j_{ion}.R_{ionic} - j.R_{ohm} \tag{4.1}$$

where η_C and η_A are the overpotential computed with Butler-Volmer. The simplified sheme gives:

$$U_{cell} = U_{Nernst} - R_{ionic}.j_{ion} - \eta_C(j_{loss}) - \eta_A(j_{loss}) - j.R_{totcell} \tag{4.2}$$

where

$$R_{totcell} = C_r.T^{p_r} + R_{ohm}^{MIC} \tag{4.3}$$

The electrolyte is assumed to be of a known thickness (10μm).
The two different electrochemical models induce different behavior for the current potential

simulation. This is illustrated here with an iV curve for the counter flow repeat element (figure 4.2). The complete scheme with Butler-Volmer (BV) shows a limitation at very high fuel utilization. The simplified scheme does not allow simulation of points at such fuel utilization.

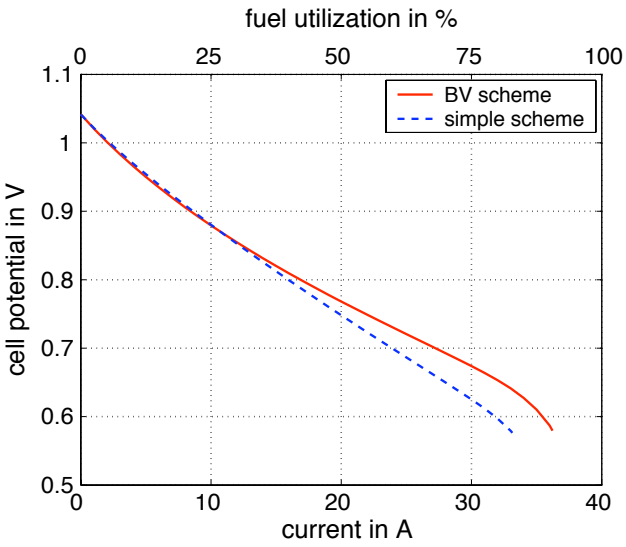

Figure 4.2: Current potential with the 2 different kinetic schemes in a counter-flow repeat element

4.2 Experimental characterization of cells and stack

This section presents the different experiments used to characterize the cells and stack performance. The experimental setups and test procedure are introduced. Comments on experimental problems encountered with SOFC cells testing are given.

4.2.1 Single cell tests

Small button cells and short stack tests are carried to study and verify the electrochemical performances of the materials used, to monitor degradation and to obtain a characteristic of the behavior of the cells and stack components produced.

Small cells tests are performed on a square anode supported electrolyte with a total area of 16 cm^2 , the cathode is screen printed on 1 cm^2 . The cell is placed in a seal-less set-up (figure 4.3) consisting of three spring-loaded flanges with a single gas inlet each (similar set-up as in Constantin et al. [2001] and Ihringer et al. [2001]). Current collection and potential measurement are carried out by pressing a nickel mesh on the anode side and a platinum

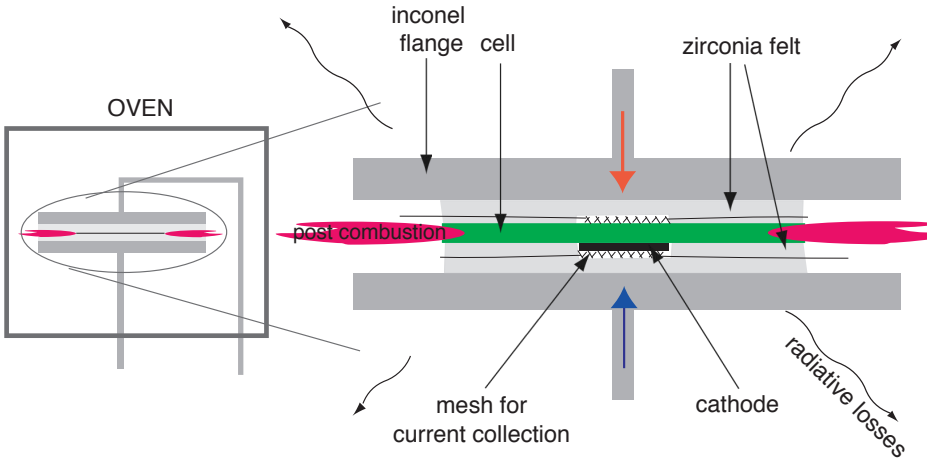

Figure 4.3: Set-up for button cell testing

grid on the cathode side. The platinum grid is usually applied with a wet current collection cathode ink composed of LSC. The cell is kept between two zirconia felts which are 90% porous to let the gas flow and provide electrical insulation. In standard tests, a thermocouple is placed close to the active area. The flow rates used are generally in large excess of fuel and air (140 ml/min hydrogen and 300ml/min air), thus the fuel utilization is below 10% even at very high current densities. At the edges of the cell the unused fuel burns with the air coming from the cathode. Electrochemical testing of the cells is controlled with a potentiostat and electrochemical impedance spectroscopy measurements have been conducted on some of the cells.

Within the frame of the recently started european project REAL-SOFC, some single cells have been tested at Forchung Zentrum Jülich (de Haart [2005]). These cells are 50x50 mm square with a cathode screen printed on 16 cm^2 . The cells where placed in a sealed set-up, sealing was achieved by a glass-ceramic seal. Current collection on the cells is also idealized by the use of nickel mesh on the anode side and platinum mesh on the cathode side. The meshes are pressed directly on the electrodes. Fuel flow rate was 300 ml/min (hydrogen with 3% vapor - bubbler with controlled temperature) and air flow rate 600 ml/min. Cells were polarized up to 20A which corresponds to a fuel utilization of ca. 50%.

4.2.2 Repeat element and stack tests

Repeat element and short stacks are tested in an oven. Stacks are assembled in-situ on one of the set-up flanges (figure 4.4). A mica sheet is placed between the first and last interconnect from the stack and the corresponding flange to avoid short-circuiting, this thin MICA sheet may induce some leakage and pre-mixing of the feeding gases. Owing to the larger flow rates used in stack testing, preheating of the reactants is necessary. This is achieved on the

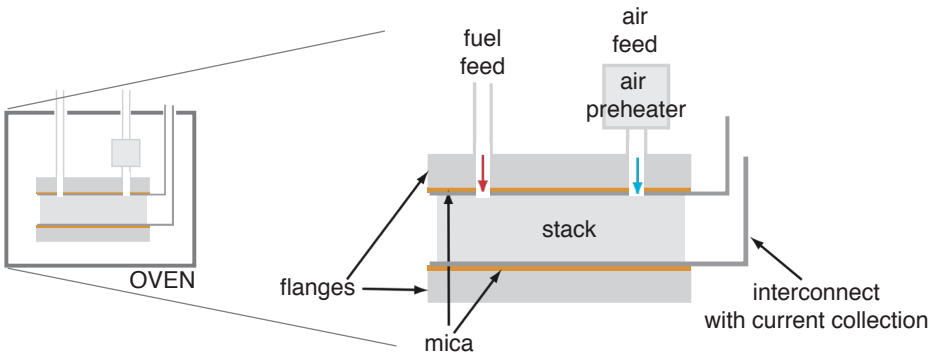

Figure 4.4: Set-up for stack and repeat element testing

fuel side with an appropriate tube length and on the air side with a large radiative heat exchanger where enhancement mixing devices are placed in order to increase heat transfer. Current collection is done through top and bottom interconnects. Each cell potential is monitored separately. Temperature of the inlet gases are measured just before the stack inlet. Usually, an extra thermocouple is placed in the oven. In standard tests, no other temperature is monitored. Characterization is carried out using an active load (Agilent 6060 or TDI EL1000) and, when necessary, a voltage source is added to the fuel cell to ensure sufficient working potential for the active load. The main points for the stack and repeat element testing procedure are:

- warm-up from room temperature to 700°C in 4 to 6 hours with a small amount of air flowing.
- introduction of reactants. First the air flow is set to ca. 1 l/min. Then fuel dilutant (argon or nitrogen) is introduced on the fuel side to purge the air and 30 minutes later the fuel is progressively introduced. For first operation, the anode has to be reduced and OCV takes ca. 1 hour to stabilize[1]
- first polarization of the cell, generally a first iV is performed in the early hours. Then the cell or stack is usually set in steady state mode (either potentiostatic or galvanostatic).
- the shut down is usually carried out under diluted hydrogen conditions with a temperature ramp from the operating temperature to the room temperature in 4 to 6 hours. To avoid anode re-oxidation, fuel gas flow is stopped when the temperature drops below 300°C .

[1]Different procedures for the first reduction of the cells have been tested, some introducing the diluted fuel at a temperature of around 350°C : these attempts were not successful though the reason of the less satisfactory performance cannot be attributed with confidence to the starting procedure. The starting procedure described above has been re-applied: its main advantage is simplicity and rapidity

Within the frame of the REAL-SOFC project, the start-up and shut-down procedures are maintained. For the operation, test procedures have been defined and the tests executed within this project follow a systematic test sequence that should allow comparison of the results.

4.2.3 Experimental issues

Experiments used for model validation, either on button cells or repeat elements, are subject to uncertainties and reproducibility problems which are clarified in the following.

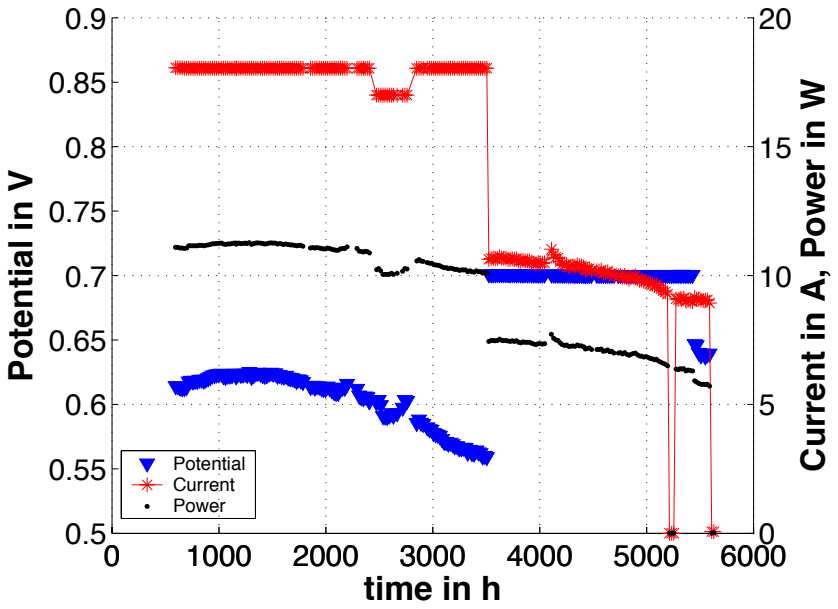

Figure 4.5: Long term operation of a repeat element. Operated at 550 ml/min hydrogen and 2.5 l/min air. During the first 1200 hours of operation, activation was observed. Then degradation.

- Steady state conditions are difficult to obtain while testing cells and repeat elements, due to the activation of the performance during the first hours of operation and then to the degradation processes (figure 4.5). The rate of variation of the performance for a button cell can reach 10% of performance increase in some of the early hours of operation. Two current potential characteristics realized within a couple of hours under the same conditions could therefore lead to significant differences.

- The cell fabrication is carried out by a number of different processes: tape-casting, sintering, screen-printing. Each of these processes has its own range of variability. For the case of the cells used in this study, only small production batches were made and

serious reproducibility problems have been encountered. Within the same batch, the performance of the cells could vary: a test performed at Forchung Zentrum Jülich on 5 cells from the same batch showed that the ASR of the cells had a 20% variability. The variability is probably even larger with different batches. The uncertainty range has not been rigorously quantified.

- The button cell electrochemical testing requires a number of operations likely to induce uncertainties. The screen printed surface of the cathode should be of 1 cm^2 . However, depending on the ink quality the surface may be slightly different. The thickness of the screen-printed cathode layer may vary as well. The current collection is performed by a nickel mesh on the anode side and by a platinum mesh on the cathode side, the latter being applied with a LSC ink to the cathode. During the last year, a reproducibility test has been conducted with 3 cells which were coming from the same production batch. The 3 cells tested under the same conditions exhibited variations of performance of 40%. These tests can therefore hardly be used to identify reliable electrochemical kinetic parameters.

- Finally the test conditions, supposed to be as constant as possible, may differ from one test to the other. As an example, the hydrogen is humidified, however the water partial pressure resulting from humidification may vary from 2.5% to 2.96% for an ambient temperature between 21 and 24°C : this small change has a large impact on the theoretical potential as the Nernst equation is highly non-linear in the low water partial pressure range. The impact of this is however moderated by the species consumption at OCV by the shorting current (figure 3.1(a) in chapter 3).

Experiments are necessary to identify the kinetic parameters; however, due to the above drawbacks, the confidence on the identified parameters is limited. In general, careful experimental procedures can minimize the number of ill-controlable processes such as the application of a wet ink for the current collection in a button cell test. Furthermore, characterizations performed with the purpose of kinetic parameter estimation should be carried out when the performance activation processes of the electrodes occur at a moderate rate but this is unfortunately not always possible because of time constraint.

4.3 Methodology for identification of parameters

In general terms, the methodology which has been adopted to perform model validation is based on parameter estimation methods: i.e. the identification -by means of an optimization algorithm- of unknown model parameters which minimize the error between the model and

the simulation. The parameter estimation problem formulation is introduced in the following and the problems considered are listed.
Model validation by parameter estimation assumes that the model is able, with the identification of some parameters, to represent the experiment. The model validation procedure has to be open to model modification in order to add a phenomenon to the model if a satisfactory simulation is not obtained. During this work, adaptation of the model has been necessary: an example being the addition of imperfect electrolyte behavior to the model to correctly simulate observed OCV. A parameter estimation optimization algorithm based on Non-Linear Programming is used to perform the model calibration and this type of methods is widely used in process engineering. The procedure is briefly described.
The objective function is the likelyhood function which accounts for the estimated standard deviation of the measurement and the sum of squared differences between simulated data and experimental data. The function is detailed in Larrain et al. [2003] and in the annex A.2.1. The objective function does no account for the bias. The first thing to define are the parameters to be identified, these have to be uncertain and the measured values have to be sensitive to the chosen parameters. If the sensitivity of a parameter on the measured values is small the optimization algorithm used (NLP) will not find an optimum. An initial guess is given for each of the parameters as well as the minimum and maximum bound. The initial guess can induce the algorithm to stay on a local optimum, therefore, different initial guess should be tried when possible.

4.4 Validation of the electrolyte behavior

Experimental OCV is generally low, the range of possible values at 750°C going from as low as 930 mV (on a repeat element) and ca. 1070 mV maximum (on a button cell).
Possible contributions to low OCV are:

1. back-flow diffusion from the post-combustion area
2. leakages from the sealing and diffusion of air into the fuel chamber
3. a short-circuiting current
4. a porous electrolyte

The latter has been verified by performing a permeation test at room temperature on a reduced cell (on which no cathode was applied) and the electrolyte was gas tight, similar measurements are reported in Middleton et al. [2004]. The back-flow diffusion alone can not explain a low OCV as the contribution computed by simulation with the worse possible

boundary condition shows a decrease in OCV of only 20 to 30 mV. Back-flow diffusion was used by Costamagna and Honegger [1998] to simulate experimental OCVs in the case of the Sulzer Hexis design for electrolyte supported cells (where post-combustion occurs at the fuel outlet. The agreement was good. Leakages from the sealing certainly contribute to the lowering of the OCV. However post-mortem analysis of stacks revealed that even for repeat element where no sign of leakages was found around the seals, OCVs were below 1050 mV. Further work to verify this is on-going: an advanced CFD model considering the leakages and diffusion though the sealing shows that contribution of leakages can reach 100 mV in some cases (Wuillemin [2005]). The contribution from the shorting current is necessary to explain the experimental OCVs (as deviation can be higher than 100mV).
Experimental OCV on the tested repeat elements and stacks are in the range of 950 to 1050 mV at 770°C , for button cells the range of possible values is the same. These tests are subject to diffusion from the post-combustion zone and leakages from sealing. This range of values for OCV is confirmed by tests carried out at FZJ where square cells of 50*50mm with 16 cm^2 cathode have been tested in a set-up sealed with glass-ceramic. The OCVs from these tests are shown in figure 4.6 where results from HTceramix cells and Forchung Zentrum Jülichcells are reported (de Haart [2005]). The dependence of the experimental values on temperature follows the theoretically expected dependence and the cells can be grouped into two clusters having similar values. For the best cells the measured OCV value is between 20 mV and 40 mV lower than the theoretical value while for the other group of cells values are around 80 mV lower.

The two different groups of values for the OCV could be explained by differences in the

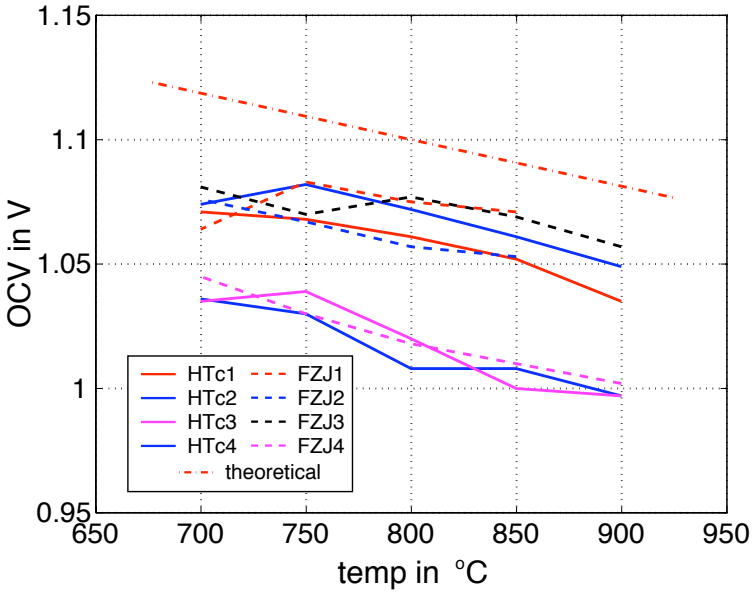

Figure 4.6: Experimental OCV as a function of temperature for cells tested in a sealed set-up

electrolyte thickness. Variability of the electrolyte thickness within the same batch has been

observed for cell batches produced by HTceramix. Specifications on the cells from FZJ for the electrolyte thickness are between 5 and 10 μm . This range may be enough to explain the differences between the cells. This data has been used to quantify the order of magnitude of the leakage current at OCV. Parameter estimation have been performed to identify the range of values for the electronic resistance of the electrolyte. For the cells with the higher values of OCV, the electronic resistance computed is of ca. 40 $\Omega.cm^2$ which gives a shorting current of ca. 0.026 A/cm^2 . For the low OCV values, the electronic resistance of the electrolyte estimated is of 25 $\Omega.cm^2$ giving 0.040 A/cm^2 .

4.5 Validation of the kinetic schemes

The electrolyte behavior has been validated. The model for the electrolyte is the same for the Butler-Volmer kinetic scheme and for the simplified scheme. In the following, parameters for both models are identified.

4.5.1 Identification of parameters with the complete scheme (Butler-Volmer)

4.5.1.1 Button cell test

A model for the button cell test in its set-up has been developed (Larrain et al. [2003]) for the identification of kinetic parameters. The model is able to simulate the temperature variation on the active surface (Larrain et al. [2003]). At high current densities, the local temperature rises from 20 to 30K on the active surface, as reported by Van herle et al. [2001] and confirmed by Larrain et al. [2003]. The model used for the present study has been modified to account for back-flow diffusion and non-perfect behavior of the electrolyte. The parameter identification is therefore possible directly from the current-potential data without transformation of the data into a current-overpotential data to avoid the OCV simulation problem.
The complete reaction scheme presented in section 4.1.1 is used. The parameters to be identified are those for the computation of the electrode overpotentials.
The measurement presented here is a button cell of batch #268 with a screen printed cathode (LSF cathode batch 1.1 from EMPA sintered at 1000°C). Current potential characteristics have been measured on this cell in a short lapse of time (within 6 hours), the cell was operated for less than 100 hours at the time the measurements were made. The performance was not yet steady as a strong activation had been observed (one of the iV was repeated

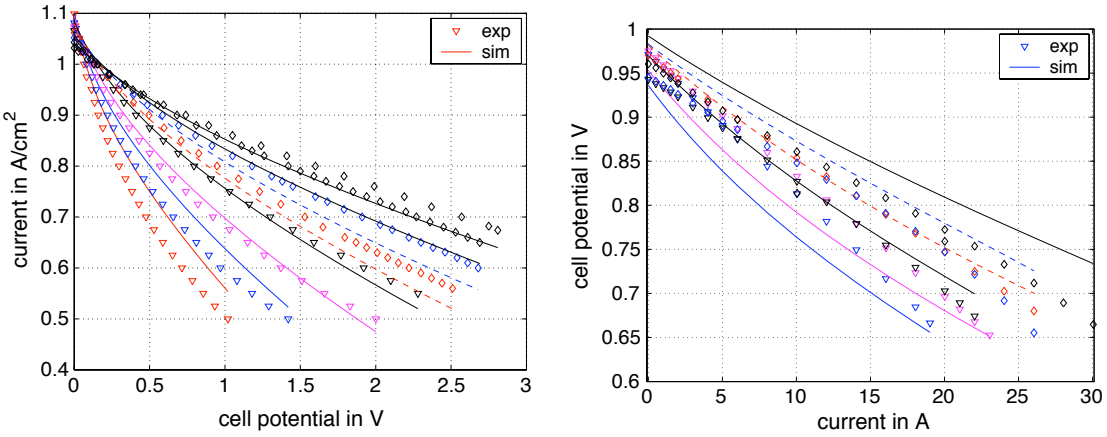

(a) Result for the identification of parameters on a button cell (for temperatures from 690 to 890°C)

(b) Result for the identification of parameters on a repeat element (for 300 and 400 ml/min at 700, 750 and 800°C)

Figure 4.7: Results from parameter estimation for the complete model with Butler-Volmer

and the operating point at 750mV cell potential shifted from 1.03A to 1.2A). The cell was operated with 140 ml/min fuel and 300 ml/min air.

The results from the parameter identification are presented in table 4.1. The comparison between simulated and experimental iVs is shown on figure 4.7(a). The simulated iVs have a satisfactory shape in accordance with the experimental data. However, the errors are significant, deviations being as large as 50 mV. Furthermore the quality of the parameters identified is poor as the confidence intervals are extremely large (table 4.1). By reducing the number of parameters, considering only one activation overpotential for the electrodes, the results are similar.

Despite the confidence interval, the parameters identified in this section for the complete

Table 4.1: Results from the parameter estimation for the complete reaction scheme

Paremeter	optimal value	confidence interval 90%	95%	99%
$E_a{}^{jo^{anode}}$	122.3	58.4	69.7	91.9
$E_a{}^{jo^{cathode}}$	144.8	10.4	12.4	16.4
$k_{jo_e}{}^{anode}$	$1.45.10^8$	$1.03.10^9$	$1.23\ .10^9$	$1.62\ .10^9$
$k_{jo_e}{}^{anode}$	$4.21.10^7$	$5.25.10^7$	$6.26\ .10^7$	$8.25\ .10^7$

model have been implemented in a repeat element model to simulate the behavior of repeat element test #MS19. This repeat element had been assembled with a cell from the same batch with the same cathode. The performances of the repeat element should therefore be predicted by the identified parameters. This has been verified on 3 current potentials

characteristics performed at 770°C oven temperature (measured) with 3 different hydrogen flow rates.

4.5.1.2 Repeat element test

Button cell tests are not performed systematically, and characteristics are usually measured at 2 or 3 different temperatures only. Therefore, in some cases, kinetic parameters have to be identified from repeat element measurements. The experiment used is the repeat element instrumented with thermocouples for which characterization has been performed at different temperatures and different flow rates (chapter 5). The simulation of the experimental current potential characteristics is the first step towards the validation of the temperature profile.
Parameter estimation has been performed with the Butler-Volmer model simplified to one activation overpotential. The fit by the simplified Butler-Volmer model is not satisfactory as errors are large (figure 4.7(b)).

4.5.2 Identification of parameters with the simplified scheme

For better quality of the identified parameters, the simplified scheme presented in section 4.1.1 has been implemented. The results are presented in table 4.2 and figure 4.8(a). The iV curves obtained by this method are linear, even for a button cell test. Hence, for a button cell, the behavior of the experimental characteristics is not well simulated. In contrast, the identified parameters are well defined and the confidence intervals are narrower.
For the case where parameters are identified from a repeat element test, the results are

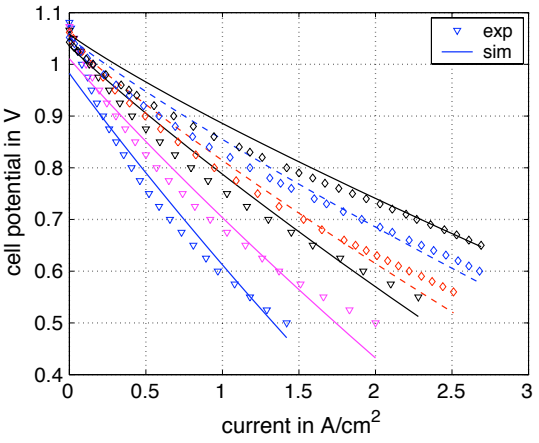

(a) Result for the parameter identification on a button cell

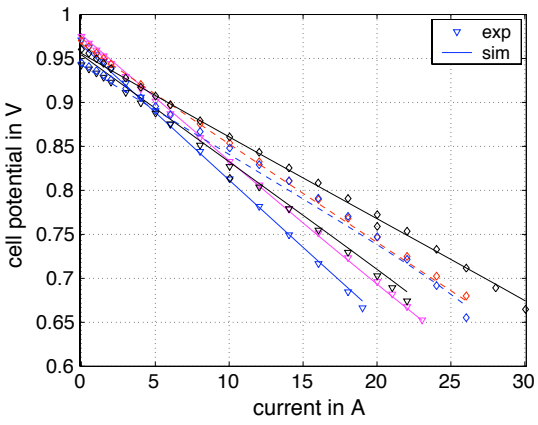

(b) Result for the parameter identification on repeat element

Figure 4.8: Simulated and experimental current potential with the simplified kinetic scheme

Table 4.2: Results from the parameter estimation for the simplified reaction scheme for a button cell

Paremeter	optimal value	confidence interval 90%	95%	99%
C_r	0.36	0.0253	0.0303	0.0401
p_r	-2.469	0.77	0.92	1.21

different and the fit is excellent as shown on figure 4.8(b). The maximum error is in the range of 10 mV. Parameters for this simplified model can be identified from repeat element tests if data at different temperatures is available.

4.6 Discussion

The results presented in the previous sections show that the model is able to predict the repeat element performances if satisfactory parameters are used. This ability was proven by the simulation of the repeat element iV curves in different cases, shown in Larrain et al. [2004] with an even more simplified kinetics scheme.

An important element is parameter estimation. However, the tests performed on button cells and repeat elements do not provide sufficient data to identify reliable parameters for a complete Butler-Volmer scheme. This is not surprising for repeat element tests. The current in a repeat element is not homogeneous and the fit is therefore conducted on the total current, which is an integral value, whereas the Butler-Volmer equation is highly dependent on local conditions (temperature and current density). The button cell tests suffer from the problem that the cells are not at steady-state. It should be verified that for a cell which is operated long enough to reach a steady-state, a characterization with 6 to 8 iV can provide data allowing to obtain a satisfactory fit. The simplified scheme shows results which are not satisfactory for the button cell simulation.

To identify kinetic parameters, the ideal situation would be to have results on half cells to measure separately the contributions from anode and cathode. For cathodes, this is feasible by screen printing the cathode on a thick electrolyte to obtain a symmetric cell. For the anode the manufacturing process (by tape casting) should be conserved as the microstructure depends on the process used.

When experimental data are not available from button cells, repeat element results can be used to identify parameters for the simplified scheme. Results are satisfactory if data at different temperatures are available. The issue with the simplified scheme is that the behavior at high fuel utilization is different than the behavior with the Butler-Volmer scheme. This

has been shown in figure 4.2. The simplified scheme should therefore be used with caution and its use should be avoided for a fuel utilization superior to 70%. In case the only available data are 2 or 3 current potential curves at the same operating temperature with different fluxes, the only parameters which can be identified are a constant resistance aggregating the total losses and the electronic resistance of the electrolyte.
The assumption of an imperfect electrolyte behavior is confirmed, though no rigorous proof is available. The measured OCV in a sealed set-up for our cells show significant deviation from Nernstian behavior and similar values were reported with sealed setups by Simner et al. [2003] and Ralph et al. [2003]. The values for the electronic resistance are in the range of 10 to 40 $\Omega.cm^2$. With such values, an OCV as low as 950mV on a repeat element is simulated. The addition of an overpotential to the kinetic scheme used previously in Larrain et al. [2004] allows the simulation of low OCVs with shorting current remaining in a reasonable range. With the previous scheme (without overpotential) OCVs in the range of 950 mV required an electronic resistance of ca. 3 $\Omega.cm^2$ and a shorting current of ca. 0.3 A/cm^2 which was not realistic. With the proposed model the experimental OCVs for repeat elements and button cells can be reproduced with satisfactory accuracy. The value for the shorting current is an estimate which need to be refined, the problem is that several solutions are possible as the OCV depends not only on the electronic conductivity of the electrolyte but also on the electrode kinetics.

4.7 Conclusion

Kinetic parameter identification has allowed validation of the ability of the model to simulate repeat element and button cell behavior with satisfactory results. However, the need for more reliable and reproducible experiments is clear as the quality of the parameters estimated is poor when the complete kinetic scheme is used.
To obtain kinetic parameters, the strategy depends upon the data available. If button cells experiments are available, identification of parameters for a complete xxxx Butler-Volmer scheme is possible though results may be of poor quality. Simulations should therefore be carried out with caution, particularly at the limits of the temperature range. If the parameters will be used in a repeat element model, the simplified model can be identified from the button cell and implemented in the repeat element model. With data from a repeat element, parameters for the simplified scheme are possible to obtain if data is available with 2 or 3 temperatures of operation.
The imperfect electrolyte behavior has not been fully proven though this phenomenon is most probably contributing significantly to the poor OCVs measured experimentally. The approximate value of the shorting current lies between 0.02 and 0.1A/cm^2 .

Perspectives in this domain would be to adapt the experimental procedures to allow a systematic parameter identification of kinetic parameters for each test performed. This would give more confidence on the parameter and will allow to define different sets of parameters depending on the cell performance. As OCV depends not only on electrolyte properties but also on the electrode kinetics, the collected experimental data could be analyzed to find a correlation between OCV and cell performance.

Bibliography

L. Constantin, R. Ihringer, O. Bucheli, and J. Van herle. Stability and performance of tape cast anode supported electrolyte (ASE) cells. *Proc. of the 5th European SOFC Forum*, 21: 132–139, 2001.

P. Costamagna and K. Honegger. Modeling of Solid oxide heat exchanger integrated stacks and simulation at high fuel utilization. *J. of the Electrochem. Soc.*, 145-11:3995–4007, 1998.

L. de Haart. personal communication of first results on cell tests at FZJ in the frame of the REAL-SOFC project, 2005.

R. Ihringer, S. Rambert, L. Constantin, and J. Van herle. Anode supported thin zirconia based cells for intermediate temperature SOFC. In S. C. Singhal, editor, *SOFC VII, Proc. of the int. Symposium, Electrochemical Society*, pages 1002–1011, 2001.

D. Larrain, J. Van herle, F. Maréchal, and D. Favrat. Thermal modeling of a small anode supported solid oxide fuel cell. *J. of Power Sources*, 114:203–212, 2003.

D. Larrain, J. Van herle, F. Maréchal, and D. Favrat. Generalized model of planar SOFC repeat element for design optimization. *J. of Power Sources*, 1-2(131):304–312, 2004.

H. Middleton, D. Stefan, R. Ihringer, D. Larrain, J. Sfeir, and J. Van Herle. Co-casting and co-sintering of porous MgO support plates with thin dense perovskite layers of $LaSrFeCoO_3$. *J. of the Eur. Ceram. Soc.*, 24(6):1083–1086, 2004.

J. M. Ralph, C. Rossignol, and R. Kumar. Cathode Materials for Reduced-Temperature SOFCs. *J. of the Electrochem. Soc.*, (150(11)):1518–1522, 2003.

S. Simner, J. F. Bonnett, N. Canfield, K. Meinhardt, J. Shelton, V. Sprenkle, and J. Stevenson. Development of lanthanum ferrite SOFC cathodes. *J. of Power Sources*, (113):1–10, 2003.

J. Van herle, R. Ihringer, R. Vasquez Cavieres, L. Constantin, and O. Bucheli. Anode supported solid oxide fuel cells with screen-printed cathodes. *J. of the Eur. Ceram. Soc.*, 21:1855–1859, 2001.

Z. Wuillemin. personnal communication LENI-EPFL 1015 Lausanne. 2005.

Chapter 5

Model calibration by locally resolved measurements

Experiment providing local values for the current density, temperature and concentration are extremely useful to model validation. The validation of a current-potential characteristic on a repeat element does not guarantee that the local current density values simulated are correct. Measurements of local current densities and measurements of local species concentration allow to evaluate the quality of the flow description and kinetic scheme chosen. Local temperature measurements allow to verify the validity of the energy balance equations and the definition of boundary conditions.
This chapter presents first results from two independent experiments:

- a repeat element with a segmented cathode where locally resolved iV characteristics have been performed
- a repeat element instrumented with thermocouples to measure local temperatures.

Both experiments are presented. Then the main results and elements of validation of the models are presented.

5.1 Experimental set-up and results

5.1.1 Segmented cell test

Measurement of local current densities is of great interest in fuel cell experimental research, as current is expected to have a non-uniform distribution over the cell surface for technical

cells (cells of sufficient surface and operated in non-idealized conditions - fuel utilization above 20% -). Similar measurement have been performed for PEMFC by different groups (Geiger et al. [2004], Yoon et al. [2003]) and for SOFC by DLR (Metzger and Schiller [2004]). This measurement requires dividing at least one of the electrodes and current collectors into electrically isolated parts: hereinafter called segments. These segments allow quantification of the current on a much smaller area. Since our repeat element is based on anode supported cells, the segmentation can only be done on the cathode side, as a segmented anode cannot be made when the anode is the mechanical support for the entire cell. Furthermore, as air is fed in excess, a modification of the repeat element geometry has a smaller impact on the air side than on the fuel side. Therefore the interconnect/current collectors and cathode have been segmented into 8 parts, figure 5.1 showing the different segments. On the cathode, the different areas have been created by removing the cathode on a width of ca. 3 mm between each segment. The assembly has to ensure electrical insulation between the segments,

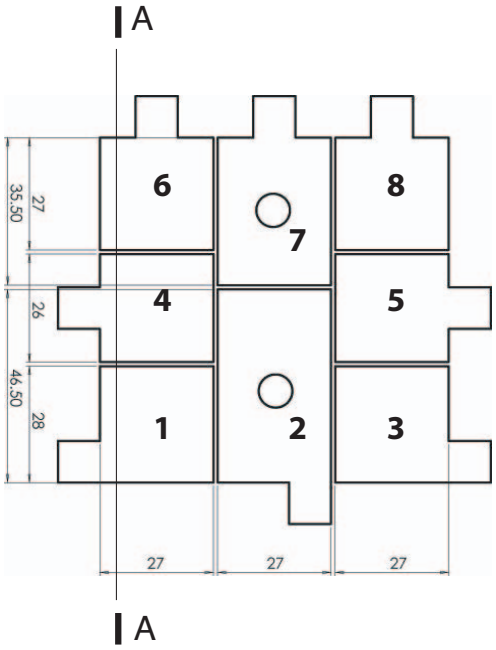

Figure 5.1: Scheme of the segmented interconnect used on the cathode side

minimize the height differences between the segments -to minimize the cell failure potential and to avoid non-uniform ohmic contact resistances -, and perturbations on the flow fields. The cathode assembly has been realized by glueing the 8 interconnect segments on a mica sheet, an underlying metal sheet ensuring the mechanical support for the whole assembly. Between each pair of segments, electrically insulating ceramic paste has been applied in order to avoid displacement of the segments at high temperature (see on the schematic 5.2 which represents a cut through the section A-A on figure 5.1). Each of the segments has a current collector and potential sensing wires. Sensing wires are attached with 10 cm of 0.35

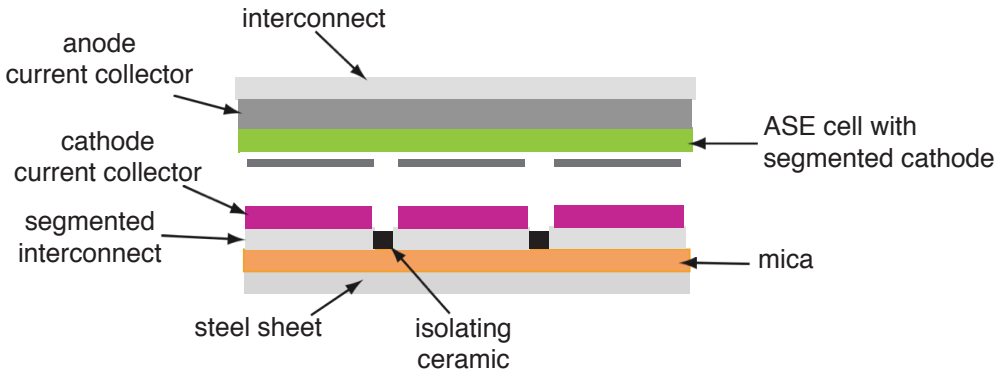

Figure 5.2: Schematic representing the segmented cathode assembly.

mm diameter platinum wire and 100 cm of 0.5 mm diameter silver wire. Current collection is ensured by Haynes 214 wires of ca. 1 mm diameter for all segments except for the numbers # 6, 7 and 8 which are expected to deliver less current and where current collection is ensured by 2 platinum/silver wires (similar to sensing wire). The interconnect used for this experiment is a Crofer 22APU from Thyssen-Krupp (1.5 mm thickness). Fuel and air channels are respectively 0.5 and 1 mm high. The ASE cell is from batch #264, the cathode is from LSF batch 2.2 (EMPA) and cathode current collection layers was of LSC.

To operate the segmented cell, a potentiostat able to reach 40A and a control unit (Zahner

Table 5.1: Areas for the different segments in cm^2

area	1	2	3	4	5	6	7	8
total	6.25	11.44	6.25	6.25	6.25	6.5	8.84	6.5
effective	6.25	9.17	6.25	6.25	6.25	6.5	6.57	6.5

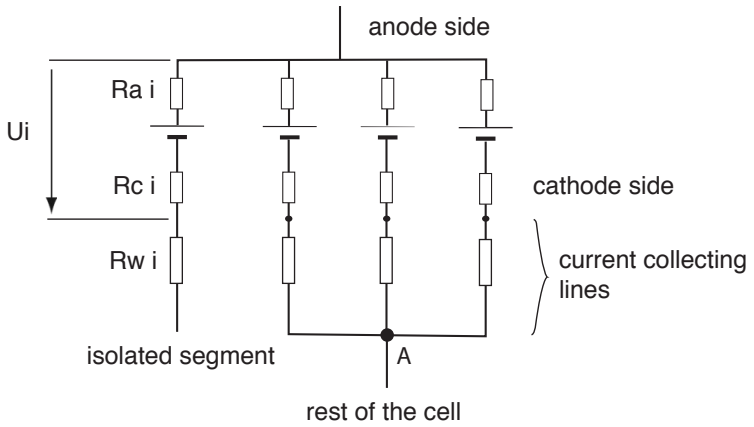

Figure 5.3: Electrical scheme of the segmented cell set-up. R_{ai}, R_{ci} and R_{wi} are the anode, cathode and the current collecting wire resistance respectively.

IM6) combined with a power multiplexer (PMUX) have been used. This device allows to operate the segmented cell in two different modes:

- in the first mode, all the segments are connected and the cell is operated as a normal cell
- in the second mode, one segment can be isolated from the others. In this configuration, the 7 segments are operated in a similar way as in the first mode whereas the isolated segment is measured and polarized individually. Impedance spectroscopy measurements can be performed on the isolated segment as well.

Figure 5.3 shows the electrical scheme of the apparatus in the second mode. The rest of the segments should be operated as a normal cell, however the resistances of the wires R_{wi} are not negligible and the segmented interconnects are not on an equipotential. The equipotential point is at the end of the current lines (at point A on figure 5.3). Therefore, when the whole cell is polarized, the measured potentials are not only the results of the local characteristics of the segment. The cell is indeed not operated as a usual cell because individual segments are not at the same potential. Furthermore, the set-up has another major drawback: the individual currents could not be measured and only the total current value was measured. As a consequence, the only operating points of the segmented cell which were completely defined where those where one isolated segment was polarized while the remaining segments were at OCV.

5.1.2 Local temperature measurement

The temperature field computed by the models is an important output as it affects the electrochemical performances, degradation and cell failure (from the thermal stresses induced by temperature gradients). Validation of the model by specific experiments where emphasis is put on local temperature measurement is therefore useful.
Such measurements have been performed by several authors like Costamagna and Honegger [1998], where measurements have been conducted in the middle cell of a 6 cell stack. Good agreement has been found by these authors between their model and their experimental values. Within our own work, several attempts have been made to measure locally resolved temperature. Only the results from the last experiment are reported, as previous attempts have provided data that were incomplete and of limited use for model calibration.
Owing to the compact design of our stack, with a total repeat element thickness of ca. 3 mm,

measurement of temperature within a stack would lead to serious experimental set-up problems. Measurements have therefore been carried out on a repeat element: thermocouples access the repeat element on the outer face of the interconnects. Furthermore, measuring a repeat element gives an understanding of the test conditions in which the large majority of our experiments has been performed so far. The main problem from measuring temperature in a single repeat element is that the expected temperature gradient is small.

The thermocouples have been set-up to measure the local interconnect temperature; they were placed on the external side of the interconnect. This prevented reactant leakage, perturbation of the flow and risk of cell failure. The experiment has been carried out with K thermocouple wire (0.5mm diameter wire) with home-made spot-welded junctions that have been spot-welded on the interconnect (figure 5.4). Thermal contact and positioning of the thermocouples is therefore satisfactory, the main drawback being the welding of the thermocouple to the interconnect which might have created a third junction and therefore altered the thermocouple accuracy. Positions of the thermocouples are shown in figure 5.5. Most of the thermocouples were placed on the cathode side interconnect, as it had no holes for the air feed and seal problems were thus avoided.

The thermocouple response has been verified at high temperature by 4 steady state points at different temperatures without gases passing through the repeat element. Most of the thermocouples showed a satisfactory response with less than 2% error on the response to a temperature change; thermocouples with larger errors were not considered. Among the thermocouples, three were probes protected with Inconel. They are therefore expected to be more accurate. These were used as reference assuming the temperature was homogeneous on the repeat element surface during the 4 steady state points. The other thermocouples were calibrated on these 3 probes.

Parameters affecting the local temperature profile are the oven temperature, the fuel flow rate, the air ratio, the amount of nitrogen dilutant fed with the fuel. The experiment allowed to carry out current-potential characterisation at different conditions reported in table 5.2.

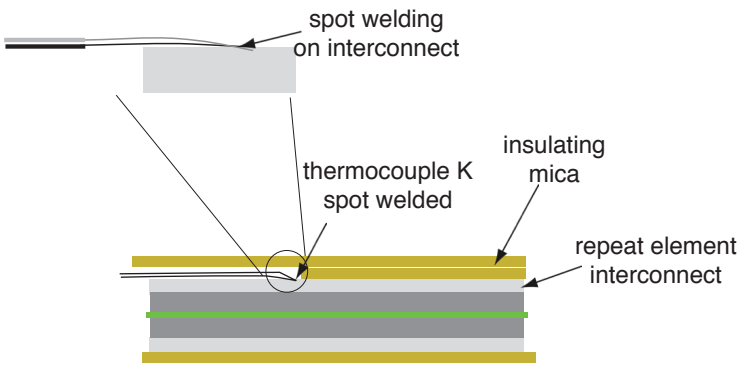

Figure 5.4: Mounting of the thermocouples on the repeat element by spot-welding

Table 5.2: Set of experiments performed on the repeat element with thermocouples

Temp	lambda	N_2	200	250	300	350	400
°C	ratio	ratio (H_2/N_2)		ml/min			
700	2	0.5	x		x		x
750	2	0.5	x	x	x	x	x
800	2	0.5	x		x		x
750	3	0.5			x		
750	4	0.5			x		
750	2	0.3			x		
750	2	0			x		

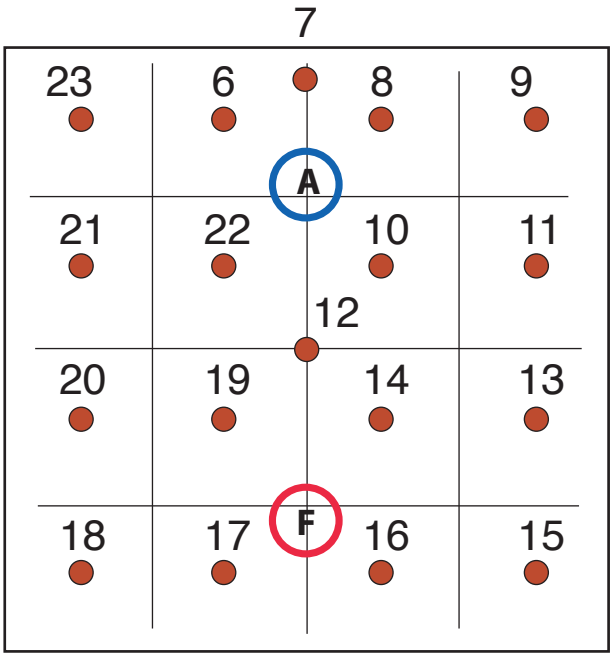

Figure 5.5: Thermocouples position on the cathode interconnect (top view)

5.2 Segmented cell results and model validation

5.2.1 Experimental results

This section presents the results from the segmented cathode repeat element test. The repeat element has been operated for more than 500 hours.
Current potential characterisation has been performed on each of the segments. The consid-

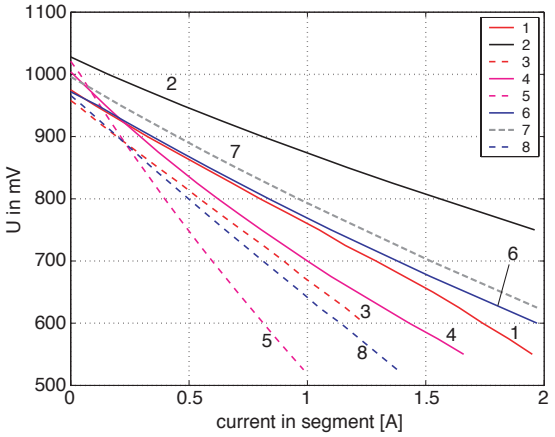

(a) Local current vs potential

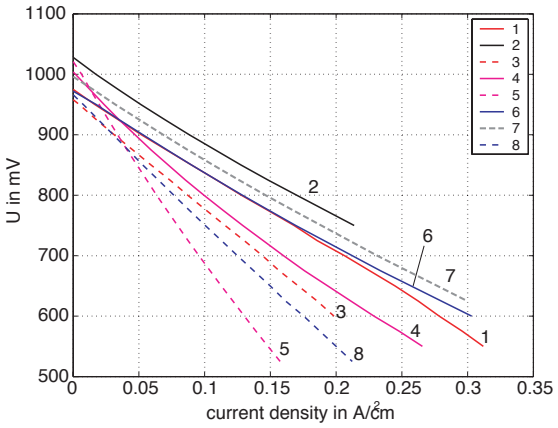

(b) Local current density vs potential

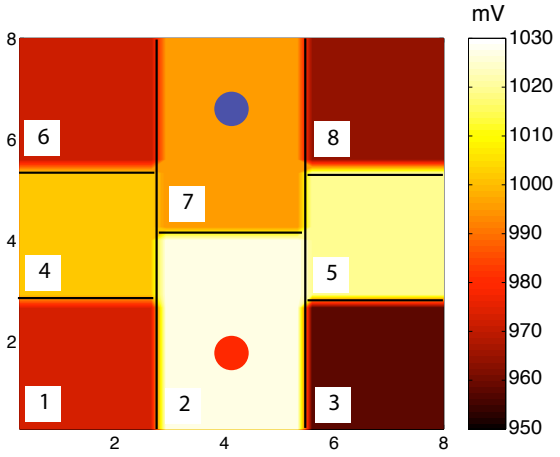

(c) OCV measured on the segmented repeat element at ca. 340ml/min hydrogen and 750°C

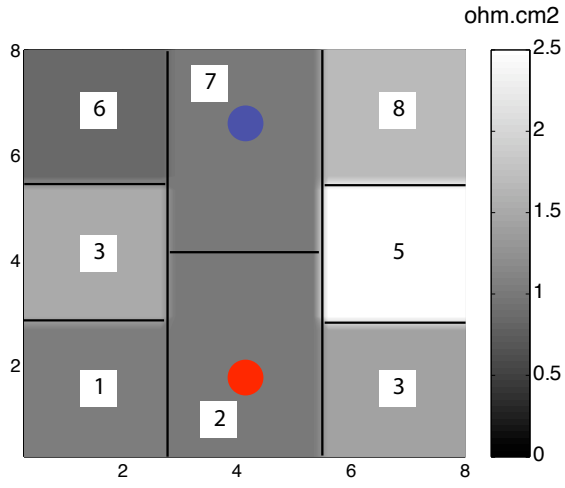

(d) AASR measured on the segmented repeat element at ca. 340ml/min hydrogen and 750°C

Figure 5.6: Current potential characteristics for each segment of the segmented repeat element, the other segments where at OCV. Test conditions 750°C and 260ml/min H2 (to be corrected)

ered experiments have one segment polarized while the others are at OCV. Measurements with the whole cell polarized are not shown: due to a problem in the set-up only the po-

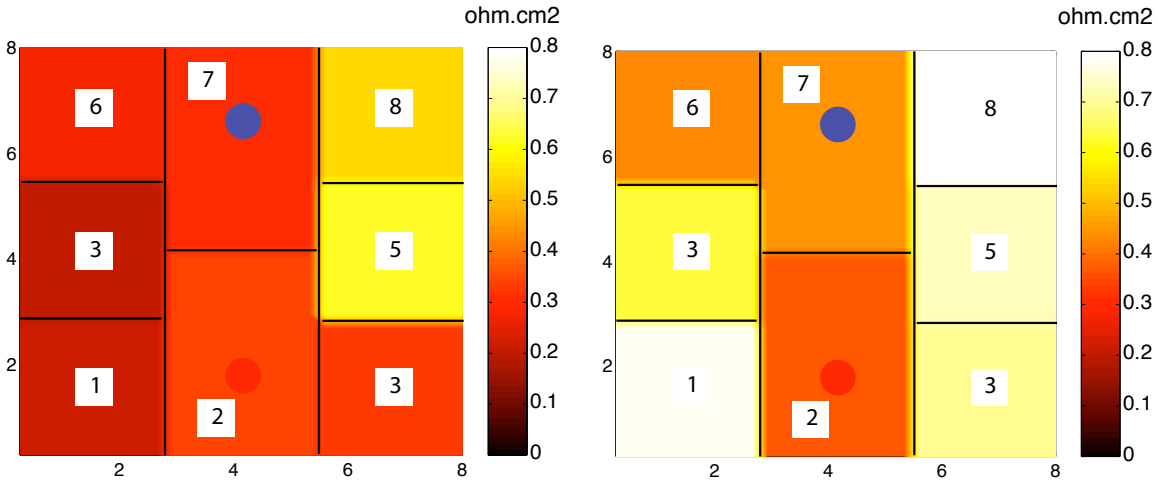

(a) Ohmic resistance by EIS at 800°C and 340 ml/min

(b) Polarization resistance measured by EIS at 800°C and 340 ml/min

Figure 5.7: Segmented cell experimental results. The AASR has been computed from the local polarization of one segment with the others at OCV.

tentials are measured and the local current are missing, therefore, the data is not complete (see section 5.1.1). Results are reported on the figure 5.6. Large differences are measured between the cell segments, reflected in OCV as well as in the apparent area specific resistance of the segments. The apparent area specific resistance (AASR) is defined as the slope of the iV characteristics which can be expressed as an area specific resistance, however the latter is not only dependent on the electrochemical properties but on the flow conditions and concentration,

$$AASR = \frac{U_{cell}@OCV - U_{cell}@I_o}{I_o}.A \tag{5.1}$$

where I_o is the current considered and A the area of the cell or segment in cm^2.
The results and distribution of OCV on the cell surface are reported in figure 5.6(c): the best OCV is found on the segment at the fuel inlet with a value close to 1030 mV (for more than 1100mV theoretical), the next best segments are downstream of this inlet segment (the segments # 4, # 5 and #7 with values in the range of 995 to 1020 mV). The value of 1030 mV is difficult to explain without the consideration of a short-circuiting current at OCV which decreases the voltage and brings some species consumption (section 2.4.1.1). Finally, corner segments show a low OCV (with values in the range of 960 to 980mV), # 1 and 3 close to the fuel inlet, and # 6 and 8 at the fuel outlet. This low OCV can be explained by poor fuel feeding to the corners close to the inlet and the electrolyte imperfect behavior; for the segments close to the outlet, these low values could be explained by diffusion of species from the post-combustion area and by the lower fuel concentration induced by the short

circuit currents at OCV.

The inhomogeneous segment performance is however not fully explained by OCV differences as the AASR of the local iV show differences as well, seen on figure 5.6(b) and 5.6(d). The AASR are quite homogeneous for the segments #1, 2, 6 and 7 (with values of around 1 $\Omega.cm^2$), while the segments # 3, 4 and 8 show much larger values (ca. 2 $\Omega.cm^2$) and finally the largest value for segment 5 (2.5 $\Omega.cm^2$). These differences are confirmed by the results obtained by electrochemical impedance spectroscopy (EIS) and reported in figure 5.7. Ohmic resistance is significantly higher for the segments #5 and 8 (figure 5.7(a)). The polarization resistance is not distributed homogeneously either (figure 5.7(b)). The differences in ohmic losses may be induced by the assembly; if the 8 segments were not exactly in the same plane, the pressure would not be homogeneous and create this difference in ohmic resistance. As for the polarization resistance, the main observation is that the distribution is not symmetrical as segments #3, 5 and 8 show higher values than the corresponding segments on the other side. This is partly confirmed by the non-symmetry observed for the OCV results (segment # 3 and 8 have lower OCV than # 1 and 6). This suggests that the gas feed may be non-symmetrical in the present case; additionally, the difference could be due to a difference in behavior of the border seal. The local iV results show, despite the experimental problems, that the behavior of the cell is not homogeneous on the whole surface, which can mainly be explained by the flow pattern and the consumption of species at OCV by a parasitic current. In the following, the impact of polarization of one segment on the others is studied.

When one segment is polarized while the others are at OCV, the local consumption of

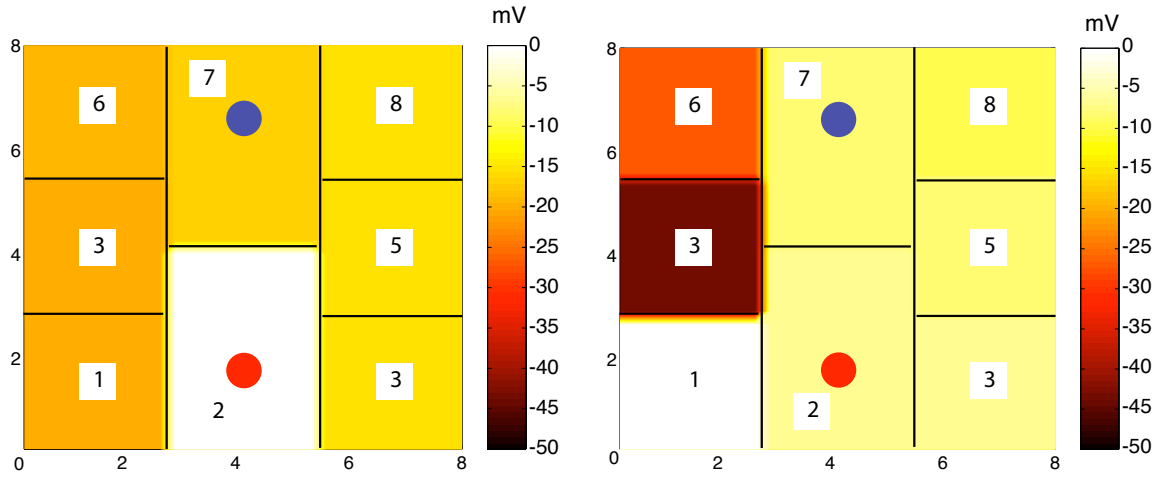

(a) OCV variations on the segment when segment 2 is polarized at 2A

(b) OCV variations on the segment when segment 1 is polarized at 2A

Figure 5.8: Local iV, impact on the other segments and sensitivity to the total current on the 7 other segments

species modifies the fuel and air concentration profiles on the cell and therefore the local OCVs. Results are presented as the variation of OCV of segment j while segment i passes

from OCV to final load (2A). This can be simply described by the equation:

$$\Delta U_{i,j} = U_j^{@I_i=2A} - U_j^{@I_i=0A} \tag{5.2}$$

The impact of the polarization of one segment on the others ranges from a few mV to -50 mV. Two different cases are reported on figure 5.8: 1) the case of the influence of the inlet segment (#2) polarization, 2) the case of the influence of polarization of one of the corner segments (#1). As it can be seen in figure 5.8(a), the impact of segment #2 on the others is quite homogeneous with values around -20 mV. This behavior is expected as all the other segments are downstream from the inlet segment; it has to be noted that the behavior here is symmetrical. On the other hand, the polarization of the corner segment #1 has a strong impact on the segments downstream (with -50 mV for segment #4 and -30 mV for segment #6) and a smaller impact, though non-negligible, on the other segments, explained by diffusive transport. Impact of convective transport is obviously higher but the importance of diffusion in the transport processes is clearly shown by these measurements. Finally, local iV were taken with the rest of the cell either at OCV or polarized at different total currents (from 3 to 8A). The local iV characteristics are only affected by the change in OCV, no significant change on the AASR was observed. The total fuel utilization was quite low for all cases ($< 30\%$) which could explain why the behavior was less affected.

5.2.2 Model validation with segmented cell measurements

The measurements presented in the previous section provide information on the cell potential and current density which has a spacial resolution. The repeat element model has been adapted in order to represent the experiment and perform a model validation. As the model uses the symmetry of the geometry, half of the cell, and therefore only 5 segments are accounted for in the model (see figure 5.9). The modeling of the segmentation has been simply realized by defining 5 different cell potentials for each of the segments. The electrochemical scheme is then defined for each of the segments i by the following equation:

$$U_{cell}^i = U_{Nernst}(x,y) - j(x,y).R_{tot} \tag{5.3}$$

where U_{cell}^i is the potential for a given segment i. To define the current carried by each segments, 5 current density integrals have been defined. The local current or the local potential values can then be assigned to each of the segments. In the real repeat element, a non-negligible surface is covered by sealing around the feed holes. This area is assumed to have a negligible contribution to current. To account for that, the local resistance value has been increased by 2 orders of magnitude to give a negligible contribution in the model outputs.

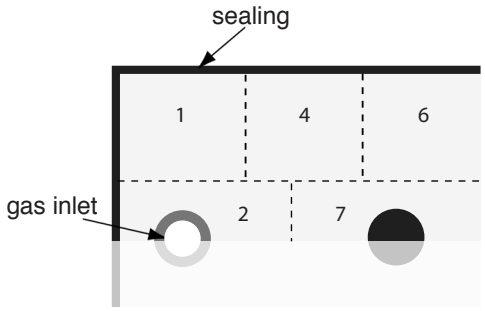

Figure 5.9: Model for the segmented repeat element

Parameter estimation has been performed. The variables which are introduced in the parameter estimation problem are the total ASR of the system $R_{totcell}$ (in a first step the value is assumed to be homogeneous on the whole surface), the electronic conductivity of the electrolyte R_{elec}, which affect the OCV and species consumption (here again the value is assumed to be homogeneous on the cell surface). Finally, as the uncertainty in fuel flow rate was quite large in the considered experiment, it has been introduced as an unknown parameter (flow controlled by rotameter with poor accuracy and fluctuating).
The experiments used in the parameter estimation are the local current potential characteristics on the segments # 1, 2 and 4 (at 770°C oven temperature and ca. 340 ml/min fuel flow rate). As experimental data show strong asymmetry, the values for symmetric segments have been averaged. Owing to computational time for the parameter estimation (which takes ca. 150 hours CPU on a P4 1.4GHz linux), the experimental data has been restricted to these 3 sets of experiments. The variables bounds and optimal values from the parameter estimation are summarized in table 5.3.
The results provided by the parameter estimation give a value of ca. 0.66 $\Omega.cm^2$ for the total ASR of the repeat element and a value of 9.4 $\Omega.cm^2$ for the electronic resistivity of the electrolyte. The latter value is very low and results in strong short-circuiting currents (of ca. 0.1A/cm^2). It has to be noted here that the cell used in this test came from a batch where low OCV have been measured on either button cells or repeat elements (985mV at 750°C for a button cell, and 935mV at 790°C for a standard repeat element operated with 350 ml/min). The 95% confidence interval for these two values is narrow. As for the fuel flow rate, the optimal value reported is on the higher bound. Finally the chi-2 statistical test (returned by the optimizer) which tests the adequacy of the model to the experiment (Rao [2002] and Cox [2002]) returns a lack of fit. The results from the parameter estimation show that the model could be not-fully adapted to represent the experiment. More details are given in the following.

Experimental local OCV and simulated OCV are presented on the figure 5.10. The local iV has been simulated and is compared to the averaged experimental data. Figure 5.11(a) shows the AASR obtained by simulation and experimentally. The order of magnitude of the

Table 5.3: Input values and results from the parameter estimation. With these results the Chi-squared test rejects the good fit assumption (sum of residual > Chi-squared reference value: 352>270)

parameter	units	bounds	optimal values	95% interval
R_{elec}	$\Omega.cm^2$	[7 15]	9.4	0.52
$R_{totcell}$	$\Omega.cm^2$	[0.5 1]	0.66	0.12
F_{fuel}	ml/min	[340 440]	415	22

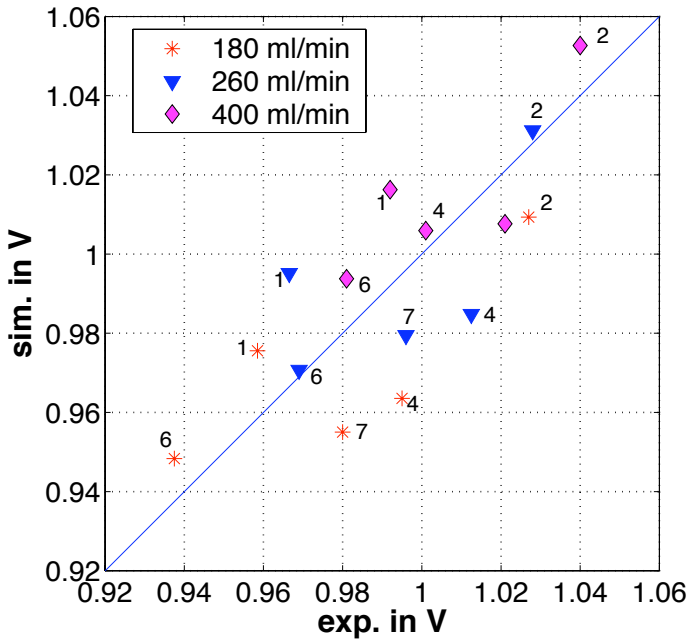

Figure 5.10: Simulated OCV vs experimental OCVs at 750°C for 3 fluxes

AASR is well simulated though the simulation tends to underestimate the effective AASR. For segments #4 and 5, the simulated value is much lower, but this error is mainly due to the local ohmic loss which was significantly higher for the segment # 5. In order to better simulate the experimental data, the value for the total ohmic resistance should be considered as non uniform over the different segments as well.

Comparison of the influence of polarization of one segment (segment #4) on the others is reported in figure 5.11(b). The comparison shows that the model overestimates the impact of the downstream segments by 35%, whereas for the upstream segments the influence is underestimated by ca. 40%. This result suggests that the real flow pattern is not perfectly represented by the model and this can be explained by some model assumptions but also from the apparent non-symmetry of the flow in the experimental repeat element. Finally a imperfect experiment with leakages on a seal could modify this influence also.

Comparison of experimental data with the simulated case shows a satisfactory agreement

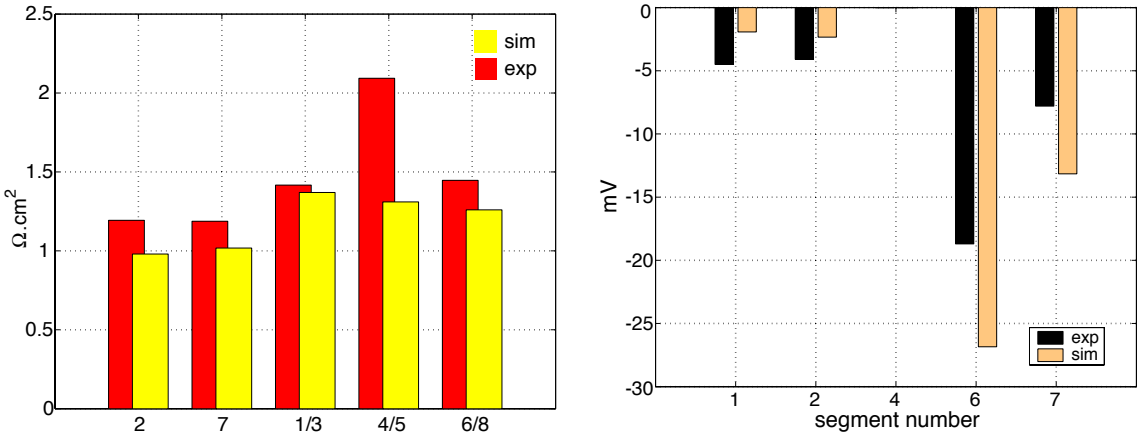

(a) Influence of polarization of segment 2

(b) Influence of polarization of segment 4

Figure 5.11: Segmented repeat element simulation and experimental validation, case at 340ml/min H2 and 750°C

for the local OCV and the local performances of the segments. The discrepancies remaining are observed on a small diffusive effect: the difference could be explained by the simulated flow pattern as well as from an experimental issue.

5.3 Local temperature measurement and model validation

5.3.1 Temperature measurement results

The main experimental results obtained from the first test of a repeat element with local temperature measurement are presented in this section. First, the boundary conditions measured in the test are given. The environment temperature measured in the oven is constant for a given set of operating conditions (oven temperature control value, fuel and air flow rates); the top of the oven was ca. 12°C colder than its bottom; the fuel inlet temperature is constant as well. The air inlet temperature shows a small linear decrease with the load current. This decrease is small as 2°C variation is observed between temperatures at OCV and at 22A at 300 ml/min hydrogen. The temperature gradient measured in the oven is explained by the set-up arrangement where the top insulation plate (which covers the mouth of the oven) is not sealed: metal tubes for gas feed, ceramic tubes supporting the thermocouples and potential wires as well as the current collection metal sheets create

significant thermal losses. The quasi-constant air inlet temperature indicates that the pre-heating device for the air feed works properly.

Given these boundary conditions, which can be assumed fairly constant for each of the iV characteristics, the behavior of the temperatures measured on the repeat element itself is now discussed. Confidence on the measured values may be small in absolute term, as differences of 10 °C could be expected (error typically of +/-1%, i.e. at least +/- 6°C). Nevertheless, the trend of temperature as a function of current should be accurate enough to use the experimental data. From the different measurements performed on the repeat element area, the thermocouples can be grouped in 3 different clusters characterized by a distinct behavior (figure 5.12(a)).

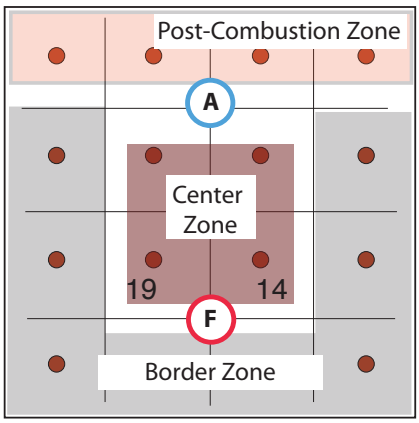

(a) Different zones of behavior

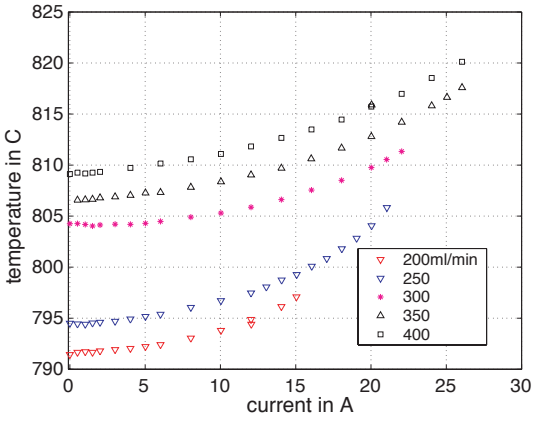

(b) Temperature at the cell center for different hydrogen fluxes at 750°C

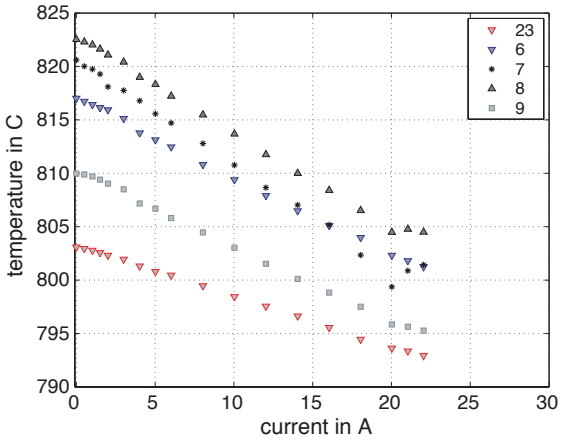

(c) Temperature for the post-combustion side at 300 ml/min hydrogen at 750°C

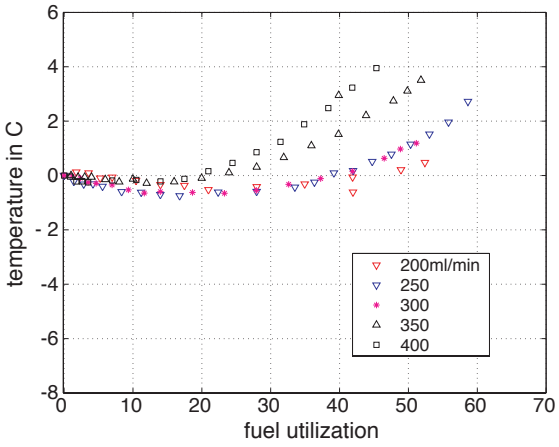

(d) Temperature variation from OCV on the border for different hydrogen fluxes at 750°C

Figure 5.12: Temperature measurements

- Thermocouples which are close to the fuel inlet show a trend of increase in temperature

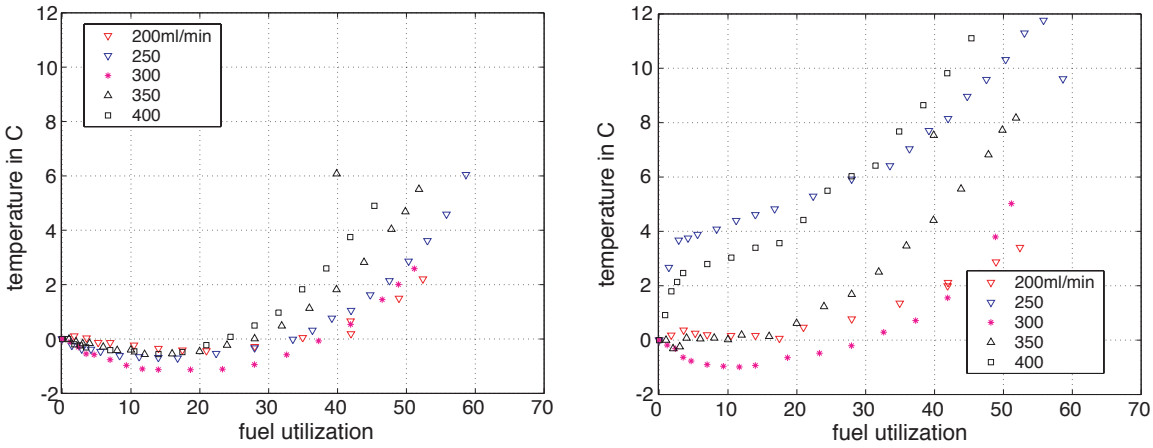

(a) T 19 (b) T 14

Figure 5.13: Non symmetry of temperature measurements

when current is drawn. In this area, the current density is highest and the temperature rise is therefore driven by the electrochemical processes. The observed temperature variation is quite small: at 20A, the increase of temperature is ca. 5-10°C at the cell center (see on figure 5.12(b) where the temperature at position T12 is plotted for 5 different fuel flow rates at constant environment temperature). Thermocouples 14 and 19 show a smaller temperature increase.

- Thermocouples at the fuel outlet are mainly affected by post combustion occuring there and they measure a decrease in temperature with increasing current (figure 5.12(c)). This decrease is logical: fuel utilization increases leaving less fuel for the post-combustion. The decrease is linear, and the maximum temperature and temperature variation is observed at the center of the outlet (ca. 20°C temperature decrease between OCV and full load at 300 ml hydrogen, oven at 750°C). For thermocouples between center and the corner of the outlet, the temperature variation is of ca. 10°C for the same operating condition.

- On the cell border, owing to the strong heat exchange with the surroundings and the lower current densities, small temperature variations are observed. The temperature differences measured by these thermocouples is inferior of 4°C between OCV and full load (figure 5.12(d)).

The temperature measurement presents an asymmetry as thermocouples symmetricaly located on both sides of the geometrical axis exhibit some significant differences. This is particularly well illustrated in figure 5.13 for 2 thermocouples close to the fuel inlet. This asymmetry could be explained by the set-up arrangement where the flanges holding the cell are not centered in the oven or by an asymmetry on the flow field as in section 5.2.1. In fact,

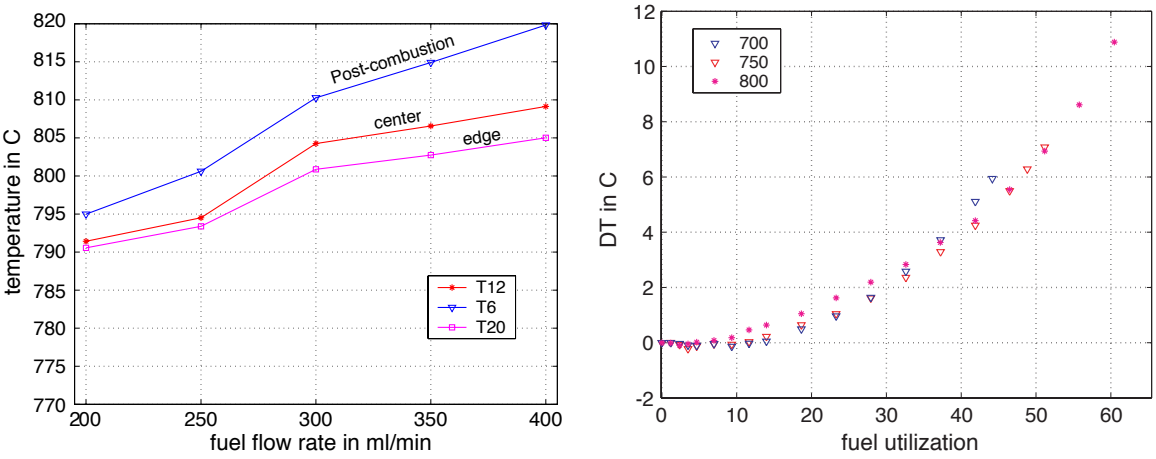

(a) Temperatures in OCV vs. fuel flow rate for 3 different thermocouples

(b) T 12 at 750°C

Figure 5.14: Flow rate and temperature impact on the temperature field

if the interconnect is not perfectly parallel to the cell, this induces a larger pressure drop on one side of the cell and could create a non symmetry flow field. This asymmetry should be verified in future experiments. Sensitivity of the temperature variations to operating parameters is discussed next.

First, temperature variations on the repeat element as a function of current are quite small (10 to 12°C between OCV and a current density of ca. 0.5A/cm^2 -figure 5.12(b)). The small variations in temperature can be explained by the intense heat exchange between the repeat element and its surroundings. This applies both for the edges of the repeat element as well as for its whole surface, even though the flanges from the set-up act like a thermal resistance and moderate the direct exchange. Next, the impact of post-combustion on local temperature has to be noticed. The gradients close to the post-combustion zone are of ca. 20°C on a 2 cm distance at OCV.

On figure 5.12(b), the impact of fuel flow rate and post-combustion can be clearly seen: the whole repeat element temperature rises with an increasing flow rate. The temperature on 3 thermocouples from each of the three zones as a function of the fuel flow rate is reported in figure 5.14(a). In fact, the heat released in the post-combustion area increases proportionally with the flow rate; on the other hand the heat removed by the flow-gases and the radiative exchange increases less (ca. 70/80% rise in the heat losses by radiative exchange for a doubling of the fuel flow rate).

Finally, the impact of the oven temperature on temperature variation is small (figure 5.14(b)). The temperature variation was slightly higher at 700°C : the differences in electrochemical reaction are small as the electrical power output at 300 ml/min hydrogen and 18 A changes from 12.35 W at 700 °C to 13.90 W at 800 °C . The current potential characteristics should have been carried out to higher fuel utilization to show larger differences but this has been

avoided to ensure a sufficient lifetime to the test to be able to perform the complete experimental program.

5.3.2 Validation of the simulated temperature profile

Validation has been performed on several sets of experimental values. The data provided by the local temperature experiment has been selected to keep the most relevant thermocouples: T12 at the cell center, T8 in the post-combustion zone. The thermocouples have been selected either on the symmetry axis or close to it, to neglect the non-symmetry of the data. The identified parameters are the following: 1) "pseudo-emissivity" on the surface of the repeat element (section 2.3.3); 2) the fraction of the post-combustion heat absorbed by the repeat element; 3) an offset value for each of the thermocouples as the confidence in the absolute values is relatively small. All these parameters are identified once basic kinetic parameters are determined. The parameter estimation is conducted on part of the experimental data, the data used are summarized in table 5.4.
For the parameter identification from the segmented repeat element, part of the experimen-

Table 5.4: Experiments used for the parameter estimation with temperature measurements

Temp	lambda	N2	200	250	300	350	400
°C	ratio	ratio (H_2/N_2)		ml/min			
700	2	0.5			x		
750	2	0.5	x		x		x
800	2	0.5			x		

tal data was not used to keep the CPU time within reasonable limits. Here, the model used for temperature calibration is less time consuming and therefore parameter estimation could be performed in 50 hours. The limits and optimal values for the parameters are given in table 5.5. The results indicate that the model appropriately represents the experiment: the Chi-square statistical test accepts the good-fit hypothesis. For the parameter determining the radiative exchange on the surface of the repeat element, the optimal value return an emissivity of 0.235 with a reasonable confidence interval.

The comparison between the model outputs and the measurements is presented in figure 5.15, the data presented is representative of the comparison for other measurements. The change in temperature with the fuel flow rate is not well represented by the model and this creates an offset for some values (figures 5.15(a) and 5.15(b)); this applies to thermocouples in the post-combustion zone or in the middle of the cell. The variations, though, are reproduced correctly as reported in figures 5.15(c) and 5.15(d). On the post-combustion side,

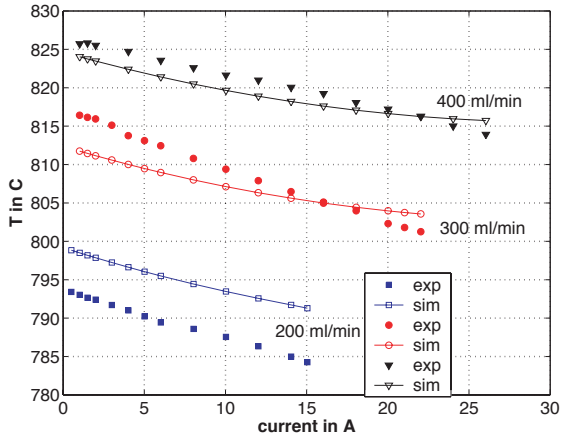

(a) T6 (on the post-combustion) exp. and sim. values at 750°C for 200, 300, and 400 ml/min hydrogen

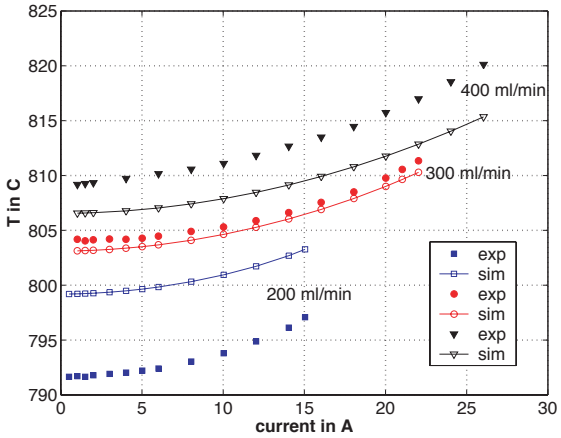

(b) T12 (cell center) exp. and sim. at 750°C for 200, 300, and 400 ml/min hydrogen

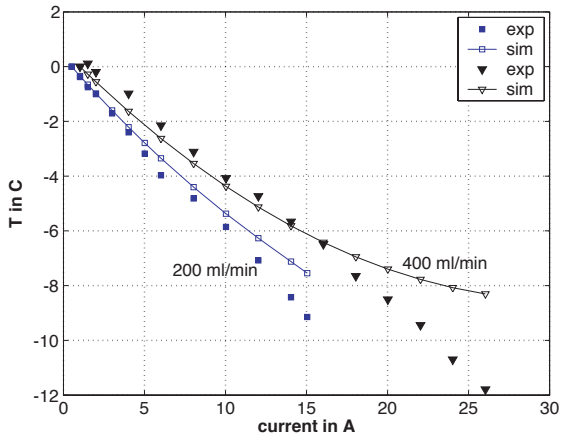

(c) T6 temperature variation from OCV exp. and sim. (at 750°C , 200 and 400 ml/min hydrogen)

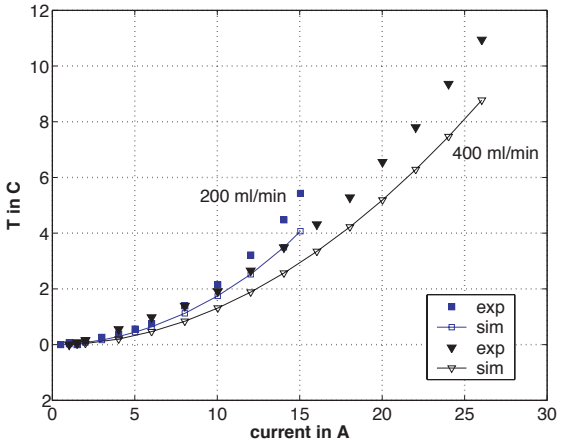

(d) T12 temperature variation exp. and sim. (at 750°C , 200 and 400 ml/min hydrogen)

Figure 5.15: Segmented repeat element simulation and experimental validation

Table 5.5: Results from the parameter estimation for the temperature measurement. With these results the Chi-squared test accepts the good fit assumption (sum of residual < Chi-squared reference value: 296<305)

parameter	units	bounds	optimal values	95% interval
ϵ_z	-	[0.1 0.5]	0.235	0.054
Pcf	-	[0.5 1]	0.795	0.075

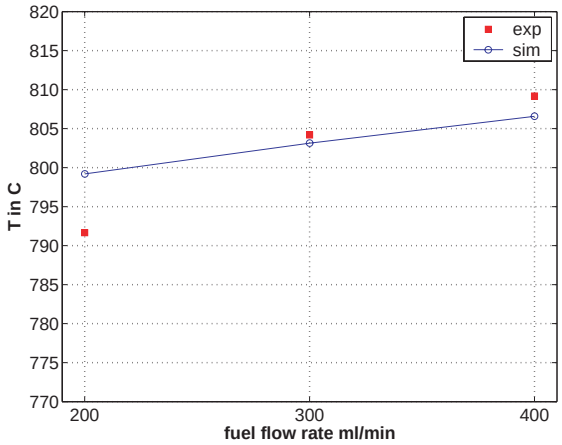

Figure 5.16: Effect of fuel flow rate on the repeat element temperature

the decrease in temperature with current is underestimated by the model at high current whereas experimental results present a linear trend with a constant slope. For thermocouple T12, the increase is well reproduced. Finally, figure 5.16 shows the difference in variation of the temperature at OCV at position 12: the simulated values underestimate the temperature rise with the flow rate. This underestimation of the temperature sensitivity to the fuel flow rate can be explained by several factors: 1) the thermal boundary condition in the oven are affected by the fuel flow rate, and although the thermocouples in the oven did not measure a significant variations, this can affect the experimental temperature; 2) the post-combustion model is very simple, in the experimental case an increase in the fuel flow rate changes the conditions at the post-combustion as the oxidant for this combustion is provided by natural convection in the oven, the stochiometry could change with the flow rate, inducing a change in the combustion temperature.

5.4 Conclusion

Local current densities and local temperature measurement have been performed. Despite the experimental problems and resulting uncertainty on the measurement, these tests have provided useful information.

From local current density measurements, the non-homogeneous behavior of the repeat element is clearly identified, this at OCV and under polarization. The flow pattern has a major impact on the current density distribution. The segments at the inlet performs better than segments at the inlet and outlet corner. The relative importance of diffusion in the transport of species has been demonstrated. The experiment could be improved by allowing operation of the cell in equipotential conditions (an apparatus allowing to work with an equipotential

on the cathode-side is being developed for a future test) and by preventing boundary effects: thus an experiment on a simpler geometry and without post-combustion would increase the confidence on the results and their interpretation.

From the local temperature measurement, the main results are: for a repeat element, the temperature variations are small between OCV and full load; the temperature profile is dominated by the post-combustion on a large area and by electrochemical reactions in the cell center. For this experiment also, boundary effects and uncertainties are significant. A future experiment could be carried out in a set-up designed to have conditions closer to the adiabatic conditions, this would increase the temperature variations.

The model validation has been performed from the experimental data. The model is able to simulate the observed behavior. Parameter estimation has been carried out to minimize the error between the model and the experiments. On the segmented cell test, the main trends are correctly simulated, however some discrepancies remain.

On the temperature measurement, the main behavior is reproduced with satisfactory accuracy as the temperature variations at the cell center and at the post-combustion reproduced within an error of less that 4°C . However, some trends are not well reproduced by the model, namely, the sensitivity of the temperature to the fuel flow rate is underestimated. Further work on the validation of the model could include the set-up flanges in the model: they are likely to participate to the heat conduction in the plane direction and act as a resistance for the radiative heat transfer with the surrounding environment.

The validation with parameter estimation is interesting as it allows use of experimental data from experiments which are not simple and verify the model validity. However, more simple geometries for the experiment would increase the confidence on the procedure as it could allow to include all the experimental data for the parameter estimation instead of using 10% of the available data as it has been done for segmented cell for computing time reasons. Finally the Chi-square statistical test adequation to the problem posed here has to be investigated: it sometimes accepts good-fit when it is obvious that this is not the case. A more appropriate statistical test should be found.

Bibliography

P. Costamagna and K. Honegger. Modeling of Solid oxide heat exchanger integrated stacks and simulation at high fuel utilization. *J. of the Electrochem. Soc.*, 145-11:3995–4007, 1998.

D. Cox. *Goodness-of-fit tests and model validity*, chapter Karl Pearson and the Chi-Squared test, pages 3–8. Birkhäuser, 2002.

A. B. Geiger, R. Eckl, A. Wokaun, and G. G. Scherer. An approach to measuring locally resolved currents in polymer electrolyte fuel cells. *J. of the Electrochem. Soc.*, (151(3)): A394–A398, 2004.

P. Metzger and A. O. Schiller, er. SOFC characteristics along the flow path. In *Proc. of the 6th European SOFC Forum*, pages 989–999, 2004.

C. Rao. *Goodness-of-fit tests and model validity*, chapter Karl Pearson Chi-Square test - The dawn of statistical inference, pages 9–24. Birkhäuser, 2002.

Y.-G. Yoon, W.-Y. Lee, T.-H. Yang, G.-G. Park, and C.-S. Kim. Current distribution in a single cell of PEMFC. *J. of Power Sources*, (118):193–199, 2003.

Chapter 6

Simplified model verification: comparison with a CFD model

6.1 Introduction

The 2D simplified model requires a number of rather significant simplifying assumptions on the flow field definition (section 2.3). These assumptions have been made under the hypothesis that they would not affect significantly the quality of the model outputs, even though some geometrical details are missing and some effects are neglected. To verify this hypothesis, a 3D CFD model for the same geometry is used.
When experimental calibration is not possible, detailed models may be used to verify the accuracy of simpler models. The first step is to verify the sensitivity of the results to the mesh size, this has been done for the simplified model in Larrain et al. [2004] and is not repeated here. The mesh used is fine enough to avoid mesh sensitivity of the results. In the literature similar mesh validations have been performed on a CFD model for a tubular SOFC by Campanari and Iora [2004]. Comparison between CFD model for a planar SOFC and a 1D model has been shown by Gubner et al. [2003], the 1D model allowed an efficient simulation of the stack behavior and has been incorporated into a system model. Dong et al. [2002] simplify the geometrical details included in their CFD model to decrease the mesh size and allow the simulation of a stack. For these cases, the outputs expected from the simpler model were satisfactory. However, this is not always the case as reported by Magistri et al. [2004] where a simple model based on global energy balance (0D model) shows completely different results for some operating points. This illustrates the importance of the proper choice of the level of detail.

6.1.1 Verification of the 3D to 2D downscaling

While the CFD model is in 3D for the fluid and solid volumes (section 2.2), the 2D model does not consider the gradients and profiles in the z direction. The main assumptions of the 2D model is to neglect the velocity profile on the height of the channel and therefore neglect the concentration gradients in the z direction (section 2.3). The flow field is 2D plug-flow. The velocity profile is shown in figure 6.1 and exhibits the typical parabolic profile of laminar flow fields. The concentration profile is shown on figure 6.2. As it can be seem, the gradient in the height of the channel is small and thus the assumption of a plug-flow is reasonable. For the temperature profile, this assumption should be valid in the case of an adiabatic repeat element, as the heat flux in the z direction is zero, temperature gradients should remain small. This is verified and illustrated in the figure 6.3 showing the temperature profile in the symmetry axis in the region close to the fuel inlet. Gradients are small, and the assumption considering an homogeneous temperature in the height is validated.

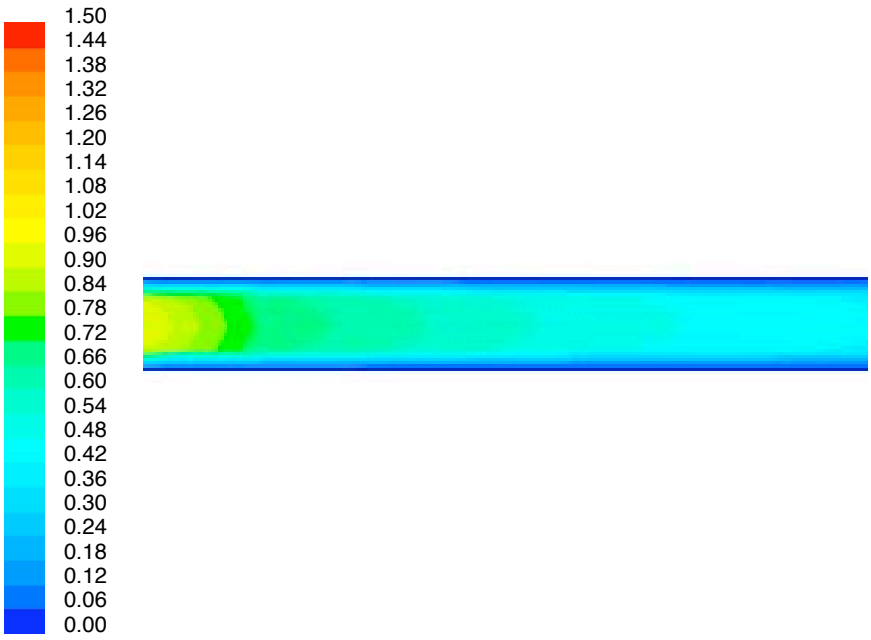

Figure 6.1: Velocity profile near the fuel inlet

6.1.2 Cases compared

The comparison strategy has been determined keeping in mind the main purposes of the simplified model, which are to produce detailed results and insight into the stack behavior (chapter 3). The model comparison assesses if the outputs for velocity, concentration,

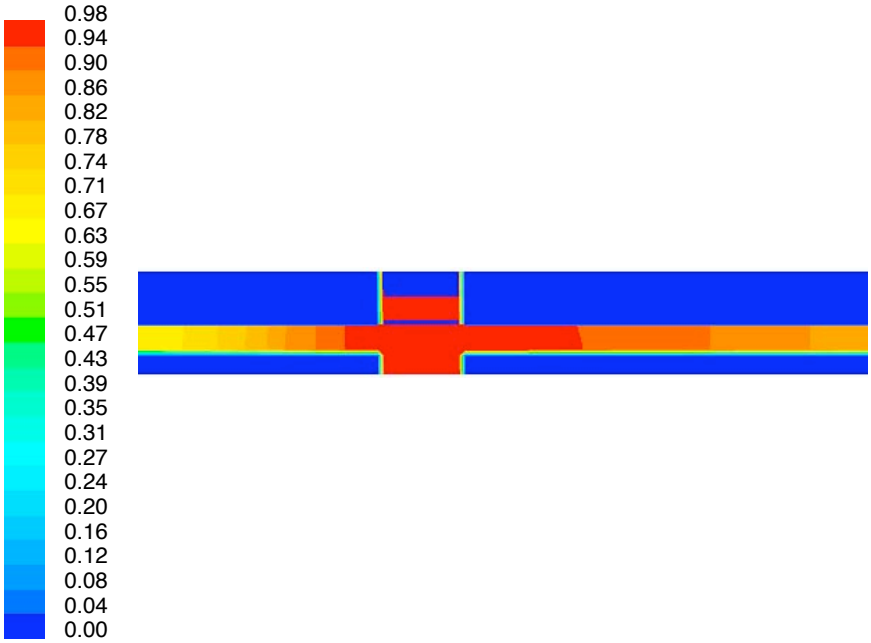

Figure 6.2: Fuel concentration profile near the fuel inlet

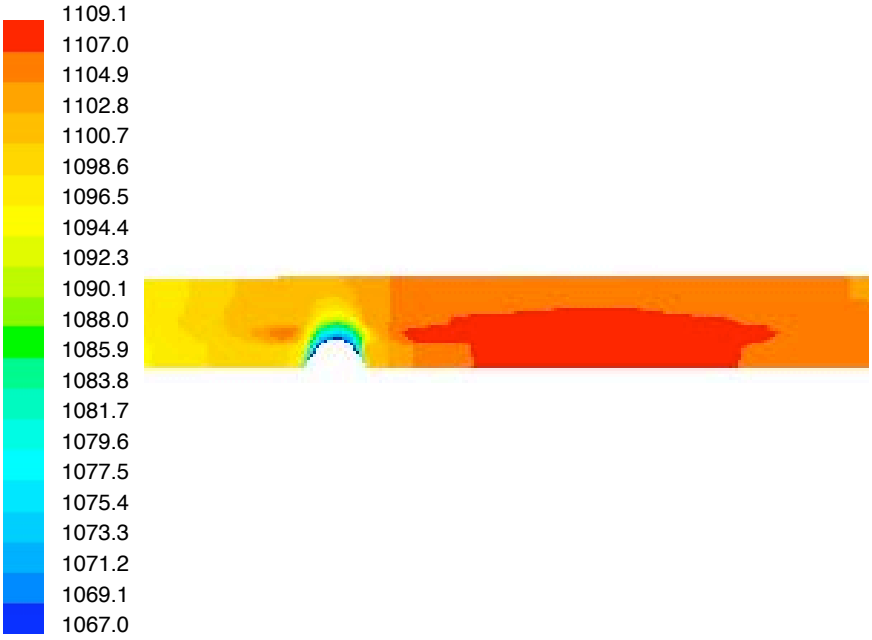

Figure 6.3: Temperature profile on the symmetry axis near the fuel inlet.

current density and temperature field are close to the output from the CFD model. The other main purpose of the simplified model is optimization and sensitivity analysis. For this, the model can potentially simulate a large range of configurations determined by decision variables such as the cell area, the interconnect thickness or the air ratio and the outputs are reduced to performance indicators (section 3.4.1). The verification of this use requires an evaluation of the sensitivity of the indicators to the design variables.
To compare the locally resolved results, the case is the counter flow repeat element, with an area of 50.5cm^2 , an interconnect thickness of 2 mm and a channel height of 1 mm. The same kinetic parameters have been used for both models, the kinetic scheme used in this study is the prior simplified scheme (without overpotentials) presented in Larrain et al. [2004] and Autissier et al. [2004]. The CFD model considered does not account for the post-combustion, as handling the combustion in this area implies a number of problems (choice and reliability of the combustion model, boundary conditions, oxidant feed). Therefore, this has been temporarily removed from the 2D simplified model. Subsequent work is ongoing to include the post-combustion in the CFD model. The operating point is at a usual operating point (300 ml/min hydrogen and air ratio of 2) and the outputs are compared at 30A (70% fuel utilization). The choice of this operating point is justified by the fact that all the fields which have a strong dependence on the reaction rate will exhibit large gradients. Here the focus will be on the validation of the hypothesis that the simplified model does capture the main trends on the distributed outputs.
The validation of performance indicators sensitivity to changes in decision variables is evaluated by performing current-potential simulations for different cases:

- sensitivity to the fuel flow rate is verified by the simulation at 200 ml/min and 400 ml/min hydrogen (air ratio of 2 and 750°C)
- sensitivity to the cell area is verified by the simulation of the same repeat element geometry (with a homothetic scaling on x and y directions) for an area of 40cm^2 and 60cm^2
- influence of the operating temperature is checked by an iV at 775°C
- sensitivity to the air flow rate is verified by iV performed at an air ratio of 3, 4, and 5.

In total, 139 simulation points are compared.
The indicators considered here are the cell potential, the maximum temperature and the temperature at the fuel outlet corner (at $x = 0$ and $y = 1$). Values are compared at the same current.
Criteria for the validity of the indicators are defined in the following. For the cell potential, the accuracy expected from experimental validation is considered satisfactory for a 20 mV

error, potential values are usually in the range of 600 to 800 mV under operation, thus the relative error is of ca. 3% . For a model comparison, the criteria will be defined similarly: the model are considered equivalent for an error in the potential evaluation of less than 20mV. For temperatures, the comparison in absolute values has to be taken with care because for a temperature evaluated at 820°C with the 2D model vs. 830°C for the CFD model, the computation of the relative error with an standard temperature of 0°C or 25°C leads to an error of ca. 1%. In an SOFC problem, the reference temperature is the environment temperature which defines the boundary conditions: therefore the relative errors have to be computed as a temperature variation from this temperature reference. The relative error for the temperature is computed as follows:

$$\epsilon_{temperature} = \frac{T_{2Dmodel} - T_{CFD}}{T_{CFD} - T_{env}} \tag{6.1}$$

where $T_{2Dmodel}$, T_{CFD} are the temperatures computed from the 2D and the CFD model and T_{env} the environment temperature.
For the previous example (820°C with the 2D model vs. 830°C), with a reference temperature at 750°C the relative error is of 12.5%. Here an error of 5% computed on this basis is considered as satisfactory and the simulations cited in this work will meet this condition.

6.2 Comparison of spatially resolved output

In the following, the fields of concentration, current density and temperature in 2D are compared.
For all cases, for which the difference between the fields is presented, the difference is expressed as:

$$diff(x, y) = gP(x, y) - CFD(x, y) \tag{6.2}$$

where $gP(x, y)$ is the output from the simplified model and $CFD(x, y)$ is the output from the CFD model.

6.2.1 Velocity field comparison

The velocity magnitude obtained with both CFD and simplified models is shown on the figure 6.4. For the CFD output (figure 6.4(a)), the velocity is shown on the median plane between the cell and the interconnect for the fuel compartement. The velocity reported is therefore

the maximum velocity. On the contrary, the velocity provided by the simplified model is the mean velocity in the channel height. This explains the difference in the magnitude reported.

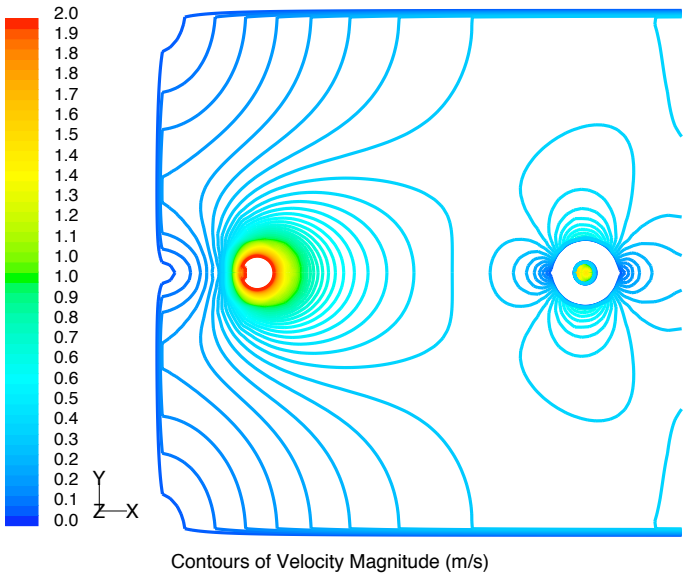

(a) Velocity magnitude on median plane anode side (where velocity magnitude is maximum)

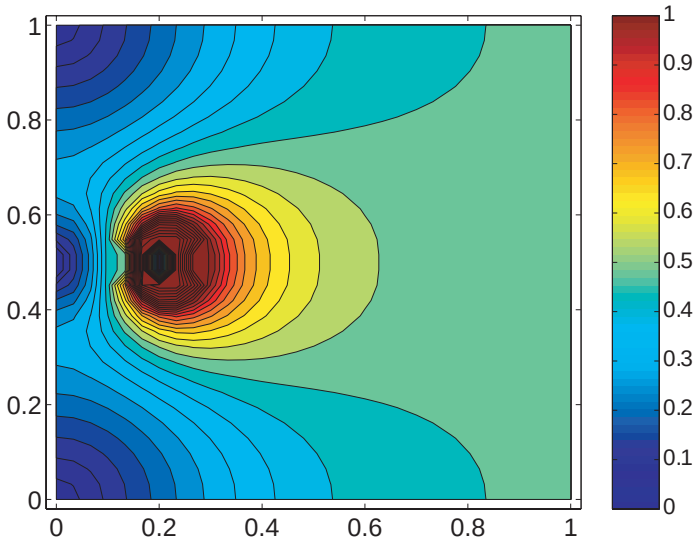

(b) Mean velocity magnitude computed by the simplified model

Figure 6.4: Velocity magnitude comparison. For the CFD model, the velocity is the maximum velocity in the height of the channel while for the simplified model it is the mean velocity: this explain the difference in the scale of values.

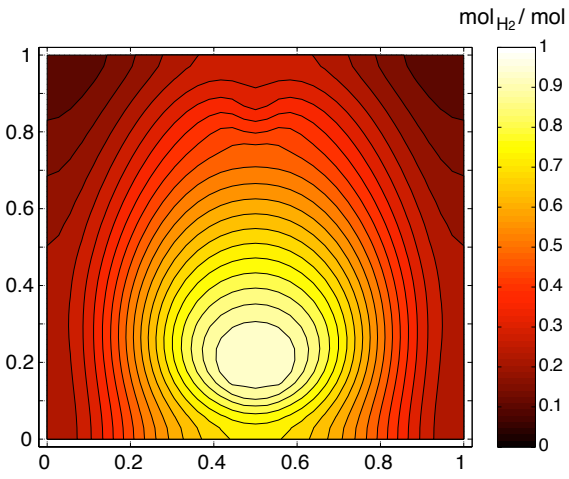

(a) Hydrogen molar fraction field: CFD model

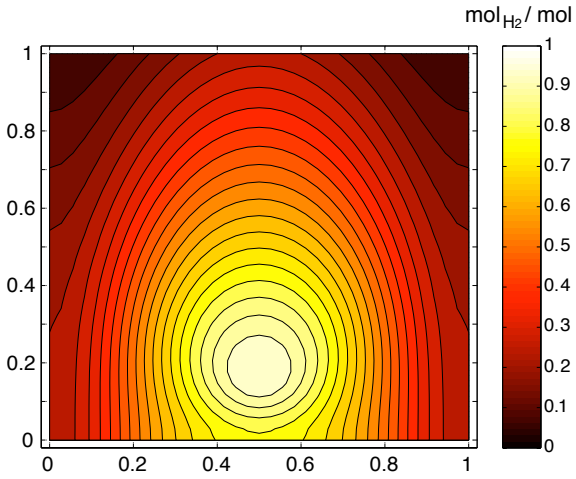

(b) Hydrogen molar fraction field: simplified model

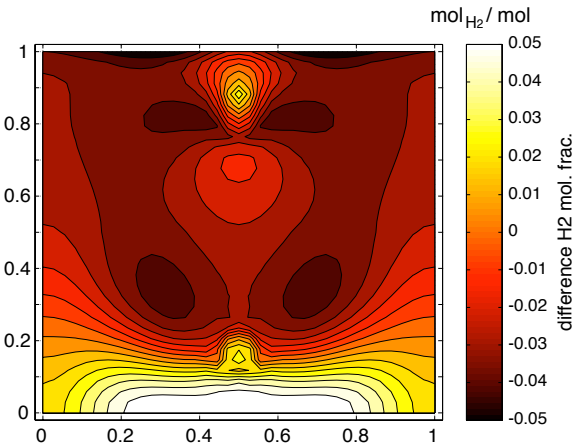

(c) Difference in the molar fraction field

Figure 6.5: Hydrogen molar fraction field from the 2 models at 30A total current

6.2.2 Current density and concentration comparison

The molar fraction and current density fields are compared for the base case at 30A, the difference in the simulated potentials at this point is of 4.8 mV (cell potential is 681mV with the simplified model).

The hydrogen molar fraction profiles are shown on figures 6.5(a) for the CFD model and on 6.5(b) for the 2D simplified model, together with a graph illustrating the differences in the figure 6.5(c).

The corresponding current density fields are presented in figure 6.6(a) for the CFD field and on figure 6.6(b)) for the 2D simplified model and 6.6(c) for the difference.

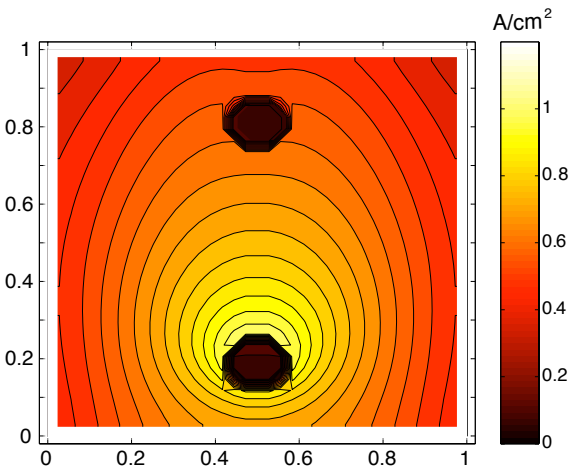

(a) Current density field: CFD model

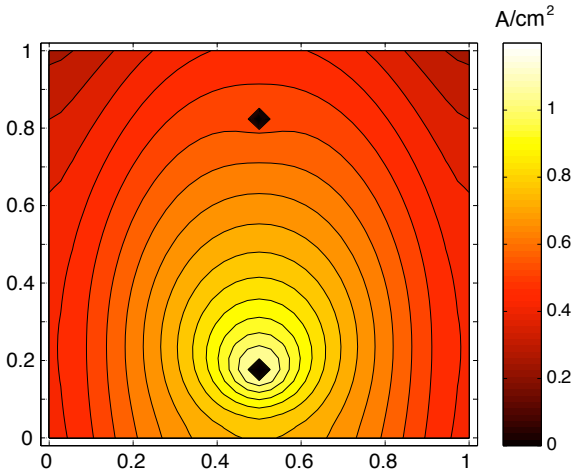

(b) Current density field: simplified model

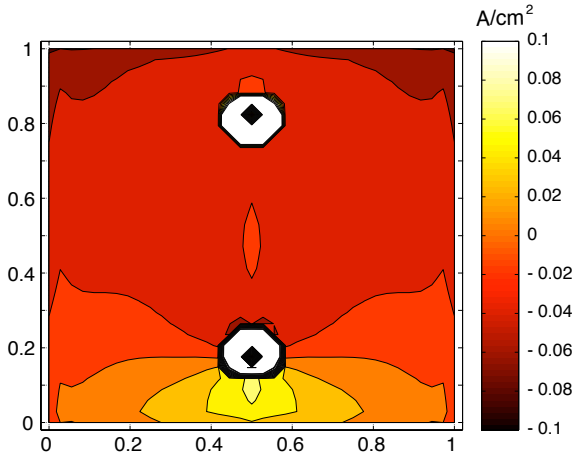

(c) Difference in the current density field

Figure 6.6: Current density field from the 2 models at 30A total current

6.2.3 Temperature field comparison

Figure 6.7(a) and 6.7(b) present the temperature field simulated respectively by the CFD model and the simplified model. For this case, the maximum temperature simulated differs by 2.13°C (the value obtained for the simplified model is 844.2°C).

6.2.4 Discussion on the fields comparison

The velocity, concentration, current density and temperature fields compared present similar trends: the main characteristics of the distributions are predicted by the 2D model. The low

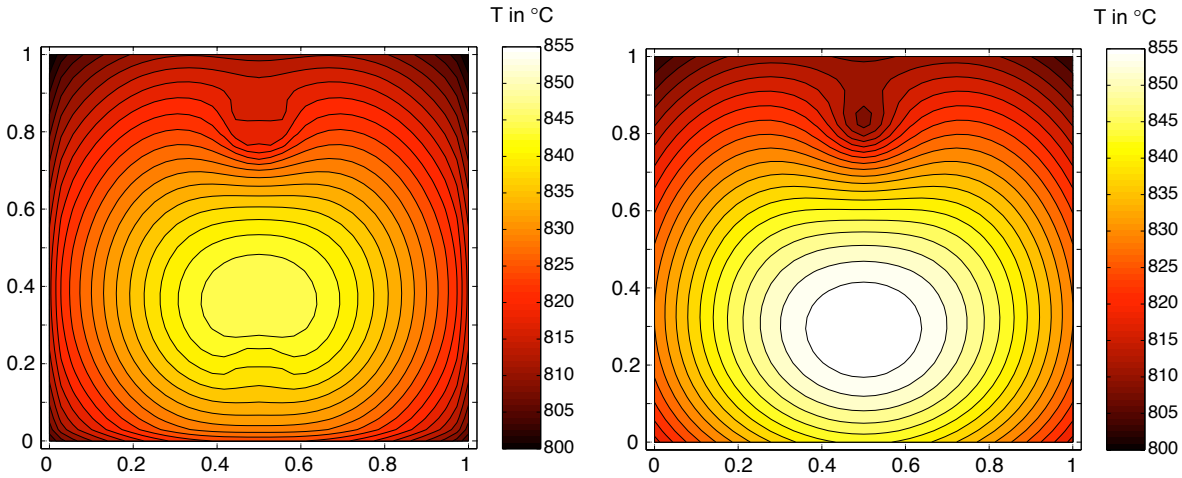

(a) CFD temperature field (in °C)

(b) Simplified model temperature field (in °C)

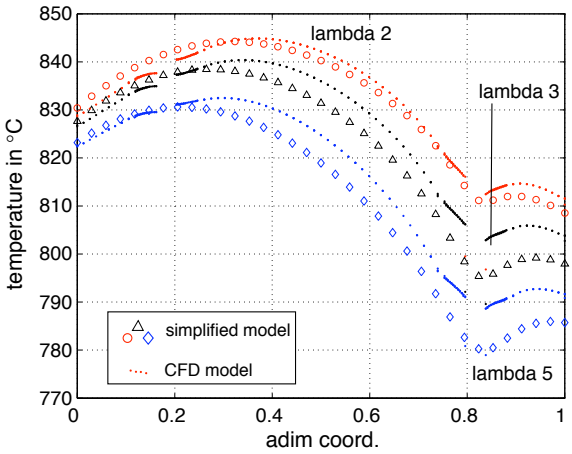

(c) Temperature profile along symmetry axis for lambda 2, 3 and 5

Figure 6.7: Temperature field comparison between the 2 models

velocity at coordinates $y < 0.35$ and the stagnant flow near the corner at $x = 0$ and $y = 0$ is predicted with satisfactory resolution by the simplified model. The characteristics of the concentration field are well predicted too: the lower fuel concentration is predicted in the same location (at $y = 1$ and $x = 0$). Current density and temperature fields are similar as well.

Differences are mainly observed near the inlets as the seals around the inlets for the fuel and air are not represented in the simplified model. Hence the acceleration of the fuel velocity around the air inlet (figure 6.4(a)) is not visible for the simplified model. For the concentration field this geometrical simplification explains the wider region at high concentration for the CFD model at the fuel inlet and the difference in concentration downstream of the air inlet (for coordinates $y > 0.8$ around $x = 0.5$). The current density of the CFD model (fig-

ure 6.6(a)) presents large areas with zero current density, for the simplified model only the point at the inlet is set to zero current (6.6(b)). Finally, temperature profile differences are explained by this inlet region also: on the CFD model (figure 6.7(a)), this region accounts for the seal and thus the thermal conductivity changes around the inlets. This modifies the temperature profile and the maximum temperature location is not predicted rigorously at the same place by the 2 models. The maximum temperature is on $y = 0.35$ for the CFD while it is at $y = 0.3$ for the 2D model and because of this difference in the maximum temperature location, the 2D model overestimates the temperature for coordinates $y < 0.3$. The detailed fields compared in this study present strong similarities: the differences are concentrated around the inlets which are not represented in the simplified model. Despite these differences, the main features of the different fields are captured by the simplified 2D model.

6.3 Performance indicator comparisons

6.3.1 Comparison of current potential curve

Using the same kinetic parameters, both model are expected to produce similar iV characteristics. Figure 6.8(a) shows the results for 3 cases out of the 9 cases performed (section 6.1.2). As expected, the 2 models show similar trends for the iV curves: the potential at a given current is the same, the shape of the IV curve (not fully linear) is similar, and values at high current output are similar as well. Figure 6.8(b) shows the distribution of the differences between the 2 models. In 80% of the simulated cases, the relative error is of 1% and for all the cases the error is below or equal to 2%.
The difference in the simulation of iV curves is small and the simplified model can thus be considered as validated for the simulation of the repeat element performance.

6.3.2 Temperature comparison

Temperature indicators comparison is given here. Figure 6.9 shows the maximum temperature-current comparison for three of the simulated cases. Here again the two models show the same trends for the temperature variation with the current and the differences between the two curves are small. The distribution of errors are shown on figure 6.10(a) for the maximum temperature and on figure 6.10(b) for the minimum temperature. The simplified model generally underestimates the temperatures (for the maximum temperature in 90% of the cases), but the maximum relative error is below 1.5% for all cases.

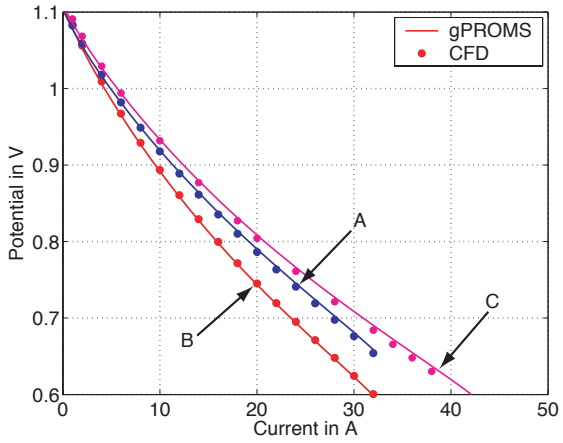

(a) Comparison for current potential characteristics performed with the simplified (gPROMS) and CFD (Fluent) model. A is the base case (300 ml/min H2, air ratio 2), B is for reduced area (40cm^2), C is at higher flow rate (400 ml/min)

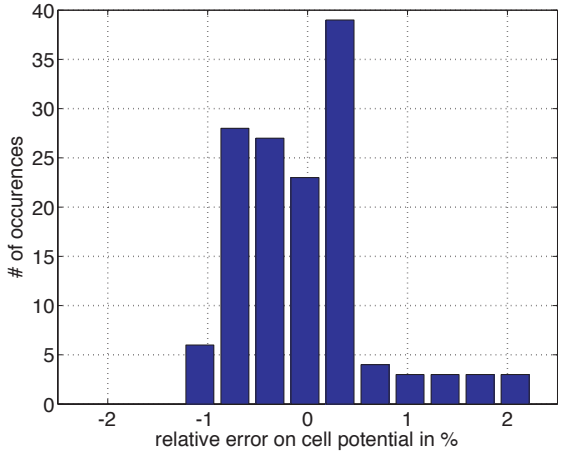

(b) Distribution of the errors between the 2 models for the potential (compared at the same current)

Figure 6.8: Current potential comparison

The evaluation of the temperature indicators and the cell potential (and thus the electric power) is satisfactory: the errors are in range below 2%. The sensitivity to decision variables is therefore validated.

6.4 Discussion

The comparison of the detailed outputs for concentration, current density and temperature shows that the outputs are comparable. The main features of the distributions are captured by both models: lean fuel region, maximum current density and location of the temperature extremes are similar for both models. The discrepancies between the two models are concentrated in regions where the simplified model does not account for geometrical details: this is particularly true for the inlet regions. This weakness of the simplified model is acceptable.
The computational efficiency difference between the two models has to be pointed out: to compute an iV curve with 15 operating points, the CFD model requires from 240 to 360 minutes on a regular Pentium4 1.4GHz Linux PC, while the simplified model requires 15 minutes to compute the same iV curve with 30 operating points. The CFD requires therefore at least 10 times more CPU time. The utility of a CFD model is therefore questionable if the goal of the simulation is to present the output considered here.
To explore the properties and characteristics of a design, the 2D simplified model is sufficient. However, the advantage of CFD is that the detailed modeling can be carried on further: some

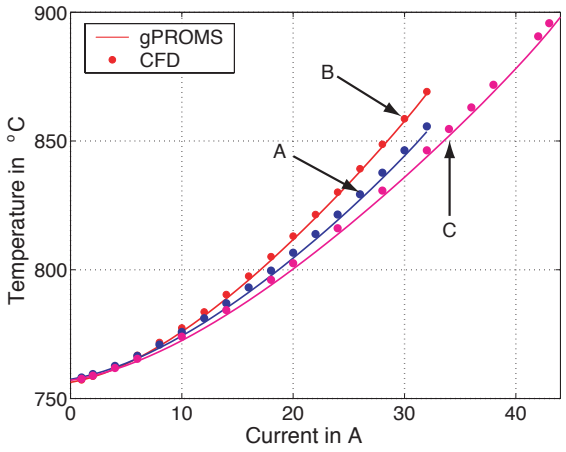

Figure 6.9: Maximum solid temperature vs current characteristics simulated by the 2 models for 3 different cases. A is the base case (300 ml/min H2, air ratio 2), B is for reduced area (40cm^2), C is at higher flow rate (400 ml/min)

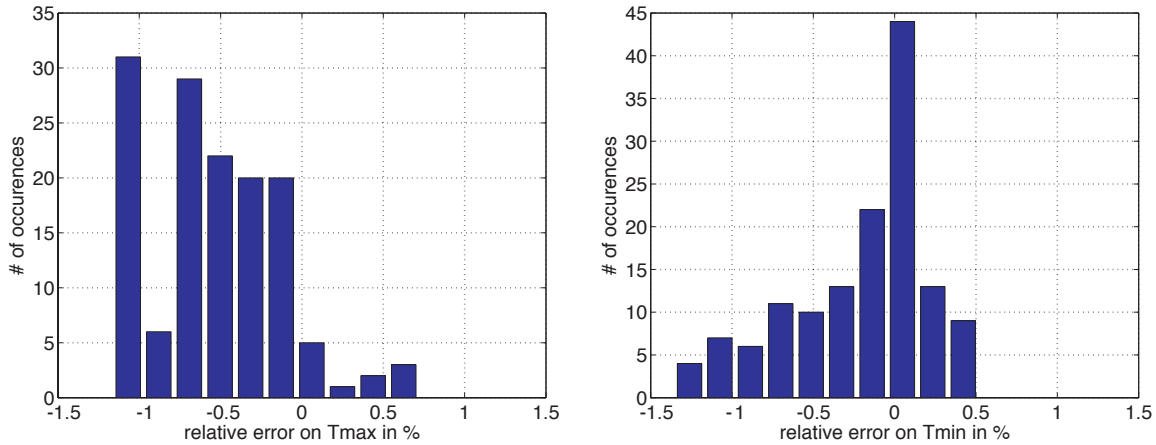

(a) maximum temperature

(b) minimum temperature

Figure 6.10: Differences for the temperature extrema simulation

flow pattern properties are in fact not represented in the current models. The fuel and air channels are here accounted as an isotropic porous media, however the real geometry is most probably not isotropic and it would be possible to account such properties a future CFD model while this would not be possible for the 2D simplified model. Furthermore, CFD can be used to predict internal reforming behavior within this complex geometry while this is excluded from the problem in the simplified model. The prediction of the thermal stresses requires a temperature field from a CFD model, which provides a much more detailed temperature field, particularly in the critical regions around the inlets.

The comparison between the simplified model and a CFD model has been performed for a given geometry. The validity of this comparison can probably be extended to other geometries. The hypothesis that the simplifications done for the 2D model do not affect the

ability of this model to represent the detailed field is accepted. For cases where the reactive area does not include details like the fuel inlets typical for this case (the co-flow case is an example - chapter 3), the results would certainly be improved.

6.5 Conclusion

The 2D simplified model, which relies on significant assumptions on the flow field description and the associated species balance equation, has been compared to a CFD model for a specific geometry. First the CFD profiles in the third dimension (the thickness) showed small gradients, making the 2D simplification reasonable. The local values on the velocity, current density, hydrogen concentration and temperature have been compared for an operating point at high fuel utilization. Results show that the main features of the local distributions are captured by the simplified model, the main difference being located in regions were geometrical details are not represented in the 2D model.
Indicators for the repeat element state have been compared between the two models for more that a hundred operating points. The output of the two models is similar: differences in the power output simulation are less than 3%. Differences on the temperature extremes are always less than 5K. The 2D simplified model is therefore considered as verified. The comparison is in general good and does demonstrate the 2D model veracity.
The comparison has been performed on a geometry that was favorable to identify differences between the 2 models: the flow pattern was complex and the complete geometry could not be represented in the 2D model. The results are therefore expected to be similar or even better for geometries where the flow field in the active area is simpler. The specifications for the 2D simplified model are fulfilled. A recommendation for a future CFD model would be to further increase the level of detail compared to the simplified model.

Bibliography

N. Autissier, D. Larrain, J. Van herle, and D. Favrat. CFD simulation tool for solid oxide fuel cells. *J. of Power Sources*, 1-2(131):313–319, may 2004 2004.

S. Campanari and P. Iora. Definition and sensitivity analysis of a finite volume SOFC model for a tubular cell geometry. *J. of Power Sources*, (132):113–126, 2004.

W. Dong, G. Price, B. Wightman, D. Ghosh, and M. Tabatabaian. Modeling of SOFC stack and system components. *Proc. of the 5th European SOFC Forum*, pages 929–936, july 2002.

A. Gubner, D. Froning, B. de Haart, and D. Stolten. Complete modeling of kW-range SOFC stacks. *SOFC VIII, Proc. of the int. Symposium, Electrochemical Society*, pages 1436–1441, PV 2003-07 2003.

D. Larrain, J. Van herle, F. Maréchal, and D. Favrat. Generalized model of planar SOFC repeat element for design optimization. *J. of Power Sources*, 1-2(131):304–312, 2004.

L. Magistri, R. Bozzo, P. Costamagna, and A. Massardo. Simplified versus detail solid oxide fuel cell reactor models an influence on the simulation of the design point performance of hybrid systems. *J. of Engineering for Gas Turbine and Power-Transaction of the ASME*, 126(3):516–523, 2004.

Chapter 7

Transient behavior of SOFC stack

Simulation of the steady-state operation of SOFC stacks provides insight on the behavior of the stacks at different operating points. However, the target applications for fuel cell systems will most probably require load following, with some applications driven by electrical demand while others by the heat demand. The transient behavior of stacks and systems is therefore of increasing interest and simulation efforts in this area have been increasing lately (Khaleel et al. [2004], Bundschuh et al. [2004], Thorud et al. [2004], Aguiar et al. [2005], Gemmen and Johnson [2005]). The SOFC stack dynamic response is determined by the electrochemical transient response, the fluid and concentration transient response and the thermal inertia, the latter being the slowest. The characterization of the response time to a step change in load is an important result for the system engineering and control.
As reliability of the SOFC system is a priority, transient phases have to be studied to verify that the state of the stack during these phases is not worse than the steady state situation. As some applications may require a fast start-up, the start-up phase is of particular interest. Finally, the influence of design decisions on the transient behavior have to be verified.
This chapter presents results on the transient behavior of the stack. The change in the transient behavior with the configuration chosen for the repeat element is evaluated with the comparison of three cases. Preliminary results on start-up simulation are presented as well.

7.1 Model for transient simulation

Transient simulation requires resolution of time-dependent equations, therefore volume averaged based models are generally applied. CFD models have been used as well, as reported

in Bundschuh et al. [2004]. In this work, as the interest is to perform transient simulation and check the sensitivity of transient behavior to design configurations, the simplified model is used.

The model presented in chapter 2 is modified for transient simulations. The only transient phenomenon considered in our case is thermal inertia: this study deals with the effect of load changes on the temperature response with a time resolution of 5 to 10s . The transient effects on the fluid flow are expected to have a characteristic time of less than 1 s : the residence time is about 0.1s on most of the repeat element surface, but some areas display larger residence times. Transients in electrochemical behavior are neglected as well (time constants are well below 1s), their modeling could nevertheless be interesting for the design of the electrical system (inverter), which is not the purpose of this study.

Therefore, within the presented assumptions, the only modified equation is the energy equation 2.28 for the solid where the thermal inertia is added

$$\lambda_{s_{x,y}}\left(\frac{\partial^2 T_{solid}}{\partial x^2}+\frac{\partial^2 T_{solid}}{\partial y^2}\right)+\dot{Q}=\rho_s.C_s\frac{\partial T_{solid}}{\partial t} \tag{7.1}$$

where ρ_s is the average solid density and C_s the averaged heat capacity of the solid parts. The latter values are computed from the different component and layer properties. Table 7.1 summarizes the main thermal properties introduced in the model. The thermal inertia of the fluid is neglected in this first approach as the thermal mass is several orders of magnitude lower than the thermal mass of the solid parts.

Table 7.1: Thermal properties of the repeat element components

part	heat capacity	thermal conductivity	density	source
-	$kJ/kg.K$	W/(mK)	g/cm^3	
interconnect	500	25.5 (@1100K)	7.8	Incropera and De Witt [1990]
cell	500	10 (@1100K)	6.5	Kawashima and Hishinuma [1996]
RE base case	340	15	4.5	

7.2 Response of the SOFC to a load change

This section discusses first a base case presenting the phenomena. Then, a comparison of transient response for three different repeat element configurations is shown. Finally, measurements of a load change on a repeat element are presented.

7.2.1 Response to a load change at constant flow rate

The response to a load change is simulated for the counter-flow base case in adiabatic and non-adiabatic boundary conditions. The sequence considered is the response to a step change in current from OCV to 26A (65% fuel utilization), the flow rates are not changed during the sequence.

Figure 7.1 presents the evolution of the cell potential and the temperature at 2 locations of the repeat element: one point at the center of the cell and a point in the post-combustion area at the fuel outlet. The potential response to this step change presents an undershoot, the potential during the transient is lower than the final potential. This undershoot has already been reported in previous work from Achenbach [1995] and Aguiar et al. [2005]. This response of the potential is explained by the thermal response. Temperature response is not instantaneous. Respectively 1 and 10 minutes are necessary to reach the new steady state points for the non-adiabatic and respectively adiabatic cases. A similar time response is reported in Aguiar et al. [2005] and Achenbach [1995] for the adiabatic case. Temperatures at the cell center (where electrochemical reaction occur) at the initial state (at OCV) are lower than at the final state, during the thermal transient the electrochemical losses decrease with the increasing temperature explaining the small undershoot in potential. In the repeat

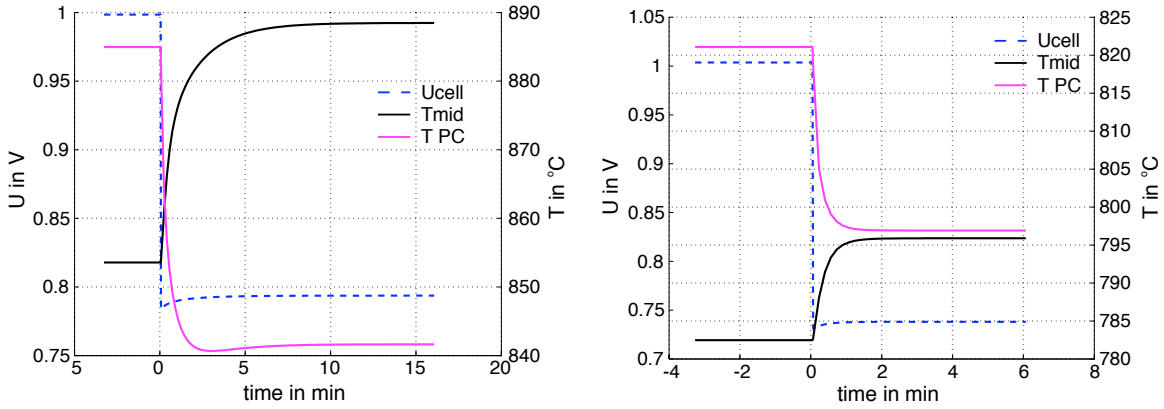

(a) Adiabatic case

(b) Non-adiabatic case

Figure 7.1: Simulated transient response from OCV to 65% fuel utilization. $Tmid$ is the temperature in the cell center and TPC is a temperature in the post-combustion area.

element considered, post-combustion occurs at the fuel outlet; temperature variation depends on the location at the repeat element surface: at the fuel outlet, the temperature decreases as the amount of species to burn drops while in the cell center the electrochemical reaction causes the temperature to rise. The evolution of temperature and current density distribution during the transient are studied next.

Local current density distribution for the adiabatic case is shown 10s after the load change

on figure 7.2(a) and 1000s (ie., in the new steady state) after the load change on figure 7.2(b). The current density distribution is more homogeneous at the beginning of the transient: as temperatures are still low, the losses are higher and therefore the current density distribution more homogeneous than in the final state.
The temperature distribution is shown in figure 7.3. The temperature field appears to be

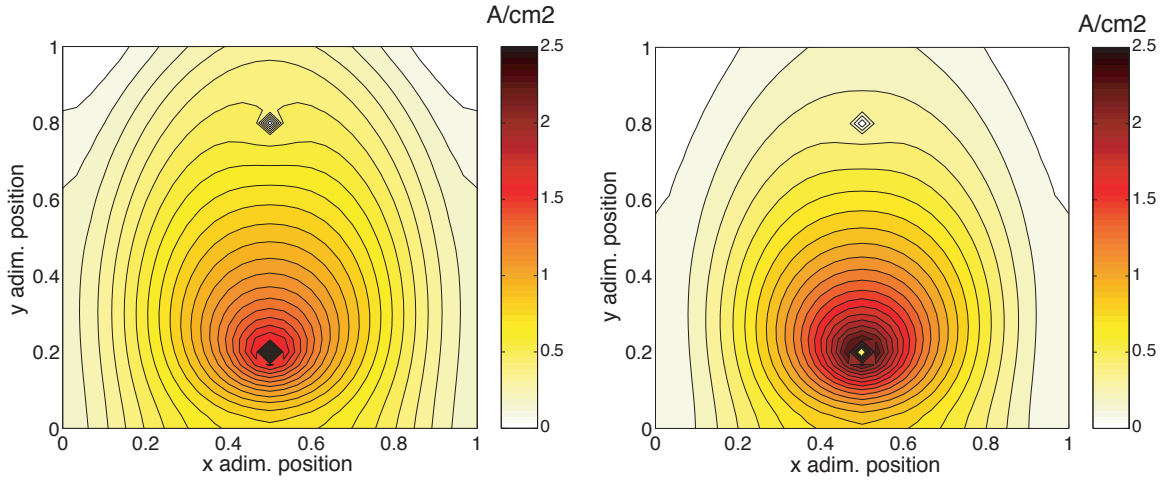

(a) t = 10s after

(b) t = 1000s after

Figure 7.2: Current density profile just after the load change and new steady-state

rapidly modified after 10s: the temperature in the fuel outlet rim has strongly decreased, the effect on the areas in the cell center is not as pronounced. The post-combustion area reacts faster than the cell center: the heat source is more concentrated and the edges are submitted to intense radiative exchange with the environment which limits the effect of the thermal inertia.

Temperature gradients during the transient are reported in figure 7.4. The gradient is reported on a line on the coordinate $x = 0.4$ defined as:

$$\forall y \in [0\ 1]\, and\ x = 0.4 :\ \ grad_T = \frac{\partial T}{\partial y} \tag{7.2}$$

The symmetry axis has been avoided as the geometrical definition around the holes is not sufficient with the simplified model. The temperature gradient during the transient does not appear to be higher than the gradients in steady state mode for the step change considered.

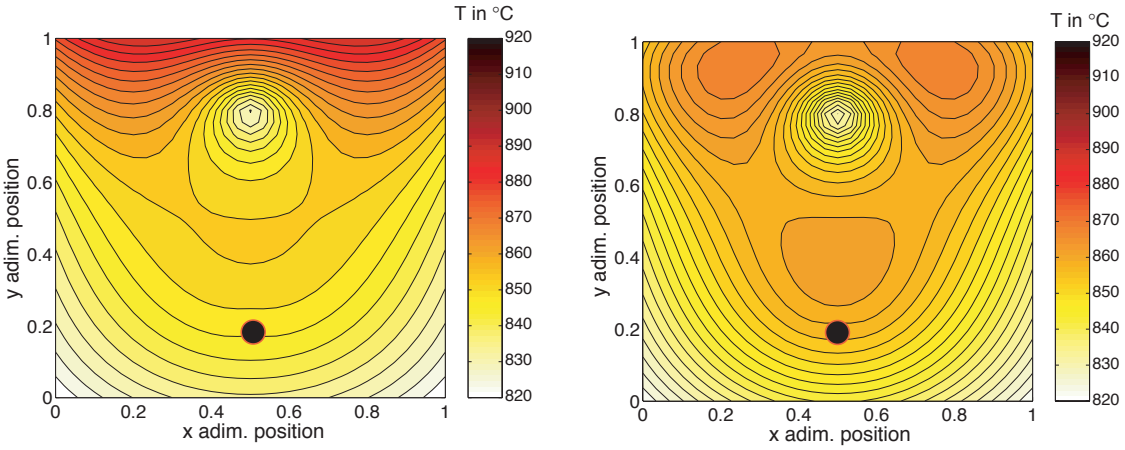

(a) t = -1s (before)

(b) t = 10s (after)

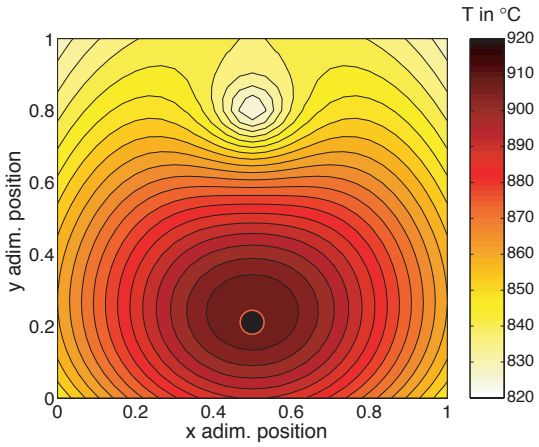

(c) t = 1000s (after)

Figure 7.3: Temperature profile just after the load change and new steady-state (in °C)

7.2.2 Sensitivity of the transient response to the repeat element configuration

The repeat element configuration has a strong impact on the steady-state temperature distribution as seen in chapter 3. This section considers the effect of the configuration on the transient behavior. The cases considered are summarized in table 7.2: case A is the base case for the counter flow repeat element, case B is a compact case where area and thicknesses are lowered, case C is a more conservative case where the area is enlarged and thicknesses are increased. The cases have been compared in a transient from OCV to 18W of electric power, the step change is current driven: the current is increased until the power output reaches 18W. The three configurations are assumed to be possible configurations for the same applications. Since area and temperature of the three cases are different, the comparison is done

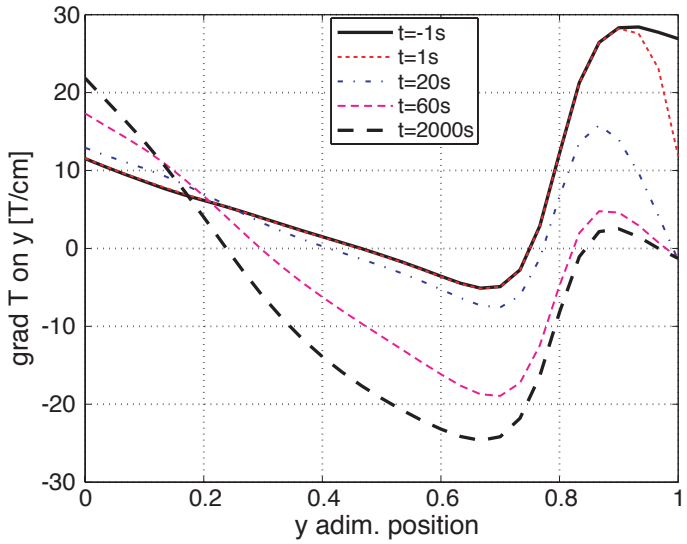

Figure 7.4: Gradient on x= 0.4

at the same power output.

The change in thermal inertia with the different configurations is limited: for the two extreme configurations, the thermal inertia increases by ca. 15% while the power density is multiplied by 3. The reason is the small difference in thermal inertia properties of the repeat element components.

The time response (defined as the time to reach 90% of the final value for the step change)

Table 7.2: Presentation of the 3 differents cases considered

Case	Area	λ	MIC	ChA	dens.	C	cond	Spe	MaxT	time
-	cm^2	-	mm	mm	g/cm^3	J/g	W/(mK)	W/cm^3	K	s
A	52	3	1	0.9	4.127	458	11.5	1.36	890	250
B	48	2	0.5	0.5	3.6	465	9.45	2.2	970	350
C	65	3	01.5	1.5	4.2	455	12	0.72	860	250

for the three cases varies from 250s for cases A and C to 350s for case B. The change in time response is quite small. The configuration of the repeat element has therefore a small impact on the thermal time response to a load change. The behaviors are nevertheless different for the three different cases as seen in figures 7.5, 7.6 and 7.7. For configurations A and B the temperature in the center rises and the post-combustion temperature decreases with a small undershoot. The undershoot in the post-combustion (figures 7.5(a) and 7.6(a)) is due to the fact that the post-combustion reacts faster: when the temperature at the post-combustion is at its minimum the temperature in the cell center is not at the final value. This can be seen in figures 7.5(b) and 7.6(b). For case C, the post-combustion slower reacts slower than the cell center, the cell center presents therefore an overshoot in temperature (figure 7.7(a)):

The temperature difference in the central region is inferior to the temperature change in the post-combustion area for this case owing to better thermal conductivity and lower current densities.

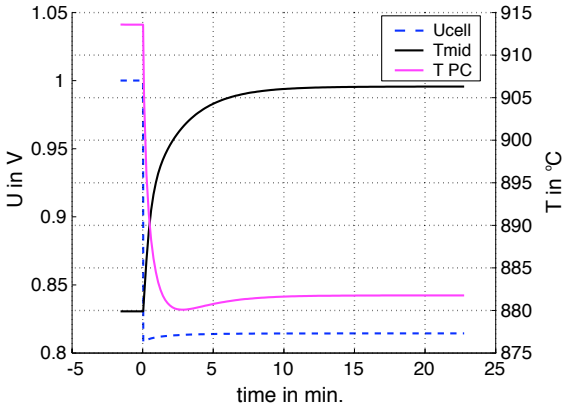

(a) cell potential and temperature

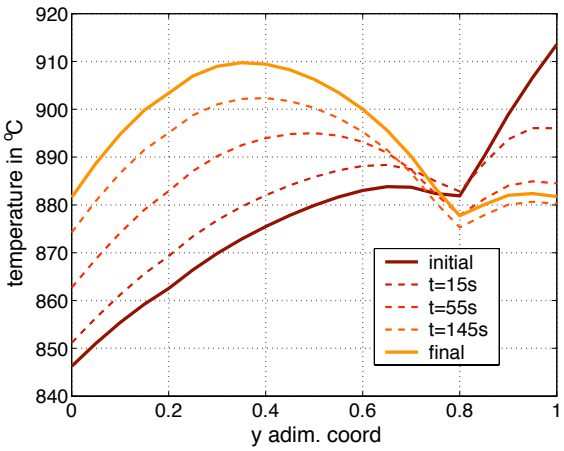

(b) Temperature profile

Figure 7.5: Transient as a function of design: Case A

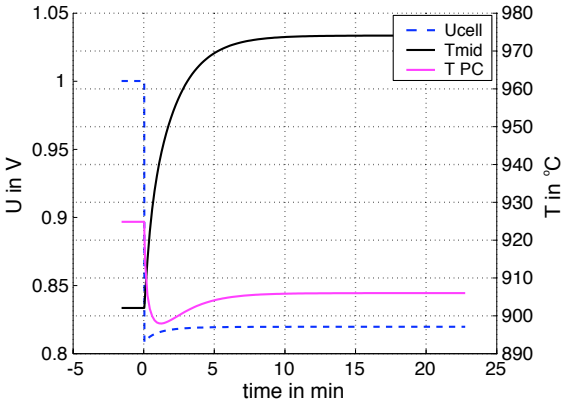

(a) cell potential and temperature

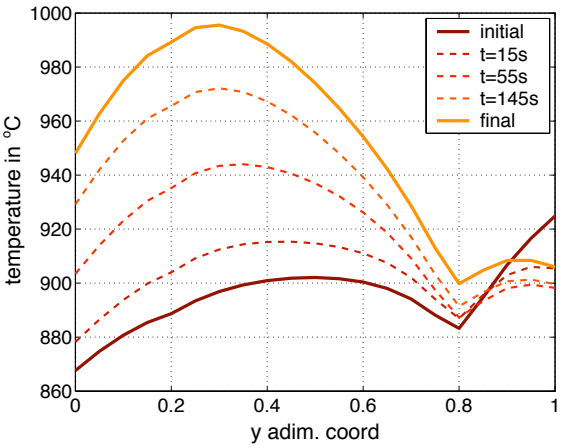

(b) Temperature profile

Figure 7.6: Transient as a function of design: Case B

7.2.3 Load change measurements on a repeat element

Some transient measurements have been performed on a repeat element mounted with thermocouples (see chapter 5). Figure 7.8(a) shows the response to load change from 12A to 20A. The repeat element was operated with 200 ml/min hydrogen diluted with 100 ml/min

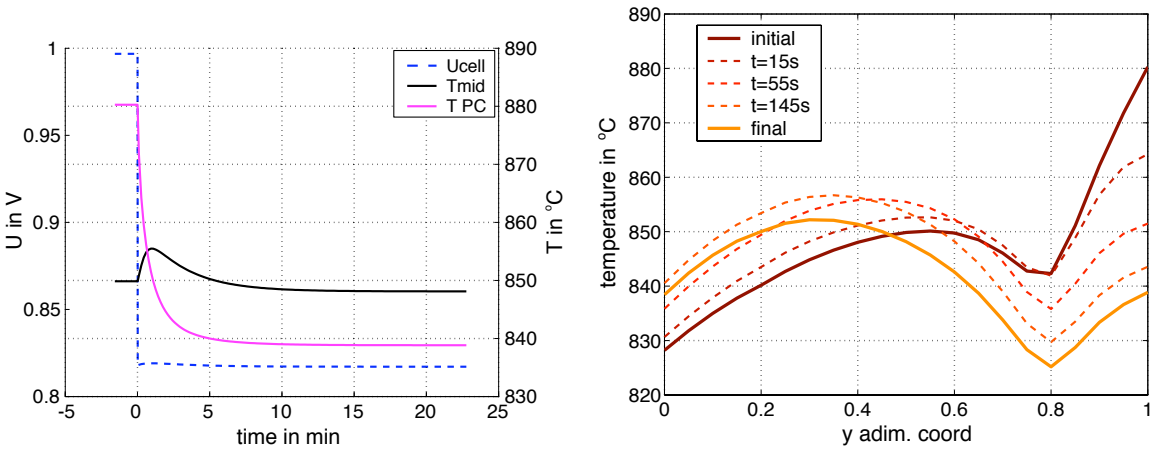

(a) cell potential and temperature

(b) Temperature profile

Figure 7.7: Transient as a function of design: Case C

nitrogen and an air ratio of 2. No undershoot in the cell potential is observed: on the contrary, the cell potential shows a small variation towards lower potentials during the 5 first minutes after the load change. The response in potential is therefore not only explained by a thermal response, at higher potentials (above 0.8V) the undershoot predicted by the simulation can be observed.

As for the measured temperature, figure 7.8(a) shows the response of a thermocouple at the center of the cell (T12) and a thermocouple located close to the post-combustion (T10). The thermocouple in the post-combustion zone shows a decrease in temperature of ca. 8K while the thermocouple in the center shows an increase of 5.5K. The thermocouple in the center shows an overshoot like for C in the previous section. The temperature variations are low as the repeat element is not in adiabatic conditions. The time response of the temperature is quite important as it is in the order of 10 minutes for both temperature reported. The large time response is explained by the thermal inertia of the flanges holding the repeat element. The dimensions of the flanges are important (10mm thick) and their thermal inertia is ca. 8 times higher than that of the repeat element. This transient measurement shows clearly the need to add the set-up flanges to the model to fully validate it.

The simulation of this transient shows a short response time (figure 7.8(b)). The magnitude of the variations is well predicted as expected from chapter 5 where the steady state temperature profile has been validated for the repeat element.

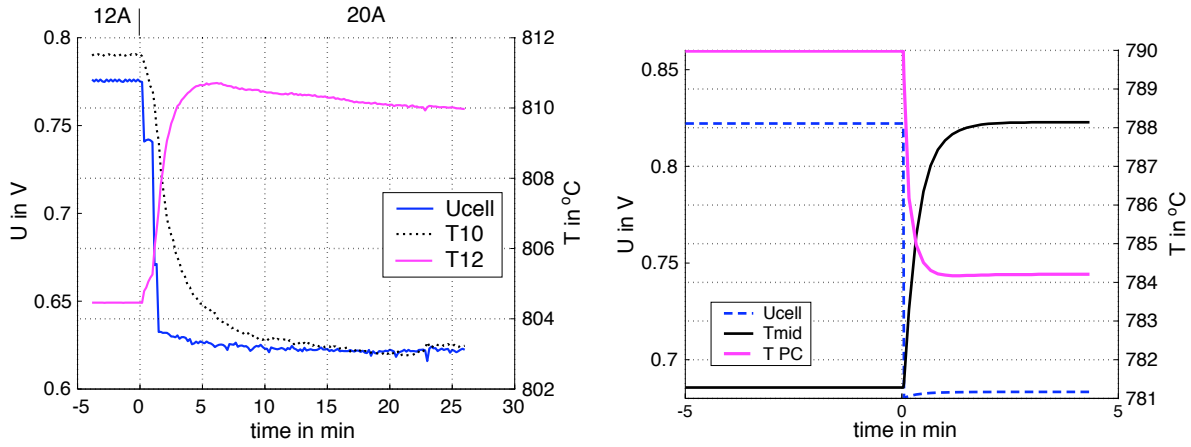

(a) Measurement: potential and current response from 12 to 20A

(b) Simulation of the response

Figure 7.8: Transient measurement on a repeat element equipped with thermocouples (T12 is in the cell center and T10 at the post-combustion) and simulation of the same transient

7.3 Start-up phase

7.3.1 Context

The high temperature of operation requires a long start-up phase to heat up the stack and the system components. Cells are expected to be sensitive to temperature gradients. To avoid stack failure, start-up is often performed in conservative conditions experimentally. The start-up procedure reported in section 4.2.2 shows that the start-up ramp in our case takes generally 4 hours.

For some applications like APUs, fast start-up is required (Singhal [2001], Mukerjee et al. [2001] claims 45 minutes). Petruzzi et al. [2003] simulated the start-up of the stack and the insulation and considered a start-up in ca. 33 min. There is therefore an interest in studying the start-up procedure. Simulation could help in this way to answer some of the unknowns of the start-up procedure: are the temperature gradients during the start-up phase important? what is the limit of fast start-up in terms of cell reliability? does the stack configuration change the start-up time?

This section presents some first results, which have to be considered as preliminary. The study was not performed for an extended number of cases and the main limitation of this work is that the system's contribution to the thermal inertia and start-up phase is not accounted. Preliminary work in this direction has been performed by Autissier [2003]. The next section presents the simulated cases and first results.

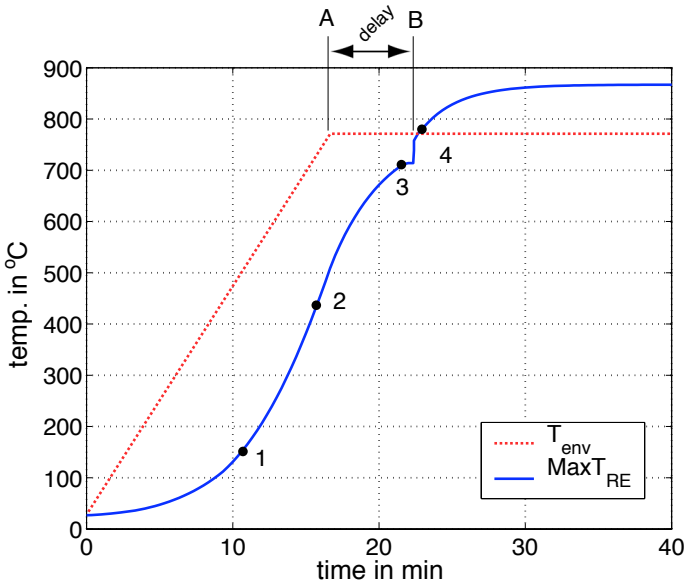

Figure 7.9: Environment temperature and stack maximum temperature evolution during a start-up phase with configuration A. At time A, the environment temperature is stabilized. At time B the fuel is introduced and the post-combustion starts. The delay is defined by the time between A and B.

7.3.2 Simulation sequence and results

Simulations are performed without any consideration on the system inertia, the only component considered is the stack. The start-up is simulated by controlling the environment temperature. The simulated sequence is:

1. warm-up, environment temperature rising linearly to 770°C , air fed to the stack at the environment temperature

2. when the stack temperature reaches 680°C at its coldest location, the fuel is assumed to be introduced and the post-combustion takes place

Figure 7.9 shows the case of a start-up for the base case (lambda 2), the temperature of environment and the maximum temperature in the repeat element are indicated. The temperature delay between the stack and the environment is noted. The delay for the stack to reach the environment temperature is in the range of 5 minutes, a similar delay was shown in Bundschuh et al. [2004]. In the first 10 minutes the rate of increase of the stack temperature is much lower than the environment temperature. During this first phase the heat-up of the stack is dominated by the air fed to the stack. Figure 7.10(a) shows the temperature profile 11 min before the fuel introduction. The main gradients are found at the air inlet as the gradients at the edges are small (area x =0.2, y =0.2) revealing a

small contribution of radiation. The rate of increase of temperature increases when the difference between the stack and environment is sufficiently high to have a contribution from the radiative exchange on the sides of the stack. Figure 7.10(b) shows a larger gradient on the edges. At the end of the start-up phase the radiative exchange seems to be the major contribution as seen in figure 7.10(c) where the gradients from the edge of the stack are important. The introduction of fuel and the initiation of the post-combustion leads to a fast temperature increase, the post combustion becoming at this point the main contributor to the stack heat-up.

The air flow rate seems to have an important contribution to the stack warm-up, particularly

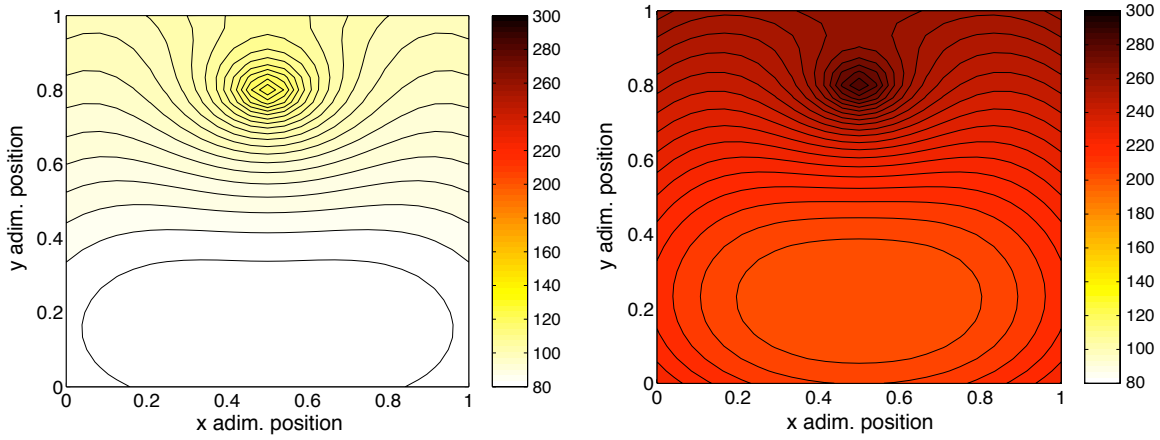

(a) T profile 11 minutes before fuel introduction (see point #1 on figure 7.9)

(b) T profile 6 minutes before fuel introduction (see point #2 on figure 7.9)

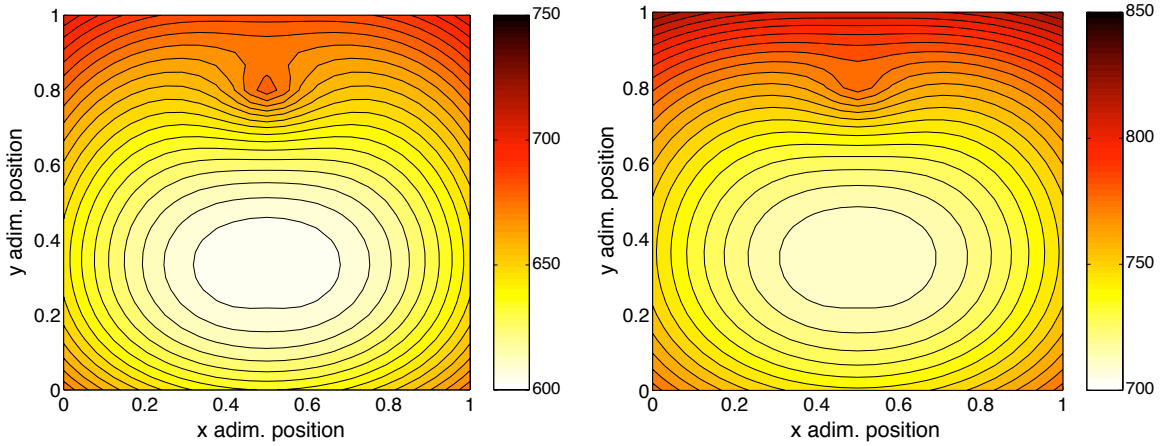

(c) T profile 1 minute before fuel introduction (see point #3 on figure 7.9)

(d) T profile 30 s before fuel introduction (see point #4 on figure 7.9)

Figure 7.10: Start-up phase temperatures

in the first phase at low temperature. The air flow rate has been changed to study its influence on the warm-up. The air flow rate has an impact on the delay to reach the conditions at which the fuel is fed to the stack. At low flow rate, the impact is quite limited, however for a

change from an air ratio of 2 to 4, the delay is decreased by 30%. The temperature gradient on the other hand increases linearly with the air flow rate. This is true for this design as the air inlet is punctual. Other work suggest to increase the air flow rate to accelerate the start-up and decrease the gradient (Petruzzi et al. [2003]); this latter work considered a classic cross-flow design where the air inlet is large.
The different designs tested in section 7.2.2 have been simulated with the same air flow rate (air ratio of 3). The effect of the design is limited.

Table 7.3: Sensitivity of the warm-up to air ratio

lambda $O_2/O_2^{stoc.}$	delai s	maxGrad T/cm
0.5	343	10.5
1	334	12.8
1.5	322	15.3
2	306	17.9
4	222	26.9

7.4 Discussion and conclusion

Transient simulations have been performed on the counter-flow configuration. The thermal inertia is significant and the temperature response to a load change is generally in the order of 10 minutes for transients from OCV to 70% fuel utilization. During the transient, temperature gradients are not worse than the steady-state gradients simulated: this will have to be confirmed in future work by CFD modeling where the geometrical resolution is superior. The ability of the stack to follow load has to be proven: the thermal response could be satisfactory, however the response of the stack to a flow rate change has to be studied in the future. In a system, the stack will probably be operated in a narrow range of fuel utilization to reach the expected efficiency; in this case, the flow rate will have to be adapted for a load increase and this will probably be the limiting factor. This aspect could be investigated: an unsteady flow motion and molar balance conservation equation will have to be implemented.
Fast start-up of the stack is an issue when considering start-up in less than 10 minutes. The thermal inertia is large, the start-up time could be decreased by an increase of the air flow rate in the stack during the warm-up phase but for the configuration considered here this has a strong effect on the gradients around the air inlet.
The stack configuration and compactness does not seem to have a significant impact on

the thermal time response: this is explained by the small change in the heat capacity and thermal conductivity with the different cases considered. The design decisions made for the stack on the basis of steady-state simulation results do not influence significantly the transient behavior.

The entire fuel cell system has to be included in the simulation of the transients: if critical situations are not identified for the stack simulated alone, the interaction and different response times of the system components could lead to critical situations. Future work should also include transient behavior on the flow rate and the species conservation as flow rate changes have been identified to be critical for the stack reliability. These effects may require the use of a CFD model.

Bibliography

E. Achenbach. Response of a solid oxide fuel cell to load change. *J. of Power Sources*, (57): 105–109, 1995.

P. Aguiar, C. Adjiman, and N. Brandon. Anode-supported intermediate-temperature direct internal reforming solid oxide fuel cell II. Model-based dynamic performance and control. *J. of Power Sources*, (in press), 2005.

N. Autissier. Transients of sofc systems. Technical report, EPFL, 2003.

N. Bundschuh, M. Bader, and G. Schiller. Modelling of the heat-up process of an SOFC stack. In M. Mogensen, editor, *Proc. of the 6th European SOFC Forum*, pages 589–598, 2004.

R. Gemmen and C. Johnson. Effect of load transients on SOFC operation - current reversal on loss of load. *J. of Power Sources*, (in press), 2005.

F. P. Incropera and D. De Witt. *Fundamentals of heat and mass transfer*. John Wiley and Sons, 1990.

T. Kawashima and M. Hishinuma. Thermal Properties of Porous Ni/YSZ Particulate Composites at High Temperatures. *Materials Transactions JIM*, 37-9:1518–1524, 1996.

M. Khaleel, Z. Lin, P. Singh, W. Surdoval, and D. Collin. A finite element analysis modeling tool for solid oxide fuel cell development: coupled electrochemistry, thermal and flow analysis in MARC. *J. of Power Sources*, 130(1-2):136–148, 2004.

S. Mukerjee, M. Grieve, K. Haltiner, M. Faville, J. Noetzel, K. Keegan, D. Schumann, D. Armstrong, D. England, J. Haller, and C. DeMinco. Solid oxide fuel cell auxiliary power unit - a new paradigm in electric supply for transportation. In H. Yokokawa and S. Singhal, editors, *SOFC VII, Proc. of the int. Symposium, Electrochemical Society*, pages 173–179, 2001.

L. Petruzzi, S. Cocchi, and F. Fineschi. A global thermo-electrochemical model of SOFC systems design and engineering. *J. of Power Sources*, (118):96–107, 2003.

S. Singhal. Low cost modular SOFC system development at Pacific Northwest National Laboratory. In H. Yokokawa and S. Singhal, editors, *SOFC VII, Proc. of the int. Symposium, Electrochemical Society*, pages 166–172, 2001.

B. Thorud, C. Stiller, T. Weydahl, O. Bolland, and H. Karoliussen. Part-load and load change simulation of tubular SOFC systems. In M. Mogensen, editor, *Proc. of the 6th European SOFC Forum*, pages 716–729, 2004.

Chapter 8

Simulation of degradation behavior of stacks

8.1 Introduction

Lifetime of systems is a major issue in SOFC towards commercial use. Lifetime is limited by the risk of failure of the stacks or system components, a cell failure in a stack can limit the whole stack performance. However, risk of failure of components is not the only problem as a degradation of stack and cells performance is observed during long term operations. This decline in performance is related to different processes in the repeat element components. Some of these processes are well identified while others are still being discussed. Operating conditions, in terms of temperature, current density and cell potential, seem to have an influence on the degradation rate but this is not fully identified nor understood. In a stack, degradation is probably not homogeneous on the whole active surface, and considering that degradation phenomena are cumulated, makes the degradation behavior measured on repeat element and stack difficult to interpret. Simulation of degradation could provide an insight. An overview of the different phenomena of degradation is necessary to identify, among all possible processes, which are sufficiently well characterized and understood to be included in a model. In this work, interconnect degradation is considered.
At first, the possible degradation processes are summarized and the possibility of simulating of these processes in the repeat element model are evaluated. Then, a model for the interconnect degradation is presented. Simulation results for repeat elements and stack long term operation are presented. The influences of operating conditions and design options have been studied as well.

8.2 Degradation phenomena

Aging of the different materials composing a SOFC stack occurs intrinsically at SOFC operating temperatures. Depending on the component, different phenomena combine to modify the materials properties and microstructure, with the common effect of decreasing the electrochemical performances of the stack.

8.2.1 Electrodes and electrolyte degradation

For electrodes, different phenomena are observed. Impurities tend to aggregate at the TPB, grain size tends to grow. On the cathode side, new phases can be produced at the interface with the electrolyte, as reported by Yokokawa et al. [1990], Clausen et al. [1994] and Lee and Oh [1996] for LSM cathodes. LSF cathodes, which are recently used in the intermediate temperature range, are subject to diffusion of Zr cations from the electrolyte (Simner et al. [2003]), thus reducing their electronic conductivity. Microstructural changes have been reported by Jørgensen et al. [2000] for LSM cathodes under load. Similar studies for LSF cathodes are not yet published. On the anode side, grain size tends to grow due to nickel sintering, the TPB length is decreased and the activation loss increases (reported in Primdahl and Mogensen [2000] and Tu and Stimming [2004]). The purity of the starting powders have an influence on the impurity formation at the TPB (Hansen et al. [2004]), and it can thus be assumed that it could influence the degradation behavior. Mobility of nickel can be attributed to formation of $Ni(OH)_2$ at high p_{H_2O} (Primdahl and Mogensen [2000]).
Degradation of electrodes is not fully understood and no reliable quantification of all phenomena is available. The rate of degradation is highly dependent on the primary materials and the manufacturing procedure.
The electrolyte, 8 mol% Y_2O_3-92 mol% ZrO_2 (called 8YSZ hereinafter), is chosen for its relatively good ionic conductivity at intermediate temperature. Thin films of 10 μm theoretically demonstrate less than $0.1\Omega.cm^2$ ohmic resistance for the electrolyte at 800°C . However, the conductivity of pure 8YSZ is known to degrade with time as reported in Hattori et al. [2004], Haering et al. [2004] and Mueller et al. [2003]. This aging of the materials property is explained by a transformation from cubic to tetragonal phase (Haering et al. [2004]). Several studies have quantified the electrolyte degradation. The available data applies to the temperature range of 950/1000°C and we did not identify data at lower temperatures. Degradation is ca. 25% in the first 1000 hours of operation. The rate of degradation decreases with time (Mueller et al. [2003]). Differences in reported degradation rates could be explained by the different starting materials and manufacturing processes.
The degradation data available for 8YSZ electrolytes concern mostly pure materials. Small amounts of doping affect the conductivity as previously stated in section 2.4.1.1. The degra-

dation behavior is most probably modified by these doping materials as well. Linderoth et al. [2001] showed that a 8YSZ electrolyte containing a significant amount of Ni (several %) degradates is rapidly in the first 30 hours after reduction (with a decrease of ca. 50% the conductivity). Afterwards (measured up to 300 hours), degradation rate was small.
Degradation of the electrolyte is fairly well characterized for pure YSZ. However, data available is for temperatures around 1000°C and the rate of degradation is most probably sensitive to temperature. Furthermore, electrolytes in anode supported cells are contaminated with nickel during the manufacturing processes and no data is published on the long term degradation of Ni-doped electrolytes.
Degradation of electrodes and electrolytes cannot be implemented in a model as the phenomena are neither fully understood nor quantified. The next section focuses on interconnect degradation.

8.2.2 Metallic interconnect degradation

For metallic interconnects, oxidizing conditions induce the growth of an oxide scale on the surface of the interconnect (Yang et al. [2003]). This oxide scale has generally poor conductive properties and therefore the contact resistance between the current collectors and the interconnect is affected. Under fuel atmosphere simulating high fuel utilization, oxidation of the interconnect is observed as well (Honegger and Plas [2001]). Finally, chromium evaporation has been measured (Gindorf et al. [2001]); chromium can be reduced ($VI \rightarrow III$) at the cathode triple phase boundary, reducing the TPB length and the electrode performance but this effect is significantly lowered in the intermediate temperature range.
The lowering of the operating temperature in intermediate temperature SOFCs allows the use of ferritic steel alloys instead of the costly chromium based alloys used at high temperatures (Piron Abellan et al. [2001] and Honegger and Plas [2001]). The requirements for the interconnect material can be summarized as (Yang et al. [2003] and Honegger and Plas [2001]):

- oxide scale interface stability in both fuel and oxidant atmosphere, the oxide scale having to remain dense and without cracks to avoid an increase in the oxidizing surface
- thermal expansion coefficient (TEC) close to the cell's TEC
- sufficient electrical conductivity for the bulk and the oxide scales formed on the surface

The critical specification for the interconnect is the ohmic resistance of the system current-collectors / interconnect. The ohmic resistance is here dominated by the contact resistance due to the oxide scale formed at the interface (see in figure 8.1).

Ferritic steels have been investigated as potential candidates for the metallic interconnect, with chromium content generally between 20 and 22% in order to be close to the thermal expansion coefficient of the cell. Minor components such as Mn, Ti, La, Y have been shown to have a strong impact on the conductivity of the oxide scale formed at the interface. Yang et al. [2004] compared two alloys and the one showing the larger growth rate for the oxide scale showed a better conductivity: this is attributed to the spinel rich scale forming in this alloy - the spinel phase being more conductive than chromium oxide.
A number of different commercial and experimental interconnect alloys have been tested in our facilities. Figure 8.2 shows the area specific resistance measured as a function of time for all the tested samples exposed to air at 800°C . Three of these materials where used as interconnect materials in our repeat element and stack testing,

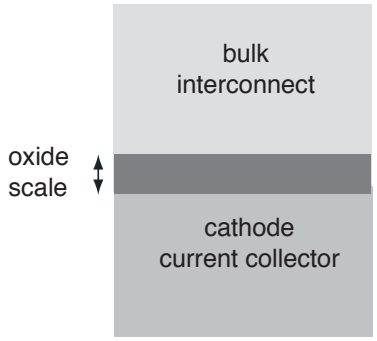

Figure 8.1: Scheme of the considered system in the model

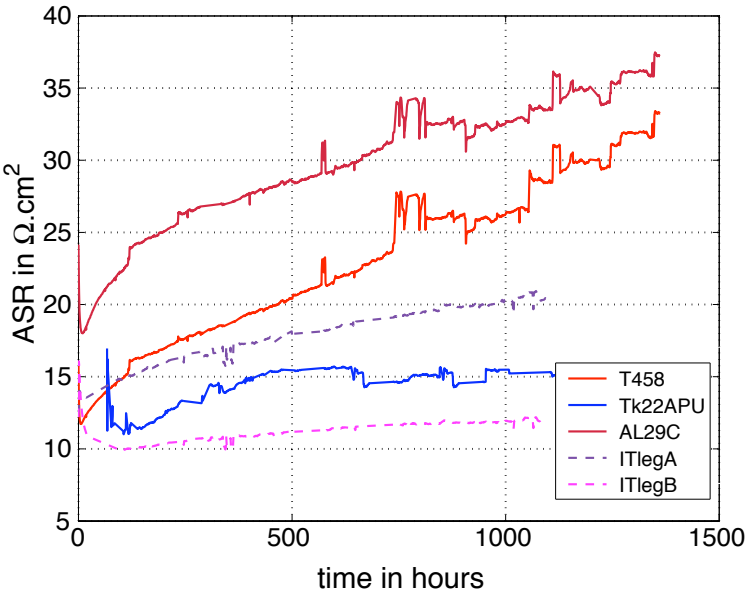

Figure 8.2: Interconnect degradation at 800°C .

8.3 Interconnect interface degradation modeling

Interconnect degradation can be described by a simple oxide scale growth. The next sections present the model for interconnect degradation, the measurements performed on three different samples at different temperatures and the parameter identified.

8.3.1 Model for a simple oxide scale growth

The interconnect/current collector interface conductivity degradation can be described by a simple Wagner's law for oxide scale growth. This assumes that transport of the oxide form (e.g. Cr_2O_3 for chromium forming scale) takes place by lattice diffusion (Huang et al. [2000]). With these assumptions the scale growth can be described by a simple parabolic law (Huang et al. [2000], Yang et al. [2003] and Yang et al. [2004]) expressed as:

$$\frac{\partial(\xi^2)}{\partial t} = \frac{k_g^O}{(\chi\rho_{ox})^2}.e^{-E_{ox}/RT} \tag{8.1}$$

where ξ is the scale thickness (in cm), χ the oxygen weight proportion in the oxide formed, ρ_{ox} the oxide density (5.22 g/cm^3 for Cr_2O_3) , k_g^O and E_{ox} the weight gain rate constant and activation energy for the oxide scale growth. Values for the weight gain growth constant are in the range of 0.3 to 410^{-12} g^2/(cm^4.s^1) while the activation energy for the scale growth is of 220 kJ/mol (Yang et al. [2003]). From the scale thickness and the oxide scale conductivity, the ASR for the oxide scale formed can be expressed:

$$ASR = \frac{\xi}{\sigma_{ox}} \tag{8.2}$$

$$\sigma_{ox}T = \sigma_{ox}^0.e^{-E_{el}/RT} \tag{8.3}$$

where σ_{ox} is the conductivity of the scale in S/cm, σ_{ox}^0 the conductivity constant and E_{el} the activation energy for the conductivity.

The validity of this model is discussed. In cases where mixed ionic protective layers are used, this simple expression is not valid (see Huang et al. [2000]) and new expressions are to be used. Concerning the Crofer22APU interconnect, which has been tested and used in our case, Kuznecov et al. [2004] claim that the growth rate cannot be fitted with a simple parabolic law whereas Yang et al. [2004] showed a good fit with the same parabolic law. The resulting area specific resistance depends not only on the thickness of the layer but also on the conductivity of the oxide formed. Spinel oxides have a better conductivity than chromium oxide. For chromium scale the conductivity is expected to be in the range of 10^{-2} to 10^{-3} S/cm at 800°C (Yang et al. [2003]), whereas for spinel, values in the range of 10^{-2}

to 1 S/cm are reported (Sakai et al. [2004]). For the spinel phase, conductivity depends on composition.
The present work which intends to study the impact of interconnect degradation on the stack performances, will use the simple growth rate model. This model is considered to be sufficient and has been implemented in the stack model for the cathode current collector interface on the whole stack surface. The rate of growth on the interconnect is therefore dependent on the local interconnect temperature. Some of the model parameters for the scale growth will be identified from experiment.

8.3.2 Identification of parameters from measurements

Conductivity measurements have been performed on two different alloys (the Crofer22APU and the Plansee) which were used in repeat element testing. The measurement was carried out with a four point set-up. The interconnect is placed between 2 SOFConnex current collectors and 2 LSM pellets (figure 8.3). Platinum paste is applied on the outer surfaces of the pellets to improve current collection between platinum mesh and the pellets. The samples are placed in an oven, the same pressure as used in stack testing is applied to the interconnect samples (ca. $4N/cm^2$). A constant current of 1 A is applied to the samples

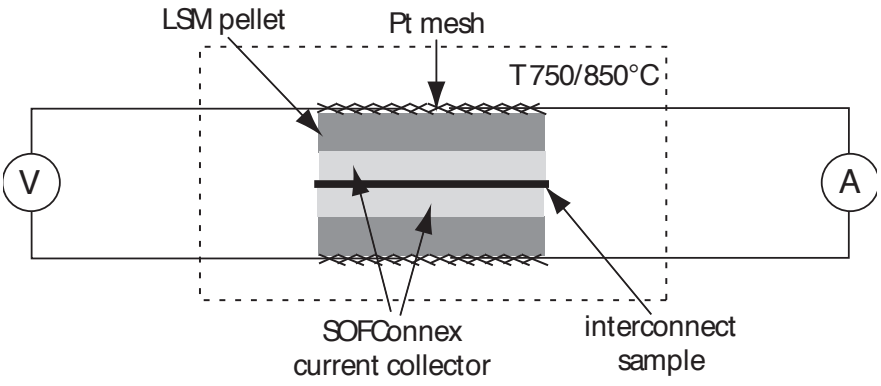

Figure 8.3: Measurement set-up for interconnect conductivity

between both Pt meshes during the whole test duration, the samples being of ca. $3cm^2$. The resistance measured is the total resistance of the pellets, current collectors and interconnect oxide layers. The resistance of the pellets and the current collectors has been measured separately at different temperatures to substract their contribution.
The test has been carried out for more than 1400 hours in total with different phases summarized in table 8.1. The conductivity measured on the samples is reported in figure 8.4.
The behavior of the measured interconnects is shown on figure 8.4. At 795°C , after more than 500 hours, the rate of increase of the resistivity is close to zero. The temperature

Table 8.1: Conductivity test on interconnect: history of the test

phase	temperature °C	time length hours	remarks
1	795	580	-
2	820	230	-
3	845	230	2 general current failures
4	748	300	temperature drift from 745 to 752
5	770	300	conductivity stable

increase causes the resistance to decrease on short term as the oxide scale conductivity is dependent on temperature. The rate of increase for the conductivity increases as well. After more than 1000 hours of exposure to high temperature, the temperature has been decreased to ca. 750°C and the conductivity was stable. From this test, the activation energy for the oxide scale has been identified on the assumption that the scale thickness increase between before and after the temperature changes is negligible (the temperature change takes ca. 1 hour). Results are summarized in table 8.2. The range of values is in agreement with the literature as Sakai et al. [2004] reports 86.2 kJ/mol for the activation energy of a spinel scale.

To determine the conductivity of the scale and the parameter for the rate of increase of

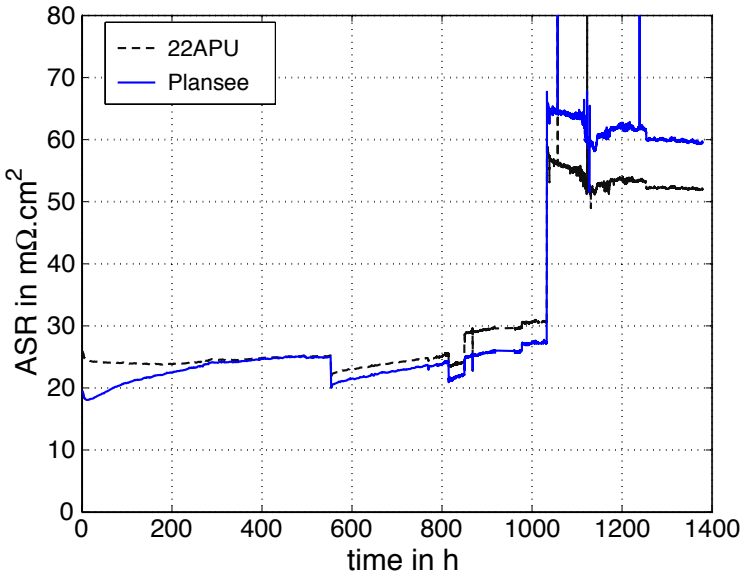

Figure 8.4: Conductivity measured on the interconnects

the scale, results from measurements presented in figure 8.2 are used. The oxide scale composition on interconnects T458 and Crofer22APU have been analyzed (at EMPA) and the depth of the scale determined. The thicknesses measured and the corresponding area specific resistance (ASR) are reported in the table 8.3. For the Crofer22APU, the scale thickness

Table 8.2: Oxide scale activation energy

sample		Crofer22APU	Plansee
E_a	J/mol	75218	108960
std dev	J/mol	7700	13000

Table 8.3: Parameters for the oxide scale, activation energy of the oxide scale growth assumed to be 220kJ/mol. The activation energy for the oxide scale conductivity is assumed to be equivalent for the T458 as for the 22APU.

sample	time exposed hours	temp. °C	scale . thick. μm	ASR mΩ.cm^2	k_p $cm^2.s^{-1}$	k_g $g^2.cm^4.s^{-1}$	σ_{ox} S/cm	${k_p}^o$ $cm^2.s^{-1}$
22APU	1130	810	∼10	15.3	$2.45.10^{-13}$	$6.66.10^{-13}$	$3.2.10^5$	0.0126
T458	1361	810	∼4	33	$3.27.10^{-14}$	$8.89.10^{-14}$	$6.2.10^4$	0.0016

measured in our case is larger the one reported by Yang et al. [2004] which is ca. 7/8 μm after 1800 hours exposure.
The value of 220 kJ/mol has been finally used in the rest of the report as the estimations of the activation energy E_{ox} from the measurements shown in figure 8.4 using the expression

$$\frac{\partial(ASR^2)}{\partial t} = \frac{k_g^O}{(\chi\rho_{ox}\sigma_{ox}^0)^2}T^2 \exp\frac{-E_{ox}+2E_{el}}{RT} \tag{8.4}$$

derived from equations 8.2, 8.1 and 8.3 is too uncertain.

8.4 Model for anode reoxidation risk

Anode supported cells rely on the anode which is composed of Ni/YSZ cermet as mechanical support for the electrolyte. Owing to this anode support the cells are sensitive to redox cycling. Depending on the manufacturer, the anode thickness ranges from 200μm to 2mm while the electrolyte is between 5 and 20μm thick. The cells are mounted in the stacks in an oxidized state. The start-up procedure includes therefore a reduction step. During this first reduction, the micro-structure of the anode changes when nickel oxide is reduced to metallic nickel and the porosity increases. No contraction of the anode is observed for a fine structured anode (Waldbillig et al. [2004]). If the reduced cell is exposed to an oxidative atmosphere, reoxidation occurs and a small expansion (on the order or 1%) is observed

(Waldbillig et al. [2004]). This expansion can create cracks in the electrolyte, in the complete cell, or even lead to cell failure (see in Robert et al. [2004] and Waldbillig et al. [2004]). The micro-cracks create a gas cross-over which decreases the measured OCV. The stacks have strong failure probabilities in case of fuel shortage for a limited time, even if they are not loaded and the anode stability is also a problem for the start-up and shut-down procedure. Redox stability of cells is a key reliability problem for intermediate temperature SOFC.
Local anode reoxidation can occur during operation as well. At high fuel utilization, the partial pressure of fuel can be locally close to zero. In case of strong fuel depletion, the fuel atmosphere is no longer oxidative and conditions for a local reoxidation of the anode can be encountered. On tested cells, local oxidation has been observed (e.g. the figure 8.5). This section presents a simple model to compute the equilibrium of the Ni/NiO reaction. Implemented in a repeat element or a stack model, this model allows the prediction of anode reoxidation risk. The equilibrium of Ni/NiO has been previously studied, and previous work

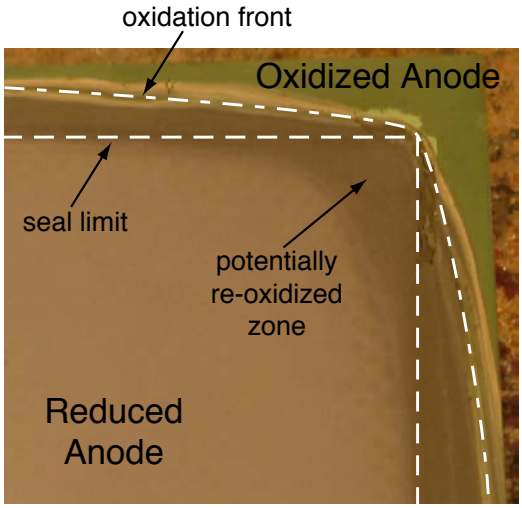

Figure 8.5: Reoxidized area in the corner of the cell.

from Middleton et al. [1989] and Seiersten and Middleton [1991] demonstrated a good agreement between the thermodynamic data and the reversible voltage of the reaction measured by cyclic voltametry. The redox reaction for the nickel/ nickel oxide oxidation is simply:

$$Ni(s) + 0.5O_2 \rightarrow NiO(s) \tag{8.5}$$

The equilibrium condition for this reaction can be computed from the thermodynamic data (reported in table 8.4): the partial pressure of oxygen at equilibrium is computed directly from the Gibbs free enthalpy of reaction (equation 8.6). Figure 8.6 plots the equilibrium value of oxygen partial pressure in the temperature range from 650 to 1000 °C .

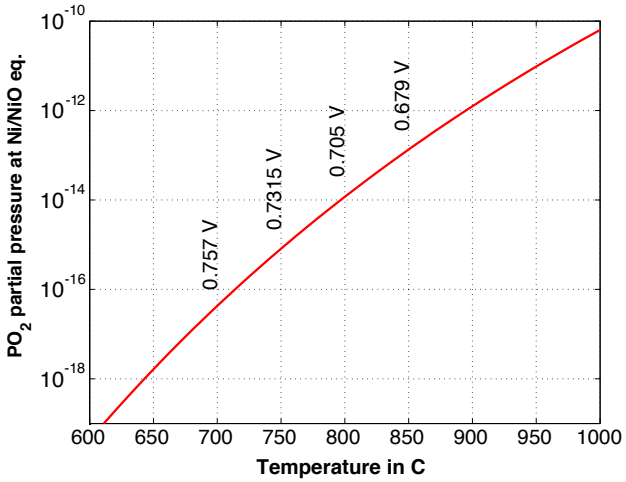

Figure 8.6: Oxygen partial pressure at Ni/NiO equilibrium

$$p_{O_2}^{eq} = e^{\frac{2\Delta G^o_{Ni/NiO}}{RT}} \tag{8.6}$$

On the anode side of a fuel cell in operation, the atmosphere is considered to be reducing. However, at high water vapor concentration, conditions can become oxidizing. The partial pressure of oxygen on the fuel side is computed from the local Nernst potential and the local hydrogen and water concentrations.

$$U_{Nernst} = \frac{RT}{4F} ln \frac{P_{O_2}^{cathode}}{P_{O_2}^{anode}} \tag{8.7}$$

For partial pressure of oxygen higher than the equilibrium partial pressure, the anode is at

Table 8.4: Thermodynamic data used for the Ni/NiO system

ΔH^f_{NiO}	$\Delta S^o_{0_2}$	ΔS^o_{Ni}	ΔS^o_{NiO}
J/mol	J/mol.K	J/mol.K	J/mol.K
-244e3	205	30.14496	38.602296

risk to be reoxidized. The kinetics of the reaction are not considered in this study although some work is published (Tikekar et al. [2003]) on the subject.
The re-oxidation risk in the anode can therefore be expressed as:

$$risk_{anodereoxidation} \;\; \exists \;\; if \;\; p_{O_2}^{anode} > p_{O_2}^{eq} \tag{8.8}$$

which is equivalent to

$$risk_{anodereoxidation} = p_{O_2}^{eq} - p_{O_2}^{anode} < 0 \tag{8.9}$$

The anode encounters risk of reoxidation if the indicator $risk_{anodereoxidation}$ is negative. This indicator will be computed locally on the cell surface with the local concentration and temperature conditions. In the present model, as diffusion transport in the anode thickness is neglected, the indicator may underestimate the re-oxidation potential. As a concentration gradient can exist in the anode, the area subject to anode reoxidation is probably larger than the computed area with the present model.

8.5 Stack degradation simulation

This section presents simulations of repeat element and stack degradation in different operating cases. Degradation is temperature activated as the diffusion of oxygen at the inteconnect interface increases with temperature. Therefore, the degradation rate is expected to be mostly dependent on the stack temperature. The local temperature in the repeat element and stack is far from being homogeneous and the consequences of the degradation on current density distribution is studied.
Simulation will be carried out under adiabatic and non-adiabatic boundary conditions, at a reference flow rate of 300 ml/min of hydrogen. Differences in operation mode will be studied. The interconnect considered in the following is Crofer22APU.
First, the different criteria for degradation of a repeat element expressed:

- as the degradation percentage of power output between initial and final state:

$$deg_{power} = \frac{E_e(t_f) - E_e(t_o)}{E_e(t_f)} \tag{8.10}$$

- as the percentage of apparent area specific resistance increase (the slope of the iV curve defined in section 5.2.1):

$$deg_{AASR} = \frac{AASR(t_f) - AASR(t_o)}{AASR(t_o)} \tag{8.11}$$

Degradation rates are often expressed as rate of power output decrease per time unit. This criterion is clear and useful. However some problems may arise like when comparing a repeat element operated at a given current in different conditions, that means when the initial potential of the cell is not the same and the initial power output neither. Is it therefore fair to compare the degradation with the power output?

8.5.1 Repeat element degradation: base case

The base case is the case of a counter flow repeat element operated with 300 ml/min hydrogen and an air ratio of 3, the repeat element was assumed to be operated in a galvanostatic mode (at 24A). The case has been tested in adiabatic and non-adiabatic boundary conditions. The environment temperature was set to 750°C .

The cell potential as a function of time is plotted on figure 8.7, the power output degradation

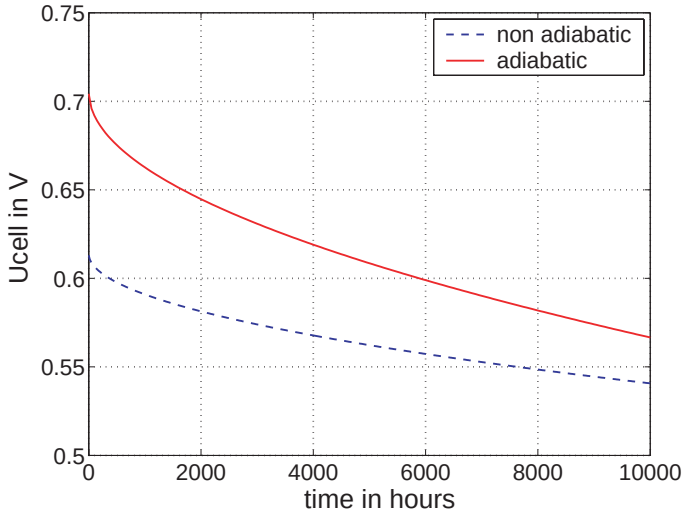

Figure 8.7: Potential evolution at 70% fuel utilization for a repeat element in adiabatic and non-adiabatic boundary conditions.

being of 19.5 and 11.8% (for 10'000h) for the adiabatic and non-adiabatic cases respectively. Degradation rates decrease with time as the oxide layer growth follows a parabolic law. The difference in degradation rate is explained by the temperature difference in the two cases: the adiabatic case operates at an averaged temperature of ca 900°C , while it reaches only 800°C for the non-adiabatic case. The degradation is obviously explained by the increase in ohmic resistance. As temperature is not homogeneous on the active surface of the cell, the rate of growth of the oxide scale is not homogeneous. Therefore, the local resistance distribution (sum of all losses) changes on the surface. Figure 8.8 shows the initial resistance profile for the adiabatic case. Initially, in figure 8.8(a) the local resistance is a function of the temperature only, the minimum resistance being at locations where maximum temperatures are found (with resistances of 0.25 $\Omega.cm^2$ minimally and 0.35 $\Omega.cm^2$ maximally). The final state shown on 8.8(b) is a function of the repeat element history of operation and temperature, the profile being here almost homogeneous with values in the range of 0.39 to 0.46 $\Omega.cm^2$. Initially the ohmic resistance represents 6% of the losses while after 10000h it amounts to 40% of the total losses.

The change in resistance distribution affects the current density distribution. On figure 8.9(a) and 8.9(b), the current density distribution is shown for the initial state, after 5000h

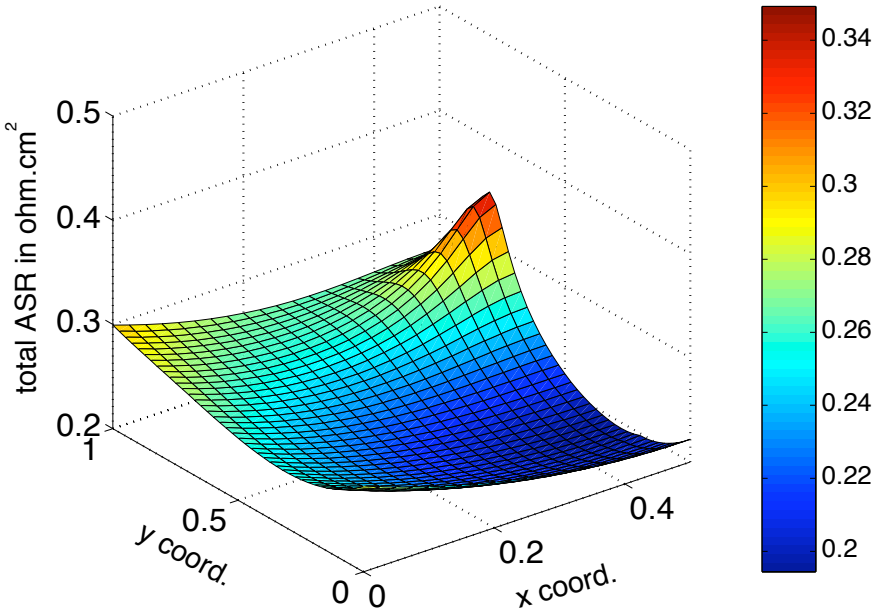

(a) Initial local ASR profile on the repeat element

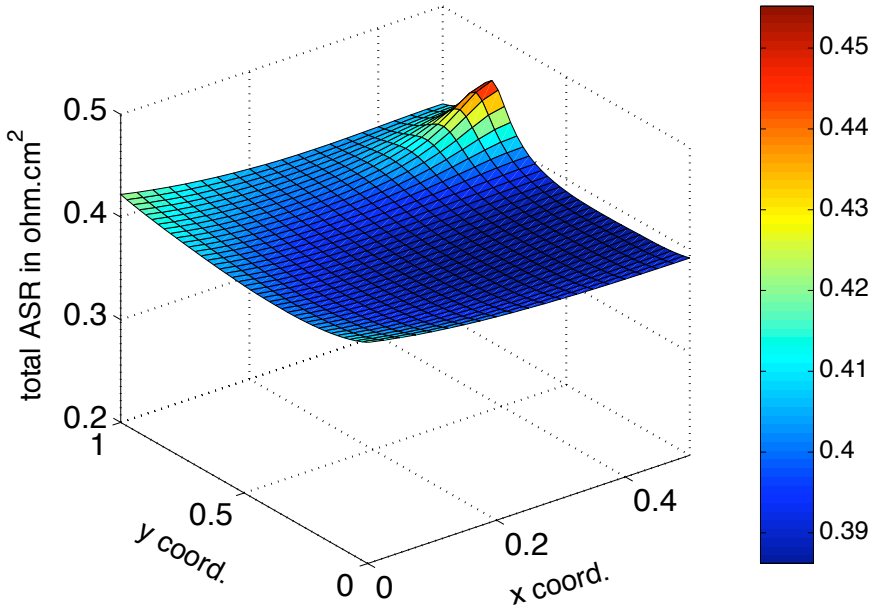

(b) Final local ASR profile on the repeat element

Figure 8.8: Degradation, evolution of the current density distribution and of the potential with time

and after 10000 h. The maximum current density decreases from 1.1 A/cm^2 to less than 0.9 A/cm^2 in the final state, the minimum values tending to increase. In this counter flow case, the current density distribution profile tends to be more homogeneous with progressing degradation: the maximum temperature area is the same as the maximum current density area in this case and therefore oxidation of the interconnects occurs preferentially in this

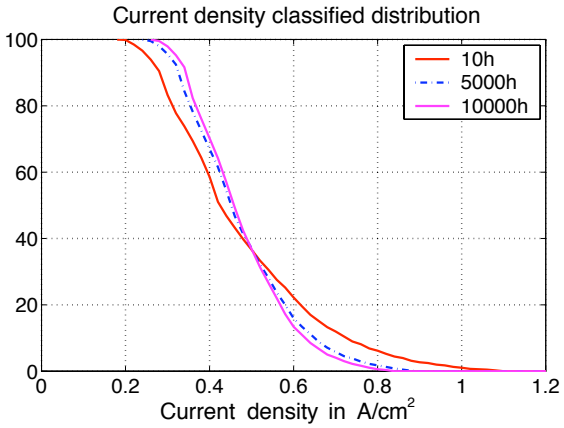

(a) Classified current density at t=50h, t=5000h and t=10000h

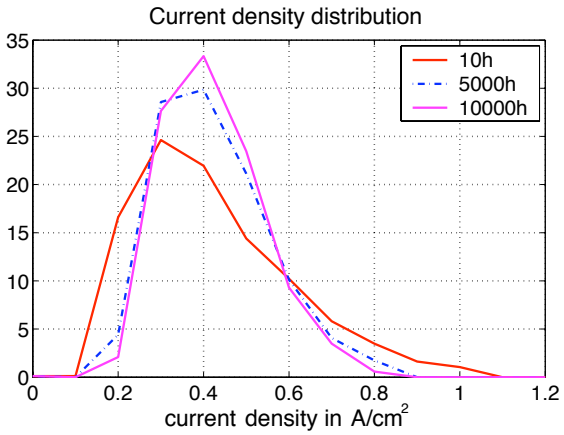

(b) Cell potential degradation at 750°C for 50, 60 and 70% fuel utilization

Figure 8.9: Degradation, evolution of the current density distribution and of the potential with time

area. This effect is seen in the non-adiabatic case as well. However, as the temperature differences as well as the degradation rate are smaller, differences in the distributions are smaller.

Degradation has been simulated for the coflow case as well. The trend is the same as for the counter-flow repeat element, in a constant current mode the potential decreases with time. However, for the same operating conditions, owing to lower temperatures in the repeat element, the degradation rate is significantly lowered.

8.5.2 Sensitivity to operating parameters

Local temperature defines the local degradation rate. As the temperature field is dependent on the operating parameters and the decision variables for the repeat element design (thicknesses, area, air excess ratio), the impact of these decision variables on the degradation behavior is studied. Sensitivity analysis has been performed on the following cases:

- for a counter-flow repeat element, with a fixed geometry (base case) and fixed flow rates (300 ml/min fuel and lambda 3), the environment temperature and the current output has been varied
- for a coflow case, the same variations have been performed (with the same cell area and flow-rates as for the counter flow)
- for a counter-flow repeat element, with a fixed flow rate and current output, the design decision variables such as cell area, interconnect thickness, air channel height and air

stoechiometric ratio have been varied.

The sensitivity of the degradation rate to these variables can therefore be defined. On figure 8.10(a), the degradation rate expressed as deg_{AASR} is plotted as a function of the fuel utilization and the mean temperature on the surface (case for the change in temperature and current in the counter flow case). The degradation shows a clear linear trend with the mean temperature in the solid. The sensitivity to the fuel utilization is small. Figure 8.10(b) shows the degradation rate as a function of the current density and the mean temperature in the solid. Again the degradation rate is a linear function of the mean temperature in the solid while the sensitivity to the current density is low. It has to be noticed that the

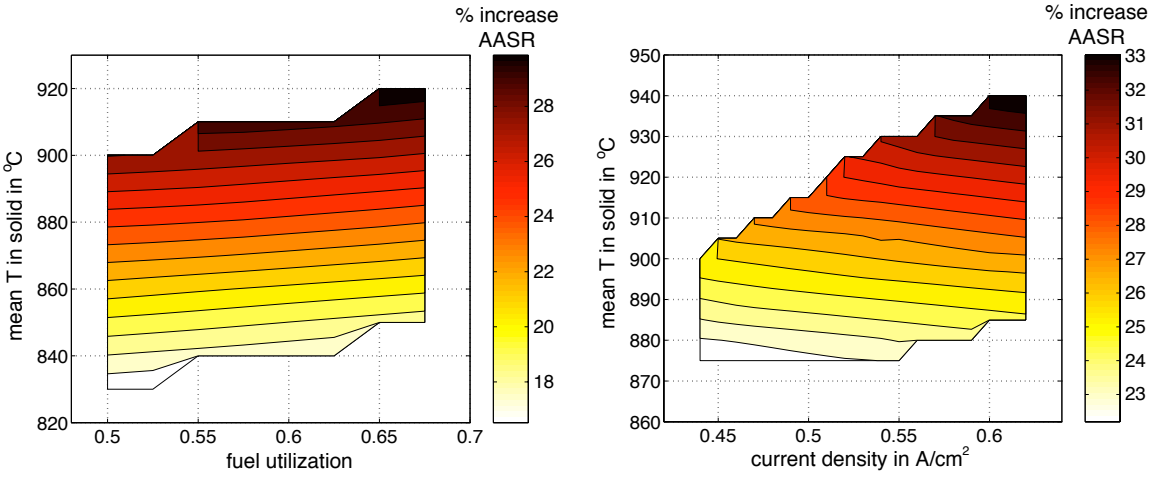

(a) Degradation for same design with changing operating parameter (temperature, current density)

(b) Degradation for the same total current and environment temperature with changing design decision variables (area, thicknesses)

Figure 8.10: Sensitivity of degradation to design and operating decision variables

the same results presented with the degradation rate expressed as deg_{power} gives a different trend. With this criterion the degradation rate has a clear linear trend with the current density and the temperature.

Finally, the results for all the sensitivity cases are summarized in figure 8.11. A linear trend between the mean temperature in the repeat element and the degradation rate (expressed in AASR deg_{AASR}) is established. This linear trend is valid for different operating conditions, current densities and even for different repeat element configurations. The use of this criterion to express the degradation of stack performances is therefore recommended as it allows to compare results even if the conditions or initial performances are not the same.

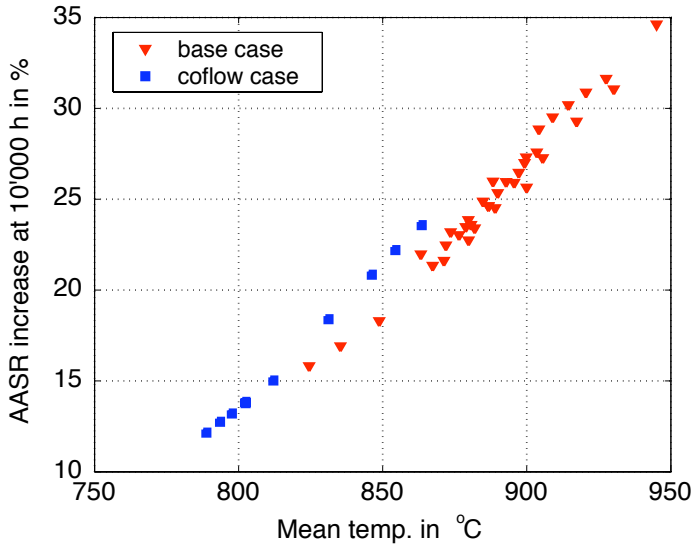

Figure 8.11: Degradaration rate expressed as AASR increase for all the simulated case (Coflow and Counter flow -design variations and operating parameters variations-)

8.5.3 Stack degradation behavior

Long term behavior of 5, 15 and 30 cell-stacks have been simulated in the same conditions (300 ml/min fuel, 750°C environment, lambda 3 and 24A) for 10000 hours of operation. Owing to the stack temperature gradient in the stacking direction, cell degradation is expected to be different in the stack center compared to the behavior at the ends.

Table 8.5: Stack degradation results, initial and final cell potential

numb. cells	middle cell			border cell		
-	t=0h	t=10000h	deg_{power}	t=0h	t=10000h	deg_{power}
5	0.717	0.654	8.7%	0.712	0.652	8.4%
10	0.729	0.656	10%	0.718	0.654	8.9%
30	0.739	0.654	11.5%	0.719	0.655	8.9%

The different simulations performed exhibit a larger degradation rate for the cell in the center when compared to cells at the edges. The degradation rate follows the temperature profile on the height of the stack. This is clearly seen in figure 8.12(a) where the cells in the stack center have a degradation between initial and final state of more than 11% while

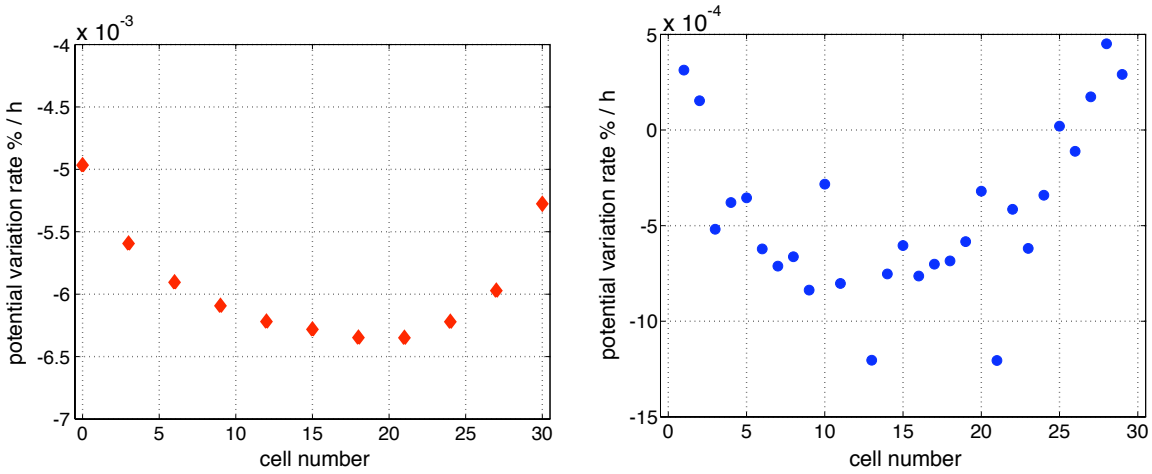

(a) Simulation of degradation on a 30 cells stack: cell potential variation rate at 80h

(b) Experimental degradation rate per hour on a 29 cells stack: cell potential variation rate at 80h

Figure 8.12: Stack degradation behavior, experimental and simulation degradation rate of a 30 cell-stack

on the edges the rate is around 9%. The maximum degradation is shifted to cell number #17 as in the model the air is fed from cell #1 and is heated along its path: the maximum temperature is therefore not exactly in the stack middle. This trend is confirmed by the degradation/activation behavior of a tested stack of 29 cells: the stack was operated in galvanostatic mode at 13A (flow rates) during 44 hours at the beginning of the test. In figure 8.12(b), the rate of change of the potentials is shown: the activation and degradation phenomena are in competition and the rate of change of the potentials aggregates both. On the border of the stack, activation is still dominating while in the stack center degradation has overcome activation and a net degradation is measured. For the experimental case, the shift in the maximum temperature is towards cell #1, this is explained by the test configuration: air is fed from both ends (for flow rate distribution reasons) and cell number #1 was the cell on top of the stack and as combustion gases are lighter than air, they are expected to go towards the top of the stack.

For shorter stacks, degradation rates decrease from 11.5 to 8.7% for the cells in the center while the variation for the cells located at the edges are lower. This is explained by the small increase in temperature for border cells with the number of cells (section 3.3). This non-homogeneous degradation rate could lead to modify the cell potential profile along the height of the stack, leading to a quasi homogeneous profile for 10'000 hours and to an inverse profile for longer operation (with cells on the border performing better than middle cells).

8.5.4 Comparison with experiment

A repeat element, the #MS21, has been tested for more than 5000 hours, the results is reported on the figure 8.13. This test was performed with T458 interconnects of 0.75 mm thick. The model has been used to simulate the behavior of a repeat element degradation in the same test conditions (environment temperature of 770°C , a fuel flow rate of 500 ml/min and an air ratio of 3). The parameters used for the T458 are found in the section 8.3.2.
The simulation includes only the interconnect degradation behavior. Therefore the strong activation measured between t= 500 h and t= 1300 h is not reproduced. The cell potential simulated is perfectly adapted to the #MS21 experiment and therefore the potentials and power output are different. Nevertheless the strong degradation in the first 500h and the general trend are reproduced. The simulated degradation is not as important as the measured one: this can be explained both by the parameter used for the T458 simulation which can be improved and the fact that the model only includes the interconnect degradation while several phenomena are aggregated in the degradation observed experimentally.

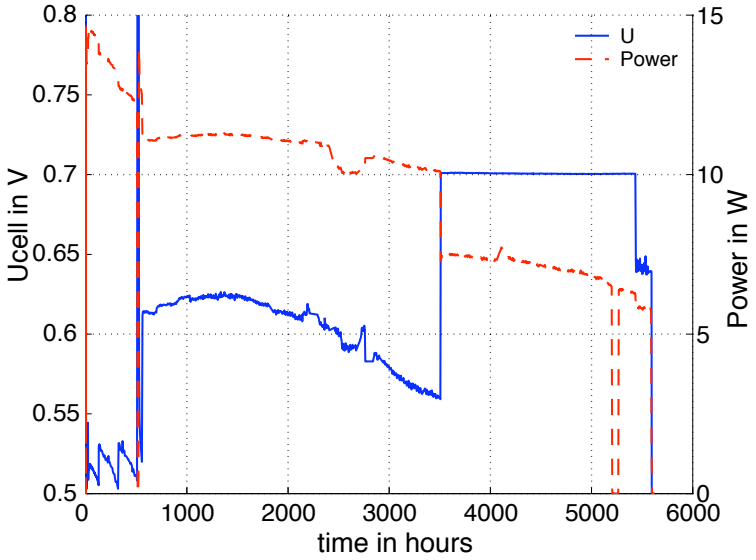

Figure 8.13: Long term test on repeat element #MS21.

8.6 Anode re-oxidation simulation

The model allowing to compute the anode re-oxidation risk (section 8.4) has been implemented in the stack model. From the equations, the regions exposed are the regions with lean fuel concentrations. In chapter 3 the region of the fuel outlet corner has been identified as the most critical for the counter-flow repeat element.

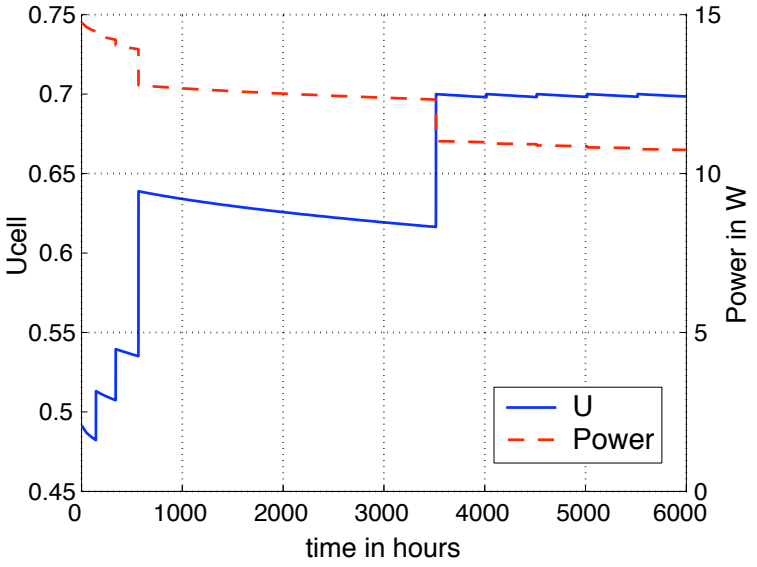

Figure 8.14: Simulation of the #MS21 repeat element test.

As the anode re-oxidation is sensitive to temperature, a sensitivity on the temperature and fuel flow rate has been performed. The limits of safe operation have been found by identifying, for each temperature and fuel flow rate, the maximum fuel utilization possible without risk of oxidizing the anode.

8.6.1 Counter flow repeat element

The simulations are performed with the complete Butler-Volmer electrochemical scheme and the parameters found in the section 4.5.1.1. The electrolyte electronic conductivity is in the range of 30 to 40Ω.cm^2 . Simulations have been performed for the case of a single repeat element (non-adiabatic case) and the case of a repeat element in a stack (adiabatic case).
The results are presented in the figure 8.15. For the adiabatic repeat element (figure 8.15(a)) operated with an environment below 710°C and for the non adiabatic repeat element (figure 8.15(a)), the maximum possible fuel utilization decreases with increasing fuel flow rate. At 710°C , the limit is at 92% at 200 ml/min fuel flow rate and decreases to 89% for the adiabatic case. For the non-adiabatic case the limit moves from 87% to 78%.
With an increasing flow rate, the diffusive transport becomes relatively less important. The lean fuel concentration areas suffer from poor convective transport, at low flow rate, which is partly compensated by diffusion, but this effect becomes limited at higher flow rate. For the adiabatic case, for environment temperature over 720°C the dependence on the fuel flow rate changes, the limit increases at low flow rate while it decreases at high flow rate.
At high temperature, the re-oxidation limit is higher (@1.10^{-13} p_{O_2} on the fuel side) and the

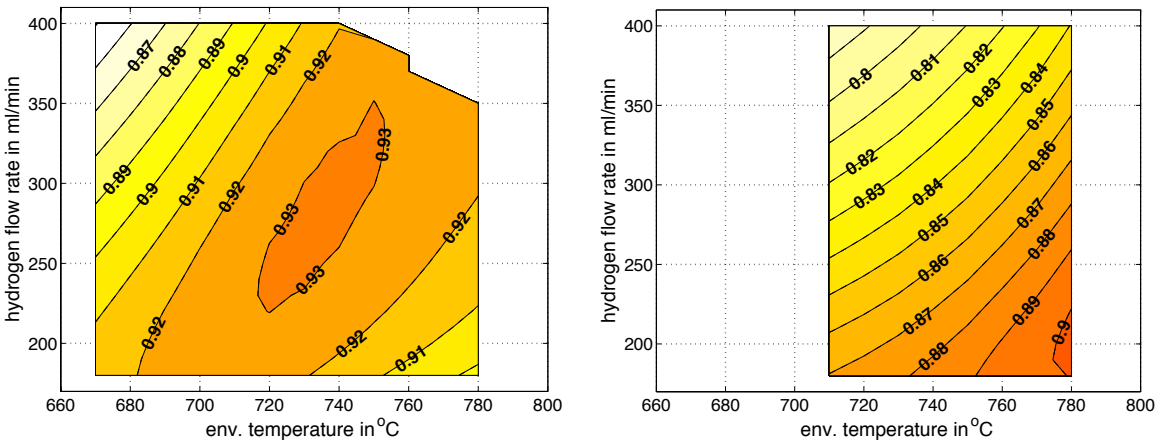

(a) Adiabatic repeat element

(b) Non adiabatic repeat element

Figure 8.15: Limit of possible fuel utilization as a function of environment temperature and fuel flow rate

trend changes. This needs to be verified, however, as the kinetic parameters used are not considered reliable, especially at high temperature.

8.6.2 Coflow case

For the coflow case, the same simulations have been performed and the operation limit is simply the complete depletion of fuel. The fuel concentration is sufficiently homogeneous at the fuel outlet to avoid the anode re-oxidation problem. The limitation is therefore only determined by the total fuel utilization (which depends on the effective current and the shorting current due to the electronic conductivity of the electrolyte).

8.7 Conclusion

The simulation of interconnect degradation allows to explore the impact of different operating conditions on the degradation behavior. The temperature is obviously the main factor on the degradation processes and a linear relation has been established between the mean temperature of the stack and the degradation rate if the latter is expressed as a rate of ASR increase. The use of this criterion to express degradation seems interesting as it allows to compare degradation for different operating points consistently. Other degradation processes such as the electrolyte degradation have not been included in this model. However most of the degradation processes are thermally activated (although some like electrode degradation are current activated as well) and therefore the results of this study can be qualitatively

extended to other degradation processes.
In general, the temperature in the stack should be minimized to decrease degradation rates. Therefore, an environment temperature lowered to 750°C or lower could be beneficial.
The simulation of the anode re-oxidation potential shows that for the counter flow case, where design problems have been identified, the operation would be limited by the potential anode re-oxidation caused by extreme fuel depletion in some areas. The limit of operation is dependent on the flow pattern. For the coflow case, this limitation is not predicted to occur by the model as the fuel concentration at the fuel outlet is homogeneous. On the contrary, for the counter-flow case, the tested repeat element is likely to be even more exposed to anode re-oxidation. The simulated values should therefore be taken as the high limit. The limit in operation for a real case is probably lowered by 5 or 10%. A more accurate flow model with CFD could estimate the operating limit more accurately.
However, the decrease in temperature is favorable to anode re-oxidation and this is in contradiction with the degradation of the interconnect for which a lowering of the temperature is favorable. The operation window for intermediate temperature SOFC is therefore limited on the high temperature by the degradation of the interconnect (and probably other components) and on the low temperature by anode re-oxidation. The operating points concerned are the points at maximum efficiency (high fuel utilization) at which fuel cell will be operated. This anode oxidation potential should therefore be accounted for when defining the operational limits. Anode oxidation should be accounted for at the design to avoid any stagnation point in the fuel flow pattern.
This study is preliminary and shows the potential of simulation to predict and provide information on degradation behaviors. To be completed, a better characterization of the interconnect degradation at different temperature is suitable. The interconnect degradation on the fuel side should be included. Degradation data should be collected for the electrolytes at lower temperature and if possible with the nickel doped electrolyte as anode supported cells are prone to modify the electrolyte composition during sintering. Electrode degradation seems difficult to implement in a near future.
On anode re-oxidation, the sensitivity to the electrode performance should be carried out, preliminary results showed that the risk increases when the electrochemical performances decreases.

Bibliography

C. Clausen, C. Bagger, Bilde-Sorensen, and A. Horsewell. Microstructural and microchemical characterization of the interface betweem $La_{0.85}Sr_{0.15}MnO_3$ and Y_2O_3-stabilzed ZrO_2. *Solid State Ionics*, (70/71):59–64, 1994.

C. Gindorf, K. Hilpert, and L. Singheiser. Determination of chromium vaporization rates of different interconnect alloys by transpiration experiments. In S. C. Singhal and H. Yokokawa, editors, *SOFC VII, Proc. of the int. Symposium, Electrochemical Society*, pages 793–802, 2001.

C. Haering, A. Roosen, and H. Schichl. Degradation of the electrical conductivity in stabilised zirconia systems Part I: yttria-stabilised zirconia. *Solid State Ionics*, (in press), 2004.

K. V. Hansen, K. Norrman, and M. Mogensen. $H_2 - H_2O - Ni - YSZ$ electrode performance: Effect of segregation to the interface. *J. of the Electrochem. Soc.*, 9(151):A1436–A1444, 2004.

M. Hattori, Y. Takeda, Y. Sakaki, A. Nakanishi, S. Ohara, K. Mukai, J.-H. Lee, and T. Fuhui. Effect of aging on conductivity of yttria stabilized zirconia. *J. of Power Sources*, (126): 23–27, 2004.

K. Honegger and A. Plas. Evaluation of Ferritic steel interconnect for SOFC stacks. *SOFC VII, Proc. of the int. Symposium, Electrochemical Society*, 2001-16:803–810, 2001.

K. Huang, P. Y. Hou, and J. B. Goodenough. Characterization of iron-based alloy interconnects for reduced temperature solid oxide fuel cells. *Solid State Ionics*, 1-4(129):237–250, 2000.

M. Jørgensen, P. Holtappels, and C. Appel. Durability test of SOFC cathodes. *J. of Applied Electrochemistry*, 4(30):411–418, 2000.

M. Kuznecov, K. Eichler, S. Megel, and P. Otschik. Application of the ferritic steels for the stack fabrication. In M. Mogensen, editor, *Proc. of the 6th European SOFC Forum*, pages 1573–1585, 2004.

H. Y. Lee and S. M. Oh. Origin of cathodic degradation an new phase formation at the $La_{0.9}Sr_{0.1}MnO_3/YSZ$ interface. *Solid State Ionics*, (90):133–140, 1996.

S. Linderoth, N. Bonanos, K. V. Jensen, and J. Bilde-Sorensen. Effect of NiO-to-Ni transformation on conductivity and structure of Yttria-Stabilized ZrO_2. *J. Am. Ceram. Soc.*, 11(84):2652–2656, 2001.

P. H. Middleton, M. Seiersten, and B. Steele. Morphology and electrochemistry of porous nickel/zirconia cermets. In S. C. Singhal, editor, *SOFC I, Proc. of the int. Symposium, Electrochemical Society*, pages 90–95, 1989.

A. C. Mueller, A. Weber, D. Herbstritt, and E. Ivers-Tiffée. Long term stability of yttria and scandia doped zirconia electrolytes. In S. C. Singhal and M. Dokiya, editors, *SOFC VIII, Proc. of the int. Symposium, Electrochemical Society*, pages 196–199, 2003.

J. Piron Abellan, V. Shemet, F. Tietz, L. Singheiser, and W. Quaddakers. Ferritic steel interconnect for reduced temperature SOFC. In S. C. Singhal and H. Yokokawa, editors, *SOFC VII, Proc. of the int. Symposium, Electrochemical Society*, pages 811–819, 2001.

S. Primdahl and M. Mogensen. Durability and thermal cycling of Ni/YSZ cermet anodes for solid oxide fuel cells. *J. of Applied Electrochemistry*, (30):247–257, 2000.

G. Robert, A. Kaiser, and E. Batawi. Anode Substrate Design for Redox-Stable ASE cells. In M. Mogensen, editor, *Proc. of the 6th European SOFC Forum*, pages 193–200, 2004.

N. Sakai, T. Horita, Y. Ping Xiong, Y. Katsuhiko, H. Kishimoto, M. E. Brito, H. Yokokawa, and Maruyama. Manganese-Chromium-Iron oxide in oxide scale of ally interconnects. In M. Mogensen, editor, *Proc. of the 6th European SOFC Forum*, pages 1646–1653, 2004.

M. Seiersten and P. Middleton. Redox behavior of plasma sprayed nickel anodes. In *SOFC II, Proc. of the int. Symposium, Electrochemical Society*, pages 569–576, 1991.

S. Simner, J. Shelton, M. Anderson, and J. Stevenson. Interaction between La(Sr)FeO3 SOFC cathode and YSZ electrolyte . *Solid State Ionics*, (161):11–18, 2003.

N. M. Tikekar, T. J. Armstrong, and A. V. Virkar. Reduction and re-oxidation kinetics of nickel-based solid oxide fuel cell anodes. In S. C. Singhal, editor, *SOFC VIII, Proc. of the int. Symposium, Electrochemical Society*, pages 670–679, 2003.

H. Tu and U. Stimming. Advances, aging mechanisms and lifetime in solid-oxide fuel cells. *J. of Power Sources*, 1-2(127):284–293, 2004.

D. Waldbillig, A. Wood, and D. G. Iveya. Thermal analysis of the cyclic reduction and oxidation behaviour of SOFC anodes. *Solid State Ionics*, (in press), 2004.

Z. Yang, J. S. Hardy, M. S. Walker, X. Guanguang, S. P. Simner, and J. W. Stevenson. Structure and conductivity of thermally grown scales on ferritic Fe-Cr-Mn steel for SOFC interconnect applications. *J. of the Electrochem. Soc.*, 11(151):A1825–A1831, 2004.

Z. Yang, K. S. Weil, D. M. Paxton, and J. W. Stevenson. Selection and evaluation of heat-resistant alloys for SOFC interconnect applications. *J. of the Electrochem. Soc.*, (150(9)): A1188–A1201, 2003.

H. Yokokawa, N. Sakai, T. Kawada, and M. Dokiya. Thermodynamic analysis on interface between perovskite electrode and YZS electrolyte. *Solid State Ionics*, (40/41):398–401, 1990.

Chapter 9

Optimisation of the repeat element geometry

9.1 Introduction

The stack design is defined by a set of decision variables: the cell area, the thickness of the different layers, the air flow rate at the design point. Design and operating conditions (environment temperature, fuel flow rate, air inlet temperature) determine the behavior of the stack. The requirements on SOFC stack are an increased compactness of the system and an increased reliability (section 1.5). Compactness of the stack can be expressed by the power density (in W/cm^3 - chapter 3) while reliability is often related to temperature field properties (chapter 8) such as maximum temperature, temperature difference, mean temperature.

To improve the stack design on the basis of simulation, sensitivity studies are a first approach, as they allow to explore the impact of a parameter on the performances. In section 3.4, the limits of sensitivity have been shown in our case: no information on a design decision is provided as each of the objective leads to another solution. Optimization with a single objective function goes a step further as not only two decision variables but all decision variables can be accounted for. Nevertheless, the output of such an optimization is limited: only one optimum design is proposed and this design pointed out is not satisfactory if another criterion is considered. Multi-objective optimization (MOO) is therefore required.

The output of a MOO is the Pareto Optimal Front which separates the unfeasible solutions (among them is the "ideal" solution) from the sub-optimal solutions. This Pareto Optimal front allows to identify the trade-off between the two objectives and therefore the best possible compromise solutions. Moreover, the result is a set of solutions in which decision can be taken on the basis of a multi-objective analysis. This method has been tested success-

fully in a number of problems dealing with complex energy systems (Bürer et al. [2003], Li et al. [2004]) as well as fuel cell systems (Godat and Maréchal [2003], Subramanyan et al. [2004] and Palazzi et al. [2005]). This chapter presents the application of multi-objective optimization to the design of a stack. The design objectives have been previously discussed in chapter 1 and 3.
In this chapter, general concepts of multi-objective optimization are first defined. The methods tested within this work are presented and their respective capability to solve various aspects of the problems is demonstrated. The results on the counter-flow and co-flow configurations are presented and discussed.

9.2 Optimisation methods

Three possible methods have been used to solve a multi-objective optimization problems: an evolutionary algorithm, a method based on parametric optimization solving a sequence of non-linear optimization under constraint and finally a hybrid method combining both algorithms. First, some general concepts in MOO are presented.

9.2.1 General definitions

Multi-objective optimization gives a trade-off between two conflicting objectives, allowing to identify the best trade-off solutions. The set of optimal solutions leads to the Pareto Optimal Front (POF) which separates the non-feasible solutions from the sub-optimal solutions (Deb [2001]). Let us define a multi-objective problem: $\vec{y}$ is the set of decision variable and $\vec{x}$ the set of model parameters (not included in the optimization):

$$minimize\ f(\vec{y}) = (f_1(\vec{y}), ..., f_m(\vec{y})) \tag{9.1}$$

$$subject\ to\ h(\vec{y}, \vec{x}) = 0\ and\ g(\vec{y}, \vec{x}) \leqslant 0 \tag{9.2}$$

where $h(\vec{y}, \vec{x}) = 0$ is the condition that the solution have to fullfill the model equations together with the imposed constraints $g(\vec{y}, \vec{x}) \leqslant 0$.
A solution $\vec{u}$ is Pareto-optimal in the objective space $\mathcal{F}$ if $\nexists\ \vec{v} \in \mathcal{F}$ such that $v_k \leqslant u_k\ \forall k = 1, ..., m$ and $v_k < u_k$ for at least one k. A point is Pareto-Optimal if there is no point in the objective space which is better in all objectives. The Pareto Optimal Front can be approached in particular with evolutionary algorithms. To define the Non-Dominated-Set (NDS), the concept of dominance needs to be introduced. A solution $\vec{u}$ dominates $\vec{v}$ if the two following conditions are fullfilled: $\vec{u}$ is not worse than $\vec{v}$ in all objectives and is strictly better than $\vec{v}$ in at least one objective (illustrated in figure 9.1). The Non Dominated Set

is then an approximation of the POF composed of all the non dominated solutions (in an evolutionary algorithm, the NDS is the "optimal" part of the population).
Evolutionary algorithms work with populations of solutions and require a large amount of simulations to define a clear NDS in the objective space (see Leyland [2002]). There is no clearly defined criteria for convergence for a EA-based multi objective optimizer. Therefore, depending on the problem, some trials are necessary to find the correct number of individual evaluations necessary to achieve convergence.

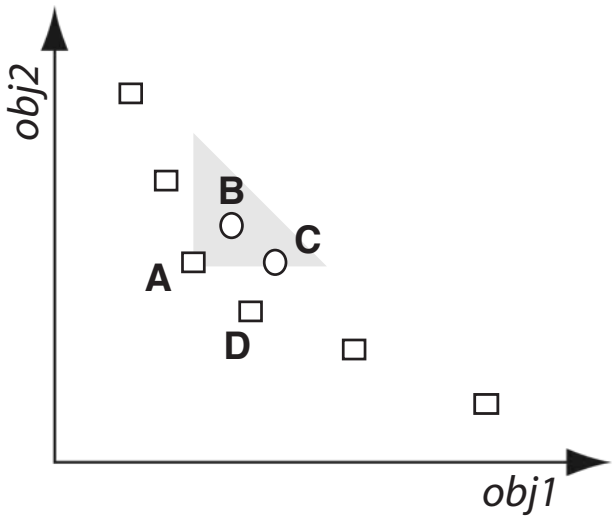

Figure 9.1: Schematic representing the dominance concept and the POF (for a case where both objectives have to be minimized). On this figure, the solution A dominates B (as it is better on both objective) and dominates C (A perform equally on *obj2* and is better on *obj1*). C is dominated by D. The square solutions represent the Non Dominated Set.

9.2.2 The evolutionary algorithm approach

Evolutionary algorithms are known as robust but time consuming for solving single objective optimization and are well suited for multi-objective optimization (MOO) problems especially when only black-box models are available. The algorithm (called QMOO for Queuing Multi-Objective Optimizer) used in this work has been developed by Leyland [2002] and Molyneaux [2002] who have demonstrated its ability to solving complex energy system optimization problems (in terms of decision variables number) and preserving local optima (Bürer et al. [2003], Li et al. [2004] and Palazzi et al. [2005]).

This algorithm has several advantages: it can be used with any model, the model is seen as a black-box by the optimizer (figure 9.2), the optimizer gives sets of variables to be simulated and the model gives back the values of the objective functions. Compared to other EA algorithm, the algorithm contains a self-tuning procedure to adapt the genetic operators

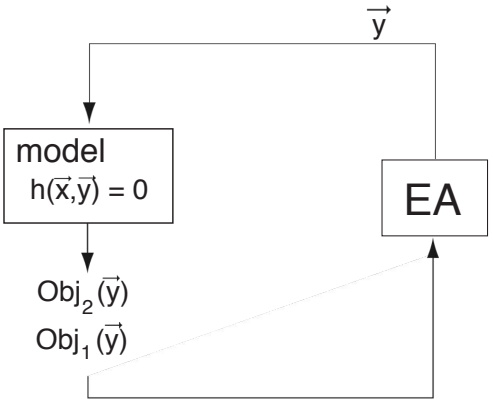

Figure 9.2: Schematic of the EA approach for multi-objective optimization

(cross-over, mutation) during the solving procedure (Leyland [2002], Molyneaux [2002]). The implemented version used in this work does not include the clustering techniques which allows to preserve several local optima.
A large number of evaluations is necessary to define NDS. Furthermore, to use the outputs of the optimization for engineering purpose, a trade-off between the objectives is not enough as clear trade offs on the variables are required. The number of evaluations necessary to obtain this trade-off on the variables is not known a priori and therefore different trials are necessary to determine the number of evaluation necessary (as the fuel cell models used were time consuming, it was not convenient to run the EA on very large numbers of evaluations).

9.2.3 Multi-objective NLP method (MOO-NLP)

The second approach is based on the use of parametric optimization by solving a sequence of single objective optimizations under a parametrized constraint on the other objective (Pistikopoulos and Grossmann [1988] and Hugo et al. [2003]). Single objective optimization is used in a wide range of problems. These problems are generally solved with nonlinear programming (NLP) or mixed-integer non linear programming (MINLP) methods. A review on these methods is presented in Biegler and Grossmann [2004] and Grossmann and Biegler [2004].
The 2D simplified model is implemented in gPROMS that is an equation solver based tool (Oh and Pantelides [1996]), which allows optimization with a NLP optimizer using SQP techniques. Consider now a multi-objective optimization problem having two objectives functions to be minimized: *obj1* and *obj2*. The NLP is able to perform an optimization on *obj1* with a constraint on *obj2*. The first step in the method developed is the calculation of the extremal solutions. For a problem where both objective have to be minimized, this is done by performing two optimizations, the first minimizing *obj1* (optimization problem

one, OP1) and the other minimizing *obj2* (OP2). Then successive optimizations of *obj1* are performed using a constraint on the second objective *obj2*, the constraint is modified at each step to cover the objective space. In our implementation, each optimization is using the same starting point. The optimization is performed for OP1 and OP2, this should allow to identify local optima. Finally, the results of the optimization for each objective are checked and the outputs that do not satisfy the dominance criteria (section 9.2.1) are removed, this procedure is done separately for OP1 and OP2 to preserve local optima (even though some solutions are dominated).
The procedure is therefore the following:

1. solve the optimization for $\min_{obj1}(x)$ without constraint, the results giving the limits of $\min_{feasible}(obj1)$ and $\max_{feasible}(obj2)$
2. solve the optimization for $\min_{obj2}(x)$ without constraint, the results giving the limits of $\min_{feasible}(obj2)$ and $\max_{feasible}(obj1)$
3. compute the step between each optimization as follows

$$d^1_{step} = \frac{\max_{feasible}(obj1) - \min_{feasible}(obj1)}{N_{step}} \tag{9.3}$$

$$d^2_{step} = \frac{\max_{feasible}(obj2) - \min_{feasible}(obj2)}{N_{step}} \tag{9.4}$$

4. for $i \in [1, N_{step}]$ solve the optimization problem OP1 defined as follows:

   $\min_{obj1}(x)$

   subject to $h(x) = 0$ (this condition expresses that the solution has to fullfill the equation system defined by the model)

   and the constraint on the second objective defined as:

$$\min_{feasible}(obj2) + d^2_{step} \cdot i \leqslant obj2 \tag{9.5}$$

5. for $i \in [1, n_{step}]$ solve the second optimization problem OP2 in a similar way:

   $\min_{obj2}(x)$

   subject to $h(x) = 0$

   and the constraint on the second objective defined as:

$$\min_{feasible}(obj1) + d^1_{step} \cdot i \leqslant obj1 \tag{9.6}$$

6. verify that the solutions for OP1 satisfy the dominance condition

7. verify that the solutions for OP2 satisfy the dominance condition

9.2.4 Hybrid method

Multi-objective optimization with an EA has the advantage that the method is robust, however in terms of CPU time, it can become extremely long if the model is complex and takes more than one minute to evaluate the objective function (in general a minimum of 3000 evaluations is necessary). The MOO-NLP method on the other hand can be efficient in terms of CPU time, however as the starting point is the same for all the optimization this method may not find local optima. To combine the EA ability to explore the variable space and the computational efficiency of the MOO-NLP method, a hybrid method has been tested.
The method uses the EA to evaluate a reduced initial population of 500 individuals (usually the initial population of 1000 individuals), with a number of evaluations limited to 600. The NDS defined by the EA is then used as starting points for a serie of NLP optimizations. Each individual from the NDS defines 2 single objective NLP problems as illustrated in figure 9.3. The procedure is:

1. run the QMOO EA algorithm for 600 evaluations (with a initial population of 500 individuals). Solve the following optimization problem $\forall i \in NDS$:

2. solve the problem OP1(horizontal move in figure 9.3) defined as:

   $\min_{obj1}(x)$

   subject to $h(x) = 0$

   and the constraint on the second objective defined as:
   $obj2 \in [obj2^i, obj2^i + \epsilon]$

   with the initial guess $\overrightarrow{x} = \overrightarrow{x_i}$

3. solve the problem OP1(vertical move in figure 9.3) defined as:

   $\min_{obj2}(x)$

   subject to $h(x) = 0$

   and the constraint on the second objective defined as:
   $obj1 \in [obj1^i, obj1^i + \epsilon]$

   with the initial guess $\overrightarrow{x} = \overrightarrow{x_i}$

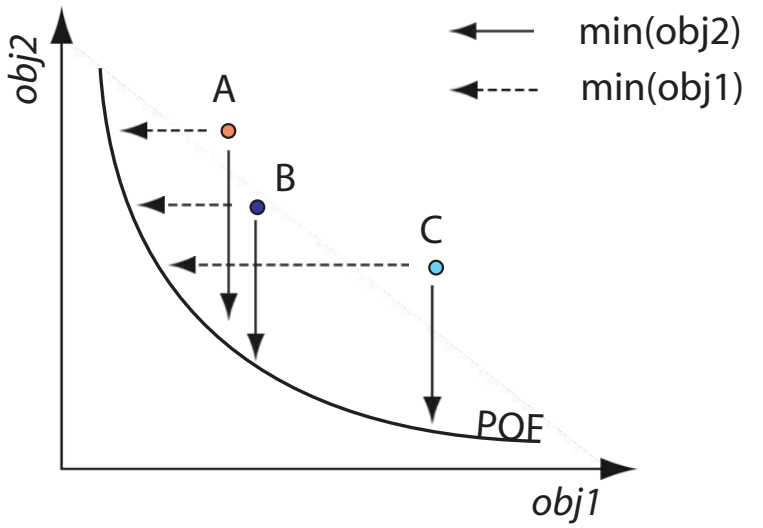

Figure 9.3: Principle of the hybrid optimization method. A, B and C are 3 points in the NDS identified by the EA, these points are used as starting points for 2 linear optimizations.

4. verify if the solution set satisfies the criteria for the NDS

The final NDS obtained is improved from the initial one found by the EA. The use of the population resulting of the EA preserves the chance of identifying local optima.

9.3 Validation of the different optimization methods

The equivalence of the different optimization methods has to be verified for the problems considered in this study. If a priori each method will solve the same problem, it is important to compare the approaches and to identify the one that is more suitable. Two criteria are of importance: computational speed and convergence properties. For the latter, it is important to consider aspects of global optimization recognizing that multiple solutions may be observed. From the computational speed, the NLP is known to be the more efficient. From the global optimization point of view, the EA have attractive properties. The hybrid method should combine both advantages. It has however to be mentioned that the local or near local optima solution identified by the EA may be eliminated by the application of the NLP procedure.

This validation is performed on the problem published in Larrain et al. [2004]. This case considered a counter flow repeat element which has to be optimized with 2 objective functions: 1) maximize power density and 2) minimize temperature difference in the cell. The post-combustion was not included in the model. The variables and their bounds are listed in table 9.1.

Table 9.1: Decision variables of the optimization problem

	bounds	
decision variable	low	high
design variables		
Aspect ratio (-)	1	1.2
Interconnect thickness (cm)	0.05	0.15
Cell area (cm^2)	50	65
operating variables		
Environment temperature (K)	1025	1065
Air Ratio (-)	2.5	4
Fuel flow (ml/min)	290	330

Multi-objective optimization have been carried out for this problem with the three proposed methods. QMOO has been run with a initial population size of 1000 individuals and 3000 evaluations have been performed. The NLP method has been carried out with 50 optimizations for each of the objectives. Finally the hybrid method has been tested with a population

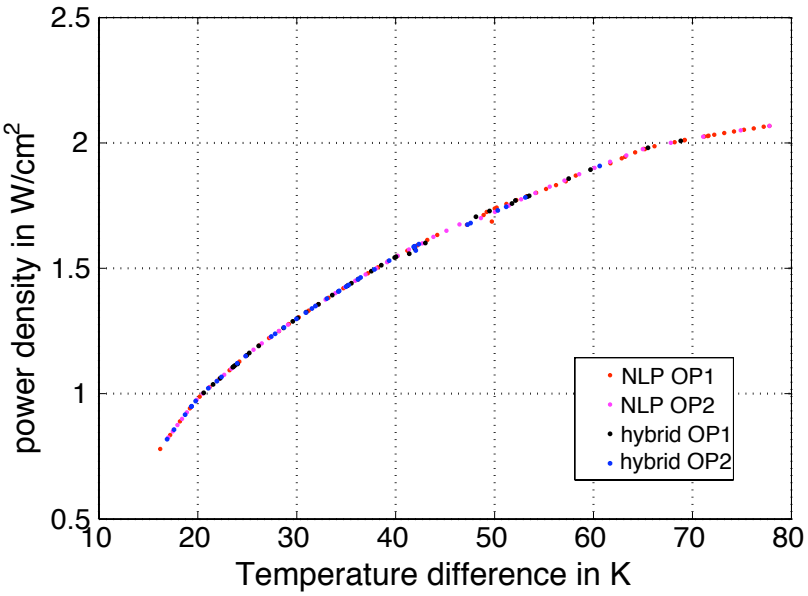

Figure 9.4: Pareto Optimal Front obtained by the MOO-NLP and the Hybrid method. OP1 is the $min(DT)$ problem and OP2 is the $max(\epsilon_{spe})$

provided by QMOO after 600 evaluations with an initial population of 500 individuals.
The results of the three methods are shown on figure 9.4. The POF are similar for the three methods. To be used for an engineering purpose, the results in the variable space are analyzed. Figure 9.5 exhibits the results for one of the variables (the interconnect thickness) represented against one objective function the temperature difference. It can be seen that the trend for the variables is similar for the three methods, interconnect thickness is at the maximum value for the low temperature difference cases and the thickness decreases for

temperature differences larger than 26K. This trend is captured by all the three methods. In the region of the POF between 45 and 60K temperature difference, multiple solutions are identified. Solutions which are quasi equivalent in the objective space show different combinations of the interconnect thickness and air ratio variables. The use of the NLP optimization with the OP1 (minimize the temperature difference) and OP2 (maximize the power density) identifies local optima. The EA version used in this work does not include clustering techniques, therefore the several local optima were not identified.

In terms of computational efficiency, the MOO-NLP method is the most favorable. Less

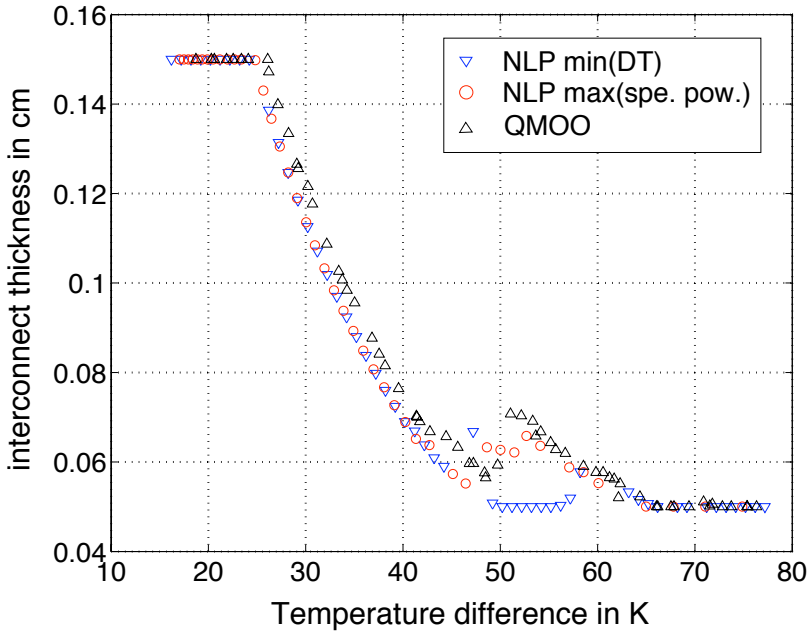

Figure 9.5: Variable space analysis for QMOO and the MOO-NLP method

than 2 hours where required to solve the problem with MOO-NLP, QMOO required 10 hours (for 3000 evaluations) and the hydrid required 2 hours for the initial QMOO step and less than 2 hours for the MOO-NLP step. The MOO-NLP method has therefore been prefered in this work as its efficiency allowed application of optimization to problems where the other methods would lead to extremely long computational times (the co-flow geometry required around 6 hours with the MOO-NLP while the estimated time with QMOO is more than 100 hours).

9.4 Optimization of the stack geometry

Two stack configurations, a counter flow and a co-flow with fuel recovery, have been optimized considering one objective that is related to the stack performance (the power density in W/cm^3) and another related to the life time expectation. For the latter, different objec-

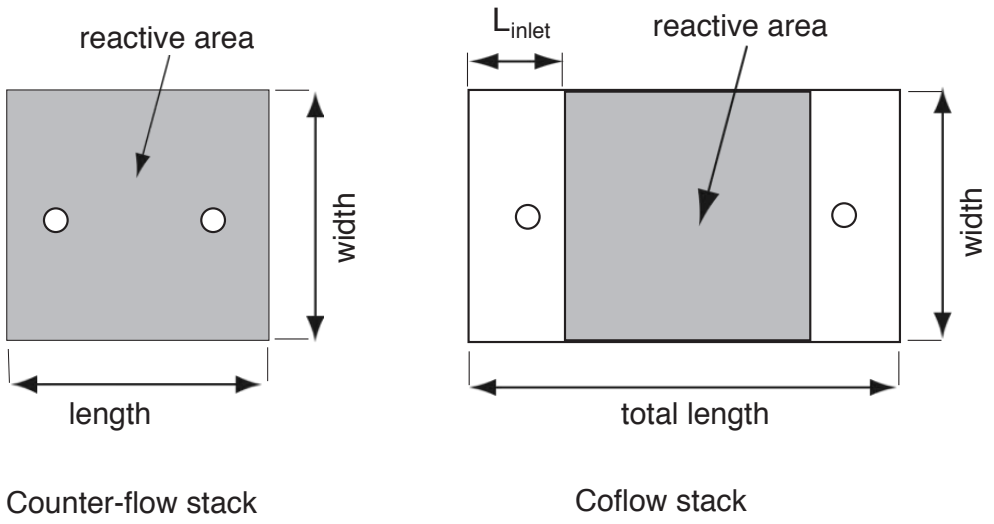

Figure 9.6: Scheme of the optimized stack configuration and definition of the reactive area

tive functions related to the temperature field are proposed: the maximum and the mean temperature in the cell which are related to degradation (chapter 8) and the temperature difference which is related to cell failure induced by thermal stress. The following objective functions pairs have therefore been tested:

- minimize temperature difference in the cell, maximize power density
- minimize maximum temperature in the cell, maximize power density
- minimize mean cell temperature, maximize power density

Seven decision variables are considered (table 9.2). The definition of some decision variables has to be detailed. For coflow, the reactive area (which is a decision variable) is different from the total area of the stack (figure 9.6) and the length of the inlet regions has been kept constant for all values of the reactive area and aspect ratio. For counter-flow, the reactive area is equal to the total area. The aspect ratio is defined on the reactive area, thus for coflow the aspect ratio of the total area is larger than the one specified by the decision variable. For counter-flow, the model used cannot support a large aspect ratio and its range of variation has therefore been limited.
The problems considered here are assuming a pressure drop of 10 mbars on the air side, therefore the air flow rate at the design point is considered to be a design variable as the flow rate will determine the resulting air channel height. The fuel channel has been set to 0.5 mm for all cases and the design is determined for a fixed electric power output of the repeat element of 18 W.
No constraint is given on the minimum width of the repeat element for the coflow case. However depending on the chosen configuration, space for the manifolding of the gases has

to be provided. Future work could address this by adding the sizing of the manifolding holes to the problem and by constraining the inlet and outlet areas to be large enough. In this case, the pressure drop could be added to the problem as a design variable (as it has an impact on the size of the manifolds).

Table 9.2: Degrees of freedom for the optimization problem

	counter-flow case bounds		co-flow case bounds	
Variable	**low**	**high**	**low**	**high**
design variables				
Aspect ratio (-)	1	1.2	1	2
Interconnect thickness (cm)	0.05	0.15	0.05	0.15
Cell area (cm^2)	50	65	50	65
Air Ratio (-)	2	4	2	4
operating variables				
Env. temperature (°C)	680	780	680	780
Fuel flow (ml/min)	250	260	250	260
Air inlet temp. difference (°C)	-100	0	-100	0

9.4.1 Maximum temperature and power density

This section considers the multi-objective optimization of the repeat element geometry with the objective to minimize the maximum temperature in the repeat element and maximize the power density.

Figure 9.7 presents the Pareto Optimal Front for this problem. As expected from the sensitivity analysis, an increase in power density implies an increase in temperature, the trade-off of all the optimal configurations is clearly identified on the POF. The power density range of the counter-flow case shows superior values to the co-flow case. This is explained by the additional surface in co-flow where the area necessary for the air and fuel inlets is accounted for in the power density. For $50cm^2$ of reactive area, the total area of the repeat element is ca. $90cm^2$ for the coflow case (figure 9.6). The POF for counter-flow shows a near linear evolution: 10°C of variation leads to $0.1W/cm^3$ power density increase.

The POF for the 2 configurations forms here a quasi continuous POF indicating a trade-off between the 2 objectives which is valid for both configurations.

The analysis of the variable evolution along the POF indicates the critical variables for the problem. In counter-flow, it appears that the linear trade-off observed on the objective space is the result of non linear variations of four decision variables. Interconnect thickness,

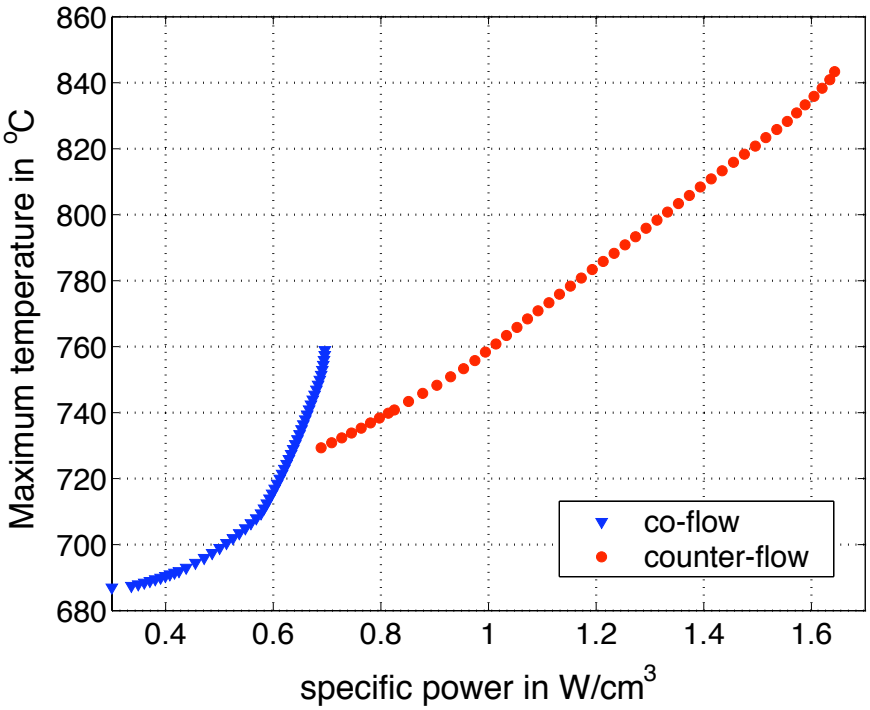

Figure 9.7: Pareto Optimal Front for the minimization of maximum temperature and maximization of the specific power with the counter-flow and co-flow cases

aspect ratio, area and air ratio change from the maximum bound to the minimum bound, the slope of the change is not always regular (figure 9.8(a)). This indicates that for the NDS, the influence of a decision variable on the objectives varies for each region of the POF. Thus this influence depends on the values of the other decision variables. The environment temperature and the aspect ratio are at the minimum bound for all cases, the air inlet difference and fuel flow rate are on their higher bound. Environment temperature and air inlet temperature being at their minimum bound is not surprising as one of the objective is to minimize the temperature. The fuel flow rate reaches at the maximum bound as expected as the temperature increases at constant power with increasing efficiency. The region of the POF between 0.8 and 1W/cm^3 is interesting as very close solutions on the objective space correspond to large changes in the decision variables: the interconnect thickness and the aspect ratio exhibit a steep change and the area has a small variation as well.

In co-flow the behavior is different as variables show successive steep changes (figure 9.8(b)). From low to high power density the order of change in decision variables variation is: air ratio, interconnect thickness, fuel flow rate, cell area and aspect ratio. On some intervals several variables can change simultaneously. An interesting region of the POF is where the points are between 0.5 and 0.6W/cm^3 where the POF shows a discontinuity. We can point again different solutions correspond to this area.

Multi-Objective Optimization provides a large amount of information on the optimal design. It is possible to find regions in the POF where for a small change on one objective function,

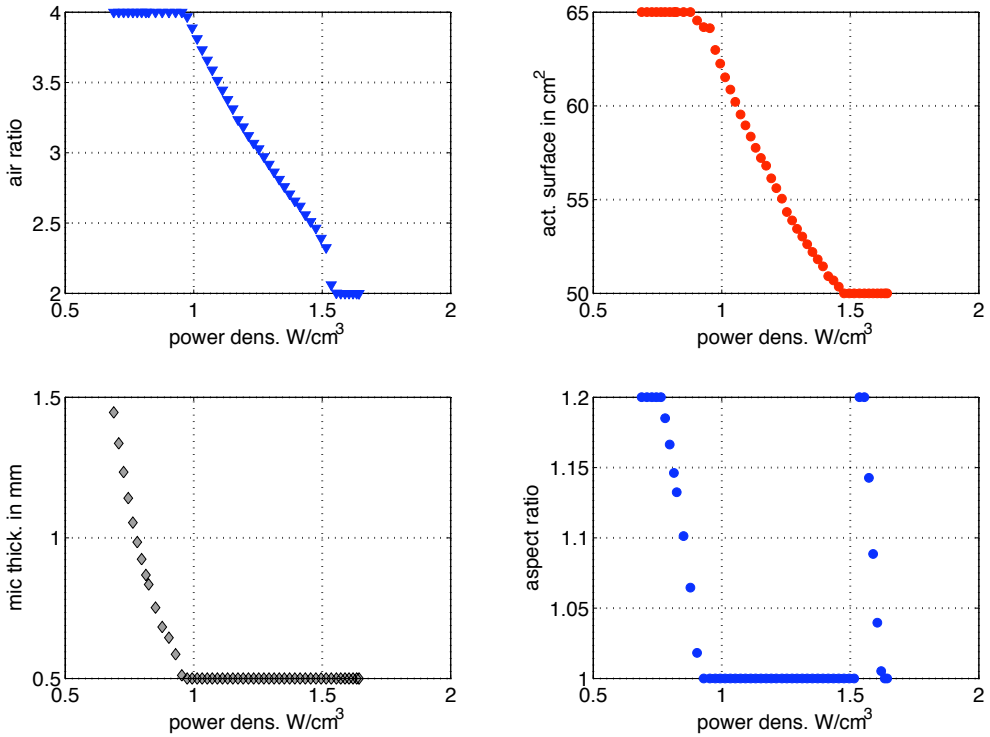

(a) counter-flow design

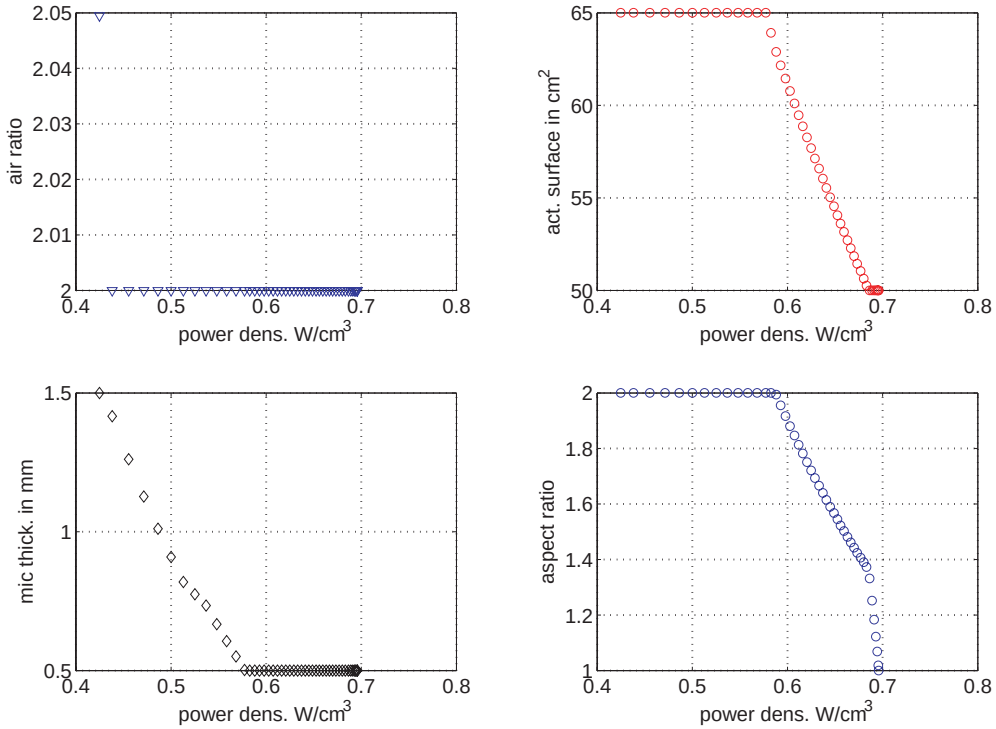

(b) co-flow design

Figure 9.8: Variable space analysis for the maximum temperature and power density problem

the set of decision variables differs significantly. This is valuable for engineering purposes as a choice can be made between these different optimal configurations: there is more than one solution identified.

9.4.2 Temperature difference and power density

The POF for the 2 configurations are shown in figure 9.9 for the problem with the temperature difference. Similarly to the previous MOO problem, the range of power densities are different for the 2 concepts. The range of values for the temperature is similar for the 2 configurations. Both POF show a clear trade-off between the 2 objectives.
The variable space analysis for the counter-flow case is quite different from that for the other problem discussed in section 9.4.1: in the low range of power density, the air ratio and the area decrease while the interconnect thickness is at its maximum bound, then the interconnect thickness decreases. The fuel flow rate is at the higher bound for power densities lower than $1.2 W/cm^3$, for higher values the behavior is not clear.
For this case, a number of optimization failures occured but intermediate results were nevertheless kept if the output from optimization was a point which had the properties of belonging to the NDS (section 9.2.3). The large number of failures required the optimization with both objective functions to define the POF. These failures could be explained by the operating point chosen for the optimization where fuel utilization is quite important ($> 70\%$). This choice of operating point is justified by the fact that the fuel cell's main advantage is their ability to operate at high efficiency (and thus at high fuel utilization), therefore it does not make sense to perform an optimization at 50% fuel utilization. Furthermore, the post-combustion is defined by a parameter which is uncertain (chapter 5), for such range of fuel utilization (60% and more) the maximum temperature is no longer in the post-combustion zone (chapter 3). Another possible explanation for the failures is multiple optima. As a result from these problems, the trends on the variables are not perfectly clear.

The variable space analysis on the co-flow solution shows a similar behavior as for the previous problem. From low power density to high power density the order in decision variables variation is: air ratio, fuel flow rate, cell area, interconnect thickness, and aspect ratio. The environment temperature being at the high bound on most of the POF (expect at the highest power density values).

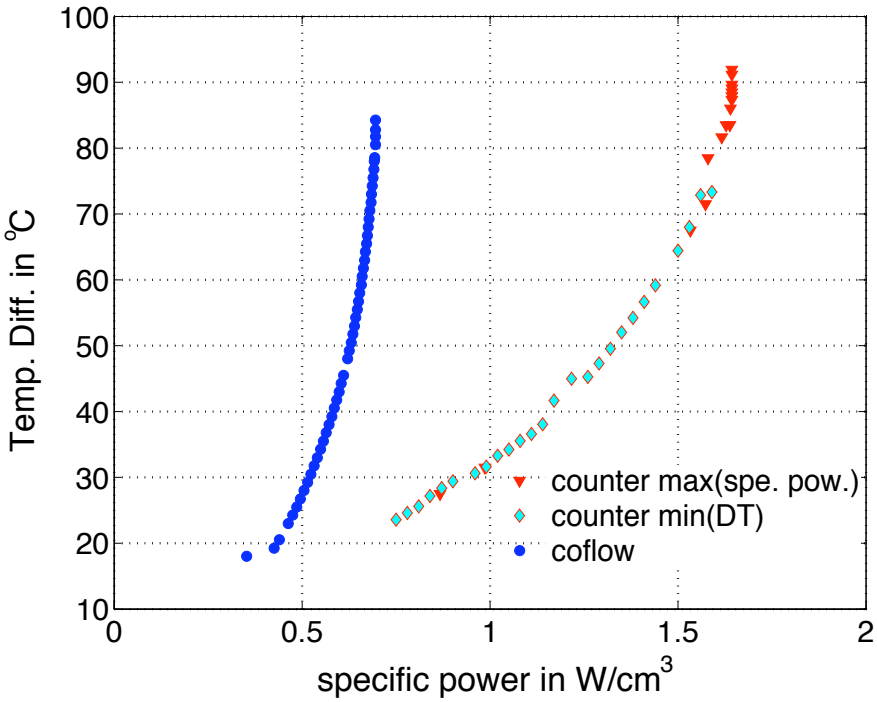

Figure 9.9: Pareto Optimal Front for the minimization of temperature difference and maximization of the specific power with the counter-flow and co-flow cases

9.4.3 Mean temperature and power density

The mean temperature has been demonstrated to be strongly correlated to the degradation behavior, the MOO problem minimizing the mean temperature on the cell and minimizing the power density is presented here.

The POF shows a bi-linear trend with a change in the trade-off between the two objectives at the value of 0.92W/cm^3 . For higher power densities, the trade-off is linear. Here the linear trade-off results from the variation of 3 variables: the air excess ratio, the cell area, the aspect ratio. On the low range of power densities, the trend is such that for a small impact on the mean temperature (less than 10°C), the power density increases from 0.68 to 0.92W/cm^3 . On this region of the POF, the variable that varies is the interconnect thickness which decreases from one bound to the other. On this area of the POF, the mean temperature increase is small, however as the interconnect thickness decreases significantly, the maximum temperature and temperature differences increase.

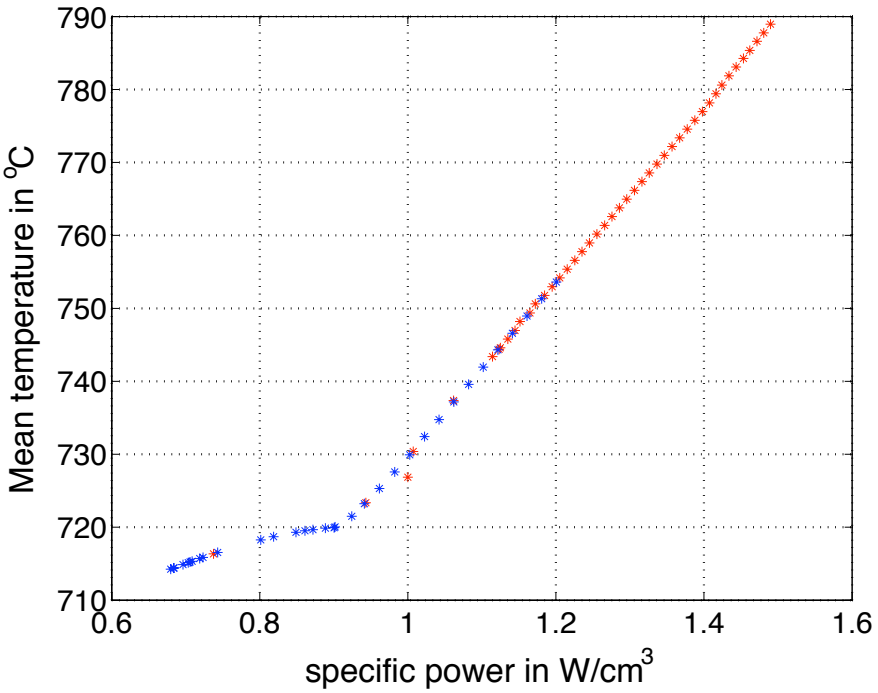

Figure 9.10: Pareto optimal front for the minimization of mean temperature and maximization of power density for the counter-flow case

9.4.4 Sensitivity of the optimal configuration to the electrochemical performance

The optimizations performed in the previous section have been performed with a set of electrochemical parameters (identified in chapter 4, section 4.5.2). The electrochemical performances are however in constant evolution, the goal is in general to improve performances. As an example, the counter-flow repeat element is usually operated with fuel flow rates in the range of 200 to 400 ml/min hydrogen, but if the electrochemical performances of the cells decrease significantly, the ideal range of fuel flow rate is shifted to lower values. This would require a decrease in the fuel channel height to adapt the pressure drop to the new flow rates. The design is therefore dependent on the electrochemical behavior of the cell.
Therefore, the robustness of the optimization results to the electrochemical performance scenario has to be verified. This is done in the following by increasing by a factor 2 the losses on the electrodes (defined by a resistance as a function of temperature).
The operating point for the optimization has been chosen in the same range of fuel utilization and the same range of fuel flow rate, the target power output has thus been decreased to 14.5W.
The optimization for the minimization of the maximum temperature and the maximization of power density have been carried out. The results are presented on figure 9.11 for the POF and on figure 9.12 for the variable space analysis. The POF, compared to the same

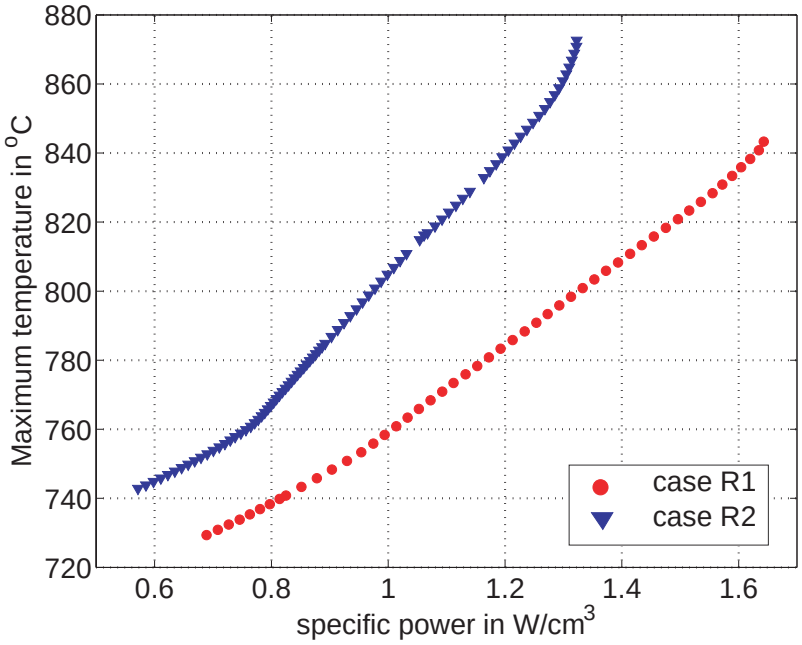

Figure 9.11: Pareto optimal front for the maximum temperature and power density problem for the 2 scenarios on electrochemical performances.

problem in section 9.4.1, shows a similar shape. However, the temperature range is larger and extended to higher temperatures and the power density range is shifted to lower values. For the variable space analysis, the trend on the variables exhibit similarities with the case in section 9.4.1. Nevertheless, the active area and aspect ratio present small differences in their variations.

A configuration which is optimal for a given set of electrochemical parameters is not necessarily optimal if the electrochemical performances change.

9.4.5 Discussion on the results

Multi-objective optimizations have been performed for different problems related to 2 different stack geometries. The output from a MOO is of great use for the repeat element and stack design: on the contrary to sensitivity analysis, which allows to identify conflictive objective but does not provide any valuable information to take a design decision, MOO provides a set of optimal solutions defining all the best compromise for the objective functions chosen. Among these solutions, different configurations can lead to close results on the objective space, thus to quasi equivalent solutions in terms of performance. The choice between these configurations can then be done on the basis of expertise or other criteria which are not included in the optimization problem.

The problems presented seem to have several optima on some regions, as for example the

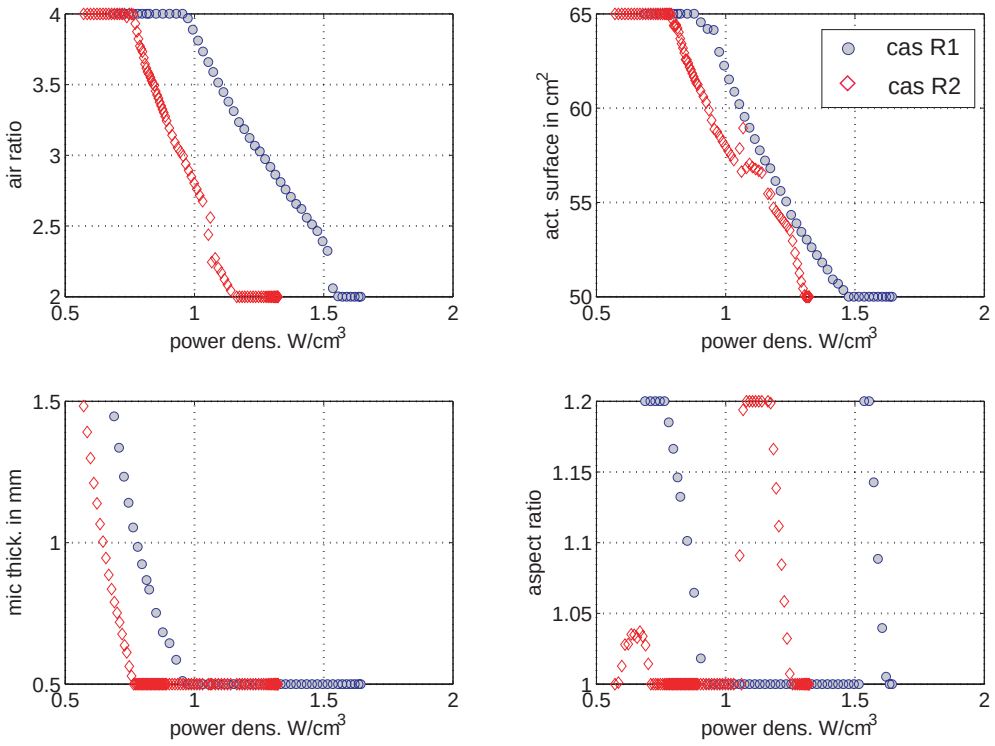

Figure 9.12: Variable space analysis for the 2 scenarios on electrochemical performances.

case of the counter flow repeat element with the minimization of temperature differences. These local optima are not always identified by the optimization method used here (the MOO-NLP). When applicable the hybrid method could be useful. Nevertheless, for the case presented here the model was always close to the unfeasible domain (because of the high fuel utilization) and the first step in the hybrid optimization (using QMOO) would give poor results because of simulation failures. This problem is solvable but this would require an excessive CPU time.

The choice of the objective function is extremely important for the choice of the configuration. To illustrate this, table 9.3 summarizes the optimal configurations at $1W/cm^3$ for the problem on maximum temperature, maximum temperature difference and mean temperature. Solutions for the mean and maximum temperature are very close (in the variable space and in the objective space), the solution of the temperature difference is very different. The choice of the objective function is therefore essential: the set of objectives has to correspond to the priorities in the design. If other criteria are important, they can be introduced in the problem as additional constraints. As an example, defining the priority on the mean temperature (as it defines the degradation), a constraint can be defined for the maximum temperature and the temperature differences. From the performed optimizations, the objective function recommended is the maximum temperature: results are close to the mean temperature but the temperature differences are slightly lower.

The dependence of the optimal solution on the electrochemical performances is an issue.

Table 9.3: Solutions for 1W/cm^3 power density for the 3 MOO problems. Values for the objective function are in bold.

Variable	min($max(T)$)	min(DT)	min($meanT$)
design variables			
Aspect ratio (-)	1	1.2	1.007
Interconnect thickness (cm)	0.5	1.5	0.5
Cell area (cm^2)	62.25	52	60.62
Air Ratio (-)	3.88	2.2	4
operating variables			
Env. temperature (°C)	680	750	680
Fuel flow (ml/min)	260	260	260
Air inlet temp. difference (°C)	100	100	100
max T	**758**	827.5	765.5
mean T	731	817.5	**729.6**
DT	82.8	**28.5**	97.7

On the methodology side first. Here the choice has been made to keep the fuel flow rate and the fuel utilization in the same range and change the power output in consequence, but the answer would have been different if the power output would have been kept constant and the fuel flow rate increased. This option has not been considered as it would have resulted in a temperature range which would have been way too high for an intermediate temperature SOFC (with temperature over 900°C).
The dependence of the optimum solutions on the electrochemical performances is a characteristic that makes the optimization of the stack configuration a global problem which cannot be solved by the only means of simulation: to provide useful and adapted solutions, the model used requires realistic kinetic parameters. And these parameters can only be identified on the basis of experiments (chapter 4). But then, the production quality has to be regular to provide cells in a range of performance close to the performance used to define the design.

9.5 Conclusion

Multi objective optimization has been successfully applied to the optimization of a stack design. The results allow to identify trends between the conflictive objectives. Several sets of objective functions have been applied and the optimal solutions are obviously different

for each of the cases. The choice of the objective function is essential. Furthermore, the dependence of the optimal solutions on the electrochemical performances of the cells calls for an integration between experiments, which allows to identify the kinetic parameters, and design procedure.

In future work, the exploration of the sensitivity of the optimal solution to the performance could be further investigated as it may be possible to define a range of electrochemical performance for which the optimal solutions remains valid. Further integration of the following problems to the optimization would be of interest: 1) The geometry of the gas distribution devices (manifolds) would add new aspects. 2) The integration of the micro-scale modeling on the electrode thickness, surface coverage of the current collectors (which have an influence on the pressure drop and on the electrochemical performances). This integration would allow to fill the gaps between the micro-scale issues and the stack design problem.

Bibliography

L. T. Biegler and I. E. Grossmann. Retrospective on optimization. *Computer and Chemical Engineering*, 28(10):1169–1192, 2004.

M. Bürer, K. Tanaka, D. Favrat, and K. Yamada. Multi-criteria optimization of a district cogeneration plant integrating a solid oxide fuel cell, gas turbine combined cycle, heat pumps and chillers. *Energy*, 28(6):497–518, May 2003.

K. Deb. *Multi-Objective Optimization using evolutionary algorithm.* Wiley, 2001.

J. Godat and F. Maréchal. Combined Optimisation and Process Integration Techniques for the Synthesis of Fuel Cells Systems. In A. Kraslawski and I. Turunen, editors, *Proc. of the 13th European Symposium on Computer aided process engineering*, pages 143–148, 2003.

I. E. Grossmann and L. T. Biegler. Part ii. future perspective on optimisation. *Computer and Chemical Engineering*, 28(8):1193–1218, 2004.

A. Hugo, C. Ciumei, A. Buxton, and E. Pistikopoulos. Environmental impact minimisation though Material Substitution: a Muliti-objective optimization approach. In A. Kraslawski and I. Turunen, editors, *Proc. of the 13th European Symposium on Computer aided process engineering*, pages 683–688. Elsevier, 2003.

D. Larrain, F. Maréchal, N. Autissier, J. Van herle, and D. Favrat. Multi-scale modeling methodology for computer aided design of a solid oxide fuel cell stack. In A. Barbosa-Povoa and H. Matos., editors, *Proc. of the 14th European Symposium on Computer aided process engineering*, pages 1081–1086, 2004.

G. Leyland. *Multi-Objective Optimisation Applied to Industrial Energy Problems.* PhD thesis, Swiss Federal Institute of Technology of Lausanne, march 2002.

H. Li, M. Burer, Z.-P. Song, D. Favrat, and F. Maréchal. Green heating system: characteristics and illustration with multi-criteria optimization of an integrated energy system. *Energy*, 29(24):225–244, february 2004.

A. Molyneaux. *A practical evolutionary method for the multi-objective optimisation of complex energy systems, including vehicle drivetrains.* PhD thesis, Ecole Polytechnique Fédérale de Lausanne, 2002.

M. Oh and C. Pantelides. A modelling and simulation language for combined lumped and distributed parameters systems. *Computer and Chemical Engineering*, 20-6/7:611–633, 1996.

F. Palazzi, J. Godat, F. Maréchal, and D. Favrat. Thermo-economic modelling and optimisation of fuel cell systems. *Fuel cells*, 5(1):5–24, 2005.

E. N. Pistikopoulos and I. E. Grossmann. Optimal retrofit design for improving process flexibility in linear systems. *Computers and Chemical Engineering*, 12(7):719–731, 1988.

K. Subramanyan, U. M. Diwekar, and A. Goyal. Multi-objective optimization for hybrid fuel cells power system under uncertainty. *J. of Power Sources*, pages 99–112, may 2004.

Chapter 10

Conclusion

10.1 Overview

Solid oxide fuel cell technology is promising for power production and cogeneration. The main challenges facing this technology are: to decrease the cost of the stack and of the whole system, to limit the degradation and to increase reliability. The design of the stack has a strong impact on the performance, compactness and degradation behavior. This work contributes to the development of a design framework where most stack design aspects can be integrated and considered globally. The focus of this work has been on the development of a model able to simulate a wide range of planar configurations. A methodology for parameter identification from experiments and model validation has been defined and the model has been validated. The model has been applied to simulate transient and degradation behavior. The application of multi-objective optimization methods to the planar design allows the identification of an interesting configuration.

10.1.1 Repeat element and stack simulation

The model presented and used in this work to perform the simulations is a 2D volume averaged model including an original 2D flow description. It allows the simulation of non-trivial flow fields. The model development is a compromise between computational efficiency and accuracy. The electrochemical model includes an imperfect electrolyte behavior.
This model has been successfully applied to the simulation of two novel stack designs: a counter-flow configuration and a coflow alternative configuration. The simulation of the counter-flow has elucidated major design problems: the internal manifold, which results on a compact design, leads to local fuel depletion on some areas which limits the achievable fuel

utilization and efficiency. The temperature field, with the combination of a counter-flow and post-combustion on the fuel outlet, shows important gradients and excessive temperatures for an intermediate temperature SOFC.
The coflow alternative configuration solves the main problems identified with the counter-flow configuration. The inlets and the active area are separated and the fuel is recovered to avoid the post-combustion.
The model has been designed to efficiently perform sensitivity analysis. The performed sensitivity analyses show that the challenges on the SOFC stack design are conflictive and sensitivity analyses alone does not provide the necessary information to assist design. Rather, optimization techniques are shown to be the preferred route.
Transient simulations have been carried out. The results show that the thermal inertia is non-negligible for an SOFC. An interesting result is that the design of the stack seems to have little influence on the transient behavior.
New phenomena have been implemented in the model: the interconnect degradation and the equilibrium of the nickel/nickel oxide. These new features allow the simulation of the degradation behavior for a wide range of different cases and the identification of operating limits at high fuel utilization to avoid anode re-oxidation. The degradation behavior is highly affected by the design and operating parameters. A new criteria to express the degradation is proposed which allows a consistent comparison of cases at different cell potential and current densities. With this criteria, a clear trade-off has been pointed out between the simulated mean temperature and the degradation.

10.1.2 Model validation

Model validation has been carried out from standard experiments and locally resolved specific experiments. Parameter identification has been used to validate the model by identifying the uncertain parameters that minimize the differences between experiments and model results. The currently performed measurement on button cells and repeat element do not provide sufficient data to identify parameters for a rigorous electrochemical model. Thus a simplified kinetic model is proposed. The methodology has nevertheless allowed simulation of the behavior of button cells and repeat elements with satisfactory accuracy.
New ideas on the explanation for observed low open circuit voltages are presented: the contribution of a non-perfect electrolyte with a shorting current is confirmed although no rigorous proof is provided. The order of magnitude for this shorting current is estimated to be in a range between 15 mA/cm^2 and 100 mA/cm^2 .
Locally resolved experiments are used to verify current density and temperature simulated by the model. The validation is not complete, however, it is difficult to determine whether the discrepancies are from the model, which does not fully represent the experiment, or from

the experiments, which have uncertainties and errors.
The model used for simulation and optimization has been successfully verified (as reasonably capturing the flow field) by the comparison with a more complete and accurate CFD 3D model.

10.1.3 Stack design optimization

Multi-objective optimization methods have been applied successfully to the stack design. Application of such methods to this type of problem is new and novel strategies are proposed. Trade-offs between temperature indicators and power density have been identified. The choice of the objective function has a strong impact on the optimal configuration identified, which is sensitive to the electrochemical performance of the cell.
The link between the design framework and the experiments is necessary to end with a design adapted to the observed electrochemical performance of the cells. The choice of the objective function is essential and priorities have to be defined as the resulting design is strongly influenced by the choice of the objective function.

10.2 Future work

A general framework for a computer aided design tool for SOFC stack has been established. Further work could be carried out in several directions:

- The model could be improved by the integration of micro-scale models, the addition of fluid distribution along the stack and system aspects.

- Reforming related processes could be included in the model (at present this is only at a preliminary stage) and the choice between steam reforming and partial oxidation could be considered. Different pre-reforming rates could be explored as well.

- The simplified model itself could be further improved on the basis of the development for the coflow model: local refinement of the mesh would allow to increase the quality of the fluid pattern description.

- The model validation needs to be continued and specifically designed experiment should be designed to decrease the uncertainty and the perturbations on the measurements. This would allow a more efficient model validation by parameter estimation methods.

- Kinetic parameter identification should be carried out more systematically to increase the confidence on the parameter used and specific experiment allowing to discriminate losses between the two electrodes would be an asset.
- Transient simulations on the repeat element and stack are limited if no system behavior is accounted for. System components could be included to the simulation.
- Degradation and operating limits simulation is at an early stage: improvement on the characterization of the degradation phenomena in different conditions is necessary. Further investigations on the phenomenon that could be included into the degradation simulation could extend the model presented in this work.

Appendix A

Appendix A

A.1 Chapter 2

A.1.1 Modeling a complex geometry with several domains with the simplified model

Modeling a complex geometry may require the definition of different domains for the fluid motion description: this allows to have a better definition in regions where a large mesh could be required without refining the mesh on the whole geometry. Furthermore, this allow to have different Darcy coefficients for the porous media depending on the zone. As an example, the co-flow geometry assumes a larger resistance in the channel zone than in the inlet areas.
The two domain are defined as

$$D_{channel} : \forall \quad x\epsilon\,[0\ L_x]\,, \forall \quad y_{ch}\epsilon\,[0\ L_{ch}] \tag{A.1}$$

$$D_{inlet} : \forall \quad x\epsilon\,[0\ L_x]\,, \forall \quad y_{inlet}\epsilon\,[L_{ch}\ L_{inlet}] \tag{A.2}$$

At the boundary between 2 different zones ($x = Lch$ on the figure A.1) the following equalities have to be specified:

- pressure field is equal

$$P_{channel} \quad = \quad P_{inlet} \tag{A.3}$$

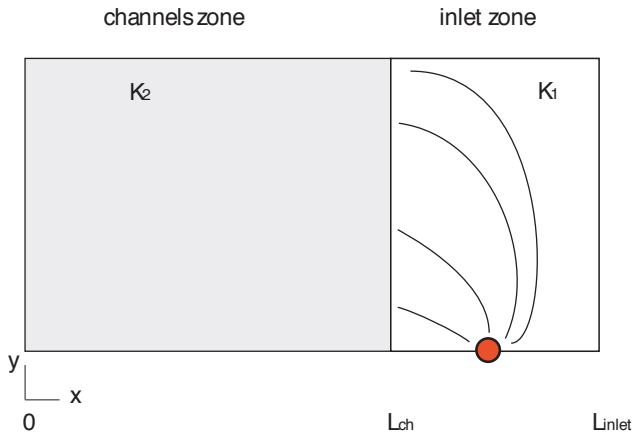

Figure A.1: Scheme showing the 2 zones: an inlet zone and the reactive area.

- velocity in the direction normal to the boundary is equal

$$v_x^{channel} = v_x^{inlet} \tag{A.4}$$

- temperatures are equal

$$T_{solid}^{channel} = T_{solid}^{inlet} \tag{A.5}$$

- heat flux is conserved in the direction normal to the boundary

$$\frac{\partial T_{solid}^{channel}}{\partial x} = \frac{\partial T_{solid}^{inlet}}{\partial x} \tag{A.6}$$

- concentrations are conserved

$$\mathcal{C}_i^{channel} = \mathcal{C}_i^{inlet} \tag{A.7}$$

$$\frac{\partial \mathcal{C}_i^{channel}}{\partial x} = \frac{\partial \mathcal{C}_i^{inlet}}{\partial x} \tag{A.8}$$

A.1.2 Post-combustion zone definition

The fields for velocity, concentrations (obviously including molar fractions) are defined on an extended domain (of length L_{PC}). The molar fraction of the fuel is defined on the coordinate

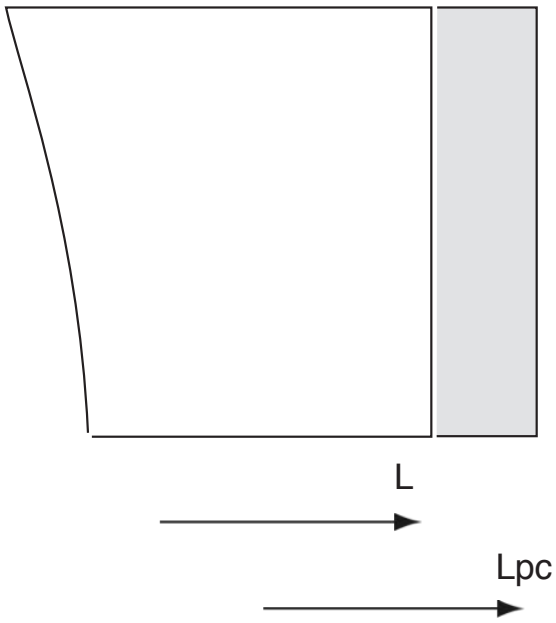

Figure A.2: Scheme of the post-combustion area

$x = L_{PC}$ by the following equations:

$$\mathcal{C}_{H_2} = 0.01 \tag{A.9}$$

$$\mathcal{C}_{H_2O} = 0.99 \tag{A.10}$$

$$\tag{A.11}$$

The assumes that at the coordinate at the end of the extended domain, the post-combustion is almost complete.

A.1.3 Numerical validation of the simplified model

A.1.3.1 Species balance errors on the simplified model

Table A.1: Results sensitivity to the mesh size:

	11x21	16x31	21x41	31x61	41X81	51x101
error on species balance (%)	1.2	0.6	0.45	0.38	0.32	0.28
Max. Temp. Solid in K	1240.2	1224.5	1217.2	1216.6	-	-
power output in W	19.80	19.92	19.92	19.93	-	-

A.1.4 Stack model validation

The main feature of this stack model is to allow computation of large stack without requiring a complete mesh for the stack. The sensitivity of the results to the number of computing cell along the height of the stack has been verified. Firstly, a 15 cells stack has been simulated with 3 different meshes, the results can be seen on figure A.3. Another check has been done on larger stack, assuming 50 cells, this stack has been simulated with 12, 15 and 20 nodes.

This validation procedure allow to use the stack model with sufficient confidence for large

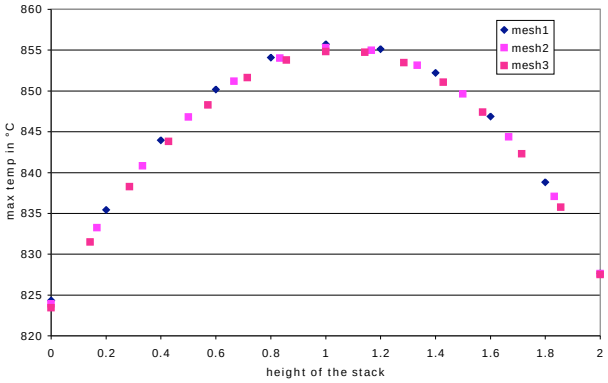

Figure A.3: Maximum temperature along the height of the stack (15 cells). The different meshes (11, 13 and 15 points used give very close outputs.

stacks. For short stack up to 20 cells, a mesh of 8 to 12 nodes is enough. For larger stack, as the gradients in the z direction can be quite important close to the edges, the mesh has to 15 nodes as a minimum. To avoid such a large mesh, in further work, the stack height could be separated in 3 zones, 2 zones for the edges where the mesh could be finer and a zone of the middle of the stack where a coarser mesh in satisfactory.

A.2 Annex

A.2.1 Parameter estimation objective function

The model can be considered as a set of mathematical equations that satisfy

$$F(\bar{X}, \bar{z}, \bar{\theta}, \tilde{\theta}) = 0 \tag{A.12}$$

where $\bar{X}$ are the non measured variables and $\bar{z}$ the measured variables. The set of parameters θ is divided in parameters $\bar{\theta}$ that will be identified by the experiment and $\tilde{\theta}$ which are fixed. The algorithm used is the tool for parameter estimation in the gPROMS package and the objective function ϕ to be minimized is detailed as follows:

$$\phi = \frac{N}{2} \ln 2\pi + \frac{1}{2} min_{\theta} \{ \sum_{i=1}^{NE} \sum_{j=1}^{NV_i} \sum_{k=1}^{NM_{ij}} (\ln \sigma_{ijk}^2 + \frac{(\tilde{z_{ijk}} - z_{ijk})^2}{\sigma_{ijk}^2}) \} \tag{A.13}$$

where:

N	Number of measurements
θ	Set of parameters to be optimised
NE	Number of experiments performed
NV_i	Number of variables in the ith experiment
NM_{ij}	Number of measurements of the jth variable in the ith experiment
$\tilde{z_{ijk}}$	kth measurement value of variable j in experiment i
σ_{ijk}	Variance of the kth measurement of variable j in experiment i
z_{ijk}	kth model predicted value of variable j in experiment i

The objective function, which has to be minimized, defines the error between predicted values by the model and the experimental values.
Optimization of parameter requires an initial guess and the definition of minimum and maximum bound. If the results are on one of the bounds, then the confidence interval cannot be computed, it is therefore usefull to re-run an optimization to have a well defined final point. The confidence interval is highly dependent on the amount of data considered in the optimization process and on the quality of the experimental data.

Diego Larrain
Pré-du-marché 35
1004 Lausanne
Switzerland
diego.larrain@a3.epfl.ch

Education

2000 : Graduated as mechanical engineer at the Swiss Federal Institute of Technology in Lausanne. Diploma thesis on energetic and economic modeling of food processes in Tunisia.

Award for the best Sustainable development project.

1994 : Baccalaureat C (scientific) in Caen (France).

Employment experience

Mai 2001- now : Laboratory for Industrial Energy Systems

PhD student in the Solid Oxide Fuel Cells group. Development of a stack in collaboration with HTceramix : testing and simulation of repeat elements and stacks. Creation of a computer aided design method for the stack, based on simulation models and optimization methods.

Supervisors : Prof. D. Favrat and Dr. J. Van herle.

April 2000 – December 2000 : Laboratory for Industrial Energy Systems

Research assistant. Responsible for the testing of a thermodynamic cycle designed for a hybrid solar power plant. Increased the efficiency achieved in the lab and demonstrated the concept by first operation with solar concentrators.

Main publications

Multi-scale modeling methodology for computer aided design of a solid oxide fuel cell stack.
D. Larrain, F. Maréchal, N. Autissier, J. Van herle, D. Favrat. Proceedings of the ESCAPE14 conference, pages 1081-1086, 2004. A. Barbosa-Povoa and H. Matos (editors). *Paper presented during an oral session*.

Generalized model of planar SOFC repeat element for design optimization.
D. Larrain, J. Van herle, F. Maréchal, and D. Favrat. *J. of Power Sources 131*, pages 304-312, 2004

Thermal modeling of a small anode supported solid oxide fuel cell.
D. Larrain, J. Van herle, F. Maréchal, and D. Favrat. *J. of Power Sources 114*, pages 203-212, 2003.

Contributions to workshops

Modeling for design: optimization of a repeat element.

D. Larrain. F. Maréchal. J. Van herle. D. Favrat. **Invited speaker** at SOFCnet worshop on modeling. Bordeaux, September the 28th, 2004.

Experimental validation of SOFC models.

D. Larrain, J. Van herle, D. Favrat. **Invited speaker** at the Fuel cell modeling and experimental validation workshop. Stuttgart, March 3-4, 2005.

Languages

French : mother tongue
English : fluent
Spanish : fluent
German : basic knowledge

Skills

Simulation tools:

Strong expertise with gPROMS (PSEnterprise Ltd), good knowledge of MATLAB, use of Fluent (CFD tool), basic knowledge in c-programming (under Linux). Use of Windows, Mac and Linux OS.

Laboratory skills :

Assembly of stacks, use of fuel cell test facilities, basic knowledge of Labview and impedance spectroscopy, .

Extracurricular activities

Involved in student association for 3 years. President of the organizing committee of a students' meeting in 95/96. President of the student association in 96/97.

Hobbies

Sports (windsurfing, rowing, back-country snowboarding), traveling.